Probing chalcogenide films by advanced X-ray metrology for the semiconductor industry

Walter Batista Pessoa

NNT : 2018SACLS330

Probing chalcogenide films by advanced X-ray metrology for the semiconductor industry

Thèse de doctorat de l'Université Paris-Saclay
préparée à l'Université Paris-Sud

École doctorale n°576 : Particules hadrons énergie et noyau : instrumentation, image, cosmos et simulation (PHENIICS)
Spécialité de doctorat : Physique des accélérateurs

Thèse présentée et soutenue à Grenoble, le 27 Septembre 2018, par

Walter Batista Pessoa

Composition du Jury :

Anne Lafosse Professeure, Institut des Sciences Moléculaires d'Orsay (ISMO) Université Paris Sud	Présidente
Philippe Jonnard Directeur de recherche CNRS, Laboratoire de Chimie Physique Matière et Rayonnement (LCPMR) Sorbonne Université	Rapporteur
Eugénie Martinez Ingénieur-chercheur, Département Technologie Silicium (DTSi) CEA-Laboratoire d'Electronique et de Technologie de l'Information (LETI)	Rapporteuse
Franck Delmotte Maître des conférences, Laboratoire Charles Fabry (LCF) Institut d'Optique - Université Paris Sud	Examinateur
Paul Ryan Director of Product Management Bruker Semiconductor Division, UK	Examinateur
Marie-Christine Lépy Directrice de recherche CEA, Laboratoire National Henri Becquerel (LNHB) CEA-Laboratoire d'Intégration de Systèmes et des Technologies (LIST)	Directrice de thèse
Emmanuel Nolot Ingénieur-Chercheur, Département Technologie Silicium (DTSi) CEA-Laboratoire d'Electronique et de Technologie de l'Information (LETI)	Co-Encadrant de thèse
Anne Roule Ingénieure-Chercheur, Département Technologie Silicium (DTSi) CEA-Laboratoire d'Electronique et de Technologie de l'Information (LETI)	Co-Encadrante de thèse

Thèse de doctorat

“Science is the search for truth, it is not a game
in which one tries to beat his opponent,
to do harm to others.”
Linus Pauling

Acknowledgements

First of all, I would like to express my gratitude to CEA-LETI and the Silicon Technology Division for giving me this opportunity to work in a unique cutting-edge facility forged by team-work spirit, multiculturalism and technology pioneering known worldwide.

I would like to express my deepest appreciation to my supervisors Emmanuel Nolot, Anne Roule and to my PhD directress Marie-Christine Lépy for the patience, kindness, expertise transfer and rigorousness to put me back on track the moments my research was going off the topic. This thesis would not be possible without you three, and each one of you had special role during this three years, you all known. I am deeply grateful to have you three as supervisors not only on the professional side but also on personal one, for all the laughs, good moments in the laboratories as well as in conferences, and I will always be in debt with you by assisting me in the hardest moments during my thesis.

I also would like to express my gratitude to Eugénie Martinez and Philippe Jonnard by accepting to be rapporteurs as well as devoting your attention to evaluate this work. I also would like to thank Anne Lafosse, Franck Delmotte and Paul Ryan by agreeing to be part of the jury and dedicating your time to exam my work.

I would like to offer my special thanks to Laurent Vandroux and Cécile Moulin by the kindness and warmly hosting me in the Deposition service (SDEP) of the Silicon Technology Division. I am also grateful for aiding me in my hardest moments in the thesis. In addition, this thesis would not be possible without the SDEP team in particular Chiara Sabbione, Mathieu Bernard and Walid Darwich for the film deposition, as well as, Agathe André, Sylvie Favier for the X-ray metrology help, and Pierre Noé, Rémy Gassilloud and François Martin for the chalcogenides expertise.

This thesis would be far from completed without the expertise and participation of the nano-characterization platform (PFNC) of LETI, Laboratoire des technologies de la Microélectronique (LTM), Laboratoire National Henri Becquere (LNHB), as well as the synchrotrons SOLEIL (Saclay, France), ELETTRA (Trieste, Italy). In particular, I would like to thank Patrice Gergaud, Francois Pierre, Jean-Paul Barnes from the PFNC, Bernard Pelissier and Sebastien Labau from the LTM, Yves Ménesguen, Jonathan Riffaud and Anastasiia Novikova from the LNHB, Paulo Da Silva and Pascal Mercere from Metrology beamline of SOLEIL synchrotron, Diane Eichert and Fabio Brigidi from the Fluorescence beamline of the ELETTRA synchrotron.

My sincere gratitude goes to Yan Mazel and Simona Torrengo who are not only great friends and sympathetic officemates but also actively contributed to complement my experiments. Also thank you Yan for teaching me creo, a dance from my own country that I never heard about it. And also thank you Simona for joining me in the synchrotron adventures in Saclay, the snow storm during the February campaign is unforgettable. Although the harsh during these campaigns, I will miss all laughs, nightshifts and Courtepaille moments.

I would like also to thank my former officemates Bérenger Caby, Hélène Rotella and Gaël Picot, not only for the kindness and sympathetic moments during my first year but also for the important GIXRF/XRR development the years before I arrive in LETI. I also would like to thank in special

Bérenger for being very kind friend and giving me moral support when things were becoming harsh.

I want also to thank the déjeuner team Jérôme Richy, Vincent Huynh, Lauraz sauze, Myriam Le Guen and Victor Yon for being part of my PhD life, for all the laughs and coffees in the most important moment of the day. I also would like thank the Pierre Noe team Philippe Kowalczyk, Jean-Baptiste Dory and Rebecca Chahine for the friendship and also being part of my PhD life, in particular Philippe whom I could actively work together the first year. I also would like to thank all my SDEP friends and my PFNC friends for all the coffees and croissants every day. Finally, I would like to thank my family and my parents for the unconditional love and the support during these three years of doctoral work.

Summary

List of figures

List of tables

Acronym list

AIST: Ag and In doped Sb_2Te

ALD: Atomic Layer Deposition

ARXPS: Angle Resolved X-ray Photoelectron Spectroscopy

ATI: Atominstitut Vienna University of Technology

BEOL: Back End Of Line

CAE: Constant Analyzer Energy

CBM: Conductive Bridge Material

CBRAM: Conductive Bridge Random Access Memory

CDW: Charge Density Waves

CHA: Concentric Hemispherical Analyzer

CRR: Constant Retard Ratio

CPE: École Supérieure de Chimie Physique Électronique in Lyon

CVD: Chemical Vapor Depostion

CXRO: Center of X-ray Optics

DFT: Density Functional Theory

EBS: Elastic Backscattering Spectrometry, a.k.a Non-Rutherford Backscattering Spectrometry

EDT: 1,2-ethanedithiol

EDXRF: Energy Dispersive X-ray Fluorescence

FEL: Free Electron Laser

FET: Field-Electric Transistor

FP: Fundamental Parameters method

FTIR: Fourier-Transform Infra-Red spectroscopy

FWHM: Full Width at Half Maximum

GIXRF: Grazing Incidence X-ray Fluorescence

GST: Ge-Sb-Te Alloy in the whole range of the ternary phase diagram

GSTN: Ge-Sb-Te-N, usually N-doped Ge-Sb-Te alloys

GST225: $Ge_2Sb_2Te_5$

HPGe: High Purity germanium detector

IBR: Ion Beam ratio

IMFP: Inelastic Mean Free Path

iPCM: Interfacial Phase Change Material

iPCRAM: Interfacial Phase Change Random Access Memory

IUPAC: International Union of Pure and Applied Chemistry

JFET: Junction Field-Electric Transistor

jGIXA: Grazing Incidence X-ray Analysis using Java

LETI: Laboratoire d'Electronique et de Technologie de l'Information

LNHB: Laboratoire National Henri Becquerel

MEDEPy: Material Elemental Depth profiling using Python

ML: Monolayer

MOCVD: Metal-Organic Chemical Vapor Deposition

NIST: National Institute of Standards and Technology

NRA: Nuclear Reaction Analysis

NVM: Non-Volatile Memory

OTS: Ovonic Threshold Switching

PC: Proportional Counter detector

PCM: Phase Change Material

PCRAM: Phase Change Random Access Memory

PIXE: Particle-Induced X-ray Emission

PPTOFMS: Plasma Profiling Time-Of-Flight Mass Spectrometry

PTB: German National Metrology Institute

PVD: Physical Vapor Deposition

RBS: Rutherford Backscattering Spectrometry

SC: Scintillation Counter detector

SDD: Silicon Drift Detectors

SF: Sensitivity Factor

SOLEIL: Source Optimisée de Lumière d'Énergie Intermédiaire du LURE

TCO: Transparent Conductive Oxide

TMDC: Transitional Metal Dichalcogenide

TOF-SIMS: Time Of Flight Secondary Ion Mass Spectrometry

TPP-2M: Tanuma, Powell and Penn, second modification

TR: Total Reflection

UHV: Ultra High Vacuum

WDXRF: Wavelength Dispersive X-ray Fluorescence

XCOM: Photo cross-sections database (NIST)

XPS: X-ray Photoelectron Spectroscopy

XRD: X-ray Diffraction

XRF: X-ray Fluorescence

XRR: X-ray Reflectometry

XSW: X-ray Standing Wave

Introduction

Advanced chalcogenides materials are present in every Key Enabling Technologies. They are of fundamental importance for state-of-the art memories, energy harvesting materials and photonics. These complex compounds (binary, ternary and often more…) are the core of both the storage element and the selector in innovative phase-change memories that feature fast and easy storage to capture the exponential growth of data from mobile devices and the Internet of Things (IoT). Complex chalcogenide-based compounds feature unique sets of properties for mid-infrared science and nonlinear optics: they are already part of innovative products for commercial, space and military applications and excellent candidates for future ultrafast optical chip-to-chip interconnects. A large number of energy harvesting systems are based on chalcogenide complex compounds, not only for photovoltaic applications but also as promising lead-free thermoelectric materials and mechanical and magnetic energy harvesting materials. Transition Metal Dichalcogenides (TMDCs) are emerging as a class of exceptional materials with many potential applications (supercapacitors, batteries, electronics, optoelectronics, etc). New deposition processes are being developed and should soon address the need for adequate and general industry-scalable fabrication methods for TMDC on large-scale substrates with atomic scale precision. TMDCs are extensively investigated in universities, Research and Technology Organizations and appear now explicitly in the roadmaps of biggest industrial players such as Intel.

Chalcogenides can be synthesized with a large variety in stoichiometry and consequently with a wide range of chemical and physical properties that can be utilized for cutting-edge technological applications. In many cases these properties, such as optical band gap, thermal and electric conductivity, or phase change properties can be influenced and fine-tuned by the chalcogen/chalcogen (e.g. S/Se) ratio or metal/chalcogen ratio, also as a function of film depth. Consequently, one of the common challenges for the development and fabrication of advanced chalcogenide-based applications is the quantitative and reliable control of the film stoichiometry along with the in-depth distribution of elements. This is a prerequisite for precisely correlating film properties to film synthesis conditions, enabling shorter development times and higher production yield.

For the next technology nodes, chalcogenide materials will be scaled by tuning the chemical composition or by reducing the film thickness, which means that their properties become more tightly influenced by the chemical composition, the surface/interface effects and the depth-profile composition. Hence, dedicated metrology protocols must be developed, first to assist the optimization of chalcogenide materials processes in cleanroom environment, then to allow non-destructive process monitoring with industry-driven uncertainties.

During the three years of this PhD thesis, we developed metrology protocols based on X-ray techniques, dedicated to thin chalcogenides materials and fully compatible with inline monitoring. The protocols were mainly developed at CEA-LETI as well as at SOLEIL synchrotron (Saclay, France) in partnership with LNHB (Laboratoire National Henri Becquerel). The chemical quantification of chalcogenides was tackled by in-line Wavelength Dispersive X-ray Fluorescence (WDXRF) and in-line X-ray Photoelectron Spectroscopy (XPS). The XPS technique was also employed to study

surface/interface effects. Elementary depth profiles were studied by angle-resolved XPS as well as the combined analysis of Grazing-Incidence X-Ray Fluorescence (GIXRF) and X-Ray Reflectometry (XRR). Therefore, this manuscript is divided in four main parts (five chapters).

The first and second chapters concern the bibliography review dedicated not only to remind the readers about fundamentals of chalcogenide materials and X-rays physics, but also to point out the issues impacting the chalcogenide properties and the proposed metrological solutions (in-line compatible) to assist the development of new chalcogenide materials.

Chapter three to five refer to the experimental development of the metrology protocols dedicated to the three main metrological issues that should be addressed to assist the scaling of chalcogenide materials: surface/interface effects, chemical composition and elementary depth profiles:

Chapter three deals with the surface and interfaces effects on chalcogenide films. We developed an in-line procedure to evaluate oxidation effects based on Ge-Sb-Te films through *quasi-in-situ* XPS measurements. This approach allows us not only to evaluate the impact of queue-time in the process flow on the surface of the chalcogenide layers, but also to determine the composition-dependent binding states in thin chalcogenide materials. We also evaluated various capping layers (Ta, SiN and C) deposited *in-situ*, not only for their efficiency to protect the chalcogenide material against ageing (oxidation), but also to assess their interface effects (e.g diffusion) with chalcogenide films.

In chapter four, we developed strategies to quantify chalcogenide films (1 nm to µm range) for large stoichiometric range, and high spatial resolution (few µm to mm beam spot) for blanket and product wafers. Inline non-destructive strategies based on WDXRF and XPS were established and then assessed through the quantification of Ge-Sb-Te compounds (from 1 to 200 nm) and ultrathin 2D transition metal dichalcogenides (e.g. MoS_2, WS_2). Extensive WDXRF and XPS analyses were able to refine values of composition-dependent relative sensitive factors for Te 4d, Sb 4d and Ge 3d allowing XPS-based metrology with mastered accuracy. We also evaluated PCRAM materials based on N-doped Ge-Sb-Te films, and highlighted the need for in-depth study due to significant matrix effects, and lack of nitrogen standards challenging WDXRF quantifications. Ion Beam analyses were extensively evaluated as possible reference for WDXRF calibration, and WDXRF protocol was elaborated for a specific process window.

Chapter five covers the elementary depth profile protocols by GIXRF/XRR combined analysies and ARXPS approaches. The GXIRF/XRR protocol was developed in state-of-the-art tools by in-lab and synchrotron strategies. We evaluated the effects of experimental conditions and instrumental parameters on the performances of GIXRF/XRR analysis to accurately probe chemical depth-profiles in Te-based stacks. We also investigated how the fine-tuning of the X-ray Standing Wave field (XSW) by means of multilayered substrates could improve the sensitivity of GIXRF/XRR analysis to small process-driven modifications on thin films. At last, we developed in-line ARXPS strategy to assist the development of ultra-thin chalcogenides, and we demonstrated its efficiency to characterize the first sputtering steps of GeTe and $Ge_2Sb_2Te_5$, providing insights of in-depth chemical distribution for the development of PCRAM and interfacial-PCRAM materials for next technology nodes.

1. Chapter I: Chalcogenide materials

Chalcogens are elements from the group VI of the periodic table (i.e. S, Se and Te). The word "chalcogen" is derived from a combination of the Greek word khalko's (copper, ore), and Latinized Greek word genes (born or produced), meaning that it is originated from minerals that contain copper in combination with sulphur, selenium and/or tellurium. In the 1950s remarkable studies highlighted chalcogens as semiconductors, ion conductor, infrared transmitting glass, and xerographic photoreceptor. For instance, in the first commercial application of chalcogenide materials dating on 1970s for xerography technology [1, 2], Se-based film was employed as photoreceptor which coated the drum dedicated to ink transfer. In 1990s the first optical disks were produced based on the reversible switching phenomena discovered by Ovshinsky in 1968 [3, 4]. Germanium-Antimony-Tellurium (Ge-Sb-Te) films were developed for the rewritable optical disks, as these thin materials have the unique ability to switch reversibly between amorphous and crystalline phases in tens of nanoseconds [5]. Since then, Te-based films such as Ge-Sb-Te compounds are extensively applied for optical disks (DVDs and Blue-Ray Disks) and Non-Volatile Memories (NVM) applications.

Chalcogenide materials can be classified as 3-D chalcogenides (atoms are bounded throughout a 3-D network) and 2-D Transition Metal Dichalcogenides (TMDCs, i.e., atomic monolayers bounded by Van-Der-Waals interactions). Whereas 3-D chalcogenides includes bulks, films and fibers covering a huge variety of applications such as Solar Cells, Optical fibers and Non-Volatile Memories, innovative 2D TMDC "such as MoS2, MoSe2, WS2 and WSe2 have sizable bandgaps that change from indirect to direct when thinned down to single layers, allowing applications such as transistors, photodetectors and electroluminescent devices" [6]. 2-D TMDCs are layered materials with strong in-plane bonding and weak out-of-plane interactions enabling exfoliation into two-dimensional layers of single unit cell thickness, and they are often referred as 'next-generation graphene' and 'wonder materials' [7].

Chalcogen atoms can form a very broad variety of bonding configurations, which results in a wide spectrum of chalcogenides with very different properties. For example, one can improve data retention of devices based on the phase-change GeSbTe by adding Ge content which decreases the hybridization and ionicity of the present atoms, enabling resonance bonding to prevail [8]. Indeed, hybridization (i.e. covalency) and ionicity are inherent characteristics which are essential to know when choosing a chalcogenide alloy as phase-change material. These terms are just examples of how important the chalcogenide chemistry is. Therefore, in the next section we will briefly discuss the main aspects of chalcogenide chemical bonds, in order to understand the effect on their properties.

1.1. Chalcogens Atomic Electronic configuration

The electron configuration of chalcogens is $ns^2p_x^1\ p_y^1\ p_z^2$, i.e. two electrons located on the atomic s-orbital, and two of the three p-orbitals possess unpaired electrons while the third one is occupied by a pair of electrons. This electronic distribution results in a broad range of bonding configurations, which results in a large range of chalcogenides with very different properties.

Indeed the atomic electronic configuration of chalcogen atoms changes when chemically bound to other species present in the compound. In the ideal case, such as elementary S, Te and Se, only two unpaired p-electrons are involved in the formation of covalent bonds, the other p-orbital electron pair remain inert. Kastner [9] described this nonbonding electron pair as Lone-pair electron, and he classified amorphous chalcogens as Lone-Pair Semiconductors.

He noted that while semiconductors such as Si and Ge are tetrahedrally bonded, the sp^3 orbitals split into bonding (σ) and antibonding (σ ∗) molecular states that are subsequently broadened into valence and conduction bands, respectively, for chalcogen materials, the s states are found well below the p states and need not to be considered. As two of the three p orbitals are employed for bonding, chalcogens are usually found in two-fold coordination. Then, one electron lone pair (LP) does not participate to any chemical bond. For solids, the unshared LP electrons creates an LP band close to the initial p-state energy. As a result, the bonding (σ) and antibonding (σ ∗) bands are split symmetrically with respect to this reference energy, and both the σ and LP bands are occupied. Then, the bonding band is no longer at the top of the valence band, and this role is played by the LP band (Fig. 1.1).

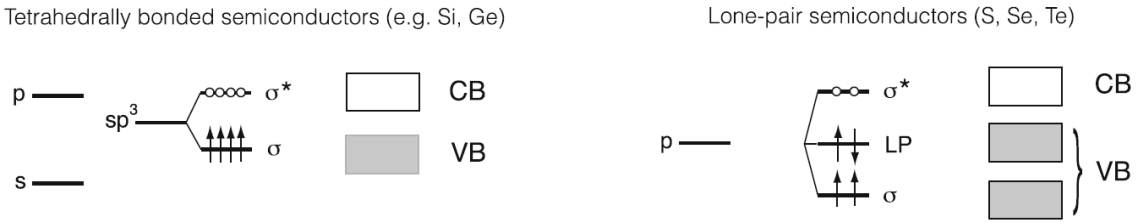

Figure 1.1. Tetrahedrally bonded semiconductors (left) and LP semiconductors (right).

Therefore, the VIb atoms can take twofold coordination with neighboring atoms. It means that the coordination number follows the so-called 8−N rule where N = 6 in the present case [10]. The covalent bond is accompanied by the anti-bonding state σ∗ forming the conduction band. We can observe that the p^4 bonding is inherent to the covalent group VIb material, regardless its crystalline or non-crystalline nature.

Although twofold is the most basic coordination that can apply for chalcogenide materials (elementary as well as few binary compounds such as As_2S_3), they can also exist in three and six fold coordination. Littlewood [11, 12] suggested a diagram to describe the different coordination numbers for chalcogens bound to the IV group elements. He explained how these elements are bound based on St. John, Simons and Bloch [13, 14] works, who introduced two coordinates:

$$r'_\sigma = r_p^A - r_p^B, \qquad \text{(eq. 1.1)}$$

$$r_\pi^{-1} = \left[\left(r_p^A - r_s^A\right) + \left(r_p^B - r_S^B\right)\right]^{-1} \qquad \text{(eq. 1.2)}$$

Here, r_s^X and r_p^X denote the valence radii of the s- and p-orbital of atom X, respectively. The coordinate r'_σ provides a quantitative measure for the ionicity of bonds (degree to which atoms are ionic), similar to Pauling's electronegativity difference. The second coordinate r_π^{-1} concerns the degree of 'covalency', degree to which atoms are covalently bound. It can be understood as a measure of the energetic splitting of s- and p-states, and scales with the difference between the radii of s- and p-orbitals. This map has been elaborated by Phillips [15] based on these two coordinates (see Fig. 1.2), and allows to predict the bonding mechanism and crystal structure for a given stoichiometry of binary chalcogenides.

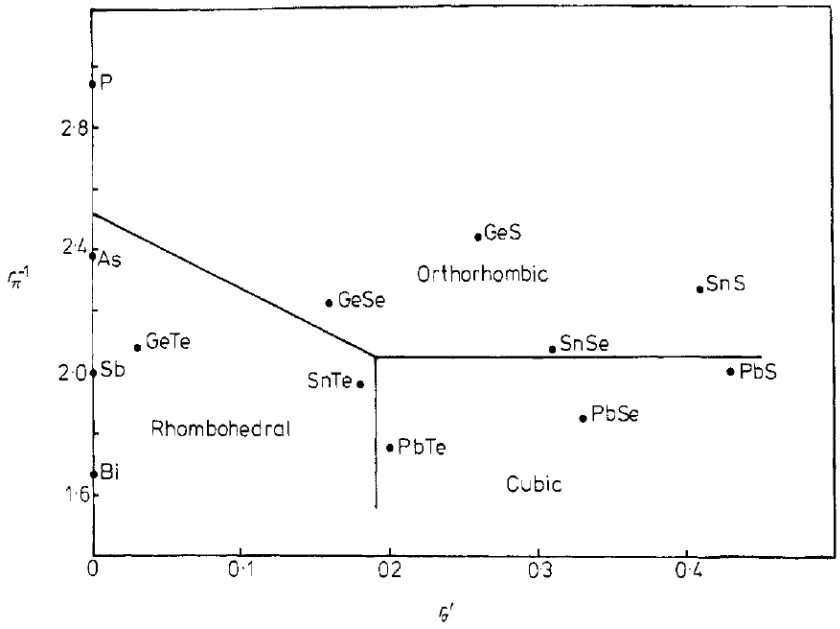

Figure 1.2. St-John-Bloch plot demonstrating the ionicity (r'_σ) and covalency (r_π^{-1}) of IV-VI compounds and group V elements [10].

For example, the ionicity (r'_σ) reduction drives the alloy to change from Cubic to Rhombohedral structure. This phase transition can be understood as the result of the large electron-to phonon coupling due to the resonant nature of the half-filled p states. The p bonds are then unsaturated, the system is therefore resonantly bonded. Shportko et al [8] identified Resonant bonding as essential property which could explain the phase-change behavior of chalcogenide materials.

On the other hand, the covalency (r_π^{-1}) induces hybridization of the alloy changing its phase from Rhombohedral or Cubic to Orthorhombic. The large split between s and p states on the rocksalt structures becomes smaller, which opens the possibility of forming directed sp hybridized orbitals. The Orthorhombic structure is then accessible, where the atoms are covalently bound in double layers (nano-sheets) with weaker interlayer bonding. This is particularly the case of 2-D transition metal di-chalcogenides (TMDCs).

2-D TMDCs exist with the general formula MX_2, where M stands for a six-fold coordinated-transition metal and X represents three fold coordinated chalcogens (similar to the case of IV-VI crystals). Although TMDCs can exist as "bulk" chalcogenide, the main interest comes when few atomic layers are conceived then exhibiting unique properties, such as sizable bandgaps that change from indirect to direct in single layers [7].

1.2. 3D chalcogenide materials:

This section covers the main features of 3D chalcogens: Phase-Change, Ionic conductivity, photonics and photovoltaics. These aspects are briefly explored from fundamentals to current applications.

i- Phase-Change properties

As mentioned earlier in the introduction of this chapter, some chalcogenide materials are able to switch reversibly between amorphous and crystalline phases in tens of nanoseconds. This reversible switching phenomena between the two phases with distinct optical and electrical properties was first discovered in 1968 by Ovshinsky [3]. It led to data storage applications such as optical disks produced in 1990s and non-volatile resistive memories developed since 2005, as illustrated in Fig. 1.3.

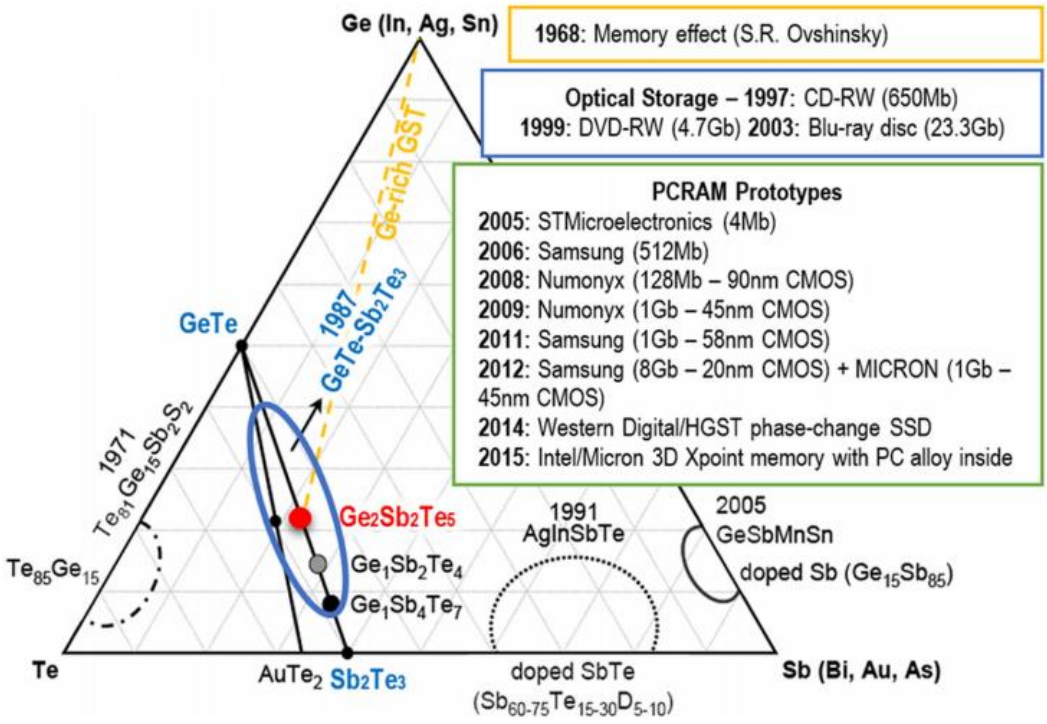

Figure 1.3. Ternary phase diagram for different phase-change alloys, and an inset highlighting the main years of PCM development [16]

Figure 1.3 also highlights the main phase change materials (PCM) with suitable properties for Phase change random access memories. For example, the compositions along the line connecting GeTe and Sb_2Te_3 in the ternary Ge-Sb-Te phase diagram (GST alloys) present very fast crystallization and notable change of optical reflectivity between the amorphous phase and the crystalline phase [17, 18]. Fig. 1.4 illustrates the phase-change behavior of GeTe and $Ge_2Sb_2Te_5$ alloys, where the amorphous phase is expressed as high electrical resistivity and low optical reflectivity, while the crystalline have unambiguous lower resistivity and higher reflectivity.

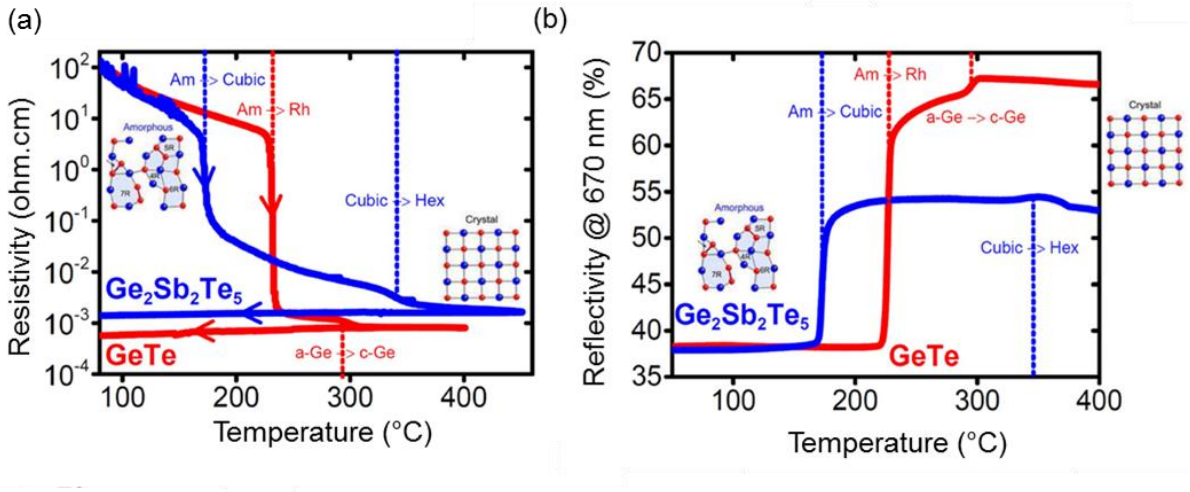

Figure 1.4. Resistivity (a) and reflectivity (b) measured as function of increasing temperature for GeTe and $Ge_2Sb_2Te_5$ films, amorphous phase correspond to high electrical resistivity and low optical reflectivity, while crystalline phase is the contrary [16].

Not only Te-based alloys are considered as PCM, but materials such as Ge-Sb [19] and Ga-Sb [20] alloys can also exhibit phase change phenomena. Based on the Littlewood diagram (Fig. 1, section 1.1), Lencer et al [21] built an exhaustive map of phase-change materials according to their tendency towards s-p hybridization and bond ionicity (Fig. 1.5). As we can see, phase-change materials are all located in a tiny region of this map towards low hybridization and ionicity. As explained in section 1.1 chalcogenides in this region have half-filled p states, when in crystalline state the system is resonantly bonded. The immense contrast of optical and electrical properties between the amorphous and crystalline phases may be related to the elimination of this resonant bonding.

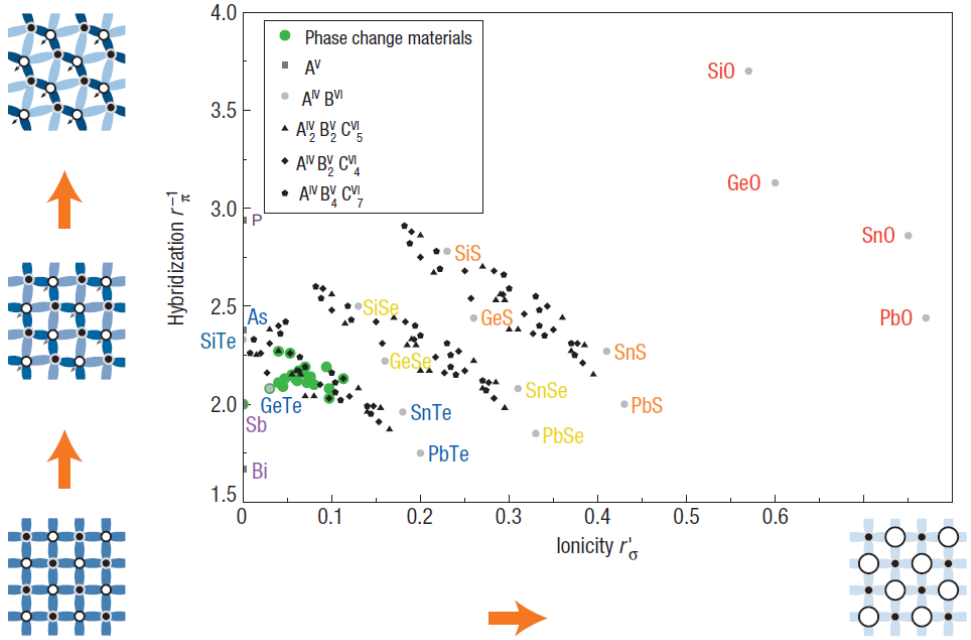

Figure 1.5. Mapping phase-change materials according to their ionicity bonds (x axis) and tendency towards s-p hybridization (y aixs). We can clearly see very distinct bands of oxides, sulfides, selenides, and telluride indicated as red, orange, yellow and green, respectively [21].

The phase-change process of chalcogenide films for memory applications as Phase Change Random Access Memory (PCRAM) is depicted in Fig. 1.6. First, a short and intense electric current (RESET pulse) is applied in order to amorphize the active zone: the temperature of the chalcogenide material increases above the melting point (T_{melt}) then rapidly decrease below the glass transition temperature (T_g) with the aim of inhibiting its crystallization. Secondly, the crystallization can be achieved with a longer and less intense pulse (SET pulse). Then, heating the active zone at a temperature less than T_{melt} but higher than T_g permits to obtain a high atomic mobility and therefore rapid crystallization [22, 23].

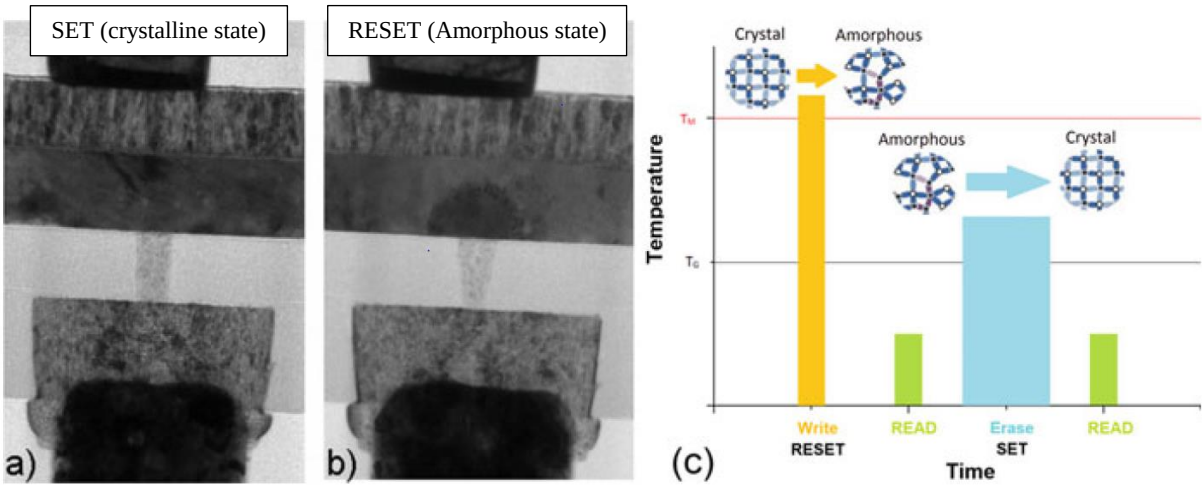

Figure 1.6. (a) Transmission Electron Microscopy (TEM) Cross-sections of Ge-Sb-Te PCM-cell in a SET state (crystalline), while in (b) it is in RESET state (active zone in amorphous state). (c) Schematically illustrates the process to SET and RESET the PCM-cell [15].

Novels PCM memory cells are generally developed by a stacking of a PCM layer and an Ovonic Threshold Switch (OTS) as selector. OTS selectors (firstly reported by Ovshinsky in 1968, [3]) are chalcogenide materials (most common Selenium based) capable to change their conductivity into two distinct levels. Differently to PCM, OTS selector are not built based on phase-change phenomena, but according to the non-Ohmic effect induced by electric fields. The two distinct levels are the ON and OFF states, when it is ON it means the OTS has high conductivity, whereas OFF means very low conductivity. The advantage of layering PCM with OTS selectors is the substantial reduction of leakage current improving the 3D stack-ability and memory endurance [69].

PCM can also be turned into interfacial Phase-change memory (iPCM) when, for example, the Ge-Sb-Te layered structure is reduced to few nanometers and ordered as Sb_2Te_3/GeTe/Sb_2Te_3. In this case, the phase change from amorphous to crystalline no longer occur, only Ge atoms switch along the same direction [24]. Therefore, the covalent (RESET) and resonance (SET) bonding states are usually employed when referring to these two phases. The Ge atoms can occupy both threefold coordinated (pyramidal) and/or tetrahedral sites [25, 26] with principally covalent bonding (RESET state). On the other hand, the cubic crystalline phase is formed by approximately octahedral subunits 'resonantly' bonded (i.e. SET state) [8, 27-28]. Then, iPCM memory should allow significantly lower switching currents and improved reproducibility when compared to PCM cells [24].

The advantages of iPCM devices are depicted in Fig. 1.7. The resistance R of iPCM- and GST-based PCRAM cells are plotted versus the applied electrical current. The graph clearly shows that the minimal currents to reversibly switch iPCM-based devices (between the SET and RESET states) are substantially lower than those needed for similar devices based on GST. In fact, the electrical energy required to SET the GST and iPCM devices was 90 and 11 pJ respectively. Moreover, the switch between the SET and RESET states was drastically more abrupt for the iPCM cells due to the homogeneity of the Ge switching environment. This generates a narrow distribution of the cell characteristics promoting accurate determination of the SET and RESET states [24].

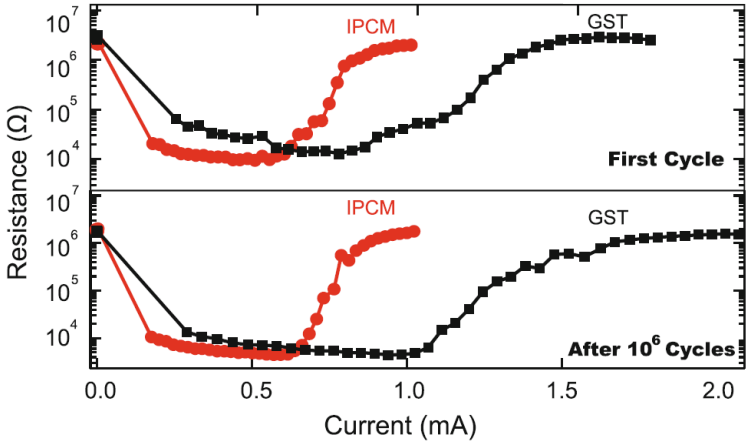

Figure 1.7. Resistance-Current relation of a $(GeTe)_4(Sb_2Te_3)_2$ iPCM (red curve) and GeSbTe cells (black curve). The upper plot corresponds to the first cycle of electrical switching, while the lower plot 10^6 cycles [23].

ii- Ionic conductivity

Cations such as Li^+, Ag^+ and Cu^+ can be incorporated in chalcogenide materials in order to increase their ionic conductivity. The movement of the ions under electric or magnetic field can be applied to create ionic devices such as Conductive Bridging Random Access Memories (CBRAM), photoresists, sensors, and batteries. Based on this concept, Utsugi et al [29], for example, demonstrated nano scale write-once ionic memories (Fig. 1.8.), where Ag^+ ions in Ag/Ge–Se bilayer structures are forced to move by electric fields in a scanning tunneling microscope.

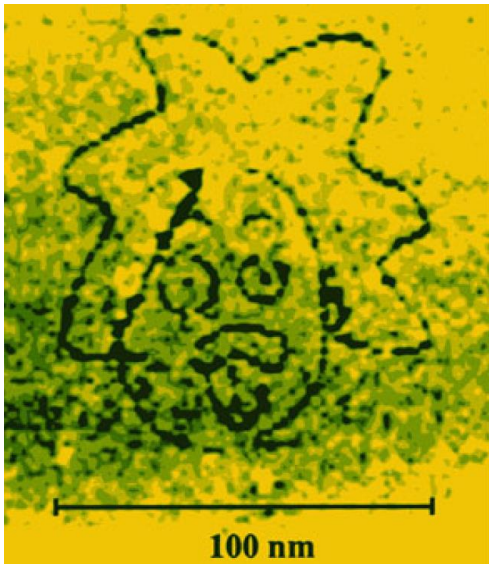

Figure 1.8. Nano-scale Einstein image written by an ionic memory [29].

Ionic conductivity is also the essential mechanism to create a conductive bridge responsible of the high (OFF) and low (ON) resistance states of the CBRAM. The memory cell is constituted of a metal-doped chalcogenide film between two electrodes, one electrochemically active (e.g., Ag, Cu, Ni) and the other electrochemically inert (e.g., Pt, Ir, W) [30].

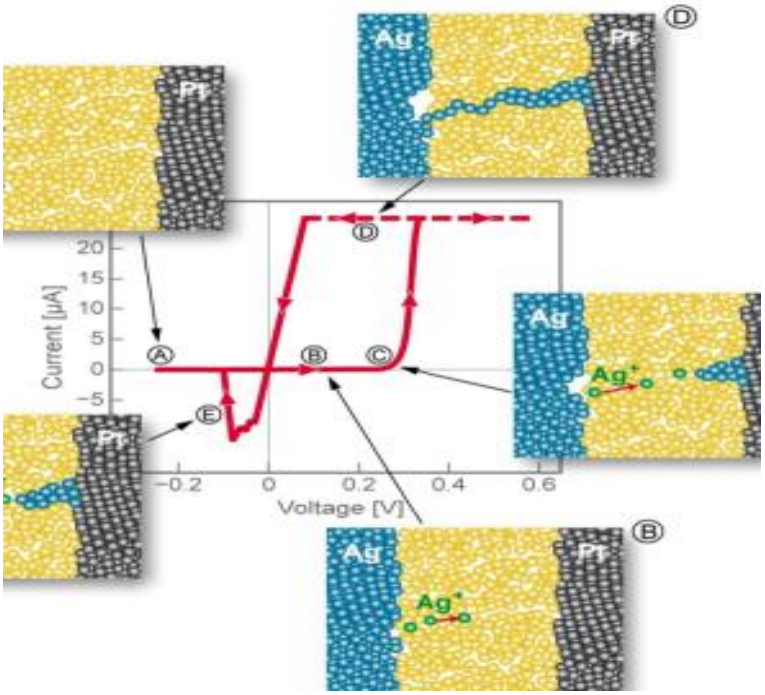

Figure 1.9. Scheme highlighting the mechanisms procedure to SET (A-D) and RESET (E) in CBRAM cell [30].

When a negative potential is applied to the inert cathode (Pt), electro-migration of dissolved positives ions occurs, forming an electro-deposition of a metallic dendrite on the cathode (Pt), then low resistance between two electrodes, characterized by the ON state. The transition to the OFF state happens when the metallic pathway is dissolved applying an inverted polarity voltage pulse, as illustrated in Fig. 1.9 [30].

Another application of ionic conductivity concerns batteries based on lithium sulfur (Li-S). This kind of battery is gaining widespread interest not only because they can theoretically supply energy five times higher than Lithium-Ion batteries (2500 vs. ~500 W h kg^{-1}) but also because sulfur is inexpensive, nontoxic, and abundant in nature [31]. The Li-S battery has a structure of anode/electrolyte/cathode, in which the glass is in powder-like in order to increase the area of reacting interfaces. For example, Kitaura et al [32] developed high-performance rechargeable batteries consisting of three-layer structure: In (Cathode), $80Li_2S20P_2S_5$ glass-ceramic powder (electrolyte), and a composite powder containing $LiCoO_2$ (anode). The reliability and safety issues should be addressed shortly, allowing the integration of such compact and light-weight batteries in electric vehicles.

iii- Photonics

As chalcogenides can transmit in the infra-red range, they are widely used in photonics. Typically chalcogenide glasses feature significant transmission values for wavelengths up to ~11 μm for sulphides, ~15 μm for selenides and ~ 20 μm for tellurides, which makes them highly valuable materials for mid-infrared science and nonlinear optics: they are already part of innovative products for commercial, space and military applications and excellent candidates for future ultrafast optical chip-to-chip interconnects.

One of the most impressive optical properties of chalcogenides is the photo-sensitivity, a tendency for the chemical bonds to change when exposed to light with a wavelength near the band edge [33], [34]. The process behind photo-sensitivity consists in the creation of electron–hole pairs, which change the valence of nearby atoms and their chemical bonds, then creating coordination defects [33]. This illumination-induced bond switching can generate macroscopic changes in the physical properties of the material, providing a wide range of phenomena that includes photo-darkening, photo-diffusion, photo-fluidity and photo-crystallization, as well as vectorial effects such as photo-induced birefringence [35, 36].

Photo-sensitivity can produce outstanding changes in the properties of chalcogenide films. For example, photo-darkening is accompanied by a change in refractive index, and this has been employed to write waveguides into evaporated films, create Bragg gratings in fabricated waveguides, and tune the wavelength emitted by quantum cascade lasers [37, 38]. Fig. 1.10 shows, for example, how the photo-sensitivity of As_2S_3 thin layer could be employed to tune the resonant frequency of a GaAs photonic crystal cavity to match the emission from embedded quantum dots [39].

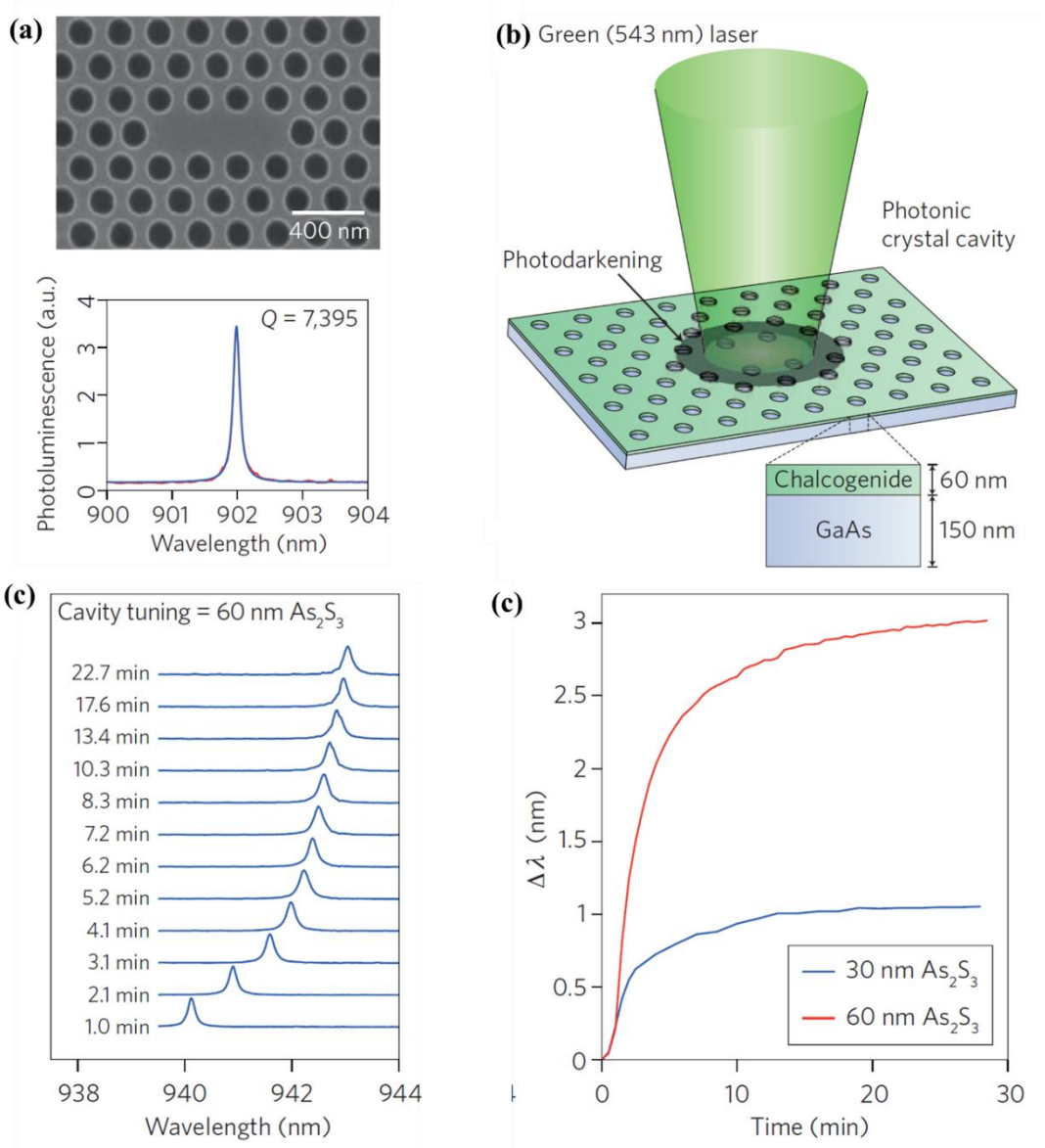

Figure 1.10. Use of photosensitive As_2S_3 chalcogenide film to tune the resonant frequency of a photonic crystal cavity. (a) An image of the photonic crystal cavity and its optical response. (b) Schematic of the method used to tune cavity. (c) Cavity response as a function of illumination time for a 60 nm As_2S_3. (d) Tuning curves for two different thickness of the As_2S_3 film [39].

iv- Photovoltaics

Photovoltaic power generation employs solar panels composed of a number of solar cells containing a photovoltaic material. Energy conversion in solar cell consists of generation of electron–hole pairs in p–n junction by the photo-absorption of light and separation of electrons and holes by an internal electric field [40]. A typical solar cell on substrate is designed as a stack consisting of a transparent conductive oxide (TCO), a buffer layer, an absorber film for primary photo-conversion, and back-contact layer, as illustrated in Fig. 1.11.a.

Chalcogenide films such as CdTe, $CuGaSe_2$ and Cu_2ZnSnS_2 are great candidates to replace silicon as absorbers for next generation solar cells having suitable bandgap (1.0 to 2.0 eV), as shown in Fig. 1.11.b. The mismatch lattice between the chalcogenide film and TCO is drastically reduced by means of a buffer layer improving the hole density and lifetime [41]. In the case of CdTe solar cells,

CdS is employed as buffer layer and annealed by $CdCl_2$ or $MgCl_2$ in order to decrease the CdTe/CdS 10% lattice-mismatch (Fig. 1.11.b). This optimization of the CdTe absorber make it impressively exceed multi-crystalline Si efficiency at 21.5% [42]. Furthermore, chalcogenide-based cells can be considered as high-performance, low cost and fab-compatible alternative to silicon based ones [43].

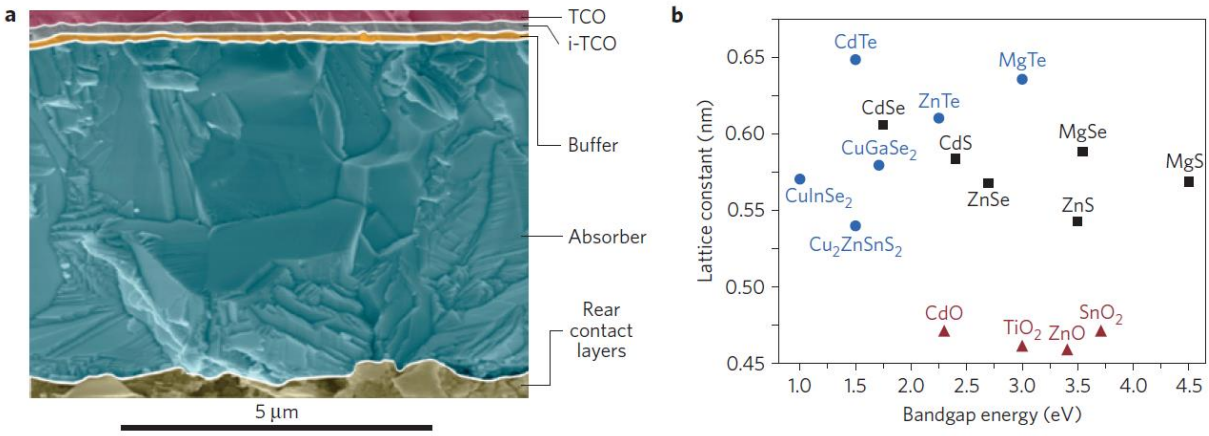

Figure 1.11. (a) Typical stack configuration of thin-film solar cell. (b) Differences in the lattice constant and bandgap energy of absorbers (blue circles), buffers (black squares) and TCOs (red triangles) [43].

1.3. 2D chalcogenide materials

As highlighted in the section 2.1, the formation of sp hybridized orbitals forms chalcogenide materials with covalent bonds bounded in double layers with weaker interlayer bonding. 2D TMDCs monolayers are known to crystallize either in trigonal prismatic (2H) or octahedral (1T) structures (Fig. 1.12.) [7, 44]. These structural phases can also be observed in terms of different stacking orders of the three atomic planes (chalcogen–metal–chalcogen) forming the individual layers of these materials. The 2H phases correspond to an ABA stacking in which chalcogen atoms in different atomic planes occupy the same position A and are located on top of each other in the direction perpendicular to the layer.

On the other hand, the 1T phases consist of an ABC stacking order. Depending on the particular combination of transition metal and chalcogen elements, the thermodynamically stable phase is either the 2H or 1T phase, but the last can often be obtained as a metastable phase. For example, for TMDCs formed by metals (Mo or W) and chalcogen (S, Se or Te) the 2H phase is thermodynamically stable and the 1T phase can be obtained as a metastable phase [45].

The structure of TMDCs is further defined by the stacking configuration of the individual layers in the case of multilayer and bulk samples, and by possible distortions lowering the periodicity. These distortions, if pronounced, can result in the formation of metal−metal bonds, which can happen, for example, in the dimerization of the 1T phase of group VI TMDCs, resulting in the 1T´ phase [44].

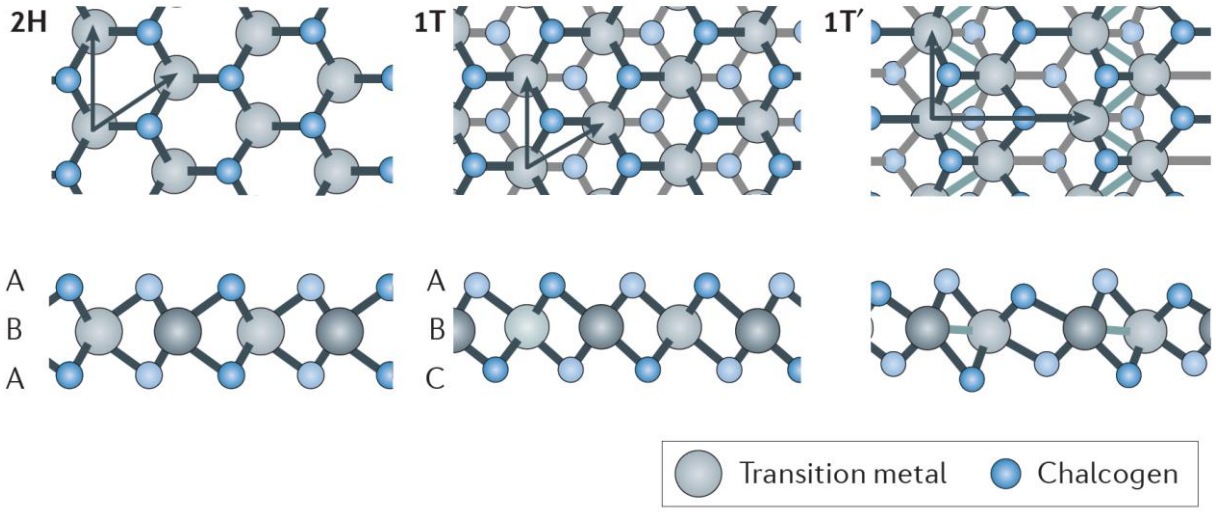

Figure 1.12. Atomic structure of single layers of transition metal dichalcogenides (TMDCs) in their trigonal prismatic (2H), distorted octahedral (1T) and dimerized (1T´) phases. Lattice vectors and the stacking of atomic planes are indicated [44].

When TMDCs are thinned down from bulk to monolayer, a critical change is the crossover from indirect band gap in bulk to direct band gap in monolayer form. Density Functional Theory (DFT) calculations highlights a direct band gap in monolayer MoS_2 located at the corners of the hexagonal Brillouin zone, i.e. at the K-points [6]. The evolution of the band structure as one goes from the bulk to a monolayer for several group VIb TMDCs is shown in Fig. 1.13.

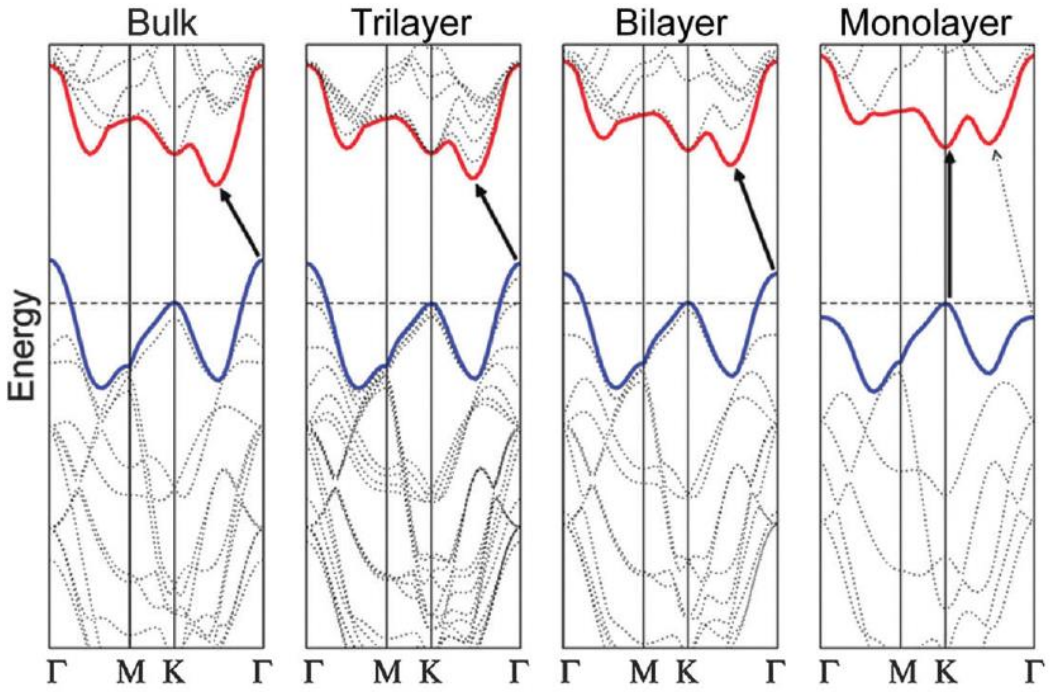

Figure 1.13. Impact of the thickness reduction on the 2H MoS_2 calculated bandgap [48].

As we can see in the 2D TMDCs monolayer, the conduction and valence-band edges are found at the corners (K and K) of the 2D hexagonal Brillouin zone. These two inequivalent valleys establish a binary index for low energy charge carriers. Due to the large valley separation in momentum space, the valley index in TMDCs is expected to be robust against scattering by smooth deformations and long

wavelength phonons, as first proposed by Xu et al. [46].

The most-studied example of an external degree of freedom of electrons is the electron spin, which is associated with the magnetic moment, and open a window to the vast field of spintronics. In this field, the spin up and down states are time-reversed images of one another and are distinguished by opposite values of the magnetic moment [47].

An example of spintronic device was demonstrated by Zhang et al. [48], who employed WSe_2 p-i-n junctions to electrically switch chiral electroluminescence (EL). When the p-i-n junction was forward-biased, circularly polarized EL was observed with the degree of circular polarization reaching values as high as 45%, which is comparable with that of polarized luminescence (PL) from monolayers. Moreover, the circular polarization was reversed (Fig. 1.14) when the source-drain bias was exchanged, validating the possibility of electrical control of circularly polarized luminescence.

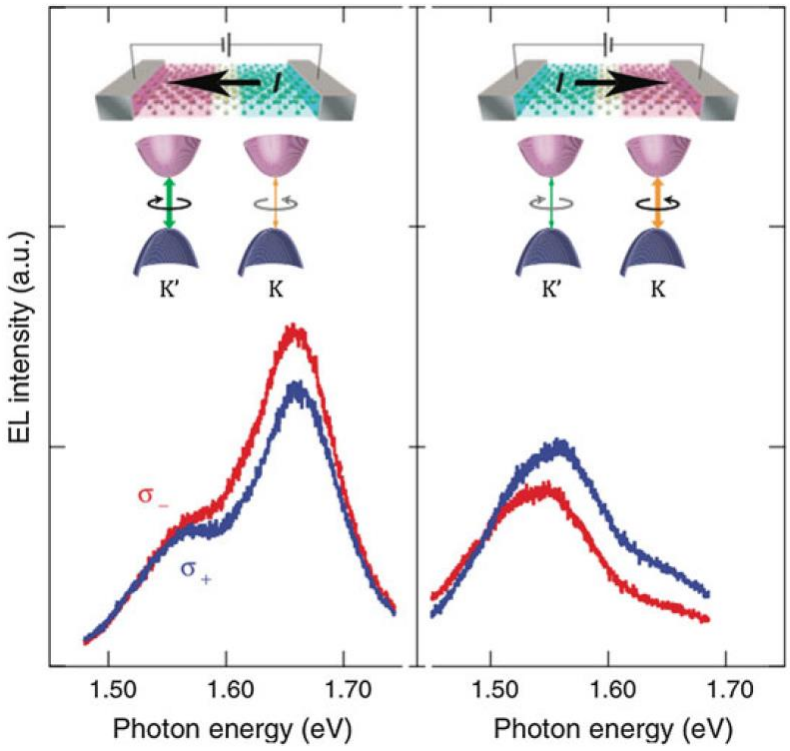

Figure 1.14. Circularly polarized EL spectra for two opposite current directions schematically indicated in the top illustration. Bottom illustration represent the contribution to EL from two valleys [48].

Another important aspect of 2D TMDCS is their exciton behavior in the absence of dielectric effects. Exciton is the bound state of an electron and a hole when attracted to each other by a Coulomb force. With the reduction to atomically layered TMDCs, exciton binding energy is four times larger in 2D than in 3D. Nonetheless, the dielectric screening is additionally reduced due to the electric field lines joining the electron and hole extend outside of the sample, which may lead to an even higher enhancement factor [49], as illustrated in Fig. 1.15.a.

Experimentally, enhancement of the exciton binding energy in 2D TMDCs was observed when high magnetic fields were employed generating a very distinct dielectric environment outside the sample. The experiment was performed by optical analysis of monolayer and bulk WSe_2 [50].

With the transition from 3D to 2D, the formation of excitons by an electron and hole is expected

to promote an increase of both the band gap and the exciton binding energy, as indicated by a dashed red line in Fig. 1.15.b.

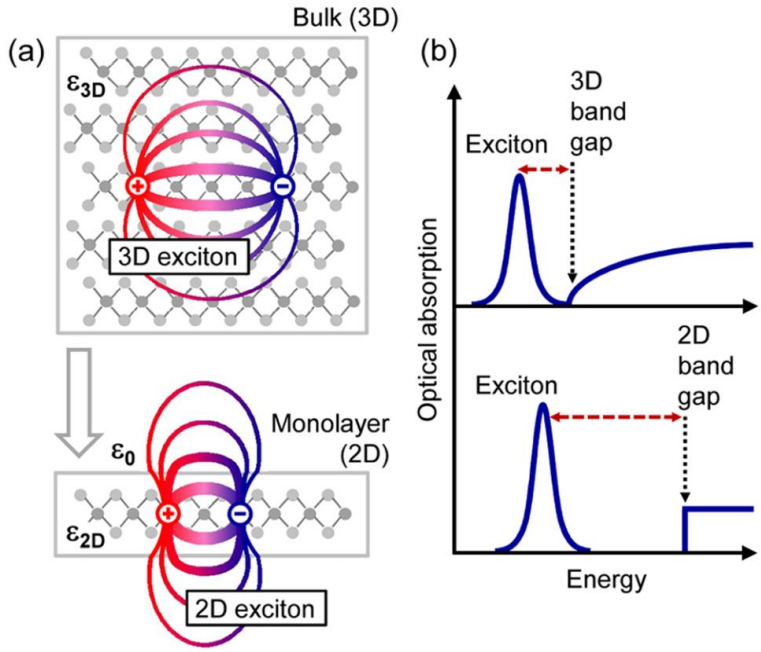

Figure 1.15. (a) Real-Space representation of electrons and holes bound into excitons for the three-dimensional bulk and a *quasi*-two-dimensional monolayer. (b) Impact of the dimensionality on the electronic and excitonic properties, schematically represented by optical absorption [50].

The increase of the exciton binding energy makes these materials great candidates for wide range of semiconductors applications such as transistors, integrated circuits, memories and optoelectronic devices. Radisavljevic et al. [51] developed a top-gated monolayer MoS_2 FET. The preparation of the cell consisted of 0.65 nm thick exfoliated MoS_2 layer deposited onto SiO_2 and covered by a 30 nm thick layer of HfO_2. In this device, MoS_2 served as the semiconducting channel and HfO_2 as the top-gate dielectric. A mobility of at least $200 cm^2V^{-1}s^{-1}$ was obtained, comparable to the mobility achieved in thin silicon films or graphene nanoribbons. The transfer curves of the device are shown in Fig. 1.16. The transistor exhibited a current ON/OFF ratio exceeding 10^8 at room temperature.

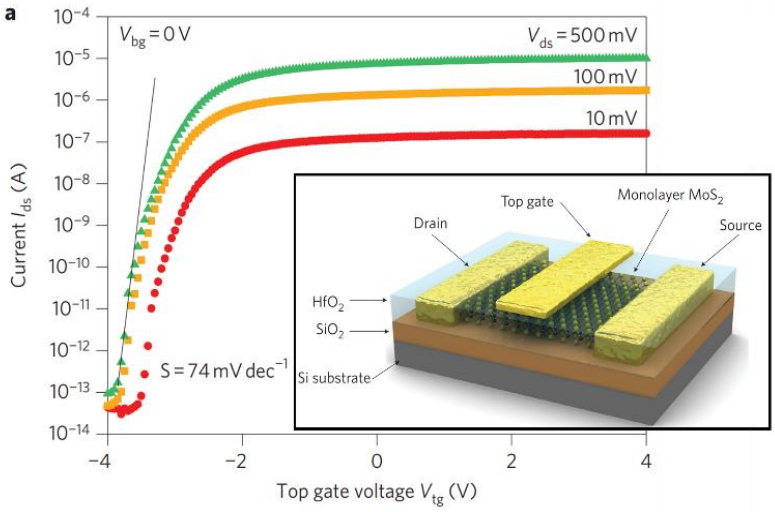

Figure 1.16. Local gate control of the MoS_2 monolayer transistor. (a) I_{ds}-V_{tg} curves recoded for a bias voltage ranging from 10 to 500 mV. Inset Three-dimensional schematic view of one of the transistors.

1.4. Scaling properties of chalcogenide materials

This brief description about 3-D and 2-D chalcogenide materials shows us the wide interest on chalcogenide properties to cutting edge technological applications. Nevertheless, in order to industrialize these materials, one must scale and control the properties of chalcogenide materials.

For example, Non-volatile memories based on GeSbTe films still lack thermal stability required for automotive applications (i.e. 10 years at 150 ºC) or for pre-encoding the data before the soldering process (i.e. 2 min at 260 ºC), which is a step to melt the solder paste and assembling the components to form the final device. These drawbacks can be overpassed by tuning the Ge proportion or decreasing the film thickness [52, 61].

Also, 2-D TMDCs can be effectively tuned in a wide range through different methods such as thickness reduction and intercalation. For example, the band structures are significantly changed as we thin down the 2D layers to the single-layer limit. Another example is that through the intercalation of guest ions, the carrier densities of 2D TMDs can be tuned by multiple orders of magnitude [53]. Hence, we highlight below important factors impacting the properties of chalcogenide films.

i- Effects of chemical composition and doping

Cheng et al [52] studied the thermal and electrical behavior of several GeSbTe films toward germanium rich. He observed that adding Ge to the system increases the crystallization temperature (Fig. 1.17.a), resulting in higher resistance at crystalline state (Fig. 1.17.b). Hence, he stated the existence of a "golden composition" Ge_2SbTe_2 which improves the thermal stability of the RESET state while maintaining a fast switching speed. Using Ge-rich compositions, Zuliani et al. were able to demonstrate the data retention during the typical soldering reflow temperature profile [54].

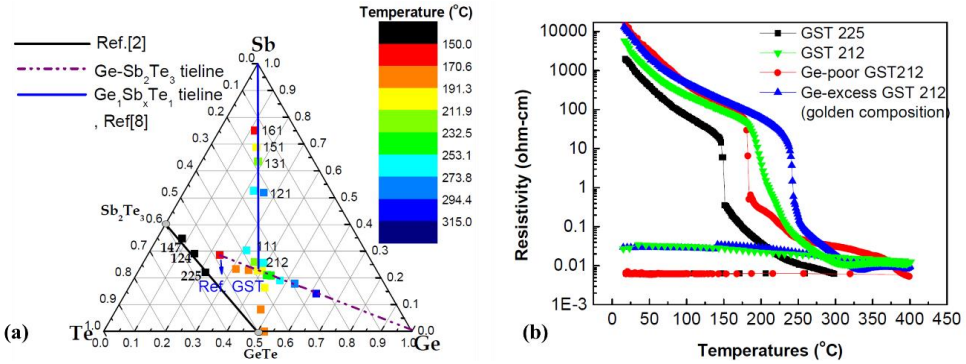

Figure 1.17. (a) Crystallization temperatures T_x as a function of compositions in the Ge-Sb-Te ternary phase diagram. (b) Resistivity as a function of temperature for $Ge_2Sb_2Te_5$ and Ge modification of Ge_2SbTe_2 films during a heating ramp to 400°C at 5°C/min and subsequent cooling back to temperature [52].

The addition of light elements such as nitrogen or carbon reinforces the thermal stability of the amorphous phase of the material [55]. In the stoichiometric alloy GeTe, for example, the addition of nitrogen promotes an increase of the crystallization temperature as well as an increase of the activation energy of the crystallization (Fig. 1.18), thus illustrating this higher thermal stability of the amorphous phase of the material [56]. This analysis was interpreted as a bigger disorder at long range, and the trapping of Ge atoms as GeN leading to reduction of cubic germanium segregated at higher temperatures [57].

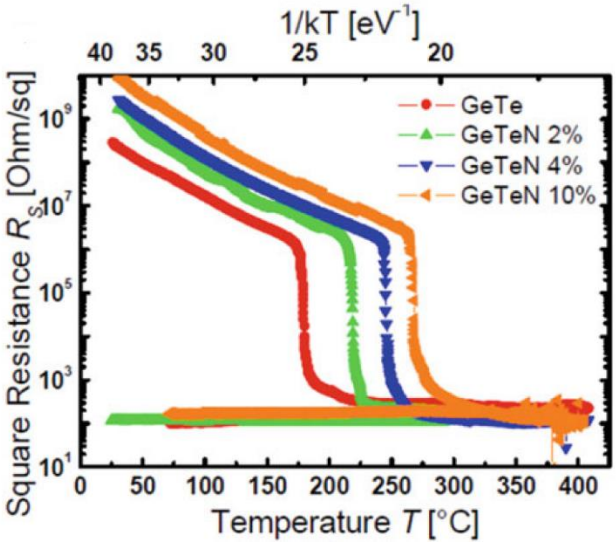

Figure 1.18. Evaluation of the crystallization temperature and activation energy for crystallization for N-doped GeTe thin films [56].

ii- Intercalation of 2-D TMDCs layers

2-D TMDCs properties can be tuned by inserting intercalants into the layered structure, the method can be considered as doping since the intercalant concentration is at a low level. The approach was first studied for bulk layered structures, but gained widespread attention with the development of 2-D materials.

The most frequent intercalants of 2-D TMDCs are atoms of alkali (e.g., Li, Na, K) and transition metals. These atoms can induce charge transfer (electrons) in order to increase the Fermi Energy and density states at the Fermi level. This "electron doping" creates a huge increase in carrier density (orders of magnitude larger than the modulation by electrostatic gating and traditional impurity doping) which alters the electronic and optical properties of layered materials substantially. Furthermore, the existence of metallic intercalants also implies that the weak interaction between layers gets stronger and the electronic structure of the whole material becomes more three-dimensional [58].

The introduction of intercalants into layered structures often induces a new type of collective electronic phenomena which does not exist in the original host material. For example, titanium diselenide (TiS_2) exhibits charge density waves (CDWs) at low temperatures. Nonetheless, with the addition of Cu (Cu_xTiS_2), a new superconducting state emerges, and the CDW transition is continuously suppressed as illustrated in Fig. 1.19 [59]. The microscopic origin of superconductivity and intercalation is not fully understood yet. Structural changes by intercalants seem to be closely related to the superconductivity, such as tetrahedral shape deformation and increasing layer separation by the spacer layer [60].

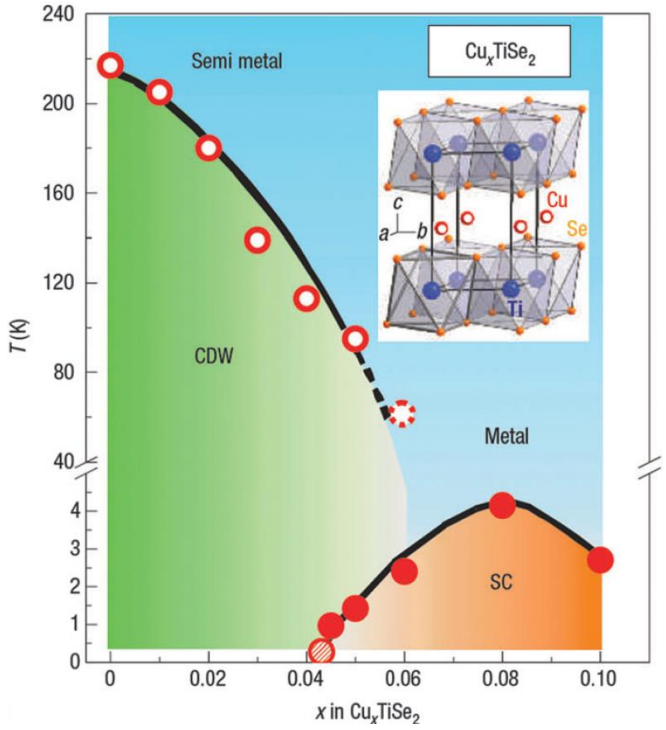

Figure 1.19. Phase-diagram of Cu intercalated $TiSe_2$, of which transition among metal, charge density wave (CDW) and superconductivity (SC) is presented [59].

Scaling the chalcogenide properties by chemical composition by either the main elements as well as by doping addition (intercalants included) need adapted metrology techniques, since the deviation from the targeted composition can drives unwanted film behaviors. As we will see in chapter II, suitable techniques to develop chalcogenide materials for the next technology nodes are Wavelength Dispersive X-ray fluorescence (WDXRF) as well as X-Ray Photoelectron Spectroscopy (XPS), not only because they are non-destructive accurate techniques but also because they are industrial-friendly tools capable to probe films with large stoichiometry, and film thickness (1 nm to mm) ranges and high spatial resolution (10 µm to mm) ideal to finished products as well as blanket wafers.

iii- Thickness reduction

Scaling in one dimension consists essentially of reducing the thickness of the chalcogenide film (while keeping other dimensions constant). The most common observation when reducing film thickness is that the crystallization temperature increases. For example, Raoux and co-workers [61] used time-resolved X-ray diffraction (XRD) to study the crystallization behavior of ultra-thin phase-change films with thicknesses in the range of 1–50 nm. Various materials were investigated, including $Ge_2Sb_2Te_5$ (GST), nitrogen-doped $Ge_2Sb_2Te_5$ (N-GST), $Ge_{15}Sb_{85}$, Sb_2Te and Ag- and In-doped Sb_2Te (AIST), each film being sandwiched between Al_2O_3 layers for oxidation protection. In all cases, films with phase-change layers having thicknesses between 10 and 50 nm showed little variation of crystallization temperature with thickness, but below 10 nm the crystallization temperature increased in some cases (i.e. for some materials) by as much as 200 ºC (Fig. 1.20). Films as thin as 2 nm for GST and N-GST, 1.5 nm for Sb2Te and AgIn-Sb2Te and 1.3 nm for GeSb were successfully crystallized. These results imply that reducing phase change materials thickness to such ultra-thin dimensions should be possible while still ensuring reversible memory switching in device applications.

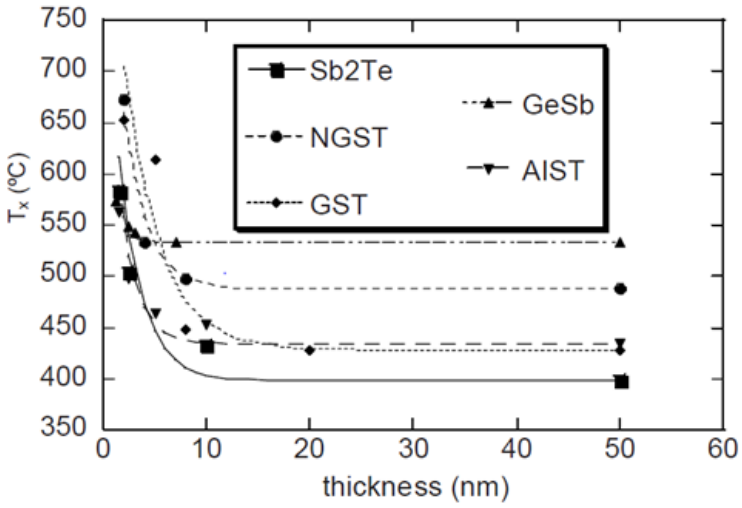

Figure 1.20. Evolution of crystallization temperature as a function of film thickness for various phase-change materials [61].

In the case of 2D TMDCs, we already have seen that their striking properties are only obtained when thinning down the bulk materials to few or single-layer. Therefore, scaling the chalcogenide properties by thickness reduction can be very challenging, because not only the surface effects such as oxidation can highly impact the film composition but also the interface effects with another material due to diffusion. Hence, as we will see in chapter II, combining WDXRF and XPS analysis allows us not only quantify the film composition, but also assess the surface/interfaces effects as well as in-depth chemical distribution when XPS is performed in angle-resolved mode.

1.5. Synthesis of chalcogenide films

In semiconductor industry, the synthesis of chalcogenide films is mainly by Physical Vapor Deposition (sputtering) and Chemical Vapor Deposition (MOCVD, ALD) since they are industrial-friendly techniques able to deposit films with high degree of chemical homogeneity and uniform thickness in the nano and micrometer-range.

i- Physcal Vapor Deposition (PVD)

PVD is constituted of several depositions techniques such as evaporation, molecular-beam epitaxy, sputtering, etc. The most common in semiconductor industry is the sputtering. In this process energetic particles bombard a target surface (cathode surface) with sufficient energy resulting in the ejection of atoms from the target surface.

The most common method to generate ion bombardment is to fill an evacuated chamber with a working gas within 1 to 100 mTorr pressure range and trigger an electric discharge with the target acting as negative electrode (cathode). Such apparatus is schematically shown in Fig. 1.21. Applied potential are typically between 500 and 5000 V. Direct currents are generally used when the target material is a good electrical conductor. Whereas, radio frequencies are employed when the target material is poorly conducting or an insulating. Deposits can also be formed by sputtering the metallic component while injecting other compounds in the gas phase, this process is known as reactive sputtering. Another

sputtering approach consists to apply a voltage bias to the substrate for negative potential relative to the plasma, hence prone to an ion bombardment that can influence the deposits properties; this method is known as bias sputtering [62].

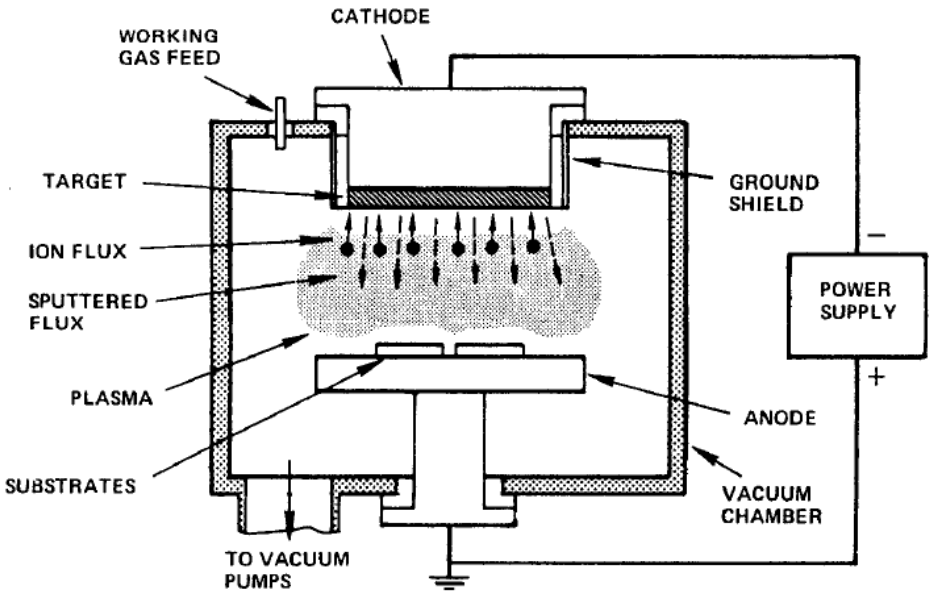

Figure 1.21. (a) Variation of the band gaps as a function of the number layers (n). (b) Position of the band edge with respect to the vacuum level [62].

The major advantage of the sputtering process is its versatility to deposit a large range of elements. In the case of chalcogenide films, although only tellurium can be sputtered from a pure Te cathode, sulfur and selenium can be deposited from a variety of compounds such as GeS, SnS ZnSe, WSe, etc. Despite of its universality as deposition tool, sputtering process lacks on film conformity due to poor step coverage at high aspect ratio (A:R). In general the relative ionization of the deposit can be inferred from the bottom step coverage at an aspect ratio of about 3:1 [63] (in ALD process it is >100:1, currently the highest conformity [64]). As we can see in Fig.1.22, with the increase of aspect ratio, sputtering results in local re-deposition across the trench, resulting in void formation. Hence, sputtering can be very costly with the reduction of technology nodes, leaving space for Chemical Vapor Deposition and its variants, discussed below.

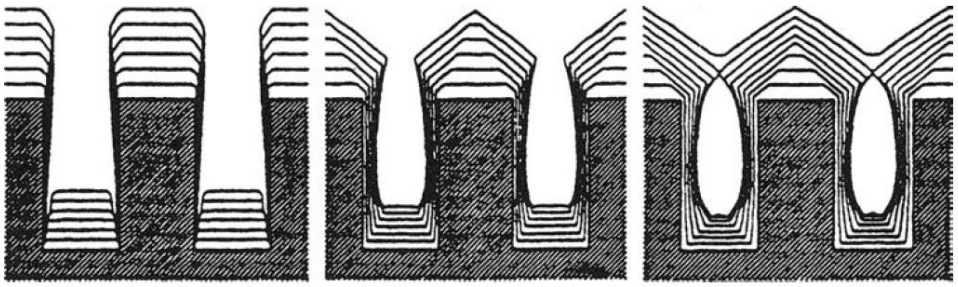

Figure 1.22. Simulation effects of the increasing levels of resputtering highlight the formation of voids [63].

ii- Chemical Vapor Deposition

Chemical vapor deposition (CVD) involves the formation of a thin solid film on a substrate material by a chemical reaction of vapor-phase precursors. This mechanism is the main factor distinguishing CVD from PVD which involve the adsorption of atomic or molecular species on the substrate.

In CVD process, vapor-phase precursors are injected in the reaction chamber and trigger the following general reaction:

$$\text{Gaseous reactants}_{(g)} \rightarrow \text{Solid material}_{(s)} + \text{gaseous products}_{(g)}$$

A more detailed picture of the basic physicochemical steps in an overall CVD reaction is illustrated in Fig. 1.23, which indicates several key steps:

1. Evaporation and transport of reagents (i.e. precursors) in the bulk gas flow region into the reactor;
2. Gas phase reactions of precursors in the reaction zone to produce reactive intermediates and gaseous by-products;
3. Mass transport of reactants to the substrate surface;
4. Adsorption of the reactants on the substrate surface;
5. Surface diffusion to growth sites, nucleation and surface chemical reactions leading to film formation;
6. Desorption and mass transport of remaining fragments of the decomposition away from the reaction zone.

In traditional thermal CVD, the film growth rate is determined by several parameters, the primary ones being the temperature of the substrate, the operating pressure of the reactor and the composition and chemistry of precursors.

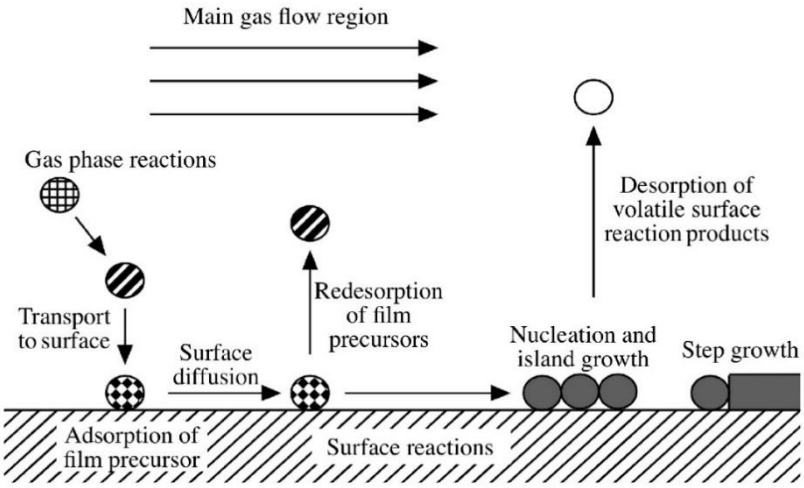

Figure 1.23. Precursor and transport reaction [65].

a. Metalorganic chemical vapor deposition (MOCVD)

In the semiconductor industry, traditional thermal CVD is not suitable since the deposited films lack homogeneity and reproducibility at the wafer scale [66]. These drawbacks lead to development of metal-organic metalorganic compounds as volatile sources for CVD, becoming the dominant industrial process for the growth of compound semiconductors.

As its name implies, MOCVD is the method for the deposition of condensed phase (solid phase in most cases) from vapor phase via a chemical reaction employing metal-organic (MO) precursors. In the case of chalcogenides, generally the transition metal is in the form of metal-organic precursors which are purged into the reaction chamber by one or more carrier gas, typically H_2 or Ar_2. The purity of precursors and the carrier gas(es) is critical in achieving high-quality materials in MOCVD growth [65]. A typical reaction occurring in MOCVD for chalcogenides is illustrated in Fig. 1.24.

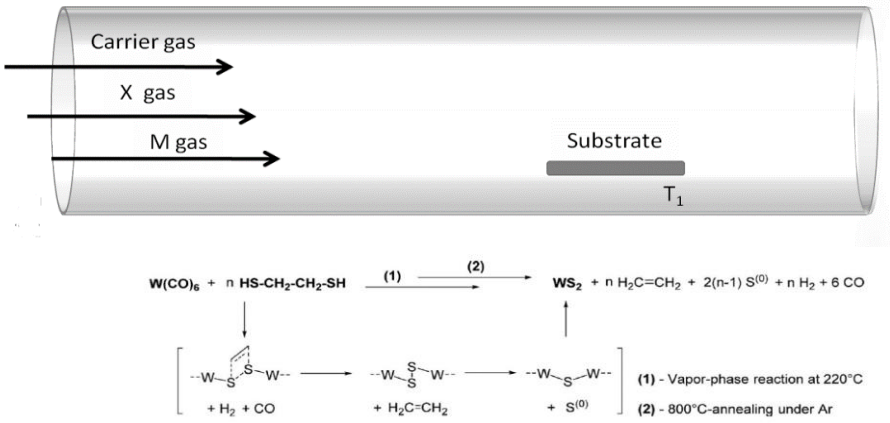

Figure 1.24. Procedure of MOCVD deposition.

Despite of the its advantage to deposit films at lower temperature compared to traditional CVD, MOCVD still has disadvantage to bring high level of carbon contamination in the deposited layer, and it is dependent to thermodynamic reaction mechanism, hence it is not as versatile as sputtering techniques.

b. Atomic Layer Deposition (ALD)

With the shrinking of devices, the next technology generation require new methods that enable highly controlled deposition of very thin and conformal films, requirements perfectly matched with ALD. Indeed, ALD has the advantage of even better conformity than MOCVD, thanks to the self-saturated monolayer deposition, with ultra-high aspect ratio > 100:1 proven [64].

ALD relies on sequential and saturating surface reactions of the alternately applied precursors. The precursor pulses are separated by inert gas purging or evacuation of the reaction chamber to avoid gas-phase reactions between the precursors. Growth proceeds in a cyclic manner, enabling easy thickness control. The basic principle of ALD is shown in a simplified manner in Fig. 1.25, where one ALD cycle of HfO_2 deposition process is presented. At first the exposure of the substrate surface to the gaseous $HfCl_4$ and its chemisorption on the available surface sites (–OH groups) leaves the surface

saturated with the metal precursor. In the example shown the chemisorption actually involves an exchange reaction with the surface groups, releasing HCl. After inert gas purging of the excess precursor and HCl by-product, the surface is exposed to the non-metal precursor, H2O. The surface reaction produces the desired HfO2, releases the rest of the Cl ligands and recreates the –OH groups. After inert gas purging the surface is ready for the next ALD cycle [67].

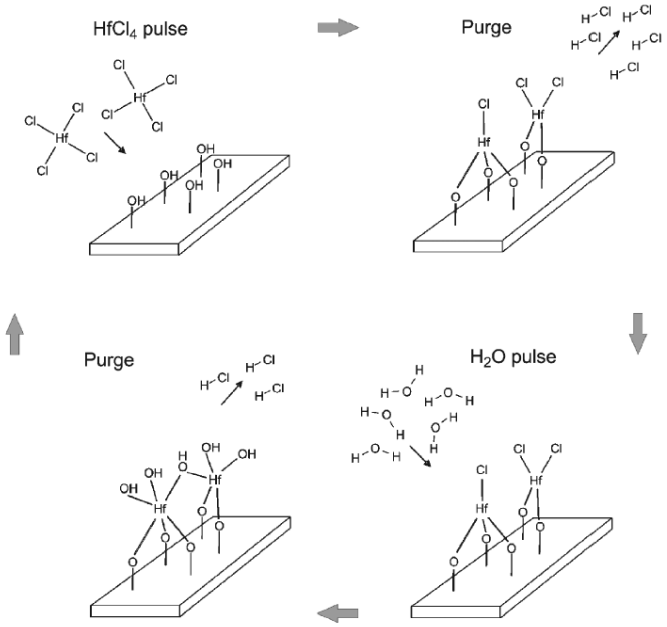

Figure 1.25. Schematic illustration of an ALD cycle of HfO_2 process where precursors, HCl_4 and H_2O are alternately pulsed and separated by inert gas purging.

The alternate exposure of the precursors alone does not qualify the process as ALD. As important is that all the reactions are saturated because only such saturation ensures that the film growth is self-limiting. Under self-limiting conditions the same amount of film is deposited on all the surfaces irrespective of the dose received, provided the dose is high enough to maintain saturation. Ideally, ALD growth proceeds by one atomic layer per cycle, but in practice, due to steric hindrances and sometimes possibly due to a limited number of reactive surface sites, the growth rate per cycle usually is only a small fraction of a monolayer (ML) thickness, typically less than 0.5 ML. As the growth proceeds in a cyclic manner, and the purging periods take some time, the ALD technique is rather slow. This low through-put is highly investigated by manufacturers to increase the number of ALD chambers used in industry [68].

1.6. Motivations of this work

This overview about chalcogenide materials point out their outstanding chemical diversity forging their unique properties for a wide range of applications such as Phase-change materials, 2D materials, photonics, photovoltaics, etc. With these turnkey properties, chalcogenide materials are already present in the semiconductor roadmaps (such as internet of things and artificial intelligence) and it is already replacing flash memories for next technology nodes (e.g. 3D Xpoint from Intel already in the market).

Nevertheless, with the downsizing of devices, chalcogenide films becomes highly influenced

by the chemical composition, the surface/interface effects and the depth-profile composition. Therefore, adapted metrology protocols need to be developed not only to tackle down these issues but also to be implemented in the industrial lines as non-destructive fast metrology. Hence, in this doctoral work, we developed adapted protocols based on three advanced X-ray techniques: Wavelength Dispersive X-ray Fluorescence (WDXRF), X-Ray Photoelectron Spectroscopy (XPS) and the combined analysis Grazing-Incidence X-ray Fluorescence with X-ray Reflectometry. The X-ray theory as well as the recursive formalisms to probe ultra-thin layered material by each technique are discussed in the next chapter.

1.7. References

[1] Fundamentals of Amorphous Semiconductors – National Academy of Sciences, Washington DC, 1972. .

[2] M. D. Tabak, S. W. Ing, and M. E. Scharfe, "Operation and performance of amorphous selenium-based photoreceptors," IEEE Trans. Electron Devices, vol. 20, no. 2, pp. 132–139, Feb. 1973.

[3] S. R. Ovshinsky, "Reversible Electrical Switching Phenomena in Disordered Structures," Phys. Rev. Lett., vol. 21, no. 20, pp. 1450–1453, Nov. 1968.

[4] M. Chen, K. A. Rubin, and R. W. Barton, "Compound materials for reversible, phase-change optical data storage," Appl. Phys. Lett., vol. 49, no. 9, pp. 502–504, Sep. 1986.

[5] S. Tyson, G. Wicker, T. Lowrey, S. Hudgens, and K. Hunt, "Nonvolatile, high density, high performance phase-change memory," in Aerospace Conference Proceedings, 2000 IEEE, 2000, vol. 5, pp. 385–390.

[6] D. Xiao, G.-B. Liu, W. Feng, X. Xu, and W. Yao, "Coupled spin and valley physics in monolayers of MoS 2 and other group-VI dichalcogenides," Phys. Rev. Lett., vol. 108, no. 19, p. 196802, 2012.

[7] Q. H. Wang, K. Kalantar-Zadeh, A. Kis, J. N. Coleman, and M. S. Strano, "Electronics and optoelectronics of two-dimensional transition metal dichalcogenides," Nat. Nanotechnol., vol. 7, no. 11, p. 699, 2012.

[8] K. Shportko, S. Kremers, M. Woda, D. Lencer, J. Robertson, and M. Wuttig, "Resonant bonding in crystalline phase-change materials," Nat. Mater., vol. 7, no. 8, pp. 653–658, Aug. 2008.

[9] "Kastner - 1972 - Bonding Bands, Lone-Pair Bands, and Impurity State.pdf." .

[10] N. Mott, "Electrons in disordered structures," Adv. Phys., vol. 16, no. 61, pp. 49–144, 1967.

[11] P. B. Littlewood, "The crystal structure of IV-VI compounds. I. Classification and description," J. Phys. C Solid State Phys., vol. 13, no. 26, pp. 4855–4873, Sep. 1980.

[12] P. Littlewood, "The crystal structure of IV-VI compounds. II. A microscopic model for cubic/rhombohedral materials," J. Phys. C Solid State Phys., vol. 13, no. 26, p. 4875, 1980.

[13] S. Judith John and A. N. Bloch, "Quantum-defect electronegativity scale for nontransition elements," Phys. Rev. Lett., vol. 33, no. 18, p. 1095, 1974.

[14] G. Simons and A. N. Bloch, "Pauli-force model potential for solids," Phys. Rev. B, vol. 7, no. 6, p. 2754, 1973.

[15] J. Phillips, "Structural pseudoion form factors," Solid State Commun., vol. 22, no. 9, pp. 549–550, 1977.

[16] P. Noé, C. Vallée, F. Hippert, F. Fillot, and J.-Y. Raty, "Phase-change materials for non-volatile memory devices: from technological challenges to materials science issues," Semicond. Sci. Technol., vol. 33, no. 1, p. 013002, Jan. 2018.

[17] N. Yamada, E. Ohno, N. Akahira, K. Nishiuchi, K. Nagata, and M. Takao, "High speed overwritable phase change optical disk material," Jpn. J. Appl. Phys., vol. 26, no. S4, p. 61, 1987.

[18] N. Yamada, E. Ohno, K. Nishiuchi, N. Akahira, and M. Takao, "Rapid-phase transitions of GeTe-Sb2Te3 pseudobinary amorphous thin films for an optical disk memory," J. Appl. Phys., vol. 69, no. 5, pp. 2849–2856, 1991.

[19] S. Raoux et al., "Phase transitions in Ge–Sb phase change materials," J. Appl. Phys., vol. 105, no. 6, p. 064918, 2009.

[20] S. Raoux et al., "Phase transitions in Ga–Sb phase change alloys," Phys. Status Solidi B, vol. 249, no. 10, pp. 1999–2004, 2012.

[21] D. Lencer, M. Salinga, B. Grabowski, T. Hickel, J. Neugebauer, and M. Wuttig, "A map for phase-change materials," Nat. Mater., vol. 7, no. 12, pp. 972–977, Dec. 2008.

[22] V. Karpov, Y. Kryukov, I. Karpov, and M. Mitra, "Field-induced nucleation in phase change memory," Phys. Rev. B, vol. 78, no. 5, p. 052201, 2008.
[23] J. Li, H. Yang, and K. Lim, "Field-dependent activation energy of nucleation and switching in phase change memory," Appl. Phys. Lett., vol. 100, no. 26, p. 263501, 2012.
[24] R. E. Simpson et al., "Interfacial phase-change memory," Nat. Nanotechnol., vol. 6, no. 8, pp. 501–505, Aug. 2011.
[25] M. Krbal et al., "Intrinsic complexity of the melt-quenched amorphous Ge 2 Sb 2 Te 5 memory alloy," Phys. Rev. B, vol. 83, no. 5, p. 054203, 2011.
[26] J. Akola and R. O. Jones, "Binary Alloys of Ge and Te: Order, Voids, and the Eutectic Composition," Phys. Rev. Lett., vol. 100, no. 20, May 2008.
[27] B. Huang and J. Robertson, "Bonding origin of optical contrast in phase-change memory materials," Phys. Rev. B, vol. 81, no. 8, p. 081204, 2010.
[28] R. Simpson, P. Fons, X. Wang, A. Kolobov, T. Fukaya, and J. Tominaga, "Non-melting super-resolution near-field apertures in sb–te alloys," Appl. Phys. Lett., vol. 97, no. 16, p. 161906, 2010.
[29] Y. Utsugi, "Nanometre-scale chemical modification using a scanning tunnelling microscope," Nature, vol. 347, no. 6295, p. 747, 1990.
[30] I. Valov, R. Waser, J. R. Jameson, and M. N. Kozicki, "Electrochemical metallization memories—fundamentals, applications, prospects," Nanotechnology, vol. 22, no. 28, p. 289502, Jul. 2011.
[31] Z. Lin and C. Liang, "Lithium–sulfur batteries: from liquid to solid cells," J. Mater. Chem. A, vol. 3, no. 3, pp. 936–958, 2015.
[32] H. Kitaura, A. Hayashi, K. Tadanaga, and M. Tatsumisago, "All-Solid-State Lithium Secondary Batteries Using $LiMn_2O_4$ Electrode and Li_2S–P_2S_5 Solid Electrolyte," J. Electrochem. Soc., vol. 157, no. 4, p. A407, 2010.
[33] K. Shimakawa, A. Kolobov, and S. Elliott, "Photoinduced effects and metastability in amorphous semiconductors and insulators," Adv. Phys., vol. 44, no. 6, pp. 475–588, 1995.
[34] H. Fritzsche, "Light-induced structural changes in glasses," in Insulating and semiconducting glasses, World Scientific, 2000, pp. 653–690.
[35] G. Pfeiffer, M. Paesler, and S. Agarwal, "Reversible photodarkening of amorphous arsenic chalcogens," J. Non-Cryst. Solids, vol. 130, no. 2, pp. 111–143, 1991.
[36] A. Kolobov and J. Tominaga, "Chalcogenide glasses in optical recording: recent progress," J Optoelectron Adv Mater, vol. 4, pp. 679–686, 2002.
[37] J.-F. Viens et al., "Fabrication and characterization of integrated optical waveguides in sulfide chalcogenide glasses," J. Light. Technol., vol. 17, no. 7, p. 1184, 1999.
[38] S. Song, S. S. Howard, Z. Liu, A. O. Dirisu, C. F. Gmachl, and C. B. Arnold, "Mode tuning of quantum cascade lasers through optical processing of chalcogenide glass claddings," Appl. Phys. Lett., vol. 89, no. 4, p. 041115, 2006.
[39] A. Faraon et al., "Local tuning of photonic crystal cavities using chalcogenide glasses," Appl. Phys. Lett., vol. 92, no. 4, p. 043123, 2008.
[40] A. Luque and S. Hegedus, Handbook of photovoltaic science and engineering. John Wiley & Sons, 2011.
[41] M. Terheggen, H. Heinrich, G. Kostorz, D. Baetzner, A. Romeo, and A. Tiwari, "Analysis of bulk and interface phenomena in CdTe/CdS thin-film solar cells," Interface Sci., vol. 12, no. 2–3, pp. 259–266, 2004.
[42] "https://www.nrel.gov/pv/assets/images/efficiency-chart.png." .
[43] J. M. Burst et al., "CdTe solar cells with open-circuit voltage breaking the 1 V barrier," Nat. Energy, vol. 1, no. 3, p. 16015, Feb. 2016.
[44] S. Manzeli, D. Ovchinnikov, D. Pasquier, O. V. Yazyev, and A. Kis, "2D transition metal dichalcogenides," Nat. Rev. Mater., vol. 2, no. 8, p. 17033, Jun. 2017.
[45] A. Splendiani et al., "Emerging photoluminescence in monolayer MoS2," Nano Lett., vol. 10, no. 4, pp. 1271–1275, 2010.
[46] X. Xu, W. Yao, D. Xiao, and T. F. Heinz, "Spin and pseudospins in layered transition metal dichalcogenides," Nat. Phys., vol. 10, no. 5, p. 343, 2014.
[47] Z. Gong et al., "Magnetoelectric effects and valley-controlled spin quantum gates in transition metal dichalcogenide bilayers," Nat. Commun., vol. 4, p. 2053, 2013.
[48] Y. Zhang, T. Oka, R. Suzuki, J. Ye, and Y. Iwasa, "Electrically switchable chiral light-emitting transistor," Science, vol. 344, no. 6185, pp. 725–728, 2014.
[49] A. Chernikov et al., "Exciton binding energy and nonhydrogenic Rydberg series in monolayer WS

2," Phys. Rev. Lett., vol. 113, no. 7, p. 076802, 2014.
[50] A. Mitioglu et al., "Optical investigation of monolayer and bulk tungsten diselenide (WSe2) in high magnetic fields," Nano Lett., vol. 15, no. 7, pp. 4387–4392, 2015.
[51] B. Radisavljevic, A. Radenovic, J. Brivio, i V. Giacometti, and A. Kis, "Single-layer MoS 2 transistors," Nat. Nanotechnol., vol. 6, no. 3, p. 147, 2011.
[52] H. Y. Cheng et al., "A high performance phase change memory with fast switching speed and high temperature retention by engineering the GexSbyTez phase change material," 2011, pp. 3.4.1-3.4.4.
[53] H. Wang, H. Yuan, S. Sae Hong, Y. Li, and Y. Cui, "Physical and chemical tuning of two-dimensional transition metal dichalcogenides," Chem. Soc. Rev., vol. 44, no. 9, pp. 2664–2680, 2015.
[54] P. Zuliani et al., "Overcoming Temperature Limitations in Phase Change Memories With Optimized $Ge_xSb_yTe_z$," IEEE Trans. Electron Devices, vol. 60, no. 12, pp. 4020–4026, 2013.
[55] G. Navarro et al., "Trade-off between SET and data retention performance thanks to innovative materials for phase-change memory," in Electron Devices Meeting (IEDM), 2013 IEEE International, 2013, pp. 21–5.
[56] A. Fantini et al., "N-doped GeTe as performance booster for embedded phase-change memories," in Electron Devices Meeting (IEDM), 2010 IEEE International, 2010, pp. 29–1.
[57] X. Biquard et al., "Effect of doping on global and local order in crystalline GeTe," Appl. Phys. Lett., vol. 98, no. 23, p. 231907, 2011.
[58] J. A. Wilson and A. Yoffe, "The transition metal dichalcogenides discussion and interpretation of the observed optical, electrical and structural properties," Adv. Phys., vol. 18, no. 73, pp. 193–335, 1969.
[59] E. Morosan et al., "Superconductivity in Cu x TiSe 2," Nat. Phys., vol. 2, no. 8, p. 544, 2006.
[60] M. Burrard-Lucas et al., "Enhancement of the superconducting transition temperature of FeSe by intercalation of a molecular spacer layer," Nat. Mater., vol. 12, no. 1, p. 15, 2013.
[61] S. Raoux, J. L. Jordan-Sweet, and A. J. Kellock, "Crystallization properties of ultrathin phase change films," J. Appl. Phys., vol. 103, no. 11, p. 114310, Jun. 2008.
[62] M. Henini, "Handbook of Thin-Film Deposition Processes and Techniques," Microelectron. J., vol. 31, no. 3, p. 219, Mar. 2000.
[63] S. Hamaguchi and S. Rossnagel, "Simulations of trench-filling profiles under ionized magnetron sputter metal deposition," J. Vac. Sci. Technol. B Microelectron. Nanometer Struct. Process. Meas. Phenom., vol. 13, no. 2, pp. 183–191, 1995.
[64] T. Hatanpää, M. Ritala, and M. Leskelä, "Precursors as enablers of ALD technology: Contributions from University of Helsinki," Coord. Chem. Rev., vol. 257, no. 23–24, pp. 3297–3322, 2013.
[65] A. Jones, P. O′ Brien, CVD of Compound Semiconductors. VCH, Weinheim, 1997.
[66] A. S. Pawbake, M. S. Pawar, S. R. Jadkar, and D. J. Late, "Large area chemical vapor deposition of monolayer transition metal dichalcogenides and their temperature dependent Raman spectroscopy studies," Nanoscale, vol. 8, no. 5, pp. 3008–3018, Jan. 2016.
[67] M. Ritala and M. Leskelä, "Atomic layer deposition," in Handbook of Thin Films, Elsevier, 2002, pp. 103–159.
[68] E. Granneman, P. Fischer, D. Pierreux, H. Terhorst, and P. Zagwijn, "Batch ALD: Characteristics, comparison with single wafer ALD, and examples," Surf. Coat. Technol., vol. 201, no. 22–23, pp. 8899–8907, 2007.
[69] D. Kau *et al.*, "A stackable cross point Phase Change Memory," in *2009 IEEE International Electron Devices Meeting (IEDM)*, 2009, pp. 1–4.

2. Chapter II: Probing chalcogenide materials

2.1. Introduction

As explained in Chapter I, chalcogenide films are receiving an extensive interest not only for applications in resistive memories (PCRAM and CBRAM), photonics and photovoltaics but also in the development of new 2-D materials (e.g. spintronics applications). Chalcogenide materials are strategically present in the semiconductor roadmaps and it is already replacing flash memories (e.g. phase change material and ovonic threshold switch in new random access memory). For the next technology nodes, chalcogenide properties can be scaled by tuning the chemical composition or by reducing the film thickness. Nonetheless, it also means that their properties become more tightly influenced by the chemical composition, the surface/interface effects and the depth-profile composition.

Hence, dedicated metrology protocols must be developed, first to assist the optimization of chalcogenide materials processes in cleanroom environment, then to allow non-destructive process monitoring with industry-driven uncertainties. X-ray based techniques such as X-ray fluorescence (XRF) and X-ray Photoelectron Spectroscopy (XPS) are particularly suitable for the characterization of thin inorganic materials with composition-driven properties. First, XRF in high-resolution wavelength-dispersive configuration (WDXRF) is a fab-compatible technique allowing quantitative analysis of the composition of complex compounds with spatial resolution in the mm range. However, WDXRF protocols dedicated to chalcogenides films and with improved accuracy in the compositional analysis must be developed to overcome the lack of standards for sulfur-based compounds, the importance of matrix effects for the quantification of low-Z elements, or to address the need for analysis of ultrathin 2D transition metal dichalcogenides.

Secondly, X-ray Photoelectron Spectroscopy can be used, not only to probe the surface of the chalcogenide films and its evolution after air break and ageing, but also as an efficient and accurate inline tool to monitor the composition of binary and ternary chalcogenide thin layers with spatial resolution in the ~ 10 µm range, *i.e* compatible with product wafer. Here also, XPS protocols dedicated to chalcogenides films are required to improve the accuracy in the compositional analysis. Lastly, the compositional depth-profile in thin chalcogenide materials, can be non-destructively revealed and quantified, either by optimized angle-resolved strategies for ultrathin films, or by the combination of XRF in grazing incidence (GIXRF) and X-ray reflectometry (XRR). GIXRF/XRR analysis are now entering labs and are getting closer to the fab, which puts hard requirements on the definition of measurement protocols and data analysis strategies.

In this chapter, we will introduce the metrology techniques and the related tools we used to develop the metrology protocols dedicated to chalcogenides.

2.2. X-Ray and matter interactions

X-rays are part of the spectrum of electromagnetic radiation with energies higher than those of ultra-violet radiation (Fig.2.1). They were discovered by W.C Röntgen in 1895 and correspond to a radiation of energy in the kilo electron-Volt range (generally from 0.1 to 100 keV) and wavelength between the Ultra-Violet and Gamma ray radiations.

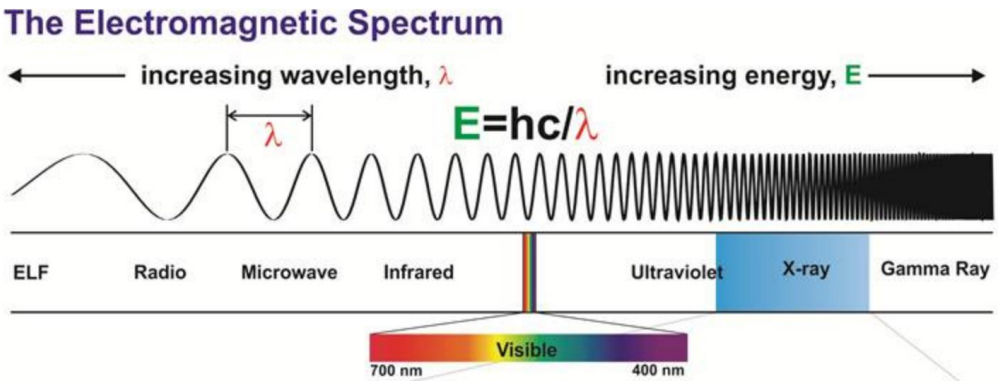

Figure 2.1. The electromagnetic spectrum range, X-ray wavelength ranges from 12 to 0.012 nm between Ultraviolet and Gamma rays.

When X-ray radiation is emitted or absorbed by atoms or molecules, it carries out energy. The energy change in the atom or molecule is related to the wavelength (or frequency) of the radiation (emitted or absorbed) by the equation:

$$E_n - E_{n+1} = hc/\lambda \quad \text{(eq.2.1)}$$

Where, h is the Max Planck constant, c is the speed of light, λ is the wavelength, and n is the electron shell (principal quantum number), K, L, M and etc.

Equation 2.1 is the basis of the photoelectric effect formalized by Albert Einstein in 1905 [1]. The X-ray beam interacts with an atom, ejecting an electron from the K shell, as illustrated in Fig.2.2. The hole created in that shell is subsequently filled by an electron from an outer shell (L). It simultaneously releases a photon with an energy equal to the difference in the binding energies of the K and L shells. The released photon also known as fluorescence radiation. The energy difference can also be transferred to an electron of an external shell that is ejected (Auger electron).

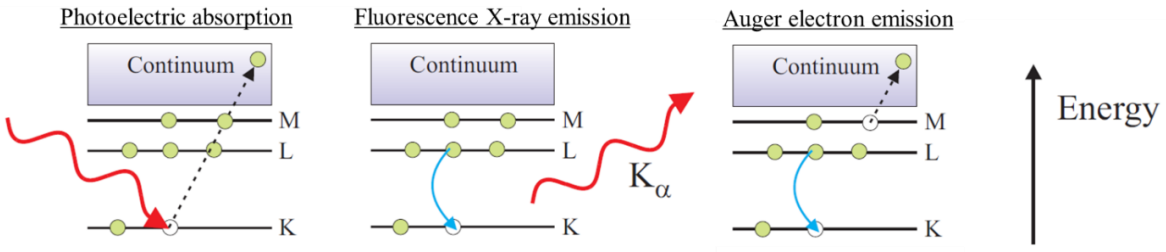

Figure 2.2. The photo-electric effect, and consecutive X-ray fluorescence, or Auger emission.

The permitted energies of atoms can be described by sets of numbers known as quantum

numbers which designate the electronic structures, i.e. electron configurations. These quantum numbers play significant roles in describing the energy levels of electrons as well as the shapes of the orbitals that explain distributions of electrons in space. The energy levels of different subshells are represented by notation such as $1s_{1/2}$, $2p_{1/2}$, $2p_{3/2}$, as shown in Fig. 2.3. States such as $1s_{1/2}$ means n = 1, l = 0, j = 1/2, $2p_{1/2}$ means n = 2, l = 1 and j = 1/2 and $2p_{3/2}$ means n = 2, l = 1, and j = 3/2, where j = (l±s), hence:

- n is the principal quantum number associated with successive orbitals, where n is a positive number 1, 2, 3 … that designates the K, L, M, N, …shells, respectively;
- l is the azimuthal quantum number, it is the measure of the orbital angular momentum defined as s, p, d, f…letters;
- s is the spin quantum number (s) which can only take two possible values +1/2 and −1/2. The spin quantum number, allows two electrons of opposite spin (or symmetry) into each orbital.
- j is the total angular momentum (l±s)

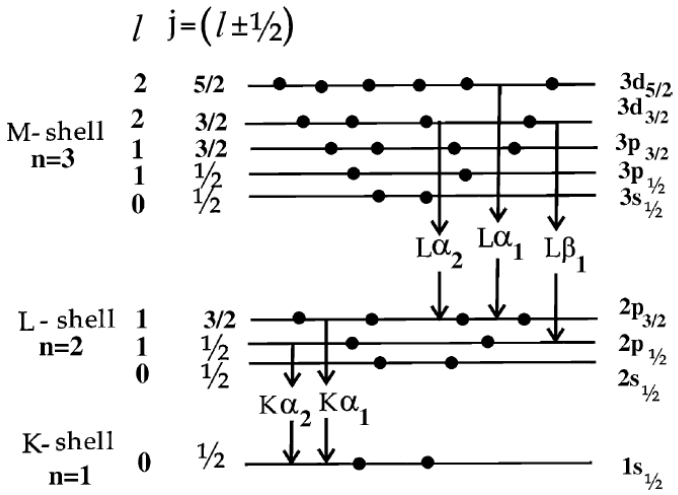

Figure 2.3. Energy levels of different subshells of an atom along with their quantum numbers and occupancy of electrons.

The characteristic radiations are emitted according to electron transitions governed by the following quantum-mechanical rules:

$$\Delta n \geq 1,\ \Delta l = \pm 1,\ \Delta j = 0, \pm 1 \qquad \text{(eq.2.2)}$$

It means that if the K-shell was ionized, the most probable electron transition is $1s_{1/2} \leftarrow 2p_{3/2}$ which corresponds to $K\alpha_1$ according to Siegbanh notation or K-L3 according IUPAC notation. The main fluorescence lines are illustrated in Fig. 2.4 in both scientific notations.

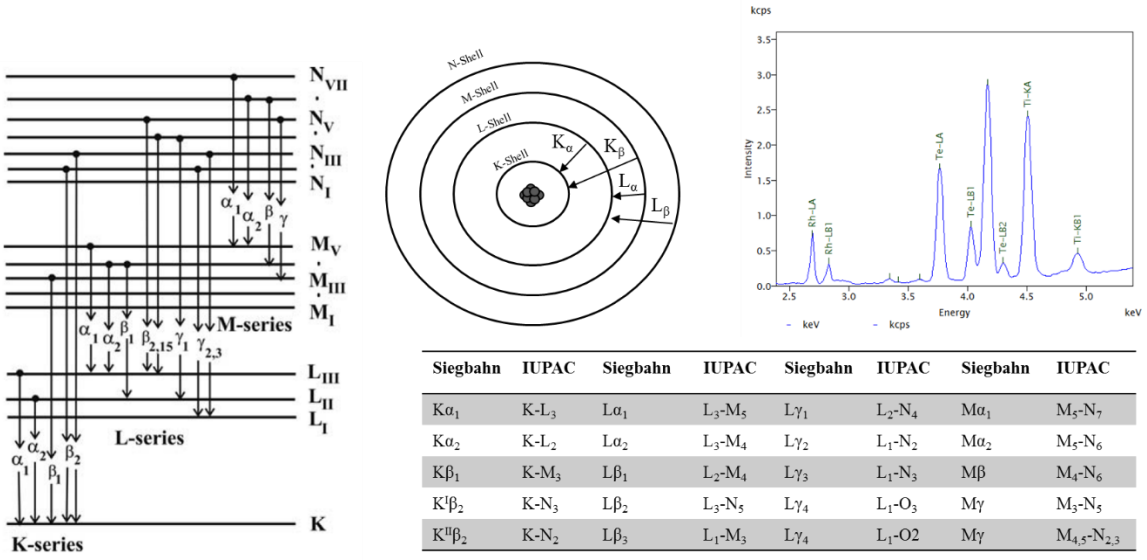

Siegbahn	IUPAC	Siegbahn	IUPAC	Siegbahn	IUPAC	Siegbahn	IUPAC
$K\alpha_1$	$K\text{-}L_3$	$L\alpha_1$	$L_3\text{-}M_5$	$L\gamma_1$	$L_2\text{-}N_4$	$M\alpha_1$	$M_5\text{-}N_7$
$K\alpha_2$	$K\text{-}L_2$	$L\alpha_2$	$L_3\text{-}M_4$	$L\gamma_2$	$L_1\text{-}N_2$	$M\alpha_2$	$M_5\text{-}N_6$
$K\beta_1$	$K\text{-}M_3$	$L\beta_1$	$L_2\text{-}M_4$	$L\gamma_3$	$L_1\text{-}N_3$	$M\beta$	$M_4\text{-}N_6$
$K^I\beta_2$	$K\text{-}N_3$	$L\beta_2$	$L_3\text{-}N_5$	$L\gamma_4$	$L_1\text{-}O_3$	$M\gamma$	$M_3\text{-}N_5$
$K^{II}\beta_2$	$K\text{-}N_2$	$L\beta_3$	$L_1\text{-}M_3$	$L\gamma_4$	$L_1\text{-}O2$	$M\gamma$	$M_{4,5}\text{-}N_{2,3}$

Figure 2.4. Energy levels of main X-ray fluorescence line series.

Although K←L3 ($K\alpha_1$) is the most likely electron transition, K←L2 ($K\alpha_2$) and K←M3 ($K_{\beta 1}$) can also be potential but with lesser probability, and therefore lower relative intensity. To be able to compute the relative intensities of allowed and emitted X-ray lines, we sum the whole intensity of all lines coming from a common initial level or to common final level. Thus, the probability that $K_{\alpha 1}$ radiation will be emitted instead of $K_{\alpha 2}$ is called $gK_{\alpha 1}$ and is given by:

$$g_{K\alpha 1} = \frac{I(K_{\alpha 1})}{[I(K_{\alpha 1}) + I(K_{\alpha 2})]} = \frac{I(K_{\alpha 1})/I(K_{\alpha 2})}{I(K_{\alpha 1})/I(K_{\alpha 2}) + 1} \qquad \text{(eq. 2.3)}$$

Similarly, the probability of K_α rather than K_β is then:

$$g_{K\alpha} = \frac{I(K_\alpha)}{[I(K_\beta) + I(K_\beta)]} = \frac{I(K_\alpha)/I(K_\beta)}{I(K_\alpha)/I(K_\beta) + 1} \qquad \text{(eq. 2.4)}$$

After the generation of characteristic radiation, the photons intensity suffers an exponential absorption before emerging from the material. This attenuation is known as the Beer-Lambert law and is given by:

$$I = I_0 . exp(-\mu_t x) \qquad \text{(eq. 2.5)}$$

Equation 2.5 is valid for both incoming and emerging radiation beam. It depends on the initial beam intensity (I_0), the traveled distance (x) and the total linear attenuation coefficient of the irradiated material (μ_t) which represents the sum of all interactions the photons can have with the material. For X-rays it means:

$$\mu_t = \mu_{Rayleigh\ scattering} + \mu_{Compton\ scattering} + \tau_{photoeletric\ absorption} \qquad \text{(eq. 2.6)}$$

Where $\mu_{Rayleigh\ scattering}$ is the elastic scattering coefficient, $\mu_{Compton\ scattering}$ is the inelastic scattering coefficient, and $\tau_{photoeletric\ absorption}$ is the photoelectric absorption coefficient, corresponding to the photoelectric effect.

- Rayleigh scattering ($\mu_{Rayleigh}$)

In this interaction, the photon simply bounces off an electron without losing energy, as shown in Fig. 2.5. The Rayleigh scattering occurs by temporarily increasing the energy of this electron even though the electron will not leave its shell. The electron returns to its initial energy level by re-emitting an X-ray photon after absorbing a negligible amount of energy and remaining almost in the same position. Thus the atom is neither excited nor ionized and no energy is lost. This kind of scattering depends upon on Z^2 and is of significance in analytical X-Ray fluorescence due to its contribution to the overall background.

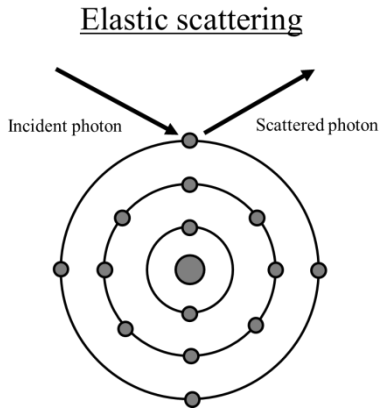

Figure 2.5. Elastic scattering.

- Compton scattering ($\mu_{Compton}$)

This inelastic interaction occurs when the incident photon has an energy (E_0) much larger than the binding energy of an electron. In this case the photon transfers some of its momentum to electron which is ejected with direction at an angle θ according to the incident direction. As the energy and momentum are conserved, the remaining energy is transferred to a scattered photon with a trajectory of angle φ according to the incident photon (Fig. 2.6). In relation to the incident X-ray photon, the Compton electron may only be driven forward compared to the incident photon (i.e. θ to 90°), while scattered photon may propagate in any direction between 0° to 180°.

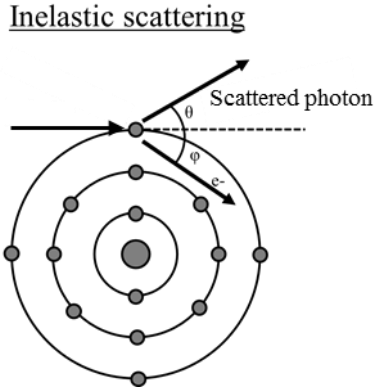

Figure 2.6. Inelastic scattering

- Photoelectric absorption (τ)

The photoelectric effect is described earlier. As illustrated in Fig. 2.7.a, it contributes to almost 95% of the total linear attenuation coefficient (μ_t) at low-energies (< 100keV), hence most of the characteristic X-ray lines of the elements. The main feature of the photo absorption coefficient is that, for any elements, it decreases rapidly with the increase of energy, and has discontinuous jumps corresponding to the binding energies of electronic shells. Therefore, these sharp discontinuities, usually referred as absorption edges, correspond to an abrupt photon attenuation increase related to the emission of the characteristic radiation.

The total photo-absorption coefficient τ is sum of the photo-absorption coefficients of the individual shells, hence: $\tau_{abs} = \tau K + \tau L1 + \tau L2 + \tau L3 + \tau M1 + \cdots$ These coefficients for the individual shells (for example, τK) are usually not easily known, but the ratios τK/τ, τL1/τ, τL2/τ, etc. can be calculated from tabulated values of absorption edge jump ratios, SK, SL1, SL2, etc. They are defined as the ratio of the photo-absorption coefficients at the maximum and minimum energy sides of an edge (Fig.2.7.b), for example the K-edge is given by:

$$S_k = \frac{\tau}{\tau - \tau_k} \text{ or } \tau_k = \frac{S_k - 1}{S_k}\tau, \quad \frac{\tau}{\tau_k} = \frac{S_k - 1}{S_k} = j_k \qquad \text{(eq. 2.7)}$$

where j_k is fraction of the K-shell absorption jump ratios.

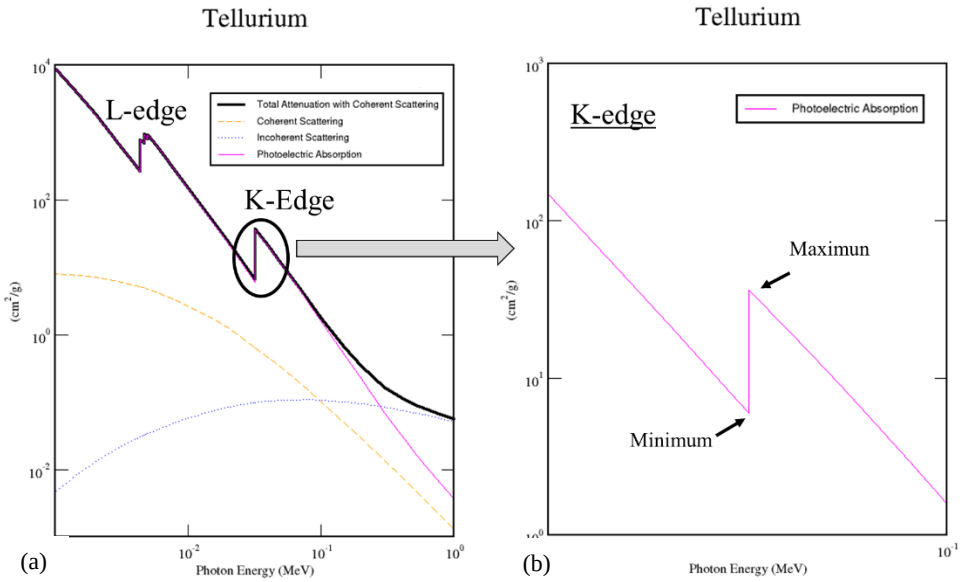

Figure 2.7. Absorption edges of tellurium [2].

- Fluorescence Yield (ω) and competition with Auger electrons

Fluorescence yield is one of the major parameter that determine the intensities of X-ray spectra. It is defined as the probability of photon emission over the total emission probabilities, after the ionization of an atom. On average the fluorescence yield (ω_f) is given by:

$$\omega_f = \frac{\tau_f}{\tau_f + \mu_a} \qquad \text{(eq. 2.8)}$$

Where τ_f is the absorption cross-section of the emitted fluorescence line, μ_a is the Auger electron cross-section.

Fluorescence yield increases with the atomic number and also differs significantly from one electron shell to another: ω_K is much larger than ω_L and ω_L is much larger than ω_M, as illustrated in Fig. 2.8.a. Moreover, Fluorescence yield has a straight competition with the Auger-probability (ω_a) as $\omega_a + \omega_f = 1$ (Fig. 2.8.b), hence probing light elements by XRF is very challenging due to low fluorescence yield.

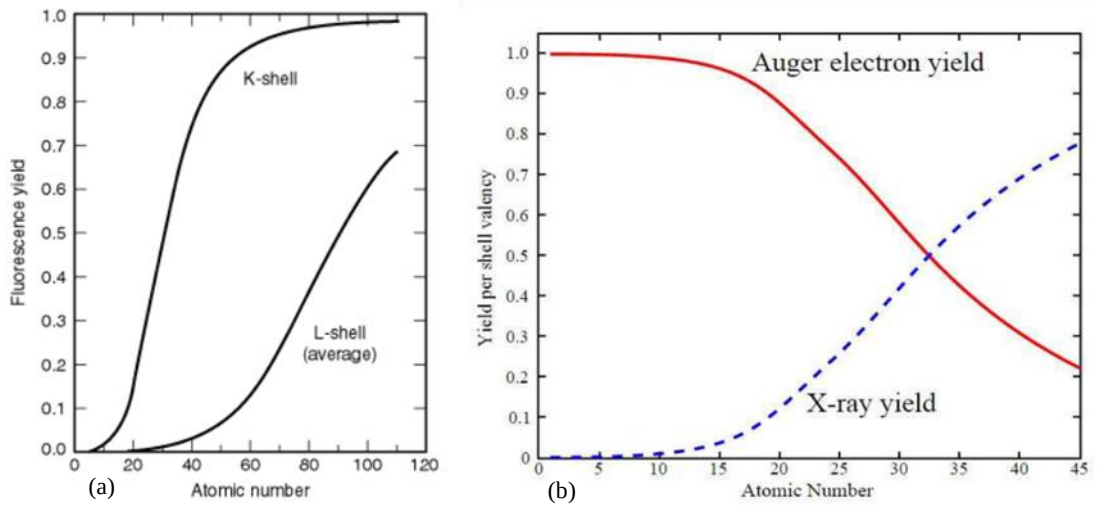

Figure 2.8. Fluorescence yields for K and L shells for $5 \leq Z \leq 110$ [3].

2.3. XRF quantitative analysis

The main advantages of XRF analysis is the elementary quantification (stoichiometric or compounds) as well as the determination of layered structures (thickness and density). XRF quantification can be performed either by theoretical approach or empirical one. Between both methods, the empirical one is the relatively simple mathematical descriptions of the relation between the fluorescence intensity and a given parameter (i.e. thickness, compositions, etc.), as illustrated in Fig 2.9.a. The method is straightforward when analyzing simple compounds (i.e. 3 to 5 standards are required if we quantify film with one element), nonetheless it becomes very complicated when probing mixed elements and it needs at least 3*(total parameters) + 2 samples to create the calibration curves. Furthermore, they may be limited in their applicability to a certain range of concentrations.

The theoretical approach most commonly known as fundamental parameters (FP) method is defined by mathematical models for the excitation of atoms and subsequent relaxation process, the absorption (attenuation) of radiation within the specimen by the probed atoms and the matrix, and possibly indirect excitation effects by certain matrix atoms. Simplified assumptions are often made, for instance, the specimen is perfectly flat and homogeneous, and incident and fluorescent beams are parallel. Compared to the empirical method, FP is more advantageous because it can employ only one standard (i.e. pure element) and its calibration curve (Fig. 2.9.b) work for entire range of compounds.

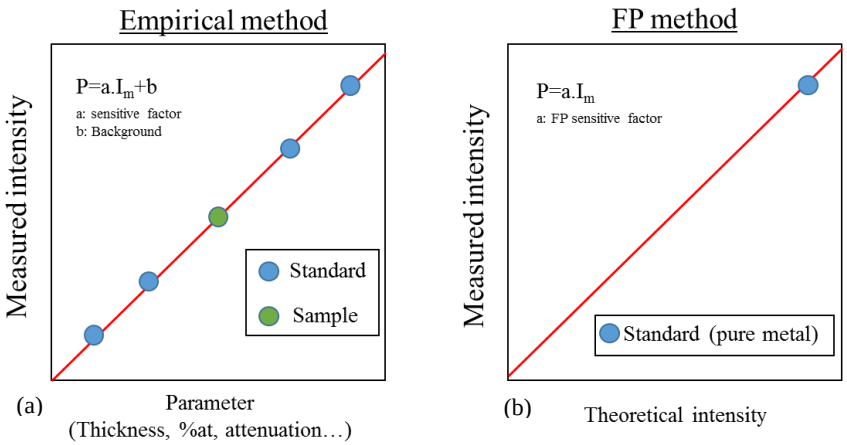

Figure 2.9. Empirical method and FP method sensitive curves.

Hence, in this section, we will limit ourselves to the fundamental parameters approach which is employed for our chemical quantifications. FP method is based on the mathematical foundations formalized by Sherman [4, 5], Shiraiwa and Fujino [6]. As illustrated in Fig. 2.10, an incident X-ray beam ($I_{primary}$) penetrating into a homogenous material at ψ' angle is absorbed according to the Beer Lambert law:

$$I_{excited} = I_{primary}.\exp(-\frac{x}{sin\psi'}\mu_{S,E}) \quad \text{(eq. 2.9)}$$

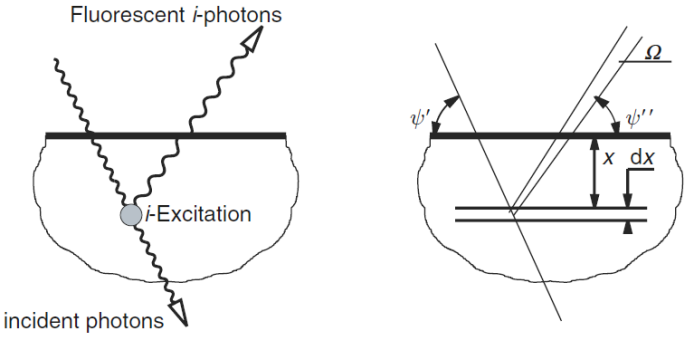

Figure 2.10. X-Ray interacting with flat homogenous material.

Hence, the emitted photons of an infinitesimal layer of the homogenous material is:

$$dI_{emitted} = -I_{primary}.\left(\frac{\mu_{S,E}}{sin\psi'}\right).\exp\left(-\frac{x}{sin\psi'}\mu_{S,E}\right)\frac{S_i-1}{S_i}C_i.\bar{\tau}_{i,E}.p_i.\omega_i.dx \quad \text{(eq. 2.10)}$$

Then, the observed photons by the detector from dx, excluding the detector efficiency is:

$$dI_{observed} = dI_{emitted}.\exp\left(-\frac{x}{sin\psi''}\bar{\mu}_{S,i}\right).\frac{\Omega}{4\pi} \quad \text{(eq. 2.11)}$$

$$dI_{observed} = -I_{primary}.\left(\frac{\mu_{S,E}}{sin\psi'}\right).G_iC_i\frac{\rho}{\rho_i}\bar{\tau}_{i,E}\exp\left(-x.\left(\frac{\bar{\mu}_{S,E}}{sin\psi'}+\frac{\bar{\mu}_{S,i}}{sin\psi''}\right)\right).\frac{\Omega}{4\pi}.dx \quad \text{(eq. 2.12)}$$

Where $\bar{\mu}_{S,E}$ is the attenuation of the primary photons in the specimen S, and $\bar{\mu}_{S,i}$ is the attenuation of the fluorescent photons from element i. They can be combined to facilitate the comprehension of the equations, as:

$$\bar{\mu}^* = \frac{\bar{\mu}_{S,E}}{sin\psi'}+\frac{\bar{\mu}_{S,i}}{sin\psi''} \quad \text{(eq. 2.13)}$$

and Gi is:

$$G_i = \frac{S_i - 1}{S_i} . p_i . \omega_i = j_i . p_i . \omega_i$$

$j_i = \frac{S_i - 1}{S_i}$ is the jump ratio of element i, $\tau_{i,E}$ is the absorption coefficient of element i from X-ray primary beam (E), p_i is the probability of transition, ω_i is the fluorescence yield, C_i is the concentration of elements i in the material, ρ is the density of the material, ρ_i is the density of element i and $\frac{\Omega}{4\pi}$ is the solid angle.

Hence:

$$dI_{observed} = -I_{primary} . \left(G_i . \bar{\tau}_{i,E} . C_i . \frac{\rho}{\rho_i} \right) . \exp(-x . \bar{\mu}^*) . \frac{\Omega}{4\pi} . dx \quad \text{(eq. 2.14)}$$

Then, integrating eq. 2.14 over all the layer T:

$$I_{observed} = \int_{x=0}^{x=T} dI_{observed} = I_{primary} . \left(G_i . \bar{\tau}_{i,E} . C_i . \frac{\rho}{\rho_i} \right) \frac{1 - \exp(-\bar{\mu}^* . T)}{\bar{\mu}^*}$$

$$= I_{primary} . \left(G_i . \tau_{i,E} . C_i \right) . \frac{1 - \exp(-\mu^* . \rho . T)}{\mu^*} . \left(\frac{\Omega}{4\pi} \right) \quad \text{(eq. 2.15)}$$

If the material studied is a bulk (T→ inf.), hence:

$$I_{observed} = \frac{I_{primary} . G_i . \tau_{i,E} . C_i . \left(\frac{\Omega}{4\pi} \right)}{\mu^*} \quad \text{(eq. 2.16)}$$

While, if it is very thin layer, $(1-\exp(-\mu^* . \rho . T) \approx \mu^* . \rho . T$:

$$I_{observed} = I_{primary} . G_i . \tau_{i,E} . C_i . \rho . T . \left(\frac{\Omega}{4\pi} \right) \quad \text{(eq. 2.17)}$$

The mathematical model described above counts for fluorescence radiation emitted by the primary beam. Nonetheless, primary photons can also cause a series of excitation processes into the material, such as secondary and tertiary fluorescence.

Secondary fluorescence occurs when primary fluorescence photons have sufficient energy to excite fluorescent radiation of other atoms in the material. The secondary fluorescence photons can excite tertiary fluorescent photons, as illustrated in Fig. 2.11. The 4th, 5th,… fluorescence radiation are also possible but have no practical importance.

In the case of transition elements, secondary fluorescence is quite strong for elements differing by 2 in atomic numbers. Stainless steel (Cr– Fe–Ni) is a common example for demonstrating it (Fe → Cr, Ni → Cr, and Ni → Fe) as well as tertiary excitation (Ni → Fe → Cr). The contributions can account up to 30% from secondary fluorescence and up to 2.5% from tertiary fluorescence, relative to the primary fluorescence photons.

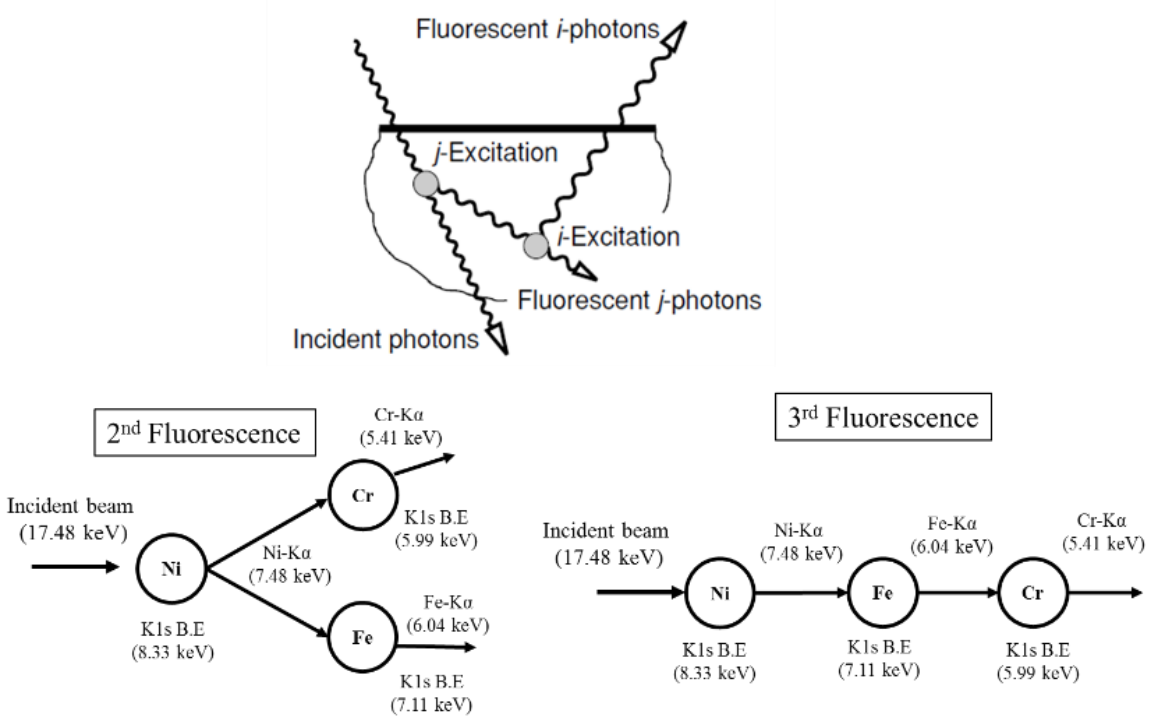

Figure 2.11. Matrix effects, secondary and tertiary fluorescence process.

In the range of light elements or L-series of some metals, a factor called cascade effect seems to be of considerable importance, when direct excitation is inefficient (which is usually the case of X-ray tubes). Figure 2.12 depicts this effect for the case of Lα emission: when an atom is ionized in the K shell by an incoming photon, it can be de-excited by emitting a Kα1 photon, by which an L3 shell hole is created. Then an X-ray photon belonging to the L3 series, such as Lα or Lβ2, can be emitted. As a matter of fact, fluorescence emission of the K shell other than Kα1 emission and non-radiative or Auger-transition processes are possible and probable [7]. This cascade effect has been studied and already implemented in some commercial software.

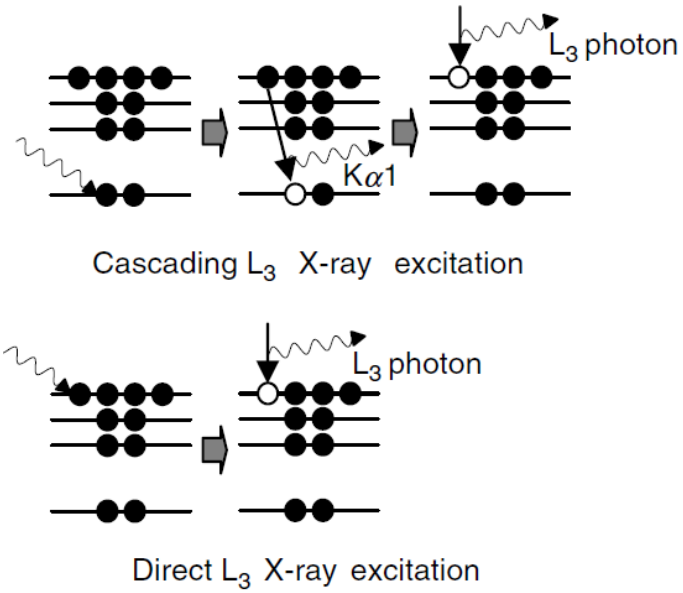

Figure 2.12. Cascade effects process triggering indirect excitation [7].

- Use of standards for FP quantification

In almost all practical applications, standards are used rather than absolute counts. Such ratios are built with the count rates from the same element in another specimen, which can be a standard of any composition, or a pure element. The main advantage is that thereby a number of unknown or less accurately known factors cancel, as well as any scaling constant in the absolute photon flux of the primary radiation (which is rarely ever known in practice), and the detection efficiency. Hence, the count-rate ratio (R_i) is given by:

$$R_i = \frac{I_{emitted}}{I_{100}} \quad \text{(eq. 2.18)}$$

Where I_{100} is the pure element (C_i=1), hence, R_i for primary excitation:

$$R_i = \frac{I_{emitted}}{I_{100}} = \frac{I_{primary}.G_i.\tau_{i,E}.C_i.\frac{1-\exp(-\mu^*.\rho.T)}{\mu^*}.\left(\frac{\Omega}{4\pi}\right)}{\frac{I_{primary}.G_i.\tau_{i,E}.C_i.\left(\frac{\Omega}{4\pi}\right)}{\mu^*}} = C_i.(1-\exp(-\mu^*.\rho.T) \quad \text{(eq. 2.19)}$$

Then, for a thin layer:

$$R_i = \frac{I_{emitted}}{I_{100}} \cong C_i.\mu^*.\rho.T \quad \text{(eq. 2.20)}$$

Therefore, after calculating R_i from equation 2.20, we can determine the concentrations of elements presented in the film as well as the product ρ.T which is the mass per unit area, hence if the film density is known we can determine its thickness and vice-versa. The quantitative analysis has to be adjusted by sensitive calibration curve which is a relation between the measured intensity $I_{measured}$ of reference sample (e.g. pure metal) and the theoretical intensity ($I_{theoretical}$) as illustrated in Fig. 2.13. The sensitive factor corrects linearly $I_{theoretical}$ upon the instrumental parameters (X-ray tube, slits, detectors, etc.). Once the sensitive curves correctly calibrated, quantitative analysis can be performed in the whole range of the alloy.

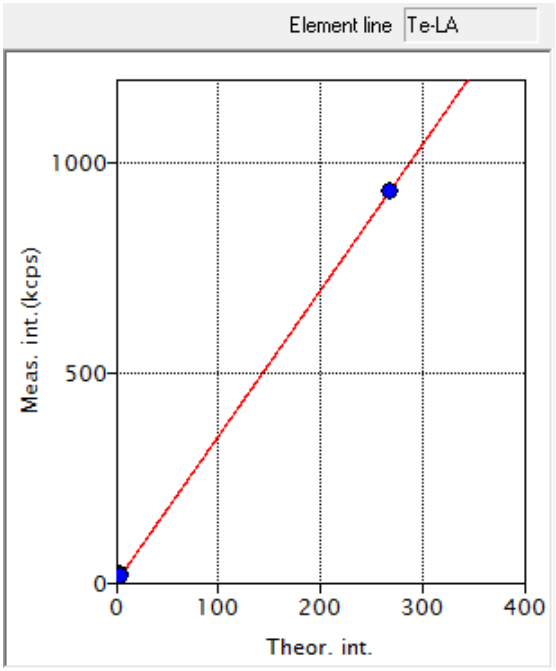

Figure 2.13. Sensitive curve calculated from FP method from RIGAKU XRF software.

2.4. Grazing Incident X-ray Fluorescence (GIXRF)

When an incoming X-ray beam interacts with a sample at grazing angles, the fluorescence radiation emitted from this sample is amplified. As illustrated in Fig. 2.14, the interaction between the incident and reflected X-ray beam generates an X-ray Standing Wave (XSW) field dependent not only to the incident beam angle but also to the atoms depth positions. The result is the capability to determine the distribution of chemical elements along the depth non-destructively, as we can see in Fig.2.14.b [8].

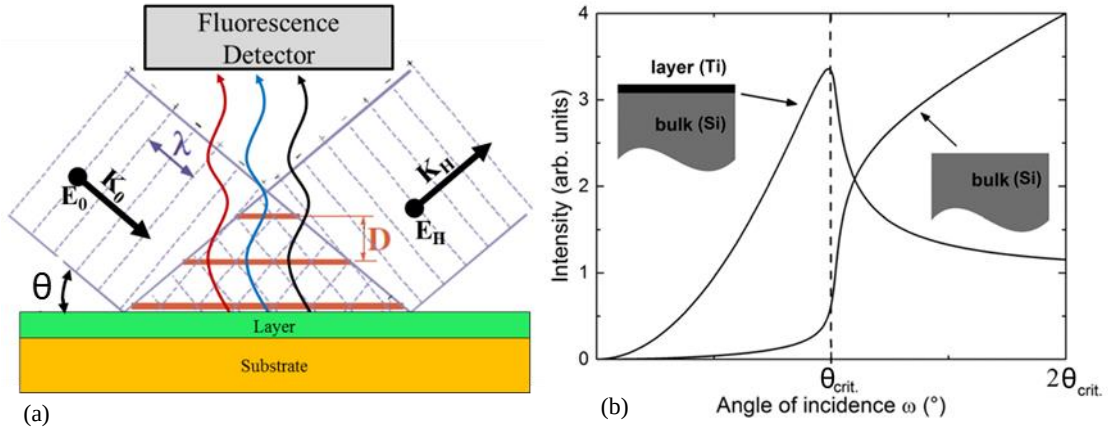

Figure 2.14. Characteristics form of the angular dependence of the fluorescence of thin layer and bulk substrate [8].

- X-Ray Standing Wave fields (XSW)

XSW fields are generated when an incident and reflected wave planes (with respective wave vectors k_0 and k_r) interfere creating planes of maximum intensity parallel to the surface and with a period given by:

$$D = \frac{\lambda}{2\sin\theta} = \frac{2\pi}{Q} \qquad \text{(eq. 2.21)}$$

Where λ is the X-ray wavelength, 2θ is the scattering angle between the two coherently coupled wave vectors K_R and K_0, and Q is the scattering vector defined as:

$$Q = k_R - k_0 \qquad \text{(eq. 2.22)}$$

The incident and reflected wave-vectors (k_R and k_0) follow the Maxwell's equations of an electromagnetic plane-wave traveling through a medium with refractive index n_1. When it impinges a stratified medium with different refractive index n_2, it splits into a reflected, transmitted and/or refracted plane-wave, as illustrated in Fig. 2.15.

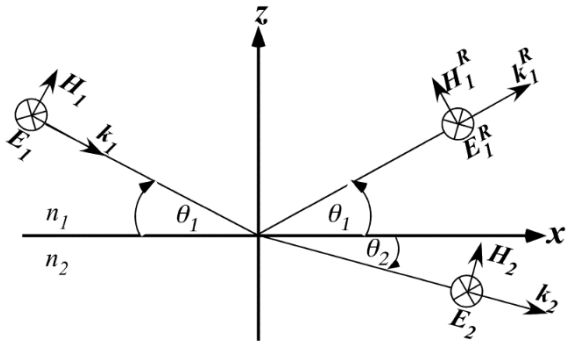

Figure 2.15. Scheme of reflection and refraction for stratified homogenous media.

The refraction index (n) in the X-ray range are given by:

$$n_j = 1 - \delta_j - i\beta_j \quad \text{(eq. 2.23)}$$

The parameters δ_j and β_j, which account, respectively, for refraction and absorption effects by the j^{th} medium [9], can be expressed as:

$$\delta = \frac{r_e \lambda^2}{2\pi} N_e' \quad \text{(eq. 2.24)}$$

$$\beta = \frac{\lambda \mu_0}{4\pi} \quad \text{(eq. 2.25)}$$

Where r_e is the electron radius ($2.818.10^{-15}$ m), N_e' is the real part of the effective electron density, and μ_0 is the linear attenuation coefficient of the medium.

The electric fields (E-fields) associated with the incident, reflected, and transmitted plane-waves are expressed respectively as:

$$\bar{E}_1(r,t) = E_1 \exp(-i(k_1 \cdot r - \omega t)) \quad \text{(eq. 2.26)}$$

$$\bar{E}_1^R(r,t) = E_1^R \exp(-i(k_1^R \cdot r - \omega t)) \quad \text{(eq. 2.27)}$$

$$\bar{E}_2(r,t) = E_2 \exp(-i(k_2 \cdot r - \omega t)) \quad \text{(eq. 2.28)}$$

At $z = 0$, the space and time variations of all three fields must be equivalent. This produces the "law of co-planarity," which requires the transmitted and reflected wave-vectors, $\boldsymbol{k}_2$ and $\boldsymbol{k}^{\boldsymbol{R}}_1$, to be confined to the same plane as the incident wave-vector, $\boldsymbol{k}_1$ (the *xz* -plane in Fig.2.15). The continuity of the tangential components of the three wave-vectors at the boundary dictates the kinematical properties corresponding to the "law of reflection" $\theta^R_1 = \theta_1$, and the "law of refraction" (Snell's Law) $n_2\cos\theta_2 = n_1 \cos\theta_1$. Using these relationships the spatial components in Eq. (2.26-28) can be expressed as:

$$k_1 \cdot r = k_1(x\cos\theta_1 - z\sin\theta_1) \quad \text{(eq. 2.39)}$$

$$k_1^R \cdot r = k_1(x\cos\theta_1 + z\sin\theta_1) \quad \text{(eq. 2.30)}$$

$$k_2 \cdot r = \frac{n_2}{n_1} k_1 \left[x\frac{n_1}{n_2}\cos\theta_1 - z\sqrt{1 - \left(\frac{n_1}{n_2}\cos\theta_1\right)^2} \right] \quad \text{(eq. 2.31)}$$

The continuity of the tangential components of the E-fields and magnetic-fields at the z = 0 boundary dictates the dynamical properties of the fields, corresponding to the Fresnel equations, which for the σ-polarization case and for small angles θ_1 can be expressed as:

$$F_{1,2}^{R} = \frac{E_1^R}{E_1} = \left|\frac{E_1^R}{E_1}\right| e^{iv} = \frac{q-\sqrt{q^2-1-ib}}{q+\sqrt{q^2-1-ib}} \quad \text{(eq.2. 32)}$$

$$F_{1,2}^{T} = \frac{E_2}{E_1} = \frac{2q}{q+\sqrt{q^2-1-ib}} \text{ (eq.2. 33)}$$

Where q is the normalized angle $q=\theta/\theta_c$, b is the ratio β/δ for the case $n_1 = 1$ (air or vacuum) and $n_2=1-\delta-i\beta$, ν is the phase of the reflected plane-wave.

Total reflection (TR) occurs when the transmitted plane-wave $\bar{E}_2(r,t)$ propagates strictly in the x-direction and is attenuated in the inward negative z-direction. From eqs. (2.28 and 2.31), TR occurs when $\theta_1 < \theta_C$. For $n_1 = 1$ (e.g., vacuum or air) and $n_2 = 1-\delta-i\beta$, the critical angle is:

$$\theta_c = \sqrt{2\delta} \quad \text{(eq. 2.34)}$$

Hence, from eqs. 2.21, 2.24 and 2.34, the critical scattering vector is given by:

$$Q_c = \frac{4\pi \sin\theta_c}{\lambda} \cong \frac{4\pi\theta_c}{\lambda} 4\sqrt{\pi r_e N_e'} \quad \text{(eq. 2.35)}$$

Figure 2.16 shows the q dependence of the reflectivity, $R = \left|F_{1,2}^{R}\right|^2$, the normalized E-field intensity at the surface, $I_{z=0} = \left|F_{1,2}^{T}\right|^2$, the phase of the reflected plane-wave relative to the phase of the incident one at z = 0, $v = arg\left(F_{1,2}^{R}\right)$, and the penetration depth is:

$$\Lambda = \frac{1}{\mu_e} = \left[Q_c R_e\left[\sqrt{1-q^2+ib}\right]\right]^{-1} \quad \text{(eq.2.36)}$$

Where μ_e is the effective linear attenuation coefficient.

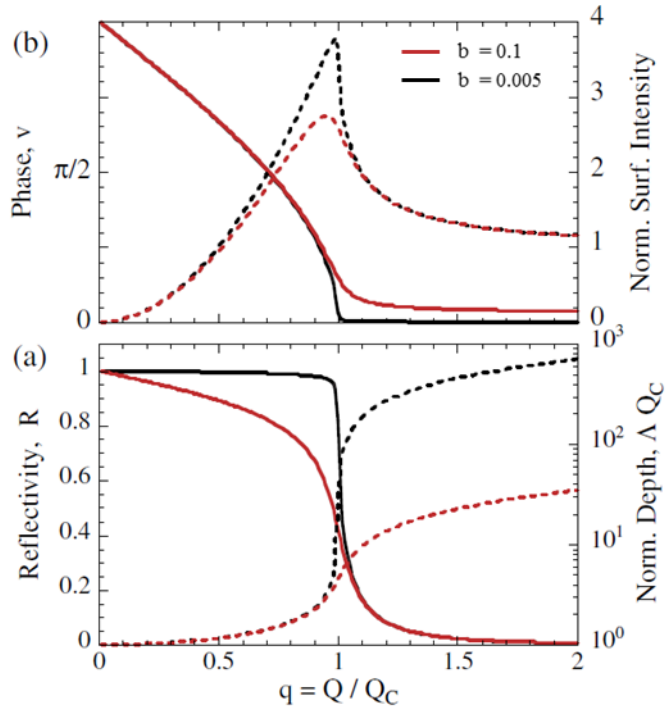

Figure 2.16. (a) Reflectivity and normalized (solid lines) penetration depth (dashed lines), (b) phase (solid lines) and normalized E-field intensity (dashed lines) [10].

As we can see, TR occurs for q < 1, where the reflectivity approaches unity, the phase shifts by π radians, and E-field intensity below the surface forms an evanescent wave [11] with a penetration depth approaching Q_c^{-1}.

The total E-field in the vacuum (or air) above the reflecting layer, where the incident and reflected plane waves are coherently coupled by $Q = k^R{}_1 - k_1$, is expressed as $\bar{E}_T = \bar{E}_1 + \bar{E}_1^R$, and below the mirror surface, $\bar{E}_T = \bar{E}_2$. The E-field intensity, $I = |\bar{E}_T|^2$ can then be expressed as:

$$I(\theta, z) = I_0 \begin{cases} 1 + R + 2\sqrt{R}\cos(v - Qz), & for\ z \geq 0 \\ \left|F_{1,2}^T\right|^2 \exp(-\mu_e|z|), & for\ z \leq 0 \end{cases} \qquad \text{(eq. 2.37)}$$

Where, $I_0 = |E_1|^2$ is the intensity of the incident plane wave.

As we can see in Fig. 2.17.a, the E-field intensity under the TR condition exhibits a standing wave above the mirror surface with a period D = 2π/Q and an evanescent wave below the surface. The height coordinate in Fig. 2.17.a is normalized to the critical period $D_c = 2\pi/Q_c$.

Figure 2.17.a, at q = 0, there is a node in the E-field intensity at the mirror surface and the first antinode is at infinity. As q increases, that first antinode moves inward and reaches the mirror surface at q = 1. This inward movement of the first antinode, which is analogous to the Bragg diffraction case, is due to the π phase-shift depicted in Fig. 2.17.a. The other XSW antinodes follow the first antinode with a decreasing period of D = 2π/Q. For q increasing above unity, the XSW phase is fixed, the period D continues to contract, and the XSW amplitude drops off dramatically.

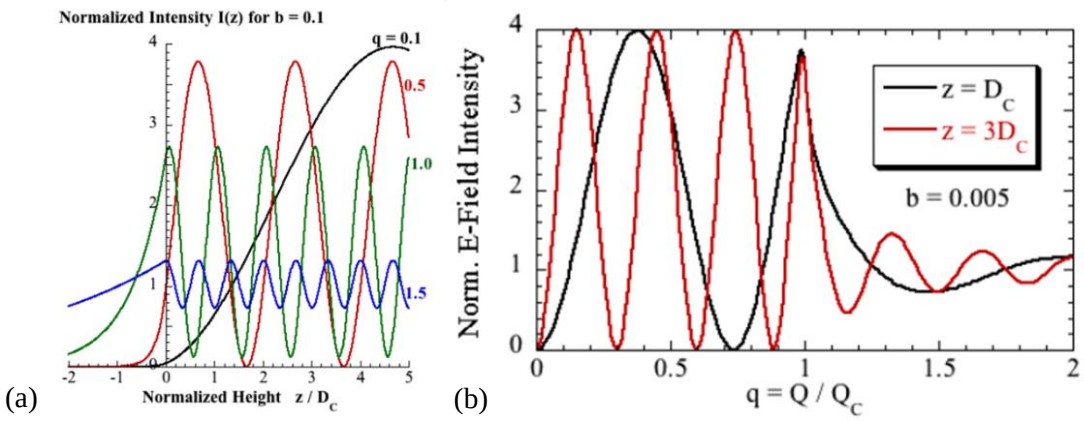

Figure 2.17(a) Normalized-height dependence of the normalized E-field intensity for different normalized incident q. (b) The normalized-angle dependence of the normalized E-field intensity for two different heights above the mirror surface [10].

Figure 2.17.b shows the normalized E-field calculated at two heights above the surface. These two curves illustrate the basis for the TR-XSW technique as a positional probe, since (in the dipole approximation for the photo-effect) the XRF intensity, $I(\theta, z)$, from an atomic layer at a discrete height z will follow such a curve. Note that in the TR range, $0 < q < 1$, the number of modulations in the E-field intensity is equivalent to $z/D_c+(1/2)$. The extra 1/2 modulation is due to the π phase shift shown in Fig. 2.17.b. Therefore, for an XRF-marker atom layer within a low-density film on a high-density mirror, the atomic layer height can be quickly approximated by counting the number of modulations in the XRF intensity that occur between the film critical angle and the mirror critical angle.

Therefore, to determine the elementary distribution profile $\rho(z)$, we must implement the XSW(θ,

z) factor into the XRF quantitative analysis model (i.e. $I(\theta) = \int \rho(z) XSW(\theta, z) dz$). This approach was developed by De Boer in 1990 [12] based on the refracting (and absorbing) X-rays model of Parratt's recursion formalism for layered materials [13]. Both formalisms are briefly described below.

- Parratt's recursive formalism for reflectivity

The Parratt recursive formalism [13] was developed in 1954 and since then is widely employed for X-Ray Reflectivity analysis of layered materials. The model considers a stratified medium with *M* homogeneous layers (Fig.2.18). The semi-infinitely thick *j* = 1 top layer will be vacuum (or air) with *n* = 1, and the *j* = *M* bottom layer will be the semi-infinitely thick substrate.

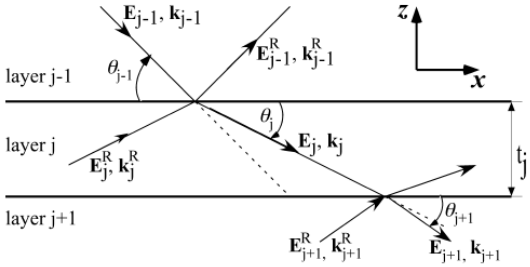

Figure 2.18. Reflection and refraction of the plane-waves at two successive boundaries in a multilayer. The boundaries are parallel and separate layers j-1, j and j+1 with indices of refraction nj-1>nj+1>nj

For the *σ*-polarization case, the continuity of tangential components of the E-field and the H-field vectors at the *j*, *j* + 1 boundary leads to the following pair of equations for the E-fields at depth *zj* and *zj*+1 below the top interface of layer *j* and *j* + 1, respectively:

$$a_j E_j(z_j) + a_j^{-1} E_j^R(z_j) = b_{j+1}^{-1} E_{j+1}(z_{j+1}) + b_{j+1} E_{j+1}^R(z_{j+1}) \quad \text{(eq.2.38)}$$

$$\left(a_j E_j(z_j) - a_j^{-1} E_j^R(z_j)\right) n_j \theta_j = \left(b_{j+1}^{-1} E_{j+1}(z_{j+1}) - b_j E_{j+1}^R(z_j + 1)\right) n_{j+1} \theta_{j+1} \quad \text{(eq.2.39)}$$

where the E-fields within the j^{th} layer at a depth *zj* below the $j-1, j$ *i*nterface are expressed as:

$$E_j(z_j) = E_j(0)\exp(-ik_j \sin\theta_j z_j) = E_j(0) exp\left(-i\frac{1}{2} Q_j z_j\right) \quad \text{(eq.2.40)}$$

$$E_j^R(z_j) = E_j^R(0)\exp(ik_j \sin\theta_j z_j) = E_j^R(0) exp\left(i\frac{1}{2} Q_j z_j\right) \quad \text{(eq.2.41)}$$

The amplitude factors (or retardation factors),

$$a_j = \exp\left(-i\frac{1}{2} Q_j z_j\right) \text{ and } b_{j+1} = exp\left(-i\frac{1}{2} Q_{j+1} z_{j+1}\right) \quad \text{(eq.2.42)}$$

account for the phase retardation effects incurred by the waves traveling to and from the *j*, *j*+1 boundary from depths *zj* and *zj*+1 within the respective layers. Using the small-angle approximation, $sin\theta_j = \theta_j$, we define

$$Q_j = Q_j' - iQ_j'' = \frac{4\pi}{\lambda_1}\sqrt{\theta_1^2 - 2(\delta_j + i\beta_j)} \quad \text{(eq.2.43)}$$

as the complex scattering vector inside the j^{th} layer. In the top vacuum (air) layer; $Q_1 = 4\pi\theta_1/\lambda_1 = 4\pi\theta/\lambda = Q$. The solution to the two simultaneous equations in eq.2.39 leads to the recursion formula:

$$A_{j,j+1} = a_j^2 b_j^2 \left[\frac{A_{j+1,j+2} + F_{j,j+1}^R}{A_{j+1,j+2} + F_{j,j+1}^R + 1}\right] \quad \text{(eq.2.44)}$$

Where,

$$A_{j,j+1} = b_j^2 \frac{E_j^R(0)}{E_j(0)} = \frac{\left|E_j^R(0)\right| e^{i\varphi_j^R}}{|E_j(0)| e^{i\varphi_j}} = \frac{\left|E_j^R(0)\right|}{|E_j(0)|} e^{iv_j} \quad \text{(eq.2.45)}$$

The Fresnel coefficients for reflectivity and transmission at the *j*, *j* + 1 interface are defined respectively as:

$$F_{j,j+1}^R = \frac{Q_j - Q_{j+1}}{Q_j + Q_{j+1}} \quad \text{and} \quad F_{j,j+1}^T = \frac{2Q_j}{Q_j + Q_j + 1} \text{ (eq.2.46)}$$

The recursion formulation eq.2.46 is solved by starting at the semi-infinitely thick *j* = *M* bottom layer, where $E^R_M = 0$ and hence $A_{M,M+1} = 0$. At the next interface from the bottom: $A_{M-1,M} = a^2_{M-1} b^2_{M-1} F^R_{M-1,M}$. The recursion is applied a total of $M-1$ times; until we get to the top interface, where

$$\frac{E_1^R(0)}{E_1(0)} = A_{1,2} \quad \text{(eq.2.47)}$$

is the E-field amplitude ratio at the top interface. This is used to calculate the reflectivity:

$$R = \left|\frac{E_1^R(0)}{E_1(0)}\right|^2 \quad \text{(eq. 2.48)}$$

For j=1, eq. 2.48 becomes $= \left|F_{1,2}^R\right|^2$, which is the reflectivity for a substrate as illustrated in Fig.2.16. Hence the algebra is straightforward, but very tedious when j>3, so dedicated algorithms are often employed for the calculations.

- GIXRF recursive formalism (De Boer model)

In the case of a single layer with a flat surface deposited on a flat substrate, it is known [14] that the time-averaged flux (*i.e.* the energy flowing through a unit surface area per unit time) is given by the Poynting vector, P_j. Therefore, we have:

$$P_j = \frac{1}{2} Re\left(E_j \times H_j^*\right) = \frac{1}{2} Re\left(E_j^* \times H_j\right) \quad \text{(eq.2.49)}$$

$$P_j = \frac{|E_j|^2}{2Z_0} Q_j' \quad \text{(eq.2.50)}$$

where $Z_0 = (\mu_0/\varepsilon_0)1/2$ is the impedance of vacuum. The position dependence of $\boldsymbol{P}_j$ is found by substituting the plane-wave in eq. 2.50:

$$P_j = \frac{\left|E_j^T\right|^2}{2Z_0} Q_j' exp\left(-\frac{4\pi Q_{jz}'' z}{\lambda}\right) \quad \text{(eq.2.51)}$$

Where E_j^T is the electric field at the top of the layer *j* and *z* is the depth position inside the material (with z = 0 representing the surface of the sample).

The absorption of the radiation must be taken into account. According to Poynting theorem, the amount of electromagnetic energy absorbed per unit of time within a volume bounded by a surface S can be written:

$$A = -\iint_s P_j \cdot u \, ds \quad \text{(eq. 2.52)}$$

where *ds* is an area element of *S*. From that, we can directly deduce that the amount of energy absorbed

by a slice of material at depth *z* with infinitesimal thickness *dz* is:

$$dA = -S_1 \frac{\partial P_{jz}}{\partial z} dz \quad \text{(eq. 2.53)}$$

where S_1 is both the bottom and the top surface area.

The factor $-\frac{\partial P_{jz}}{\partial z}$ from eq.2.53 can be approximatively considered as:

$$-\frac{\partial P_{jz}}{\partial z} \approx \frac{\left|E_j^T\right|^2}{2Z_0} \mu_{j\lambda} exp\left(-\frac{\mu_{j\lambda}.z}{\sin\psi_j}\right) \quad \text{(eq. 2.54)}$$

Where $\mu_{j\lambda}$ is the linear attenuation coefficient of j layer at λ and $\sin\psi_j$ is the incident angle to j layer.

Therefore, the X-ray fluorescence intensity (I_{aj}) (the number of photons emitted per unit of time by atoms of a particular element *a* in the layer *j*) of a multi-structure is given by:

$$I_{aj} = \frac{\lambda}{hc} C_{aj} \frac{\tau_{a\lambda}}{\mu_{j\lambda}/\rho_j} J_{a\lambda} \omega_a g_a exp\left(-\sum_{n=1}^{j-1} \frac{\mu_{na} d_n}{\sin\psi_d}\right) S_1 \times \int_0^{d_j} dz \left(-\frac{\partial P_{jz}}{\partial z}\right) exp\left(-\frac{\mu_{ja} z}{\sin\psi_d}\right) \quad \text{(eq.2.55)}$$

where C_{aj} is the mass fraction of element *a* in layer *j*, ρ_j the material density *j*, $\tau_{a\lambda}$ is photo-absorption coefficient for element *a* at wavelength λ, $J_{a\lambda}$ is the absorption jump factor at wavelength λ for the creation of holes in the considered shell of element *a*, ω_a is the fluorescence yield in the considered shell of *a*, g_a is the relative emission rate for the considered XRF line in preference to other lines originating from the same hole in *a*, and μ_{na} the linear attenuation coefficient of the considered fluorescence radiation from element *a* in layer *n*, ψ_d is the detection angle and *S1* is the irradiated detected sample area.

Equation 2.55 works only to a single layer, if we consider a multilayer system the absorption of the incident radiation $\partial P_{jz}/\partial z$ can be reformulated by taking in account the total energy flow and absorption within each layer of a multiple thin-film sample. Therefore, a formula for the derivative of the Poynting vector becomes:

$$-\frac{\partial P_{jz}}{\partial z} = \frac{|E_j|^2}{2Z_0} \mu_{j\lambda} Re\left(\sum_{m=1}^{3} A_{jm} \exp(-b_{jm} z)\right) \text{ (eq. 2.56)}$$

Where,

$$A_{j1} = \frac{2\pi\epsilon_j''}{\lambda\mu_{j\lambda}} \frac{\left|E_j^T\right|^2}{|E_0|^2}, A_{j3} = \frac{2\pi\epsilon_j''}{\lambda\mu_{j\lambda}} \frac{\left|E_j^r\right|^2}{|E_0|^2}, A_{j1} = \frac{2\pi\epsilon_j''}{\lambda\mu_{j\lambda}} \frac{2E_j^T * E_j^r}{|E_0|^2}, \quad \text{(eq. 2.57)}$$

$$b_{j1} = \frac{4\pi Q_{jz}''}{\lambda}, b_{j2} = -b_{j1}, b_{j3} = -\frac{4\pi i Q_{jz}'}{\lambda}, \quad \text{(eq. 2.58)}$$

Replacing $\partial P_{jz}/\partial z$ from eq. 2.56 by the reformulated $\partial P_{jz}/\partial z$, the XRF can be determined as:

$$I_{aj} = I_0 C_{aj} \rho_j \tau_{a\lambda} J_{a\lambda} \omega_a g_a S_1 \exp\left(-\sum_{n=1}^{j-1} \frac{\mu_{na} d_n}{\sin\psi_d}\right) \times Re\left\{\sum_{m=1}^{3} A_{jm} \int_0^{dj} dz \exp\left(-\left(b_{jm} + \frac{\mu_{ja}}{\sin\psi_d}\right) z\right)\right\}$$

(eq. 2.60)

Where $I_0 = |E_0|^2 \lambda/(2Z_0 hc)$ is the number of incident photons per unit surface area per unit time. Integration yields:

$$I_{aj} = I_0 C_{aj} \rho_j \tau_{a\lambda} J_{a\lambda} \omega_a g_a S_1 exp\left(-\sum_{n=1}^{j-1} \frac{\mu_{na} d_n}{\sin\psi_d}\right) \times Re\left\{\sum_{m=1}^{3} A_{jm} \frac{1 - exp\left(-(b_{jm} + \mu_{ja}/\sin\psi_d)\right)}{b_{jm} + \mu_{ja}/\sin\psi_d}\right\} \quad \text{(eq.2.61)}$$

For a very thin layer, $1 - exp\left(-(b_{jm} + \mu_{ja}/\sin\psi_d\right) \approx b_{jm} + \mu_{ja}/\sin\psi_d$, and eq. 2.61 becomes:

$$I_{aj} = I_0 C_{aj} \rho_j \tau_{a\lambda} J_{a\lambda} \omega_a g_a S_1 exp\left(-\sum_{n=1}^{j-1} \frac{\mu_{na} d_n}{\sin \psi_d}\right) \times \frac{2\pi \epsilon_j''}{\lambda \mu_{j\lambda}} . \frac{\left|E_j^T + E_j^R\right|^2}{|E_0|^2} \quad \text{(eq.2.62)}$$

From eq.2.62 we can easily see that the emitted intensity from j layer is directly dependent on $|E^T_j + E^R_j|^2/|E_0|^2$, which is the XSW field generated. Hence, it is also possible to deduce that I_{aj} is dependent on the spatial distribution of the incident beam intensity and the instrumental set-up. Indeed, the XRF intensity needs to be corrected by a geometrical function G(θ). The formulation of this function is detailed by Li et al. [15] and summarized in equation 2.63.

$$I(\theta) = I_{aj}(\theta) G(\theta) = I_{aj}(\theta) \frac{\Delta\Omega}{4\pi} I_0 \varepsilon_{det} T_{air} S(\theta) \quad \text{(eq.2.63)}$$

where ΔΩ is the detection solid angle, ε_{det} is detector efficiency and T_{air} is the transmission in air. Therefore, only S(θ) (the detected irradiated area) strongly affects the GIXRF curve. As illustrated in Fig.2.19, S(θ) = $W_\perp \times W_\parallel$, where $W_\perp$ is the width perpendicular to the plane (constant because the incident beam is assumed large and homogenous along this direction) and $W_\parallel$ is the width parallel to the plane which is angular dependent. Therefore, G(θ) becomes only dependent on $W_\parallel$ which is a relation between the detected length (L_d) and the illuminated length (L_i). L_d depends on the collimator geometry and distance to the sample, while L_i is influenced by the footprint of the incident beam (width, shape and divergence). Thus $W_\parallel$ is a rectangular function $\prod$ of L_d weighted by the beam intensity distribution as a Gaussian profile g(θ, t) over sample surface is given.

$$G(\theta) = I_0 \frac{\Delta\Omega}{4\pi} \varepsilon_{det} T_{air} \times W_\perp \times \int_{-L_s/2}^{+L_s/2} g(\theta, t) \Pi_{ld}(t) dt \quad \text{(eq.2.64)}$$

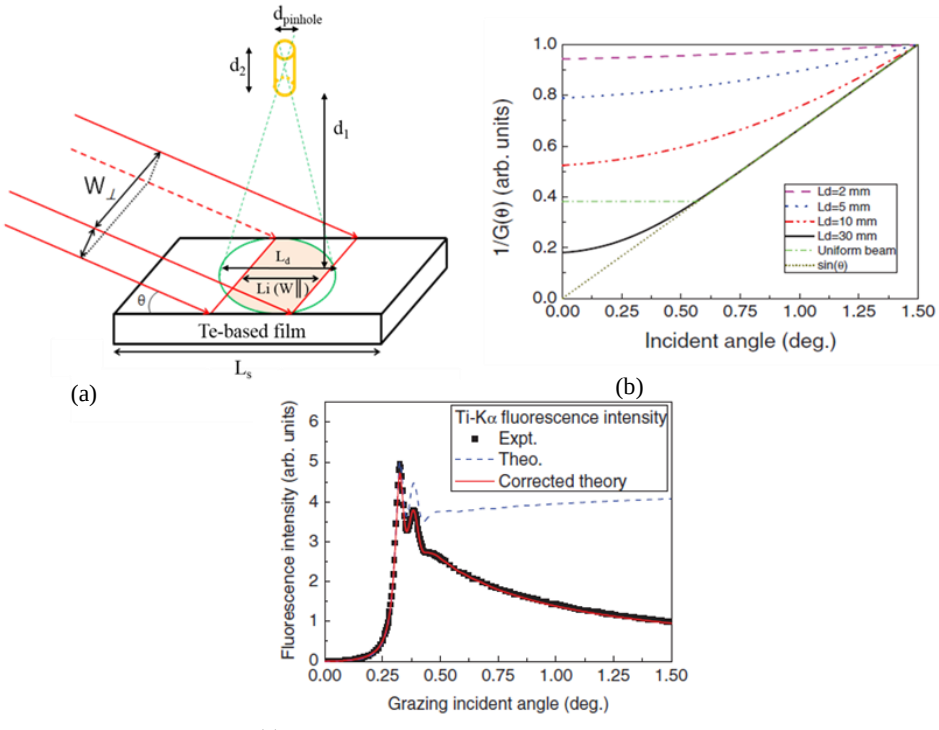

Figure 2.19. (a) 3-D schematic of the geometrical parameters in GIXRF experiments. (b) Reciprocal of G(θ) calculated for different widths Ld, with Ls 30 mm and b0 15 mm. (c) Influence of G(θ) in a Ti-Kα XRf intensity for a Si/Ti/Ni/Ti/Si(Sub) multilayer sample.

- GIXRF/XRR combined analys

GIXRF can be combined with XRR in the same instrument, providing a very powerful method to probe thin layered materials due to the correlation between the atomic density (GIXRF) and electronic

density (XRR). This combined analysis is very attractive for semiconductor industry not only because it is a non-destructive technique but also because the probed depth (few nm to few hundred nm) with high depth resolution (1 nm) is unique among others non-destructive techniques (ex. ARXPS). As we can see in Fig.2.20, a typical analysis by GIXRF/XRR provides unambiguous measurement of chemical depth profiles as well as density, thickness and roughness of the layered material.

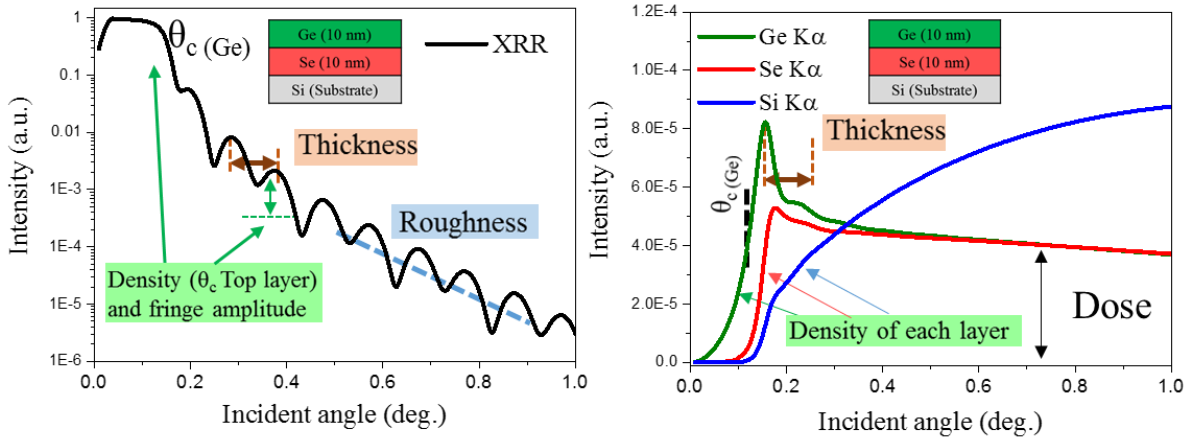

Figure 2.20. Probing wafers by XRR-GIXRF combined analysis, example of a multilayer Ge/Se/Si(Sub) stack.

The data processing of GIXRF/XRR measurements can be performed by dedicated software which treats the data of both techniques simultaneously based on the Parratt's and De Boer's formalisms. A typical flowchart employed in such software is depicted in Fig.2.21, initially the experimental data (GIXRF and XRR) and the fixed parameters (Beam energy, divergence, detector dimensions, etc.) are inserted as input. Then an initial layered model (Thickness, density, stoichiometry and roughness) is processed through the optimizing procedure until the generation of the best layered model agreed with the experimental data.

At present, no commercial software is available to process GIXRF data. A collaboration between CEA-LETI and Atominstitut Vienna University of Technology (ATI) was then stablished to fulfill the high demand to GIXRF measurements. Two softwares were therefore developed: MEDEpy [17, 18] which stands for Material Elemental Depth profiling using Python developed by CEA-LETI, and jGIXA [19] which means Grazing Incidence X-ray Analysis using Java developed by the ATI. Both software are dedicated to GIXRF and/or XRR analysis; it means that the process to extract the angle-dependent fluorescence was performed by an external software, in our case PyMca. Several publications concerning the main features of each software are already available [17-19].

Therefore, the processed data in this work were performed with both software in order to demonstrate their maturity. As GIXRF data processing takes several steps, only the treated results are discussed on this doctoral work. Detailed information about data processing by each software were reported by Caby et al. [17] for MEDEpy, Ingerle et al. [19] for Jgixa and Sole et al. [20] for PyMca.

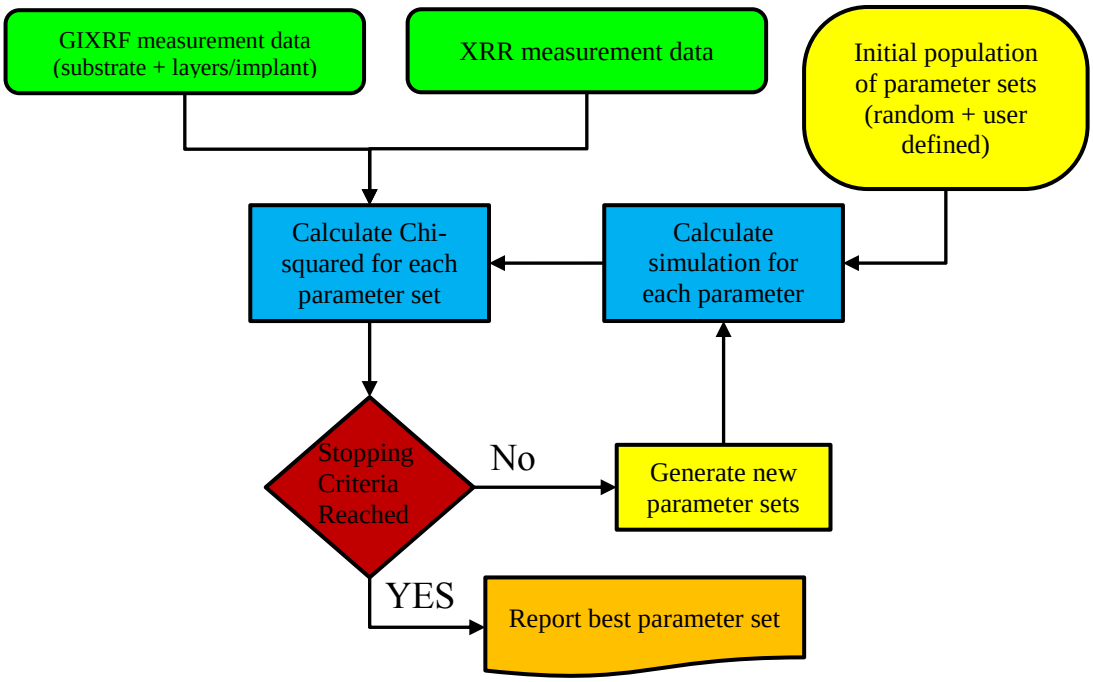

Figure 2.21 Flowchart of typical GIXRF and XRR data simultaneously processed [18].

2.5. Photoelectron emission

Photoelectrons are ejected from the atoms when an excitation source (e.g. X-ray beam) is absorbed by the atoms through the photoelectric effect discussed earlier. We can determine their binding state by the energy difference between the incident X-ray energy and the ejected kinetic energy. However, a photoelectron is only emitted from the sample when surmounting the work function threshold (i.e. Vacuum level), as depicted in Fig. 2.22. Hence the kinetic energy of that electron in vacuum is given by hν- Eb - ϕs, where ϕs is the work function of the sample, and ϕ_A is the work function of the analyzer, the kinetic energy E_{kin} measured by the analyzer is given by:

$$E_b = h\nu - E_{kin} - \phi_A \quad \text{(eq. 2.65)}$$

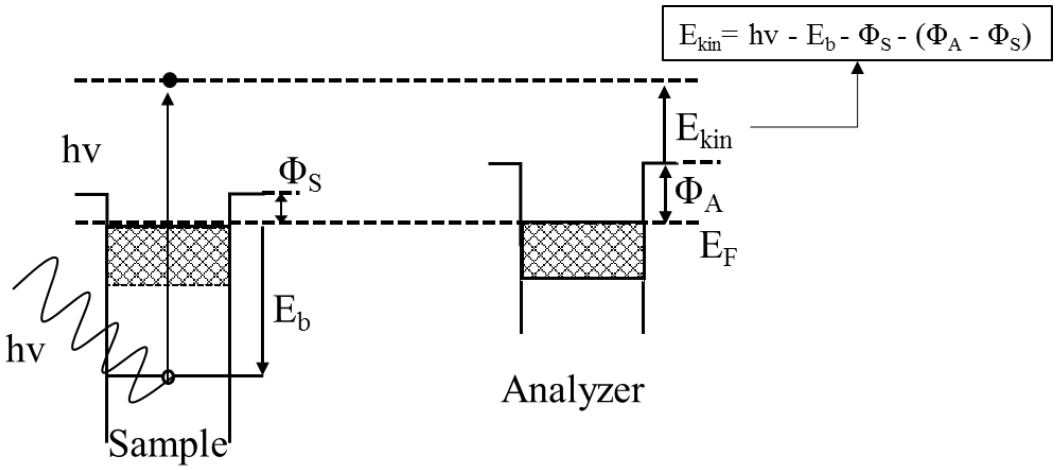

Figure 2.22. Schematic process of photoelectron emission, the electron excited by the incident X-ray beam has to overcome the worth function ϕA to be measurable.

The constant analyzer work function is empirically determined (around 4–5 eV) and the energy scale is set to zero at the Fermi edge of reference samples. The binding energies of electrons are determined through the acquisition of their kinetic energies. Of course, it can only be possible when the X-ray source energy (hν) is known. Generally it is a monochromatized source made of Mg-Kα (hν 1253.6 eV, linewidth 0.70 eV) or Al-Kα (hν 1486.6 eV, linewidth 0.85 eV).

XPS spectra are usually given by intensity (counts per second) as a function of the binding energy, from high to low energy. Fig. 2.23 illustrates an example XPS spectra of elementary tellurium film deposited on Silicon substrate. We can observe peaks corresponding to the core-level photoelectrons (e.g. Te4d, O1s, C1s) as well as other effects such as Auger electrons, valence peaks, shake-up and plasmon peaks.

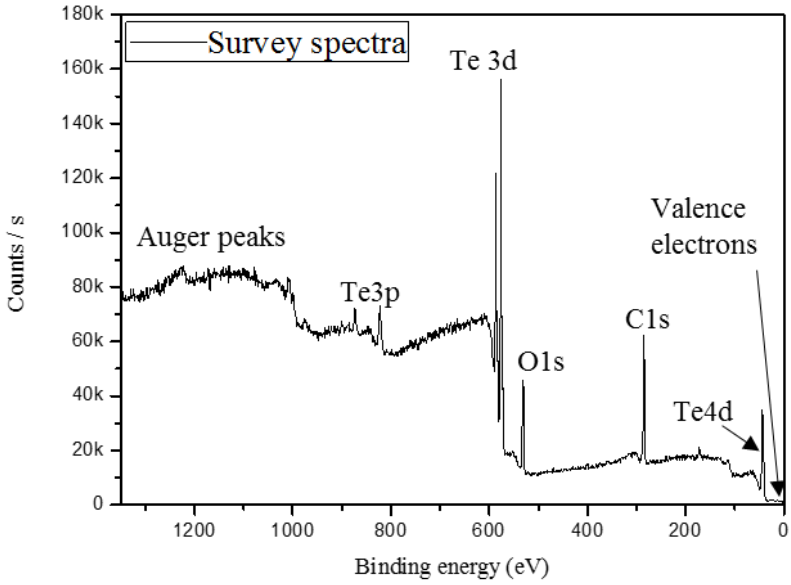

Figure 2.23. Survey spectra of tellurium oxide film.

- Core-level photoelectrons

The photoelectrons from the core-levels are labeled using the quantum notation nl_j (described in section 2.1). All orbital levels except the s levels (l = 0) give rise to a doublet with the two possible states having different binding energies. This is known as spin-orbit splitting (or j-j coupling) and reflects the 'parallel' or 'anti-parallel' nature of the spin and orbital angular momentum vectors of the remaining unpaired electron following photoemission.

The relative intensities of these doublets are based on the degeneracy of each spin state, i.e. the number of different spin combinations that can give rise to the total j (see Table 2.1). For example, for the 2p spectra, where n is 2 and l is 1, j will be 1/2 and 3/2. The area ratio for the two spin orbit peaks (2p1/2:2p3/2) is 1:2 (corresponding to 2 electrons in the 2p1/2 level and 4 electrons in the 2p3/2 level). These ratios must be taken into account when analyzing spectra of the p, d and f core levels.

An example of this splitting for the Sb 3d peak of a Sb film is shown in Fig. 2.24. Spin-orbit splitting

values (eV) can be found in a variety of databases [20]. These values are needed when fitting spectra where the chemical shifts are larger than the spin-orbit splitting. For example, the Sb 3d peak in Fig. 2.24 shows that the 3d3/2 and 3d5/2 doublet are constrained to have 2:3 peak area ratios, equal FWHM, and a peak separation of 9.36 eV.

Table 2.1. Spin-orbit split intensity ratio.

Subshell	j values	Intensity ratio (peak areas)
s	1/2	-
p	1/2, 3/2	1:2
d	3/2, 5/2	2:3
f	5/2, 7/2	3:4

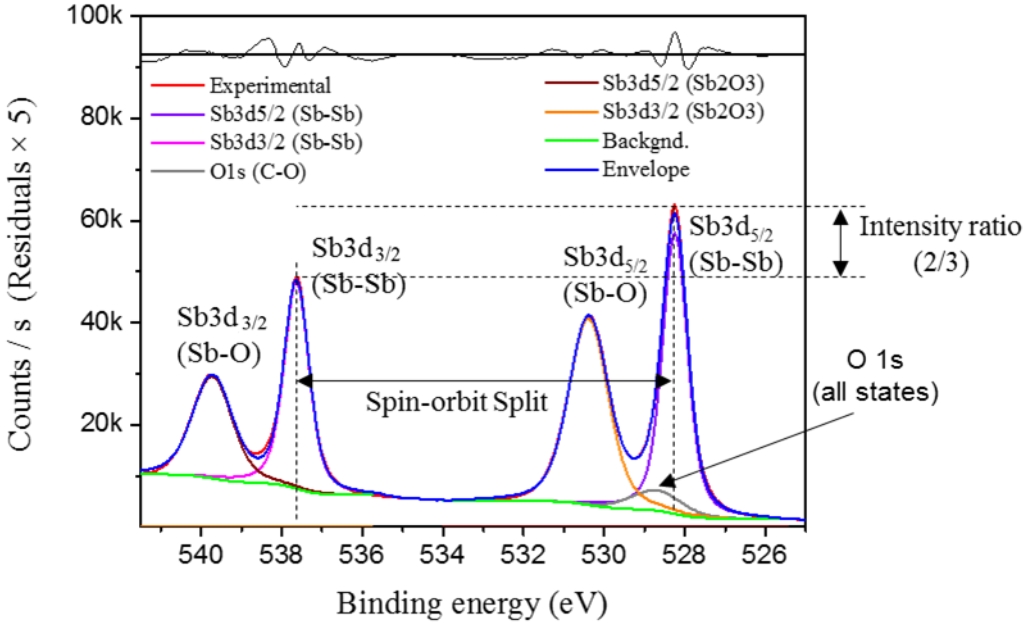

Figure 2.24. Sb 3d core-level range, XPS high resolution spectra core level. Composition deduced from deconvolution based on spin-orbit split and intensity ratio.

- Auger electrons

As we have seen in the photoelectric effect in section 2.1, Auger electrons are generated based on three steps: first, the creation of a core hole; second, the filling of this hole by an electron dropping from outer bound level; third, the emission of an (Auger) electron which takes up the remaining excess energy as kinetic energy, illustrated in Fig. 2.25. If the levels involved are, respectively, of energy C_1, C_2 and C_3, then the kinetic energy of the Auger electron is given by:

$$E^{A}_{k} = C_1 - C_2 - C_3 \qquad \text{(eq. 2.66)}$$

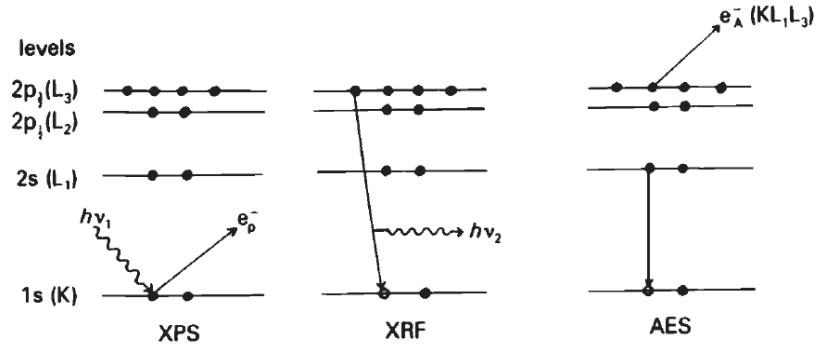

Figure 2.25. Schematic mechanism of Auger electron emission.

Since all three levels are characteristic from the atom, E^A_k is also characteristic of the element involved. Therefore, Auger electrons have unique kinetic energies, hence essential for elemental identification as well as chemical state analyses. A calculated value from both photoelectron and Auger peak positions is the modified Auger parameter (α'). This parameter is particularly effective for chemical state analysis and has no interference of surface charging. Originally defined by Wagner [21] and modified by Gaarenstroom and Winograd, the modified [22] Auger parameter is calculated as:

$$\alpha' = Ek(C_1C_2C_3) - Eb(C) \quad \text{(eq. 2.67)}$$

where $Ek(C_1C_2C_3)$ is the kinetic energy of the Auger transition involving electrons from C_1, C_2 and C_3 core levels and Ek(C) is the binding energy of the photoelectron from core level C. This form of the equation allowed for negative values of original Auger parameter (α).

The chart in Fig. 2.26 known as Wagner plot relates the most intense photoelectron line binding energies with the kinetic energy position of the sharpest core-core-core Auger line. Position of compounds on these plots indicate both relaxation energy and initial state effects [23]. Hence, the modified Auger parameter can be used in addition to the binding energy to give additional insight into the shift in electronic state between transition metal compounds.

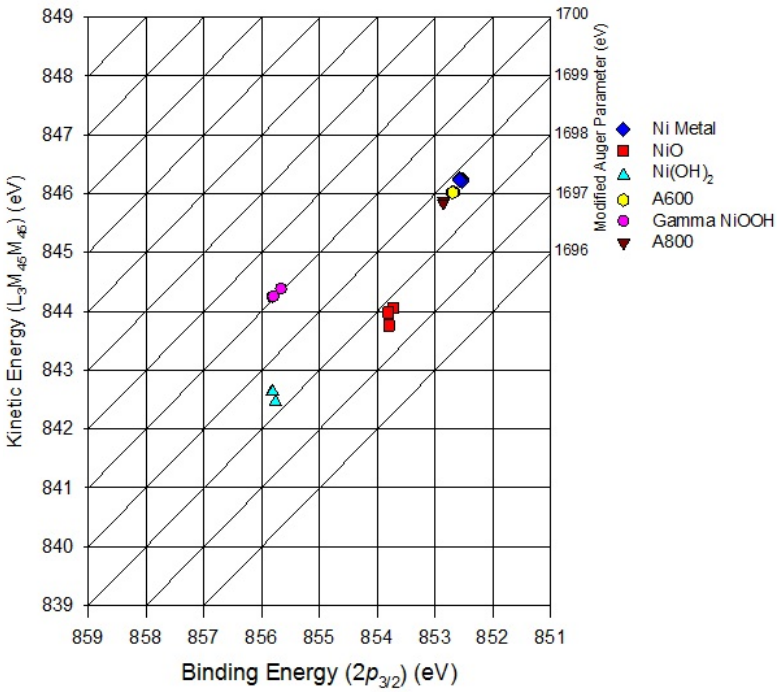

Figure 2.26. Ni $2p_{3/2}$ –Ni LMM Wagner plot for Ni metal, Ni alloys, NiO, $Ni(O/H)_2$ and NiOOH [24].

- Valence electrons

Valence electrons are found in low binding energy (i.e. 0-15 eV) known as delocalized or bonding orbitals. The valence spectra consist of many closely spaced levels giving rise to a band structure usually referred as valance band. As illustrated in Fig. 2.27.a, valence band is classified either as insulator or conductor. The valence band for insulator is separated from the empty conduction band, while for metallic conductors these bands are superimposed and the highest occupied state is termed the Fermi level, E_F. Figure 2.27.b. illustrate a valence spectra of silver where we easily spot the Fermi level boundary. For reference purposes, it is conventional to consider $E_F = 0$eV [25].

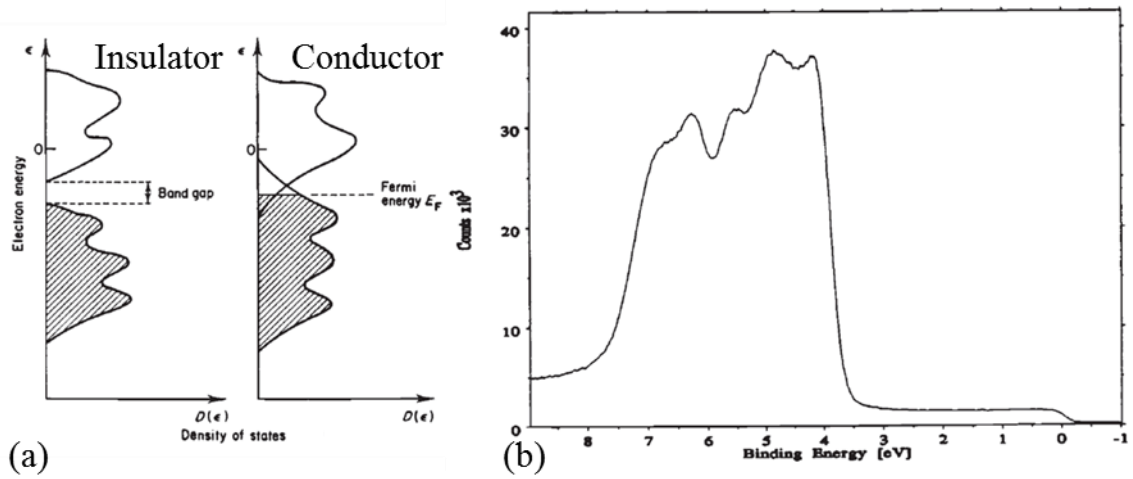

Figure 2.27. (a) Insulators and conductors bands of materials, (b) Typical Valence spectra [25].

- Loss features
  - Shake-up peaks

There is a finite probability that an ion (after photoionization) will be left in a specific excited energy state a few eV above the ground state through excitation of the ion by the outgoing photoelectron. When this happens, the kinetic energy of the emitted photoelectron is reduced and this will be seen as a "shake-up" peak at a higher binding energy than the main line. Shake up lines are common with paramagnetic states. The classic example of shake-up structure is seen in the 2p3/2 spectrum for Cu(II) species such as that for CuO seen in Fig. 2.28. The shake-up seen for transition metals can also be described as a strong configuration interaction in the final state involving significant ligand-metal charge transfer that results in an extra 3d or 4f electron compared to the initial state. The strength and shape of the shake-up features can aid in the assignment of chemical states. This can be seen in Fig. 2.28 where the Cu(II) oxide shows different shake-up structures [26].

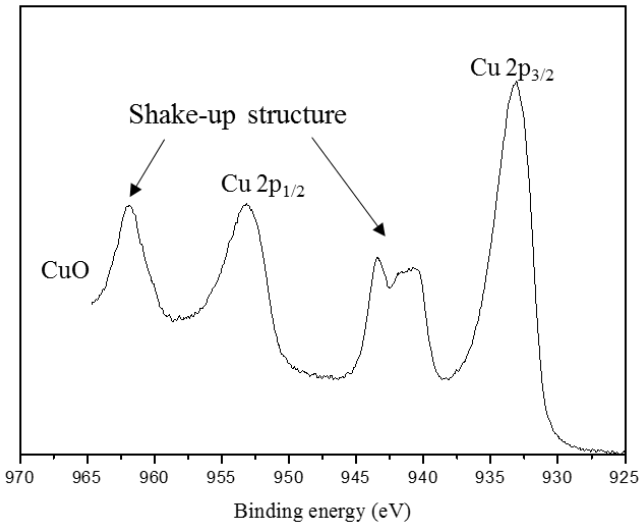

Figure 2.28. Shake-up structure in Cu 2p of copper (II) oxide.

- Plasmons peaks

For some materials, plasmon loss peaks may occur. These involve an enhanced probability for loss of a specific amount of energy due to the interaction between the photoelectron and other electrons. For conductive metals, the energy loss (plasmon) to the conduction electrons occurs in well-defined quanta arising from group oscillations of the conduction electrons. Plasmons attributed to the bulk of the material and its surface can sometimes be separately identified [26]. An example of plasmon loss peaks in a spectrum of aluminum metal is presented in Fig. 2.29. In some cases, such as with Al, the plasmon loss structure can interfere with the assignment and quantification of other spectral peaks such as Si 2p (99.6 eV) and Si 2s (150.5 eV) [20].

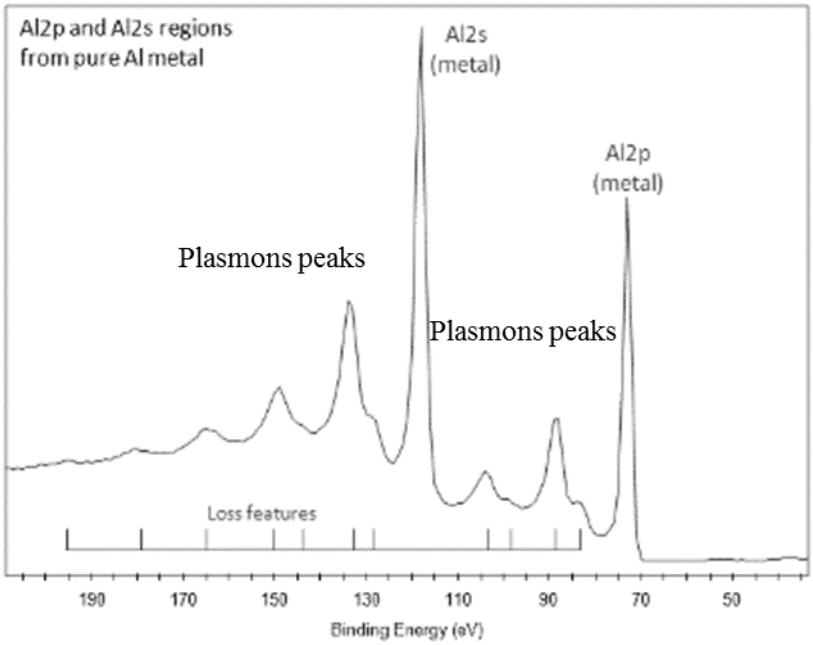

Figure 2.29. Plasmon loss structure in spectrum of aluminum metal [26].

- Binding energy shifts (Chemical environment contributions)

Core-level peaks can be shifted along the binding energy axis due to relaxation process, electrical charges, and chemical shifts (atoms are bonded to different elements). The energy shift (ΔEB) is then the sum of three contributions and is given by [26]:

$$\Delta E\text{B} = \Delta\text{R} + \Delta E_{\text{Charging effects}} + \Delta E_{\text{chemical shift}} \quad \text{(eq. 2.67)}$$

$\boldsymbol{\Delta R}$ is the relaxation effect factor: The relaxation process occurs when a core-level electron is ejected from the atom leaving a hole. This "final state" induces the deexcitation of outer electrons by contracting their orbitals, lowering the measured binding energy compared to the initial state.

$\boldsymbol{\Delta E_{\text{Charging effects}}}$ is the charging effects factor : Emission of electrons from the surface of an insulator during irradiation leads to the creation of a positive surface potential since electrons from the bulk of the sample or from the sample mount cannot compensates for this loss. This results in a shift of the peak position towards higher binding energies. This means that a source of compensating electrons has to be introduced for charge neutralization. This source is referred as electron "flood" gun, and is intend to flood the sample with low-energy electrons. It is not usual to attempt to balance the charging exactly, an excess of electrons is used to produce a uniform negative charge of known magnitude to be produced at the surface of the sample. The peaks can then be shifted to their correct positions during data processing. This technique minimizes the risk of differential or non-uniform charging.

$\boldsymbol{\Delta E_{\text{chemical shift}}}$ is the chemical shift: it reflects the effects of charge potential change on an atom when it is chemically bonded to a different element. Hence, when an atom is bonded to another element with higher electronegativity, a charge transfer to the latter occurs and the effective charge of the former becomes positive, thus increasing the binding energy. In the opposite, the binding energy of the atom with higher electronegativity is decreased. Figure 2.30 depicts the effects of chemical shift on N1s photoelectrons from the NSi_3 compound. A substantial shift towards higher energies is observed when NSi_3 forms NSi_2O $NSiO_2$ due to oxidation, which drastically increases with the oxidation states.

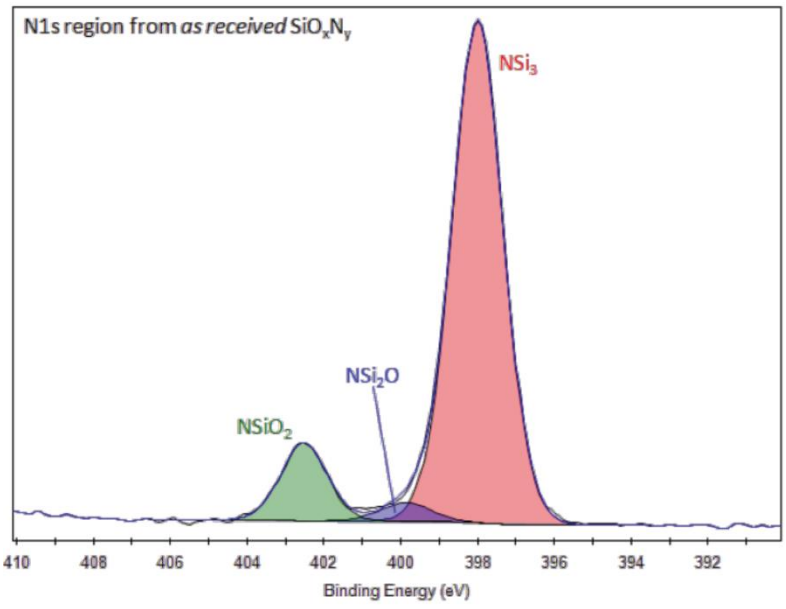

Figure 2.30. Influence of chemical shift on binding energy, elements with higher electronegativity induces compound to shift towards higher binding energies [27].

As the final binding state of the compounds is not always the same value, references to standard spectra have to be employed to interpret measured energy shifts. Auger parameters can be employed to determine the energy shifts, also tabulated values from the literature are very helpful (e.g., handbooks [28] and NIST website [20]).

To suppress any bias related to the energy shift, the binding energy axis is calibrated to a reference value. The instrument work function is calibrated to give an Au 4f7/2 metallic gold binding energy of 83.95 eV. The photoelectron peaks can be adjusted to the carbon C1s (284.8 eV) value, because most samples have been exposed to the atmosphere have a detectable quantity of hydro-carbon as surface contamination (typically with 1-2nm thick).

2.5.1. Photoelectron spectra

Quantification of peak intensity data is performed using peak areas. Although the peak area of a single photoelectron spectra can be easily extracted by integrating its surface and subtracting its background. Multi-elementary compounds, on the other hand, can be limited by this approach when different photoelectrons spectra are superimposed. The solution is to deconvolute all the contributions from the experimental spectra based on relative intensities, spin-orbit splitting and binding energies of the photoelectrons from each element.

- Photoelectron spectra peak fitting

The fitting process of a photoelectron spectra is based on a complex convolution of a Gauss-Lorentzian mix with the possibility of weak asymmetry (tailing to high binding energy which is only likely to be manifested at high resolution) [29]. The Gauss-Lorentzian ratio will depend on the relative importance of the instrumental contributions. As an example Fig. 2.31 shows the $Ge2p_{3/2}$ peak from a GeO_2 film fitted with pure Gaussian, pure Lorentzian and mixed Gaussian-Lorentzian (30 % Gaussian) lineshapes. Several such measurements will define the appropriate starting lineshape and a reasonable Gauss-Lorentzian ratio range (if this is an allowed variable) for the components in any attempted curve fitting process.

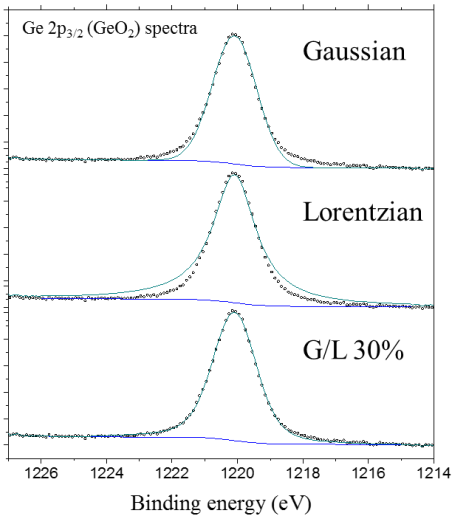

Figure 2.31. $Ge2p_{3/2}$ data processing is highly impacted by G/L deconvolution, for proper process a G/L mix has to be considered.

The curve fitting needs an appropriate background function (described below), low signal/noise and data has to be smoothed. As we have seen on quantum nomenclature, superimposed components can be separated based on the doublet relative intensity, spin-orbit splitting and their specific binding energies. Figure 2.32 shows an example of deconvolution spectra, in this case an oxidized selenide sample (Bi_2Se_3).

The processing software calculates the sum of the components and from comparison with the experimental data obtains a measure of the "the best solution" (usually chisquared by the least squares method). By iteration, with variation of allowed parameters describing the peak position, width, intensity etc, the fit is refined until convergence to reasonable minimum results. In this way the fitting process can be 'guided' towards a very reasonable solution according to the probed sample.

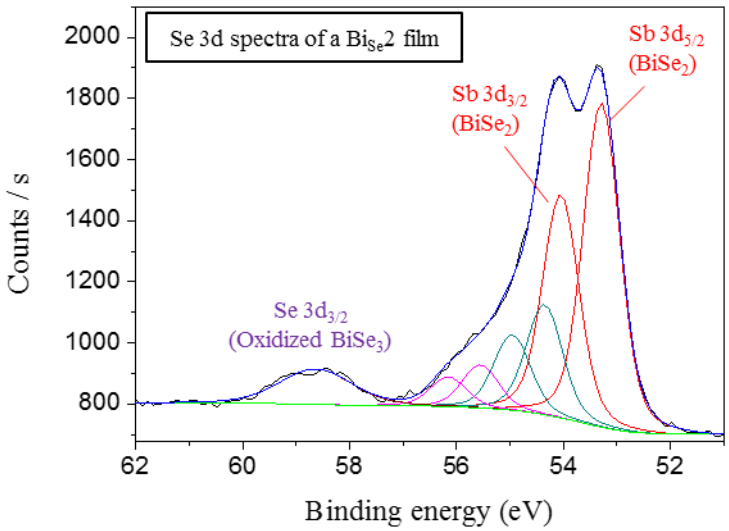

Figure 2.32. The complex Se3d spectra from a BiS_2 film can be processed by spectra deconvolution [27].

- Background subtraction

The most common background modellings employed in XPS data processing are the linear, the Shirley method and the Tougaard method. The first two are commonly available on most software while the latter is quite a recent approach. A detailed description of the relative merits of the three approaches has been given (for metallic systems only) by Tougaard & Jansson (1993) [30]. In the following analytical expressions J is the measured spectrum (strictly following correction for the analyzer transmission function, see Section 2.2.3.2), F is the background-corrected spectrum over the chosen kinetic energy region $E_{min}<E<E_{max}$ with corresponding channels (width AE) $i_{min}<j<i_{max}$. For the linear background:

$$F(i) = J(i) - k\sum_{j=i+1}^{i_{max}} \Delta E \quad \text{(eq. 2.68)}$$

where k is found by the requirement that $F(i_{min}) = 0$.

For the Shirley method:

$$F(i) = J(i) - k\sum_{j=i+1}^{i_{max}} F_{n-1}(j)\Delta E \quad \text{(eq. 2.69)}$$

Where k_n is found by the requirement that $F(i_{min}) = 0$. This requires iteration but the series typically converges to $F_n \sim F_{n-1}$ within five iterations.

For the Tougaard method

$$F(i) = J(i) - B_l\sum_{j=i+1}^{i_{max}} \frac{(j-i)\Delta E}{[C+(j-i)^2]\Delta E} J(j)\Delta E \quad \text{(eq. 2.70)}$$

Where C = 1643eV. B_1 is a parameter adjusted to give F~0 in a wide energy range below that of the real structure (typically 50eV). The choice of E_{max} is usually straightforward, i.e. within a few eV of the onset of the peak (on the high kinetic energy side). The choice of E_{min} is often more difficult, especially when shake-up structure is involved, or when a range of chemically shifted components 'fills in' the gap between the core line and the onset of the steeply sloping loss structure.

However, the derivation of the Tougaard algorithm is beyond the scope of this work. It appears to be very successful for treating spectra from metallic systems, revealing the large fraction of the 'real' peak area usually ignored by the other methods necessarily applied over a much smaller energy range.

Since the Shirley method assumes that each unscattered electron is associated with a flat background of losses, the background intensity at a point is proportional to the intensity of the total peak area (above background) at any point, and gives a step-like increase with energy, see Fig. 2.33.

For general quantitative analysis, the use of the Shirley background is recommended provided some care is taken to ensure consistent application (i.e. choice of end-points).

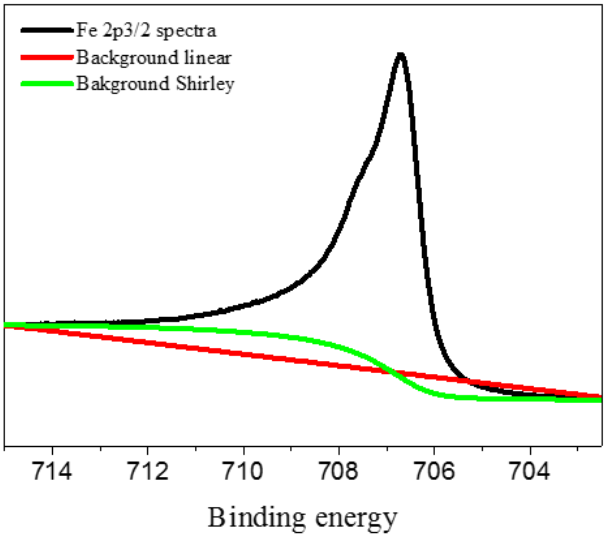

Figure 2.33. Comparison between linear and Shirley background. Shirley background properly modeled spectra range, while linear have some misleading range [27].

2.5.2. XPS Quantitative analysis

Considering a layered material with homogenous composition undergoing photo-absorption process from a monochromatic X-ray source. The amount of photoelectrons emitted from a core-level X of an element A experience some intensity decay by Beer-Lambert law and are ejected from the sample at θ angle, arriving in the detector with:

$$I_A(X) = I_0 p\sigma(hv, E_x)L(hv, X)G(E_X)D(E_X)\int_0^\infty N_a(z)exp\{-z/\lambda_X(E_x)cos\alpha\}dz \quad \text{(eq. 2.71)}$$

Where, I_0 is the X-ray flux irradiating the sample, p is the surface roughness factor (which affects X-ray illumination and photoelectron ejection through shadowing effects), σ(hv, E_x) is the photoionisation cross-section for ionization of X by photon *hv*, L(hv, X) is the angular asymmetry factor for emission from *X* by photon *hv*, G(E_x) is the transmission function of the instrument at the kinetic energy E_x, D(E_x) is the detector efficiency at energy *Ex*, N_a(z) is the distribution of atoms A with depth z, $\lambda_X(E_x)$ is the inelastic mean free path of electrons X in the material, and α is the angle of emission (to the surface normal).

If we assumed that the X-ray flux is constant and that the analyzed volume is homogenous, then equation (2.21) can be simplified to:

$$I_A(X) = K\sigma L N_A \lambda_X \cos(\alpha)\, GD \text{ (eq. 2.72)}$$

which describes the factors affecting the measured peak intensity. Terms relating to the excitation process are σ and *L*. The photoionisation cross-section, σ, is the transition probability per unit time for excitation of a single photoelectron *(Ax)* under an incident photon flux of *L* $cm^{-2}s^{-1}$. σ depends on *hv*, atomic number (Z) and core level *(n, I).* Values calculated by Scofield (1976) [31] are shown in Fig. 2.34, for Al-Kα source. *σ* also depends on the angle between the incident photon direction and the direction of photoelectron detection (γ) and this is embodied in the angular asymmetry factor, L_A*:*

$$L_A = 1 + \frac{\beta}{2}\left(\frac{3}{2}sin^2\gamma - 1\right) \quad \text{(eq. 2.73)}$$

where β_A, the asymmetry parameter, is a constant for any given atom/subshell/ photon combination. Note also that for γ = 54.74°, L_A does not depend on γ and for many of the more recent instrument designs γ is within 10° of this 'magic angle'.

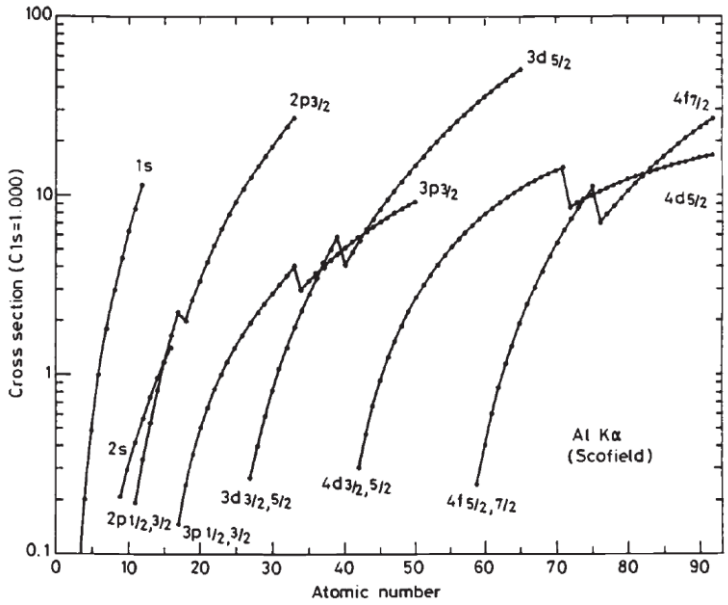

Figure 2.34. Scofield values of cross-section σ for Al-Kα source. The values are referenced to C1s as 1.0 [31].

The instrumental terms in eq.2.72 are G and D. The transmission function was derived by Seah [32] from electron-optical principles. He determined that G not only depends on kinetic energy E_k but is also function of input lens set-up (magnification, aperture/slit dimensions), analyzer parameters (pass energy, operation and type) and the X-ray illumination (large area flood, or monochromated focused spot).

The effect of detector efficiency, which can be markedly dependent on E_K, can be ignored when operating at constant pass energy since all electrons are detected at this energy. With the pass energy constant, the detection energy will vary with Ek/R (R=E/ ΔE) and this could mean a variation in D of a factor of 2 or more over the range $100<E_k<1500$eV for a typical channeltron [32]. The change in detector performance with time and the variation in individual detectors are additional reasons why constant pass energy is preferred for quantitative work.

Equation 2.71 can be used for direct quantification (the so-called first principles approach), but in practice this approach is difficult since all the instrumental and physical parameters are hard to determine in the whole energy range. Hence, quantification is usually determined by sensitivity factors (SF). Once a set of peak areas has been calculated for the elements detected, *I* in eq. 2.71 has been determined. The terms σ, *K*, and λ are incorporated into a set of SFs appropriate for the spectrometer used, or explicitly incorporated into the algorithm used for quantification. If the X-ray flux remains constant during the experiment, we can determine the atomic percentage of the elements concerned, by dividing the peak area by the sensitivity factor and expressing it as a fraction of normalized intensities sum as:

$$[A]\ at\% = \frac{\frac{I_a}{SF_a}}{\sum\frac{I}{SF}} \times 100 = \frac{\frac{I_a}{\sigma_a K_a \lambda_a}}{\sum\frac{I}{\sigma K \lambda}} \times 100 \quad \text{(eq. 2.74)}$$

In practice, SFs are tabulated values determined by each XPS manufacturer. Nonetheless, when the provided values does not reflect an accurate quantification, they can be adjusted by taking a quantification reference from a validated technique (e.g. RBS, WDXRF) as follow:

$$\frac{SF_{\mathrm{B}\ corrected}}{SF_{\mathrm{A}\ corrected}} = \frac{SF_A}{SF_B}.\left(\frac{[A]at\%_{ref.}}{[B]at\%_{ref.}}\right)/\left(\frac{[A]at\%}{[B]at\%}\right) \quad \text{(eq. 2.75)}$$

Although The SFs are straightforward corrected by the reference chemical compositions, and the SFs are determined based on the transmission function as well as the photo-absorption cross-section library and electrons attenuation length. The latter can represent different values if calculated from the Inelastic Free Mean Path (IMFP) based on $KE^{0.6}$ (IMFP as function of kinetic energy power 0.6), or the escape depth from TPP-2M method. The difference between these methods calculations are described below.

2.5.3. Depth dependence of photo-emitted electrons

The probability that photoelectrons generated just below the surface will leave the solid is mainly determined by the inelastic scattering process the photoelectrons suffer traveling through the solid. Although the Inelastic Mean Free Path (IMFP) is main factor contributing the photoelectron emission, elastic scattering can also impact the final scape depth of photoelectrons.

As shown in Fig. 2.35, photoelectrons are created at a depth z below the surface with a certain angular distribution depending on the orbital involved. For the case of the straight-line trajectory only inelastic scattering leads to electron attenuation, which also follow the Beer-Lambert formula as:

$$I_z = I_0 \exp(-\frac{z}{\lambda \sin\theta}) \quad \text{(eq. 2.76)}$$

where *Iz* is the intensity emanating from the atoms at depth z, I_0 is the intensity from the surface atoms and θ is the electron 'take' off angle to the surface (θ=90-α). In this case λ is the inelastic mean free path of the measured electrons, defined as the average distance that an electron with a given energy travels between successive inelastic collisions [26].

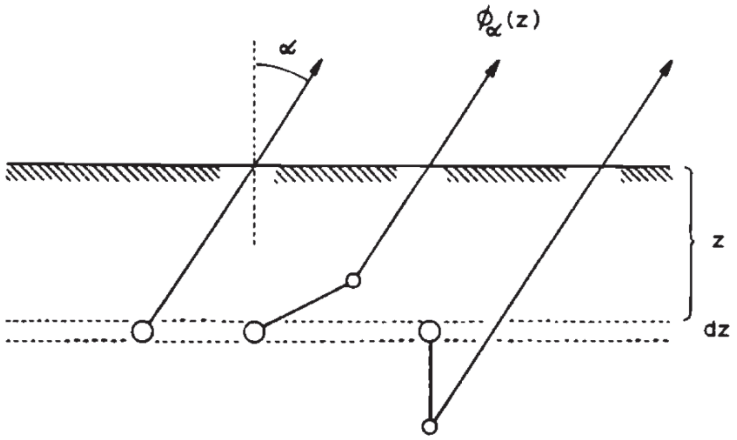

Figure 2.35. The left trajectory is pure inelastic scattering, towards grazing angles elastic scattering increases the electron trajectory [26].

Nevertheless, as depicted in Fig. 2.35, elastic scattering events lead to longer trajectories compared to the straight-line trajectory (for inelastic scattering only). According to theoretical calculations this will lead to attenuation length (λ_{AL}) values less than the inelastic mean free path by 30% or more [26]. Hence, it is highly important to determine λ_{AL} accurately in order to reduce its impact on quantitative analysis as well as elementary depth-profiles.

Experimental values for λ_{AL} up to 1978 were compiled [33] and fitted by universal curves so that unknown λ_{AL} could be estimated. Typical values of λ for pure elements are in the range of 1 to 10 atom layers, see Fig.2.36. In this case, the fitted equation was determined as:

$$\lambda_{monolayers} = \frac{538}{E^2} + 0.41(aE)^{1/2} \quad \text{(eq. 2.77)}$$

where $\lambda_{monolayers}$ is attenuation length expressed in atomic layers, *E* is the kinetic energy in electron volts, p is the density in kilograms per cubic meter, and a is the lattice parameter in nm. To be most useful, these data should provide the general relationship between λ_{AL} and *E* for the material in question. This is most frequently expressed as a simple power relationship

$$\lambda_{AL} = KE^x \quad \text{(eq. 2.78)}$$

Where x is between 0.5 and 0.7 for a wide range of materials.

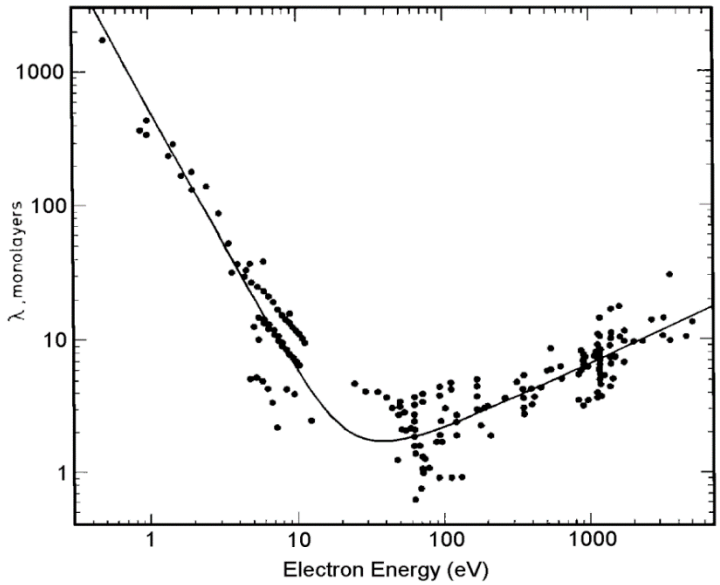

Figure 2.36. Compilation of experimental attenuation lengths for inorganic compounds [34].

Inelastic mean free paths can be calculated from experimental optical data. The most complete source of data arises from work by Tanuma et al. [35]. The calculations generate inelastic mean free path (λ) values over the energy range 50-2000 eV and these values can be fitted by a modified form of the Bethe equation for inelastic scattering:

$$\lambda = \frac{E}{E_p^2\left[\beta \ln(\gamma E) - \left(\frac{C}{E}\right) + \left(\frac{D}{E^2}\right)\right]} \quad \text{(eq. 2.79)}$$

where λ is in angstroms, *E* is the kinetic energy (in electron volts), $E_p = 28.8(N_v p/M)^{0.5}$ is the free-electron plasmon energy (in electron volts), *p* is the density (in grams per cubic centrimetre), *Nv* is the number of valence electrons per molecule and M is the molecular weight. The fitting parameters β, γ, *C* and *D* can be empirically related to other material properties as follows:

$$\beta = -0.10 + 0.944/\left(E_p^2 + E_g^2\right)^{0.5} + 0.069p^{0.1} \quad \text{(eq.2.80.a)}$$

$$\gamma = 0.191p^{-0.5} \quad \text{(eq.2.80.b)}$$

$$C = 1.97 - 0.91U \quad \text{(eq.2.80.c)}$$

$$D=53.4-20.8U \quad \text{(eq.2.80.d)}$$

where $U=N_v p/M$ and E_g is the band-gap energy (in electron volts). Eqs 2.79 and 2.80 are referred to as TPP-2M (Tanuma, Powell and Penn, second modification).

Another approach, yet simpler than TPP-2M method was developed by Cumpson and Seah [36], it consisted to determine the λ_{AL} empirically with the following relation:

$$\lambda_{AL} = 0.316a^{3/2}\left\{\frac{E}{Z^{0.45}[\ln(E/27)+3]} + 4\right\} \quad \text{(eq. 2.81.a)}$$

$$a = 10^8\left(\frac{\mu}{pN_{AV}}\right)^{1/3} \quad \text{(eq. 2.81.b)}$$

In eq. 2.81.a, E is the kinetic energy of the electron from the core-level, Z is the atomic number of the element. Whereas, in eq. 2.81.b, $N_{AV} = 6.02x10^{23}mol^{-1}$ is the Avogadro constant, ρ is the density of the matrix (in $kg.m^{-3}$) and μ is the average atomic mass of the matrix (in g).

The advantage of equation 2.81 is its simplicity to estimate λ_{AL} compared to the TPP-2M method, and can be employed for general purposes.

2.5.4. Angle resolved X-ray Photoelectron spectroscopy (ARXPS)

The depth dependence of photoemitted electrons described above can be employed to determine the depth distribution of elements. The ARXPS method works according to eq. 2.76, as the take-off angles of the photoemitted electrons are related to their scape depth. From eq.2.76, *escape depth* (z), it is the distance, normal to the surface, at which the possibility of an electron escaping without significant energy loss due to inelastic scattering process drops to 36.8% (e^{-1}). Indeed, 95% of the detected signal comes from $z = 3\ \lambda_{AL}$.

Hence, we can record the spectra by covering their angular range up to the scape depth of three times the IMFP (3λ) of electrons, as depicted in Fig 2.37.a. As a result, we can distinguish, for example, an over-layer of element A from a substrate of element B by measuring their intensities according to their take-off angles (Fig. 2.37.b).

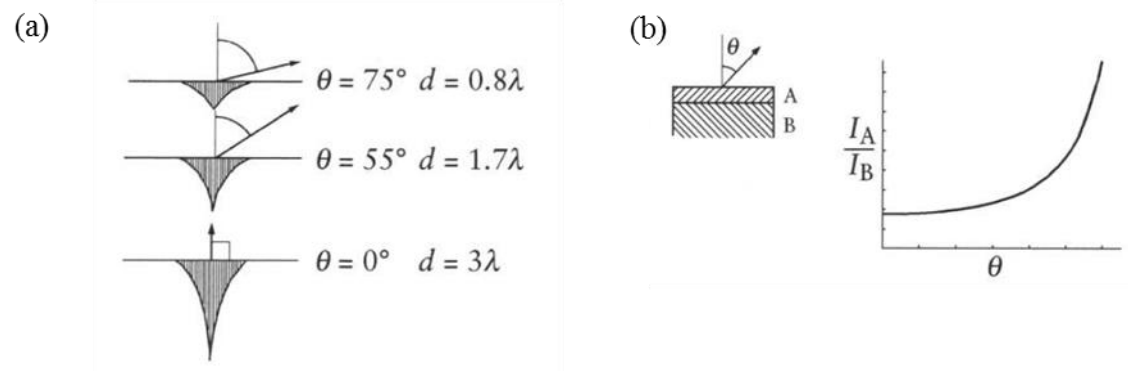

Figure 2.37. (a) Sample depth as function of electron take-off electron θ, the width of the shaded areas represent the proportion of the detected electrons emitted as function of depth; (b) overlayer (A)/substrate(B) and intensity (I) versus θ.

To cover the angular range, we can probe the sample either by conventional ARXPS where the sample is tilted or by parallel ARXPS where the sample is in constant position and the different take-off angles are resolved by the optics and detector set, as illustrated in Fig. 2.38. Although conventional ARXPS was the first to be developed, parallel ARXPS is becoming more popular. The main advantages of parallel ARXPS compared to conventional one are:

1. ARXPS can be applied to large samples. It would be difficult to tilt a large sample in a typical XPS system, especially if data is required from a region near the edge of the sample, suitable for probing semiconductor wafers.
2. Small area ARXPS is possible on parallel ARXPS but would be very difficult using conventional instrument because:
    a. At all angles, the analysis position would have to be accurately aligned with the feature to be analyzed. This is difficult, especially if the analysis position is at some distance from the tilt axis and the required analysis area is very small.
    b. The analysis area changes as a function of angle, as can be seen in Fig. 2.38. A worst case occurs when the transfer lens is used to define the analysis area. Using parallel angle acquisition, the analysis area and position is completely independent of the emission angle.
3. If an insulating sample is tilted, the required charge compensation conditions also change. Changes in peak position or shape may then be due to changes in the efficiency of charge compensation. Using parallel acquisition of angular data, the compensation conditions are the same for all angles and any changes in the spectra as a function of angle must reflect real chemical differences.

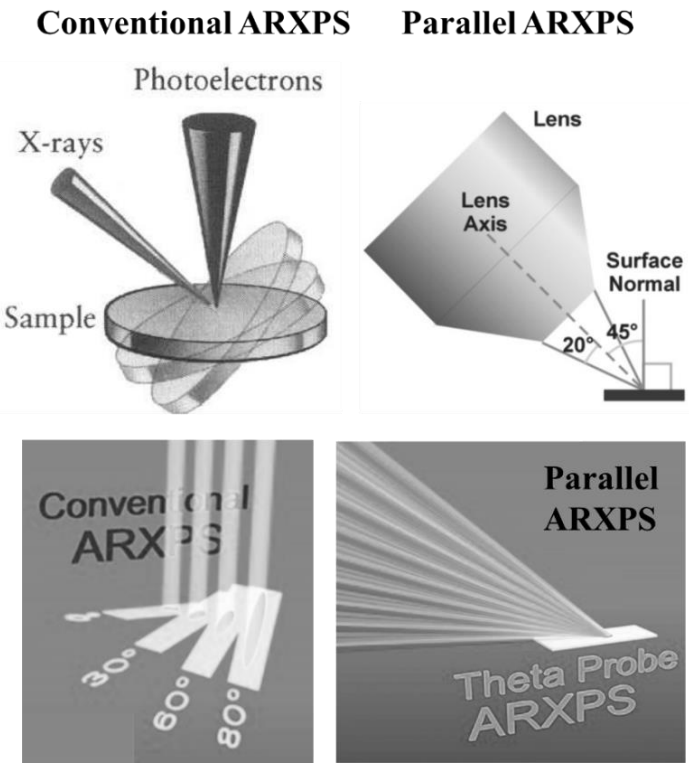

Figure 2.38. Conventional ARXPS (right) requires tiltong the sample, while parallel ARXPS (left) perform analysis with sample stationary [37].

- ARXPS data processing

When ARXPS data are collected from a number of angles, it is possible to use the data to obtain nondestructive depth profiles. One method for depth-profile reconstruction is by using the "Beer-Lambert" law, but in this case interfacial effects are not taken in account, since the layers are well defined. Hence, a suitable method to take in account realistic variations on the depth distribution is the Max Entropy method. This method was firstly introduced for image reconstruction and demonstrated a useful algorithm for depth-profile reconstruction by ARXPS [38].

In this method, the sample is considered to consist of "slabs" of the material, each slab having uniform composition. Trial concentrations of each component material in each slab are then assumed and the ARXPS characteristics calculated. Further iterations then take place to find the "best fit". A typical data processing by this method is depicted in Fig. 2.39 for a Sb_2Te_3, there we can even observe a thin layer of carbon contamination (<0.5 nm on 3 nm film of Sb_2Te_3 with Sb/Te proportion close to theory (~2/3).

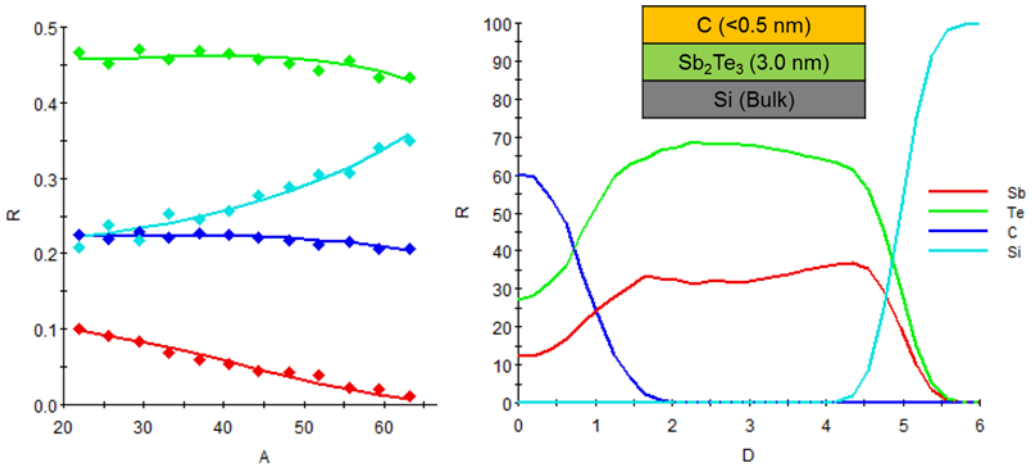

Figure 2.39. ARXPS data processing by Max-entropy method reveals very consistent elementary depth profile with Sb/Te proportion close to theory (~2/3).

2.6. Sources and instrumentation

2.6.1. X-Ray sources

In 1895 X-rays were discovered by Röntgen when he was investigating external effects on vacuum tubes and observed electrical discharge passing through them. This discovery not only made him earn a Nobel prize in Physics in 1901 but also triggered a huge revolution in the X-ray science. The development of new X-ray sources and the pursuit of brighter X-ray sources led the creation of huge facilities such as synchrotrons and free-electron lasers (FEL) as shown in Fig. 2.40. Although the development of laboratory X-ray sources is less remarkable (due to limited brightness, 10^{12} less bright than synchrotron), the need of brighter lab-sources for the development and industrialization of advanced technologies (e.g. nanomaterials, cutting edge medical devices) led to the creation of new X-ray sources based on rotating or metal-jet anodes. Indeed, much of the work in material science are conducted either in laboratories or synchrotrons, then both sources are briefly described below.

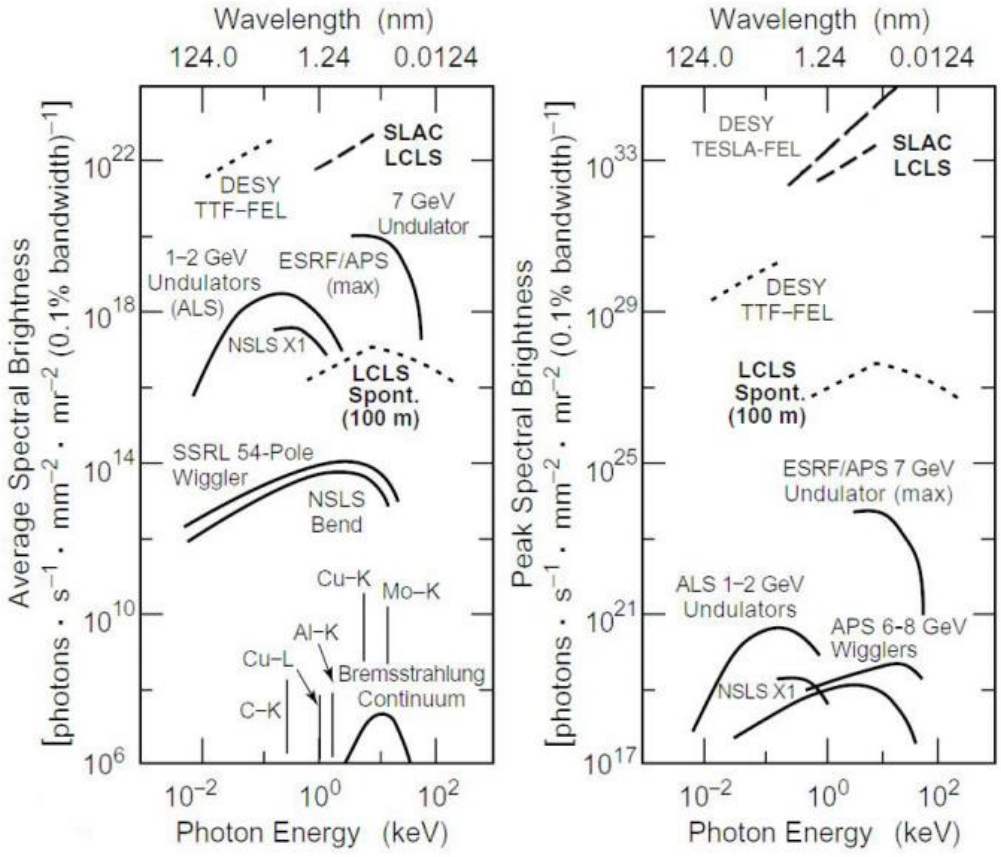

Figure 2.40. The average and peak brightness of photon beams at LCLS, ESRF, FEL, and some others advanced synchrotron sources [39].

- X-ray tubes

X-ray lab-sources are generated from electrons impinging on a metal anode. This source has two distinct components as emitted spectra (Fig. 2.41). There is a continuous part due to the electrons being decelerated, and eventually stopped in the metal. This is consequently known as bremsstrahlung radiation (from the German word “bremsen” for brake), and has a maximum energy according to the high voltage applied to the tube. Overlapped on this broad spectrum there are sharp spectral lines corresponding to the fluorescence characteristic radiation of the target anode. The Kα and Kβ radiations are then several order of magnitude more intense than the bremsstrahlung background.

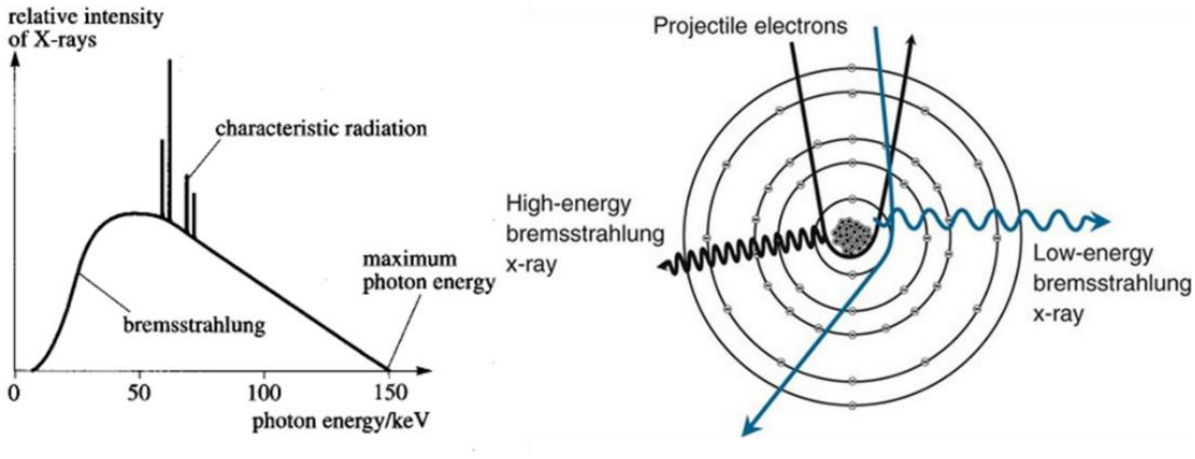

Figure 2.41. X-ray generation from a target.

The most popular X-ray tube in laboratories is the solid target. It is basically composed of a stationary solid target (anode) being bombarded by electrons generated from the filament (cathode). The X-ray brightness can be improved by increasing the electron current, but it is limited by the melting temperature of the anode, since the focal spot of the electrons impacting on the anode is very hot. Although the high temperature issue can be reduced by water cooling system, no substantial increase on X-ray intensity is obtained [40].

The need of higher X-ray brightness can be achieved by rotating anode X-ray tubes. Different to stationary solid target, the anode under rotation increases effective area of the anode exposed to the beam. By this mean, the heating of the anode is reduced and the tube loading can be increased [40].

Despite of the solid anode rotation, the thermal power loading of the anode is still a barrier for increasing brightness of laboratory sources. Recent development, however, brought a new X-ray source consisting of a liquid-metal anode flowing at very high speed, melting is no longer a problem. In this case, the metal-jet anode is continuously regenerated so that very high electron power can be handled, and therefore extreme brightness can be achieved [41]. Figure 2.42 is a summary of the main X-ray lab-sources and their respective brightness range which are related to low source diameter with very high power loading.

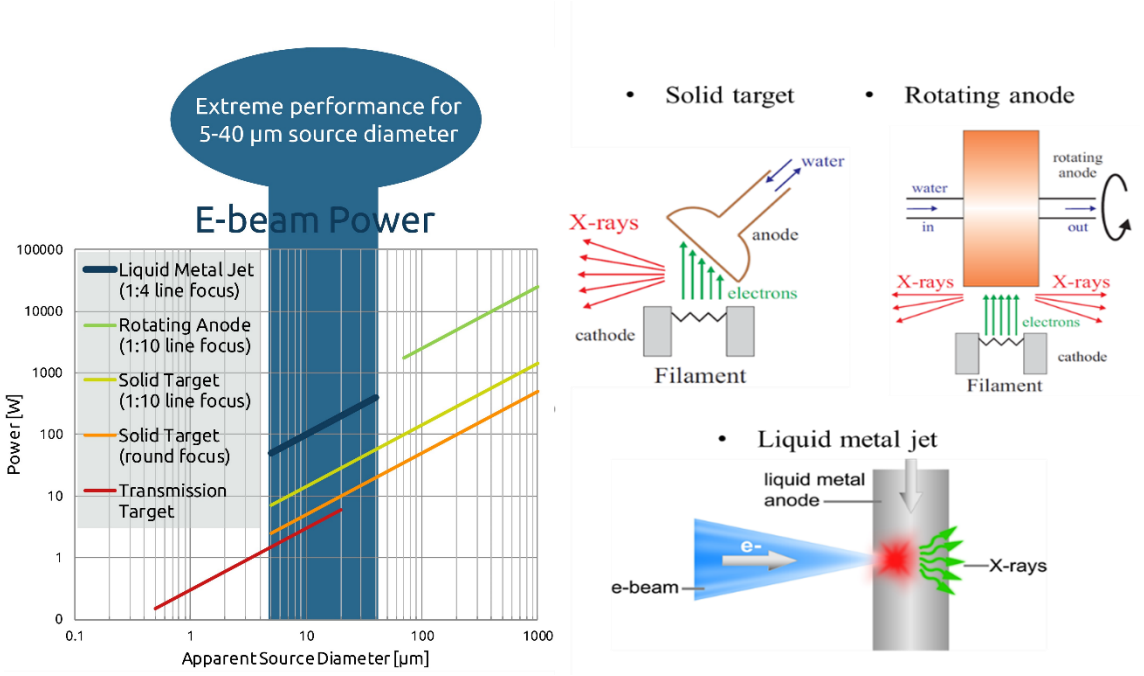

Figure 2.42. Main types of X-ray laboratory sources as well as their respective brightness as a relation between power and apparent source.

- Synchrotron sources

Synchrotron radiation is generated when electrons moving at relativistic speeds are forced by magnetic fields to follow curved trajectories, then emitting electromagnetic radiation in the direction of their motion. The creation of synchrotron radiation starts in the linear accelerator or 'linac' where electrons are accelerated up to reaches several millions of electron volts (MeV). At this point, they pass through a booster ring that gives them a boost in energy from millions to billions or giga electron volts (GeV), then they are transferred to the storage ring, as illustrated in Fig.2.43.

When electrons are injected in the storage ring, they are forced to travel in a circular path; to be focused and brighter, they pass through an array of bending, focusing and undulator magnets placed along the circumference. During each turn, the electrons loose part of their energy by emitting synchrotron radiation. The energy lost is fully regained when electrons are accelerated passing through radio-frequency (RF) cavities also placed throughout the circular path. The loss of electrons is also recovered by injecting a bunch of 6 GeV electrons from the booster, every 50 milliseconds.

The X-ray beam emitted by the electrons has continuous energy (white beam) and is directed toward beamlines that surround the storage ring in the experimental hall. Each beamline is designed for use with a specific technique with specific energy range selected by dedicated monochromating systems.

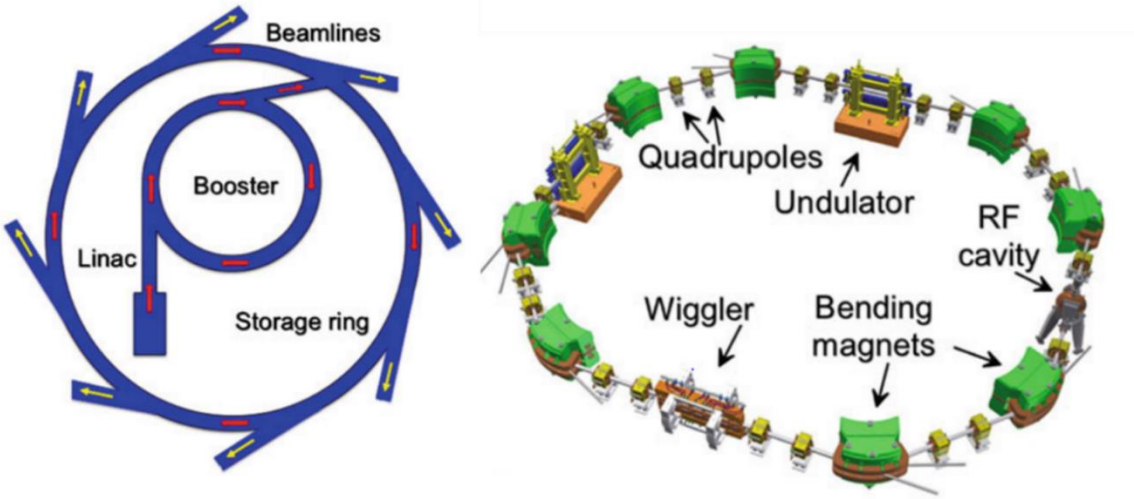

Figure 2.43. Schematic synchrotron source (left), storage ring and magnets (right) for electron conditioning.

- Monochromators

The main objective of a monochromator is to select one wavelength and its bandwidth from the X-ray source. The name come from the Greek roots “mono” for “single” and “chroma” for “color”. Monochromators are crystals (natural or artificial) exploiting the diffraction, refraction as well as total external reflection phenomena. They are placed in the path of the X-ray source, and by orienting it according to Bragg’s law, it diffracts the beam to a specific wavelength as Shown Fig. 2.44. The common monochromator setup consists of flat or curved mirrors. Flat mirrors also known as bounce monochromator consisting of a setup of double or four mirrors which provide monochromatic beam in the same direction as the incident white beam. While, focusing mirrors, not only monochromatize the beam, but also concentrate it into a very small spot on the sample surface.

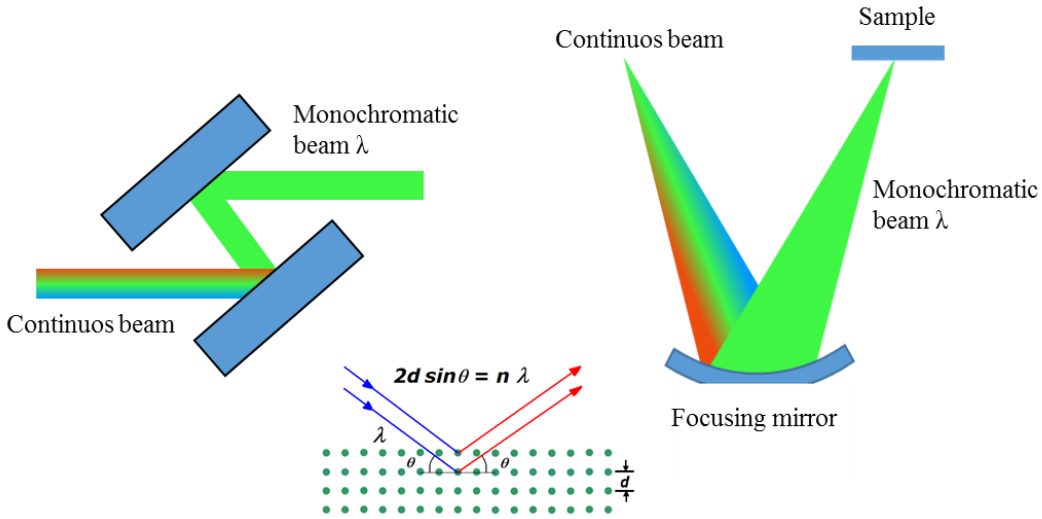

Figure 2.44. Monochromatization process by double monochroamtor (rigth) and focussing mirror (left).

2.6.2. XRF instrumentation

2.6.2.1. Energy Dispersive mode (EDX)

As illustrated in Fig. 2.45, the basic components of an Energy Dispersive X-Ray Fluorescence (EDXRF) spectrometer are X-ray source, sample, and detector. Several devices such as source filters, secondary targets, collimators, monochromators and focusing optics are used to modify the shape or intensity of the source spectrum or the X-ray beam shape. The X-ray photons emitted from the sample are directly collected by a detector counting the individual photons and determining their different energies. Semiconductor detector is usually employed for EDX signal acquisition, not only because it has higher energy resolution than other detectors (i.e. scintillation detectors or gas proportional counters) but also it comparatively has good counting rate.

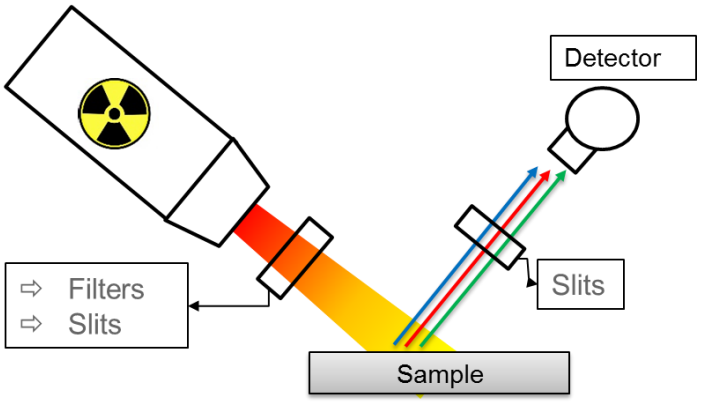

Figure 2.45 . Schematic principle of EDXRF, spectra resolution (>150 eV).

2.6.2.2. Wavelength Dispersive mode (WDX)

In contrast to the EDX mode, a Wavelength Dispersive X-Ray Fluorescence (WDXRF) spectrometer needs parts of a goniometer (Fig. 2.46), which have to be mechanically moved with a high precision. A total spectrum is not recorded simultaneously but sequentially, that is, the spectral lines of the individual elements of a sample are registered one after the other. Consequently, the spectral resolution is much better in comparison to an EDX, even for detection of light elements (i.e. Be, C, O, N, etc.

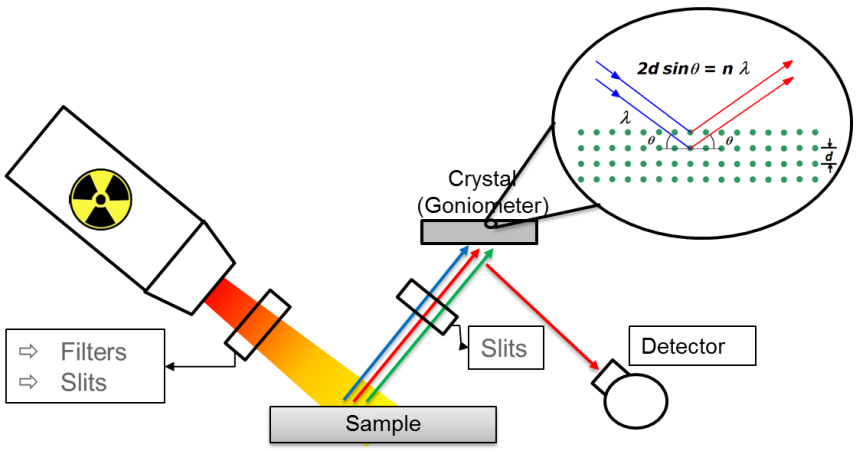

Figure 2.46. Schematic principle of a WDXRF, spectra resolution (5 eV).

The WDXRF spectrometer is based on Bragg diffraction with crystals to disperse X-rays. As we know Bragg's equation is written as:

$$n.\lambda = 2.d.\sin\theta \qquad \text{(eq. 2.82)}$$

n is the reflection order, λ is the wavelength of incident X-rays, *d* is the lattice spacing of the crystal and θ is the incident angle. Eq. 2.82 shows λ must be smaller than 2*d*. Practically, the scanning range of the goniometer (usually $2\theta < 150°$) limits $\lambda < 2d \sin 7°$◦. Angular dispersion of a spectrometer is obtained by differentiating Eq. 2.82 as:

$$\frac{d\lambda}{d\theta} = \frac{2.d.\cos\theta}{n} \quad \text{(eq 2.83)}$$

Equation 2.83 shows us that higher reflection angle θ and/or higher diffraction order *n* gives better wavelength resolution. The relation between angular resolution and relative wavelength resolution is derived from eq. 2.82 and 2.83 as:

$$\frac{d\lambda}{\lambda} = \frac{d\theta}{tan\theta} \qquad \text{(eq. 2.84)}$$

Equation 2.84 indicates that higher reflection angle θ yields higher wavelength resolution (i.e. smaller 2*d* value crystal).

Analyzing crystals are then chosen according to their 2d value (spectral range) and to the resolution or reflectivity needed. It can be either a natural crystal such as Ge, LiF or synthetic multilayer crystal. To analyse light elements, i.e. detecting longer wavelength X-rays, we need a dispersion material, with a larger 2d available among natural crystals. Table 2.2 shows the main crystals employed in WDXRF spectrometer.

Table 2.2. Common crystals for WDXRF [42].

Crystal	Miller indices	2d (nm)	Lightest measurable element	Typical energy resolution	Remarks
LiF	(220)	0.281	Cr	14 eV, Mn-Ka	High resolution
LiF	(200)	0.403	K	25 eV, Mn-Ka	General use
NaCl	(200)	0.564	S	5.5 eV, S-Ka	For sulfur High resolution deliquescent
Ge	(111)	0.653	P	5 eV, P-Ka	Eliminate second order reflection
InSb	(111)	0.748	Si	4.5 eV, Si-Ka	For silicon
PET	(002)	0.876	Al	4 eV, Al-Ka	Higher reflectivity
ADP	(101)	1.065	Mg	4 eV, Mg-Ka	For magnesium deliquescent
TIAP	(001)	2.576	O	15 eV, Na-Ka	Deliquescent

2.6.2.3. XRF detectors

In X-ray fluorescence techniques, different types of detectors can be employed like semiconductor detectors, gas proportional counters and scintillation detectors. We will limit ourselves here to a short description of the general features of the main detector classes, only in sufficient detail, to understand their different performances and operating features.

- Semiconductor detectors

When an incident X-ray photon interacts within the crystal, primary interactions result in producing photoelectrons (photoelectric effect) and Auger electrons (atomic relaxation). These electrons then pass on their energy in several steps and move outer electron from the valence band into the conduction band of the crystal lattice, the left vacancy being referred as a hole. An entire cascade of electron-hole pairs is generated before the energy of the incident photon can be consumed. Due to the applied high voltage, the electron-hole pairs separate into electrons and holes and quickly drift towards the negative and positive electrodes, respectively, as shown in Fig. 2.47. A charge pulse is generated for single photon counting. Since the amount of electron-hole pairs is directly proportional to the energy of the specific photon detected, the magnitude of the charge pulse is related to the photon energy as well. Therefore, the solid-state sensor is capable of counting single X-ray photons and recording their energies [42]. Semi-conductor detectors for photon spectrometry are using "high purity" germanium or silicon drift with lithium (Si(Li)). However, these must be operated at liquid nitrogen temperature. Recently Silicon Drift Detectors (SDD) (Fig 2.47) have grown in popularity because they need only moderated cooling provided by a Peltier module. The central small contact anode is surrounded by concentric drift electrodes which allow collecting the charges while minimizing the noise.

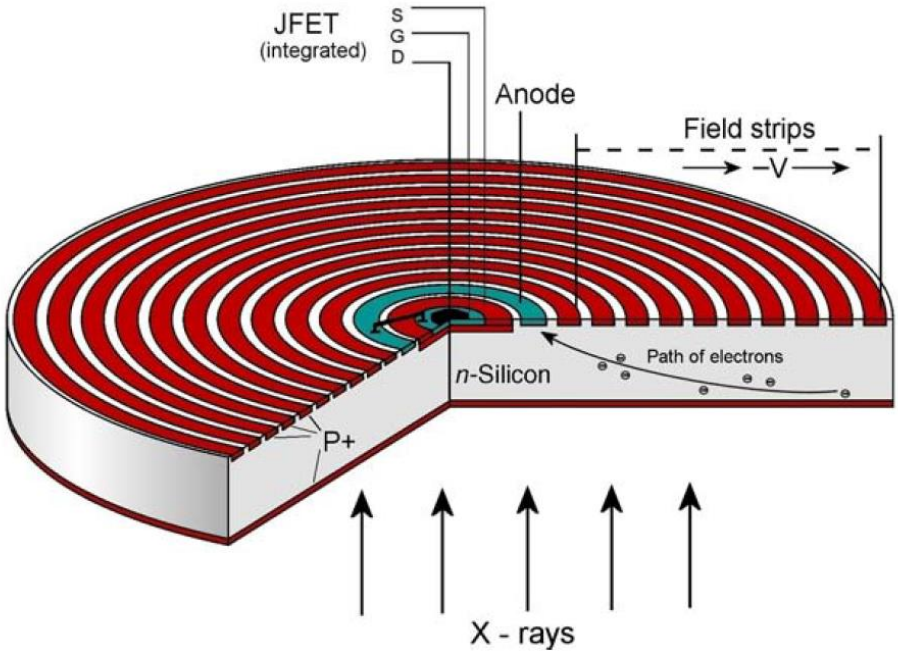

Figure 2.47. Schematic diagram of a SDD detector with n-channel Junction gate field-electric transistor (JFET), the transistor gate is connected to the anode ring by a metal strip [42].

- Semiconductor acquisition signal electronics

The different charge pulses produced by the detector have to be processed by an elaborate electronic system. They are amplified, shaped, and sorted according to their amplitudes. Among all the complexity of readout detector electronics, peaking time strongly affects the resulting output pulse: it is the time required for a shaped pulse to go from the baseline to the pulse maximum. Effective noise suppression is achieved by selecting a sufficiently high peaking time (6 or 8 μs rather than 1 or 2 μs). On the other hand, the probability of a pulse overlap increases with higher peaking time. Such an overlap of two coinciding pulses leads to the registration of one pulse, also known as pile-up effect. It can be avoided by a device called *pulse-pileup rejector* at least in those cases when the two pulses are not exactly coincident in time but arrive at least 1 μs apart [42].

- Spectrum obtained with semiconductor detectors

The resulting spectra (energy deposited) thus show "full energy peaks", or more simply, peaks, corresponding to the absorption of the full incident energy and background corresponding to partial energy deposition (mainly scattering in or outside the detector, bremmstrahlung, etc.). The peaks contain the information of interest: their position depends on the incident energy, i.e. identification of the element if fluorescence X-rays are studied, and their intensities are roughly proportional to the element concentration. Another particular phenomena called escape peak arises when the incident photons are sufficiently high that induce X-ray fluorescence radiation of the detector atoms (e.g. Si atoms). As a result, emitted fluorescence radiation from the detector atoms (mostly Kα or Kβ photon) can also escape from the sensor creating discontinuities in the detector efficiency. The residual energy shows up as an individual photon related to difference between the incident photon energy (E) and the $E_{K\alpha}$ or $E_{k\beta}$ from detector atoms. Such "packages" of energy or "photons" appear as a separate peak in the spectrum [42].

- Detector efficiency

The detector efficiency depends on the incident energy, corresponding to the probability that an incident photon deposits all its energy in the semi-conductor detector. The intrinsic detector efficiency (independent on the detection solid angle) can be expressed in first approximation as the probability of transmission of the incident energy through the detector window (W) and dead layer (D) and the probability of total absorption in the semi-conductor crystal (C):

$$\varepsilon = e^{-(\mu_W \cdot x_W + \mu_D \cdot x_D)} (1 - e^{-\mu_C \cdot x_C}) \qquad \text{(eq. 2.85)}$$

μ_i and x_i are respectively the linear attenuation coefficient and the thickness of material *i*.

The detector efficiency can be experimentally determined using radioactive standard sources, or via detailed detector characterization, as shown in Fig.2.48 [44, 45].

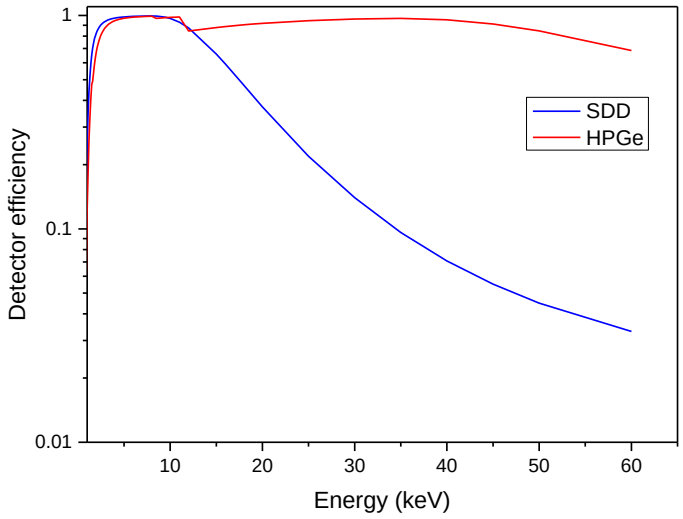

Figure 2.48. Detector efficiency of Silicon Drift Detector and High Purity Germanium detector,

- Scintillation Counter (SC) Detector

A scintillation counter (SC) is one of the most common X-ray photon counters because of ease of handling, low noise characteristic and high counting rate. The SC consists of a scintillator and a photomultiplier, as illustrated in Fig. 2.49. When the X-ray penetrates into the scintillator, it produces a light pulse of around 410 nm for the NaI(Tl) (sodium iodide crystal doped with thallium 0.1 mol%), the most employed scintillator. The intensity of the light pulse is proportional to the incoming X-ray photon energy. Owing to the photomultiplier optically connected to the scintillator, the light pulse is then converted to electric pulse, which height is proportional to the X-ray photon energy. SC is employed for X-ray radiation above 4 keV due to low energy resolution in the soft energy range [42].

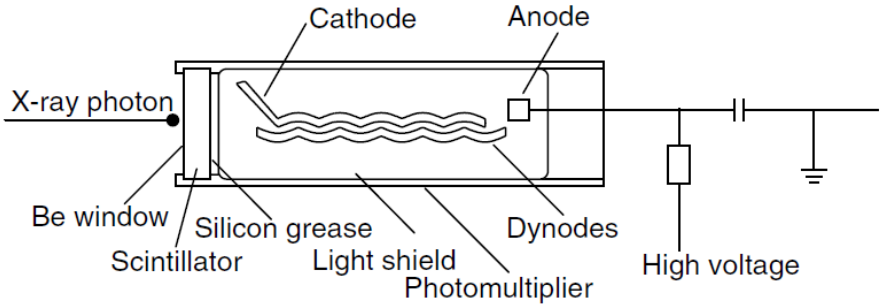

Figure 2.49. Structure of scintillation counter.

- Gas proportional counter

The gas proportional counter consists of a gas chamber filled with noble gas and a center wire under high positive voltage, as illustrated in Fig. 2.50. The incoming X-ray photon ionizes a gas atom generating cation and electron moving toward the body (cathode) and the center wire, respectively. The electrons induce an avalanche effect, and a current pulse is formed which is proportional to the energy of the incident photons. The gas proportional counters are intended for 100 eV to 20 keV energy range.

If the transmission rate of the window is critical to detecting efficiency in low energy region, thin (less than 1 μm) polymer film can be employed as an incident window. Nonetheless, inevitable gas leakage from such a film requires constant gas flow into the chamber (flow proportional counter-F-PC).

The most common gas for F-PC is Ar+10% CH_4 (called P-10 gas). In the case of energy range above 1 keV, one can use a sealed proportional counter (S-PC). It has a window of beryllium foil, which has sufficient transmission rate and practically no gas leakage. The detecting efficiency in this region depends on the absorption of the gas and the window transmission rate [42].

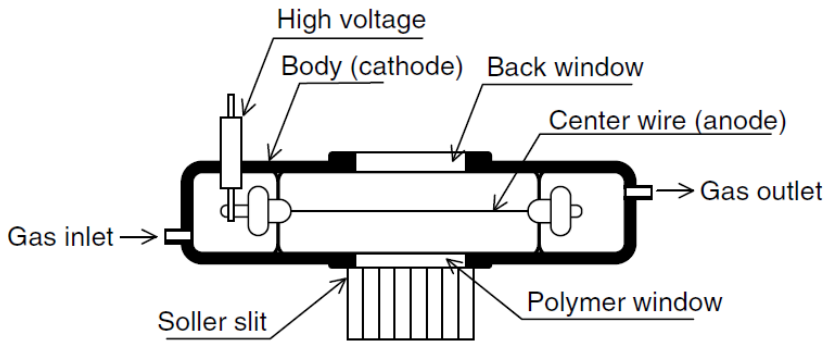

Figure 2.50. Structure of gas-flow proportional counter.

2.6.3. XPS instrumentation

The basic components of an XPS spectrometer consists of chamber linked to a pumping system for Ultra high Vacuum (UHV, ~10^{-9} mbar), X-ray source, sample handler, electron analyzer and detector system, as illustrated in Fig. 2.51. Others components such as source filters, slits, collimators, focusing optics and lens are also present for proper and reliable measurements.

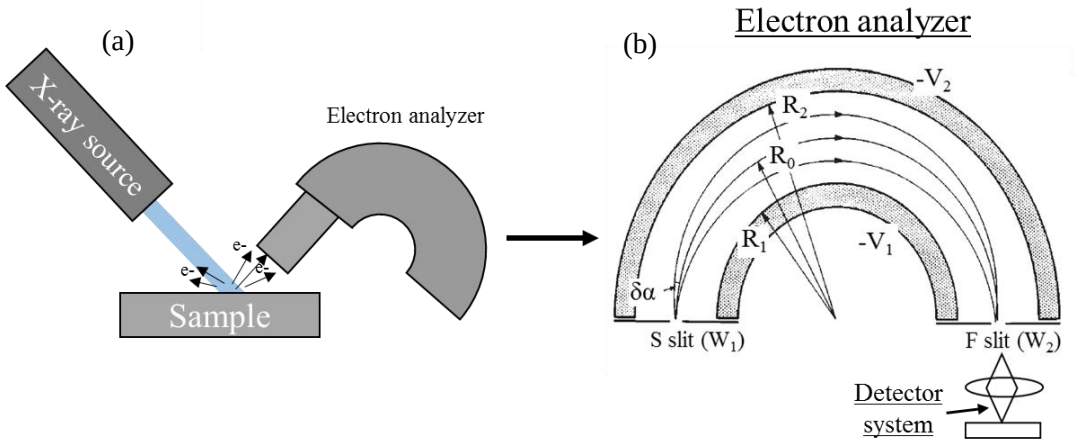

Figure 2.51. Schematic working principle of a XPS tool (right), electron analyzer for spectra acquisition.

2.6.4. Electron analyzer and detectors

The electron energy analyzer measures the energy distribution of electrons emitted from the sample (i.e. the relation between intensity and kinetic energy). The most common analyzer in XPS instruments is the hemispherical analyzer (CHA), also referred as spherical sector analyzer.

The essential aspects of the CHA are depicted in Fig. 2.51.b. The two concentric hemispheres, radii R_1 and R_2, have a mean equipotential surface between them of radius R_0. Ideally $R_0=(R_1 + R_2)/2$. Potentials $– V_1$ and $–V_2$ are applied to the hemispheres as shown with $V_2 > V_1$. If electrons of energy E_0 are injected at S tangentially to the equipotential surface they will be carried to a focus at F, regardless of the plane of their circular trajectory, according to:

$$e\Delta V = e(V_2 - V_1) = E_0\left(\frac{R_2}{R_1} - \frac{R_1}{R_2}\right) \quad \text{(eq. 2.86)}$$

For electrons injected at an angle α to the correct tangential direction and with an energy $E>E_0$ under the same deflection potential (ΔV) conditions, the shift away from F along the radius R_0 (ΔR) is given by:

$$\Delta R = 2R_0\left[\frac{E-E_0}{E_0-(\delta\alpha)^2}\right] \quad \text{(eq. 2.87)}$$

from which it is possible to derive an expression for the energy resolution (ΔE):

$$\frac{\Delta E}{E_0} = \frac{W_1+W_2}{2R_0} + (\delta\alpha)^2 \quad \text{(eq. 2.88)}$$

where W_1 and W_2 are the entrance and exit slit widths usually $(W_1=W_2=W)$. From Fig. 2.51.b, we can easily see that slit width and entrance angle (defined as the half-angle, a radians) have an impact on the energy resolution (eq. 2.88) as well as intensity, while the relative values of the slit and angular factors influence the peak shape. Then, the usual arrangement is to design the analyzer as $\alpha^2<W/2R_0$ leading to an approximate expression for relative resolution:

$$\frac{\Delta E}{E_0} \sim \frac{W}{2R_0} \quad \text{(eq. 2.89)}$$

Since the analyzer dimensions have fixed values, it is clear from eq. 2.86 that when increasing the deflection voltage (ΔV), electrons of progressive higher energy are focused at F. The measurement of electron intensity as the energy range is scanned yields the photoelectron spectra [26].

In reality, an input (or transfer) lens is employed primarily to transport electrons from the sample to the analyzer so that an image of the analyzed area is projected onto the analyzer entrance slit. This allows the sample to be conveniently placed away from the analyzer [26].

The photoelectrons ejected from the sample are not analyzed at their initial energy but also retarded before entering into the analyzer. It can be obtained, for example, by applying to two closely spaced meshes. Retardation can be performed in two ways. The first one is the electrons are retarded to the same energy (so-called constant analyzer energy, CAE, mode), second one is they are retarded to a certain fraction of their original energy (constant retard ratio, CRR, mode) [26].

- Detectors

The simplest detector system is a single channel electron multiplier (channeltron) placed at F in Fig. 2.51.b. This is a coiled tube of semiconducting glass connected to a cone of about 1 cm diameter at the open end (the shape is shown in Fig. 2.52), which provides single electron counting. Initially the amplified and discriminated pulses were fed to a rate-meter, with intensity measured in counts/s [26]. Nowadays, the pulses are acquired by a digital system and the intensities are generally displayed as counts/channel. Channeltrons run into saturation in the region of 10^5-10^6 counts/s and have a dark count rate of only 1-2 counts/min [26].

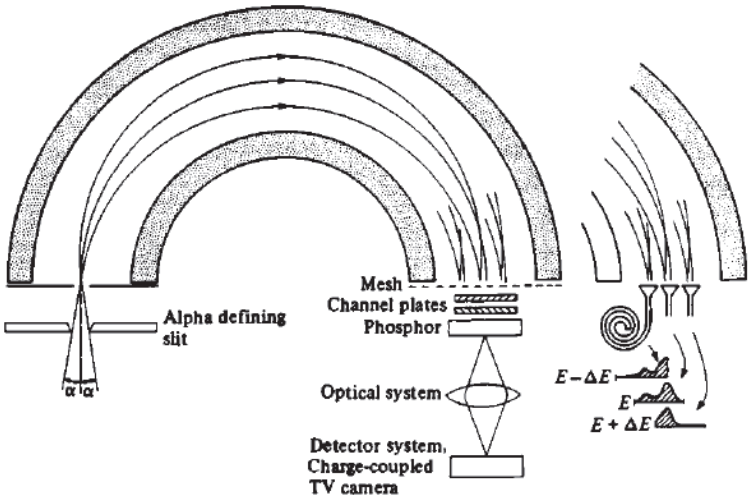

Figure 2.52. Detector system for hemispherical analyzer.

Another type of detector widely employed for CHA analyzers is the multi-detector schemes. In these type of detectors, the transmitted electrons are dispersed in energy across the analyzer exit plane by $2R_0/E_0$ mm.eV^{-1} (E_0 is the pass energy). In this case, the exit slit and detector are replaced by a series of detectors and equivalent slits along the dispersion direction, leading to a huge advantage by parallel acquisition. Two approaches can be considered to achieve this advantage, either by the increase of the number of channeltrons, or by the use of position sensitive detector (PSD), as illustrated in Fig.2.52 [26].

The exit slit can be replaced by a pair of microchannel plates consisting of an array of channel multipliers a few tens of microns in diameter fused into a thin disc. The exiting electrons can registered (as function of position) by converting them into light pulses, and detected a charge couple detector (CCD) camera (Hicks *et al*, 1980), as shown in Fig. 2.52 [26].

2.7. X-Ray instruments employed in this work

- In-line High-resolution WDXRF spectrometry tool

The WDXRF tool employed in this work is the sequential spectrometer AZX 400 from Rigaku (Fig. 2.53). It is R&D/industrial tool handling 200/300 mm wafers as well as small targets and samples. It operates under high vacuum (10^{-5} Pa). It is equipped with a 4 kW polychromatic Rh-tube, and can probe elements starting from Be ($Z \geq 4$). Its goniometer containing 10 crystals make it possible to quantify light elements (i.e. C, N O) with high spectral resolution (5 eV). The quantitative analysis can be performed by empirical method as well as fundamental parameters (available pure metals and embedded sensitive library). The photons can be acquired either by a scintillation counter (SC) or gas proportional counter (PC). The beam-diameter ranges from 0.5 – 30 mm and the probed depth from 1 nm to mm.

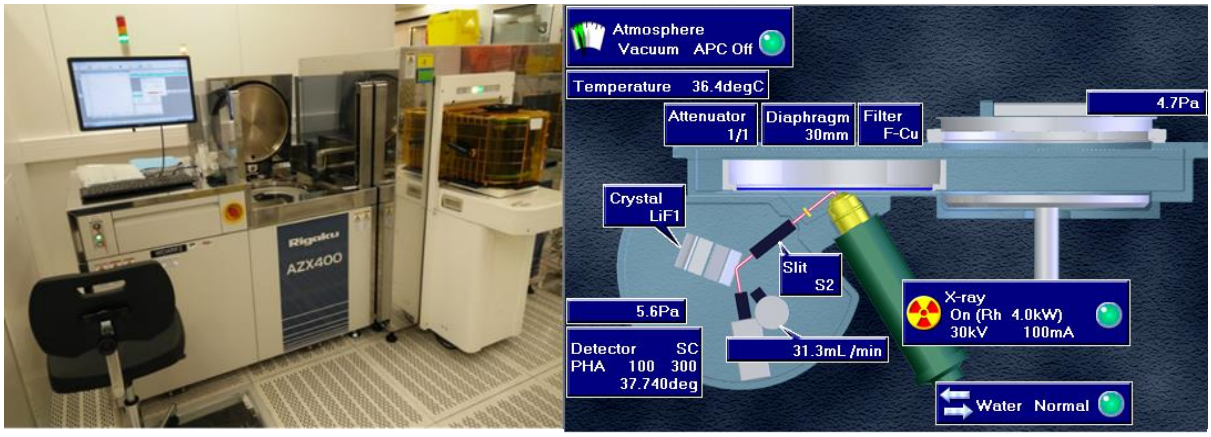

Figure 2.53. WDXRF tool available at CEA-LETI.

- Multipurpose diffractometer RIGAKU SmartLab® (GIXRF-XRR lab-tool)

This laboratory equipment is also available at CEA-LETI. It is a fully automated system with five-axis high resolution goniometer for multi-purpose analysis operating under atmospheric pressure (Fig. 2.54). Hence, it can be equipped with a 9 kW rotating Cu or Mo anode generator. The X-Ray Reflectivity are measured by a Scintillation counter (SC) detector with count-rates from 0.1 to several 100 000 s^{-1} after counting-loss correction. The XRR measurements are recorded in θ/θ configuration. While the XRF signal are acquired by a Silicon Drift Detector (SDD) Hitachi Vortex 920EX which was mounted in a customized set-up provided by RIGAKU. The SDD detector was placed at 90° from the sample surface from the incident beam direction, at 10 mm from the sample.

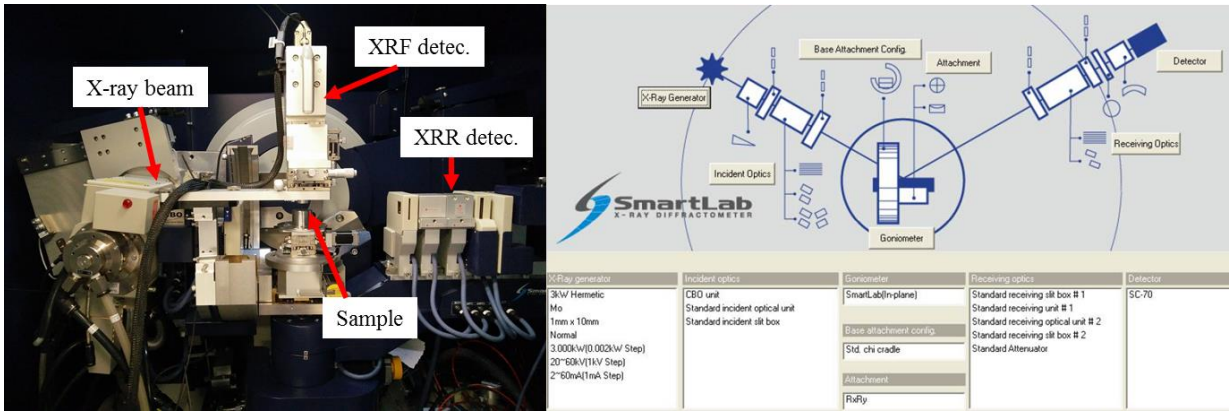

Figure 2.54. Diffractrometer with GIXRF state-of-art functionality available at CEA-LETI.

- Multipurpose Analyze chamber (GIXRF-XRR synchrotron tool)

This state-of-art tool was developed and built by collaboration among the Laboratoire National Henri Becquerel (CEA-LNHB), PTB (National Metrology Institute of Germany) and Technical University of Berlin. It is a seven-axis manipulator (4 translations 3 rotations) and operates at 10^{-6} Pa vacuum [45], see Fig. 2.55. This tool is primarily designed for XRF, Total reflection-XRF and combined GIXRF-XRF measurements, but can be upgraded for Grazing-Exit XRF. Furthermore, it can perform analysis under high temperatures by means of a dedicated sample holder with a heating system (allowing to heat samples up to 300°C). The XRR measurements are acquired by a photo-diode in a θ/2θ

configuration, while the XRF signals are recorded by a high-purity germanium (HPGe) from Oxford instruments, or a Silicon-Drift Detector from Amptek. The XRF detector is placed at 90° from the sample surface, at variable distance according to measurement conditions. This tool operates at the Metrology beamline at the SOLEIL synchrotron facility (Saclay, France) where it can be mounted at the hard X-rays branch (3-40 keV) as well as at the soft X-rays branch (30eV – 1.9 keV). In both branches, the synchrotron beam is monochromatized by a Si-double crystal or a plane grating and re-shaped in 300x300 µm (horizontal x vertical) through two set of slits which also limit its divergence to a few tenths of µrad

The same tool is also available at the Fluorescence beamline from the ELETTRA synchrotron (Trieste, Italy). Some differences arises compared to LNHB tool, the XRF detector is a SDD from Bruker placed 90° from the sample surface with fixed distance to the sample of 10 mm. The incoming beam covers 2-14 keV energy range, before interacting with the sample it is monochromatized by double-Si crystal and re-shaped to 250x100 µm (horizontal x vertical) through exit slits, resulting in 0.15 mrad divergence. This chamber also operates at 10^{-6} Pa vacuum, but has no dedicated sample holder with a heating system. Table 2.3 summarized the main features of both irradiation chamber as well as the RIGAKU SmartLab for GIXRF-XRR combined analysis.

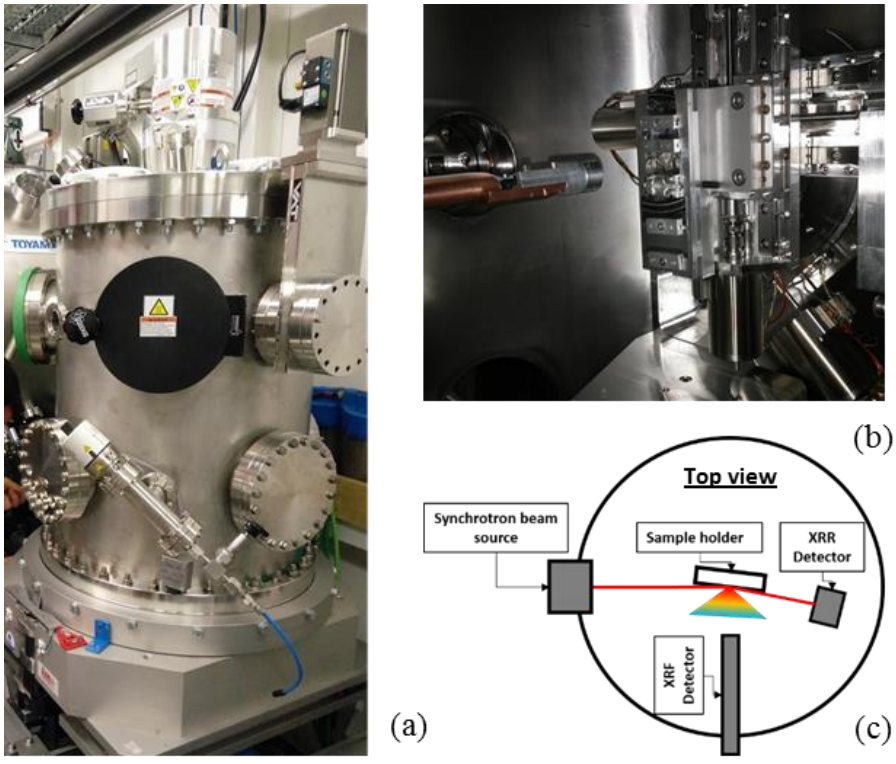

Figure 2.55. Irradiation chamber for GIXRF-XRR synchrotron measurements performed in this work.

Table 2.3. Main features of GIXRF-XRR tools employed in this work.

Parameter	SmartLab®	SOLEIL Synchrotron	ELETTRA Synchrotron
Energy range (keV)	Cu-Ka or Mo-Ka	3-40 keV or 30-1900eV	2-14 keV
Beam width (µm)	30 um	300	250
Beam Divergence (mrad)	0.2	0.012	0.15
Distance sample to XRF detector (mm)	10	100	10
Detected zone, Ld (mm)	7.0	1-40	0.8
XRF detector	SDD	HPGe	SDD
Pressure (Pa)	Atmospheric	10^{-6}	10^{-6}

- In-line XPS and ARXPS tool

The XPS equipment employed in this work is the in-line tool ThetaProbe Theta300 from ThermoFischer (Fig 2.56). It is able to handle 300 mm wafers and perform *quasi in-situ* analysis through vacuum carrier setup system. The tool is equipped with micro-focused monochromated Al-Kα X-ray source with beam spot ranging from 15 to 400 µm diameter over the sample surface, hence able to probe blanket wafers as well as product wafers. It also come with low-energy electron/ion flood gun for charge neutralization and an argon ion gun for sample cleaning and sputtering-based depth profiling. A CCD camera for sample viewing is perpendicular to the 5-axis sample stage. The electron analyzer is a double-focusing full 180° spherical sector that collects the ejected electron by an electrostatic lens having a large angular acceptance (60°), the radian lens. The axis of the lens is 50° from the sample normal and so electrons are collected over the range 20 to 80°. This means that multiple angle-resolved XPS spectra can be acquired in parallel and without tilting the sample. All components are inside a spherical ultra-high vacuum (10^{-9} mbar) chamber.

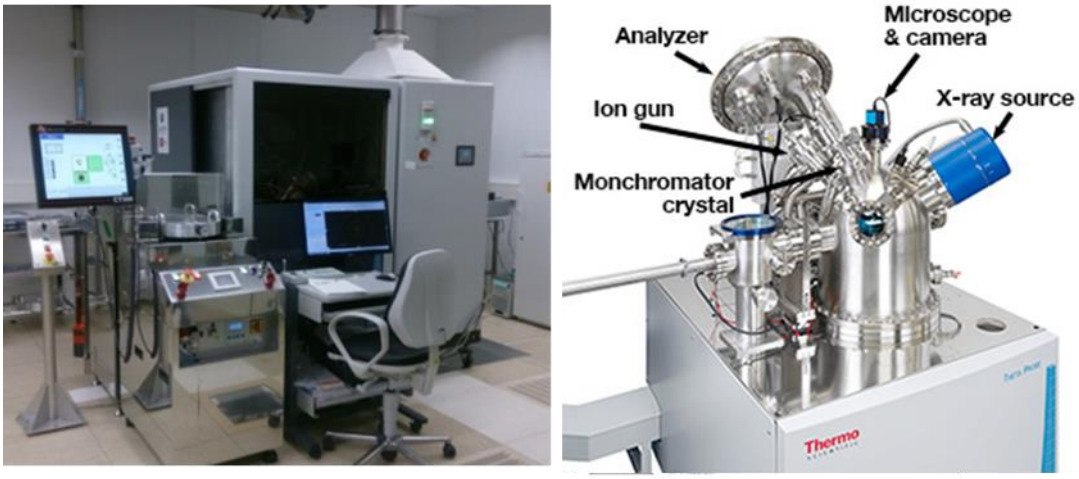

Figure 2.56. XPS tool available at CEA-LETI, it can also works with the parallel ARXPS functionality.

2.8. Conclusions

X-ray techniques are non-destructive methods very powerful to probe thin and ultra-thin layered-materials. The techniques are suitable to the development of new chalcogenide materials for next technology generations. Therefore, the process monitoring and production development of new chalcogenide materials requires metrology techniques to cover large range of chemical composition and probed depth with high spatial and in-depth resolution. Hence, in this PhD we developed adapted protocols based on three advanced X-ray techniques: Wavelength Dispersive X-ray Fluorescence (WDXRF), X-Ray Photoelectron Spectroscopy (XPS) and the combination of Grazing-Incidence X-ray Fluorescence with X-ray Reflectometry. The main objectives of the protocols developed here are the following:

- Surface/interfaces protocols:
    - Develop an in-line procedure to evaluate oxidation effects based on Ge-Sb-Te films through *quasi-in-situ* XPS measurements. This approach not only allows us to evaluate the impact of queue-time in the process flow on the surface of the chalcogenide layers but also to determine the composition-dependent chemical states in thin chalcogenide materials;
    - Assess some capping layers (Ta, SiN and C) deposited *in-situ*, not only for their efficiency to protect the chalcogenide material against ageing (oxidation), but also evaluate their interface effects such as inter-diffusion into the chalcogenide films.
- Chemical quantification protocols:
    - Develop in-line routine for chemical quantification of thin and ultra-thin Te-based chalcogenide films for blanket and product wafers. Combine in-line WDXRF and XPS in order to determine and improve the accuracy of our protocol;
    - Build a method to quantify nitrogen doping-level in Ge-Sb-Te films by WDXRF by taking in account the unavailability of nitrogen standards and the substantial influence of the matrix effects;
    - Elaborate an approach to determine the WDXRF accuracy to quantify S-based films considering no pure sulfur standard exists for this technique. combine XPS and WDXRF to probe ultrathin 2D MoS_2, compare the deduced composition with values measured at the German National Metrology Institute (PTB) using reference-free XRF.; Demonstrate the benefit of the combination of XPS and WDXRF for the development and the monitoring of 2D disulfides processes (MoS_2, WS_2).
- Elementary depth profiles protocols:
    - Demonstrate the influence of experimental conditions and instrumental function on the ability of combined GIXRF-XRR analysis to accurately probe chemical depth-profiles in Te-based stacks ;

- Demonstrate that the sensitivity of GIXRF/XRR analysis to small variation in the in-depth chemical distribution can be significantly improved by fine tuning the profile of the X-ray standing wave field by the use of multilayer substrate (Mo/Si)*40;
- Develop a method to evaluate the first deposition steps of GeTe and $Ge_2Sb_2Te_5$ sputtered films through angle-resolved XPS.

2.9. References

[1] A. Einstein, "On a heuristic point of view concerning the production and transformation of light," *Ann. Phys.*, pp. 1–18, 1905.
[2] M. Berger, "XCOM: photon cross sections database," *http://www.nist.gov/pml/data/xcom/index.cfm*, 2010.
[3] M. O. Krause, "Atomic radiative and radiationless yields for K and L shells," *J. Phys. Chem. Ref. Data*, vol. 8, no. 2, pp. 307–327, Apr. 1979.
[4] J. Sherman, "The correlation between fluorescent X-ray intensity and chemical composition," in *Symposium on Fluorescent X-ray Spectrographic Analysis*, 1954.
[5] J. Sherman, "The theoretical derivation of fluorescent X-ray intensities from mixtures," *Spectrochim. Acta*, vol. 7, pp. 283–306, Jan. 1955.
[6] T. Shiraiwa and N. Fujino, "Theoretical Calculation of Fluorescent X-Ray Intensities in Fluorescent X-Ray Spectrochemical Analysis.," *Jpn. J. Appl. Phys.*, vol. 5, no. 10, p. 886, Oct. 1966.
[7] W. BAMBYNEK *et al.*, "X-Ray Fluorescence Yields, Auger, and Coster-Kronig Transition Probabilities," *Rev. Mod. Phys.*, vol. 44, no. 4, pp. 716–813, Oct. 1972.
[8] U. Weisbrod, R. Gutschke, J. Knoth, and H. Schwenke, "X-ray induced fluorescence spectrometry at grazing incidence for quantitative surface and layer analysis," *Fresenius J. Anal. Chem.*, vol. 341, no. 1–2, pp. 83–86, Jan. 1991.
[9] A. H. Compton and S. K. Allison, "X-rays in Theory and Experiment," 1935.
[10] M. Bedzyk, *XSW at the total reflection condition, in*. in press, 2009.
[11] R. S. Becker, J. A. Golovchenko, and J. R. Patel, "X-Ray Evanescent-Wave Absorption and Emission," *Phys. Rev. Lett.*, vol. 50, no. 3, pp. 153–156, Jan. 1983.
[12] D. K. de Boer, "Glancing-incidence x-ray fluorescence of layered materials," *Phys. Rev. B*, vol. 44, no. 2, p. 498, 1991.
[13] L. G. Parratt, "Surface studies of solids by total reflection of X-rays," *Phys. Rev.*, vol. 95, no. 2, p. 359, 1954.
[14] M. Born and E. Wolf, *Principles of optics: electromagnetic theory of propagation, interference and diffraction of light*. Elsevier, 2013.
[15] W. Li *et al.*, "Geometrical factor correction in grazing incident x-ray fluorescence experiment," *Rev. Sci. Instrum.*, vol. 83, no. 5, p. 053114, 2012.
[16] "Caby B. Développement de l'analyse combinée par Réflectométrie de rayons X (XRR) et Fluorescence des rayons X en Incidence Rasante (GIXRF) pour des applications micro et nano-électroniques (Doctoral dissertation) 2015. Retrieved from http://www.ecole.ensicaen.fr/~chateign/pdf/Caby_Berenger_PhD.pdf." .
[17] "Caby B. et al. Comparison of four data analysis software for combined X-ray reflectivity and grazing incidence X-ray fluorescence measurements. 16th International Conference on Total Reflection X-ray Fluorescence Analysis and Related Methods (TXRF) 2015." .
[18] D. Ingerle, G. Pepponi, F. Meirer, P. Wobrauschek, and C. Streli, "JGIXA — A software package for the calculation and fitting of grazing incidence X-ray fluorescence and X-ray reflectivity data for the characterization of nanometer-layers and ultra-shallow-implants," *Spectrochim. Acta Part B At. Spectrosc.*, vol. 118, pp. 20–28, Apr. 2016.
[19] V. Solé, E. Papillon, M. Cotte, P. Walter, and J. Susini, "A multiplatform code for the analysis of energy-dispersive X-ray fluorescence spectra," *Spectrochim. Acta Part B At. Spectrosc.*, vol. 62, no. 1, pp. 63–68, 2007.
[20] "NIST X-ray Photoelectron Spectroscopy Database, NIST Standard Reference Database Number 20, National Institute of Standards and Technology, Gaithersburg MD, 20899 (2000), doi:10.18434/T4T88K, (retrieved [July 7th 2018])." .
[21] C. Wagner, "Auger lines in x-ray photoelectron spectrometry," *Anal. Chem.*, vol. 44, no. 6, pp. 967–

973, 1972.
[22] S. Gaarenstroom and N. Winograd, “Initial and final state effects in the ESCA spectra of cadmium and silver oxides,” *J. Chem. Phys.*, vol. 67, no. 8, pp. 3500–3506, 1977.
[23] G. Moretti, “Auger parameter and Wagner plot in the characterization of chemical states by X-ray photoelectron spectroscopy: a review,” *J. Electron Spectrosc. Relat. Phenom.*, vol. 95, no. 2–3, pp. 95–144, 1998.
[24] M. C. Biesinger, L. W. Lau, A. R. Gerson, and R. S. C. Smart, “The role of the Auger parameter in XPS studies of nickel metal, halides and oxides,” *Phys. Chem. Chem. Phys.*, vol. 14, no. 7, pp. 2434–2442, 2012.
[25] D. Clark, “Handbook of X-ray and ultraviolet photoelectron spectroscopy,” *Lond. Briggs Heyden Son Ltd*, vol. 211, 1977.
[26] D. Briggs, “Practical Surface Analysis second edition Vol. 1, Auger and X-ray Photoelectron Spectroscopy,” *John Wiley Sons Ltd N. Y.*, 1990.
[27] “https://xpssimplified.com/periodictable.php.” .
[28] *Moulder, John F., et al. “Handbook of X-ray photoelectron spectroscopy: a reference book of standard spectra for identification and interpretation of XPS data; Physical Electronics: Eden Prairie, MN, 1995.” (2000): 261.* .
[29] J. Riviere, “Surface Analysis Techniques,” *Monogr. Phys. Chem. Mater. Oxf. Sci. Publ. Clarendon Press Oxf.*, 1990.
[30] S. Tougaard and C. Jansson, “Comparison of validity and consistency of methods for quantitative XPS peak analysis,” *Surf. Interface Anal.*, vol. 20, no. 13, pp. 1013–1046, 1993.
[31] J. H. Scofield, “Hartree-Slater subshell photoionization cross-sections at 1254 and 1487 eV,” *J. Electron Spectrosc. Relat. Phenom.*, vol. 8, no. 2, pp. 129–137, 1976.
[32] “Seah, M.P. (1989) in Methods of Surface Analysis, ed. Walls, M.J. (Cambridge University Press, Cambridge) p. 57.” .
[33] M. P. Seah and W. Dench, “Quantitative electron spectroscopy of surfaces: A standard data base for electron inelastic mean free paths in solids,” *Surf. Interface Anal.*, vol. 1, no. 1, pp. 2–11, 1979.
[34] M. P. Seah and W. A. Dench, “Quantitative electron spectroscopy of surfaces: A standard data base for electron inelastic mean free paths in solids,” *Surf. Interface Anal.*, vol. 1, no. 1, pp. 2–11.
[35] S. Tanuma, C. J. Powell, and D. R. Penn, “Calculations of electron inelastic mean free paths. V. Data for 14 organic compounds over the 50–2000 eV range,” *Surf. Interface Anal.*, vol. 21, no. 3, pp. 165–176, 1994.
[36] P. J. Cumpson and M. P. Seah, “Elastic scattering corrections in AES and XPS. II. Estimating attenuation lengths and conditions required for their valid use in overlayer/substrate experiments,” *Surf. Interface Anal. Int. J. Devoted Dev. Appl. Tech. Anal. Surf. Interfaces Thin Films*, vol. 25, no. 6, pp. 430–446, 1997.
[37] “Angle Resolved XPS - Thermo Fisher Scientific, application note 31014.” .
[38] G. Smith and A. Livesey, “Maximum entropy: A new approach to non-destructive deconvolution of depth profiles from angle-dependent XPS,” *Surf. Interface Anal.*, vol. 19, no. 1–12, pp. 175–180, 1992.
[39] J. Arthur *et al.*, “Linac coherent light source (LCLS) conceptual design report,” 2002.
[40] L. E. Etter, *The Science of Ionizing Radiation: Modes of Application*. CC Thomas, 1965.
[41] T. Tuohimaa, M. Otendal, and H. M. Hertz, “Phase-contrast x-ray imaging with a liquid-metal-jet-anode microfocus source,” *Appl. Phys. Lett.*, vol. 91, no. 7, p. 074104, 2007.
[42] B. Beckhoff, B. Kanngieber, N. Langhoff, R. Wedell, and H. Wolff, *Handbook of practical X-ray fluorescence analysis*. Springer Science & Business Media, 2007.
[43] M.-C. Lépy, J. Plagnard, P. Stemmler, G. Ban, L. Beck, and P. Dhez, “Si(Li) Detector Efficiency and Peak Shape Calibration in the Low-Energy Range Using Synchrotron Radiation,” *X-Ray Spectrom.*, vol. 26, no. 4, pp. 195–202.
[44] J. Plagnard, C. Bobin, and M.-C. Lépy, “Accurate efficiency calibration of a low-energy HPGe detector using a monochromatic x-ray source,” *X-Ray Spectrom.*, vol. 36, no. 3, pp. 191–198.
[45] J. Lubeck *et al.*, “A novel instrument for quantitative nanoanalytics involving complementary X-ray methodologies,” *Rev. Sci. Instrum.*, vol. 84, no. 4, p. 045106, 2013.

3. Chapter III: Surface and interfaces protocols

3.1. Introduction

As discussed in chapter I, chalcogenides properties can be scaled through thickness reduction. For example, the crystallization temperature of $Ge_2Sb_2Te_5$ films can be exponentially increased when thinned down to 10 nm and below [1]. This approach is very attractive for automotive industry where PCRAM memories are needed with high thermal stability. Nonetheless, when chalcogenides are reduced to few nanometers thick, surface and interfaces effects become predominant and should be accurately probed and mastered in order to ensure the functionality of the device.

Indeed, surface effects such as oxidation can significantly change the chemical composition at the surface, and therefore highly impact on the chalcogenide properties. Two typical approaches in the semiconductors industries consist either to employ a limited queue-time between two steps in the process flow, or to deposit a passivation layer on top of the film of interest.

The optimization of the queue-time is highly driven by the material and its composition, and require a careful investigation of the oxidation kinetics. By contrast, passivation / barrier layers act as protection against ageing of the interested film, and relax the queue-time constraints in the process flow. Nonetheless, the interface between the barrier layer and the interested layer has to be well studied to avoid diffusion effects.

When queue-time constraints are too tight to be integrated in the industrial process, or if barrier layers cannot be employed (limited efficiency or no compatibility with the process flow), one can employ vacuum carriers. The method consists to create ultra-clean and oxygen-free mini-atmosphere (10^{-2} mbar) in vacuum carriers which can be connected and disconnected from dedicated modules installed on both process and metrology tools [2]. The approach is very powerful for *quasi in-situ* process and monitoring, and can be even employed to evaluate optimized queue-time.

Therefore, in this chapter, we compare XPS strategies based on limited queue-time and vacuum carriers to characterize the evolution of the surface of thin Ge-Sb-Te based films. We report on the influence of the composition, not only on the binding states of these elementary, binary and ternary materials, but also on the oxidation kinetics. Furthermore, we studied the efficiency of different barrier layers for several Te-based films. Thin films of Ta, SiN and C deposited *in-situ* in the PVD reactor were investigated as barrier layers and demonstrated different behavior against ageing as well as interfacial diffusion.

3.2. Probing Surface effects on Ge-Sb-Te films

3.2.1. Introduction

As seen in section 1.4 of chapter I, scaling the properties of Te-based films through thickness reduction was observed by Raoux et al. [1], who observed that the reduction of the thickness of Te-based films substantially increases the crystallization temperature (specially below 10 nm), hence improving the thermal stability and data retention of PCRAM cells. Nonetheless, the use of much thinner films increases the relative importance of surface, interface of Ge-Sb-Te films and their evolution with oxidation / ageing.

Gourvest et al. [3] studied the impacts of oxidation on $Ge_2Sb_2Te_5$ and GeTe films properties by XPS and optical measurements, as depicted in Fig. 3.1. The XPS measurements revealed a significant influence of oxidation as function of air-exposure time. According to the authors, after 90 days of aging, the oxidation effects not only degraded the film surface by forming 6 nm oxide film but also induced substantial change on the film stoichiometry towards Te-rich. This serious change on the film chemistry has led to a significant reduction of the crystallization temperatures (Fig.3.1.b).

Although the remarkable work of Gouverst highlights the effects of oxidation, little information is available about composition-dependent binding states of fresh and oxidized Ge-Sb-Te films. Therefore, in this section, we develop a protocol to study the oxidation effects on Ge-Sb-Te films with several compositions: elementary Ge, Te and Sb materials, binary and ternary materials. The protocol is not only important to study the oxidation effects on Ge-Sb-Te films but also important for XPS quantification and ARPXS depth profiles.

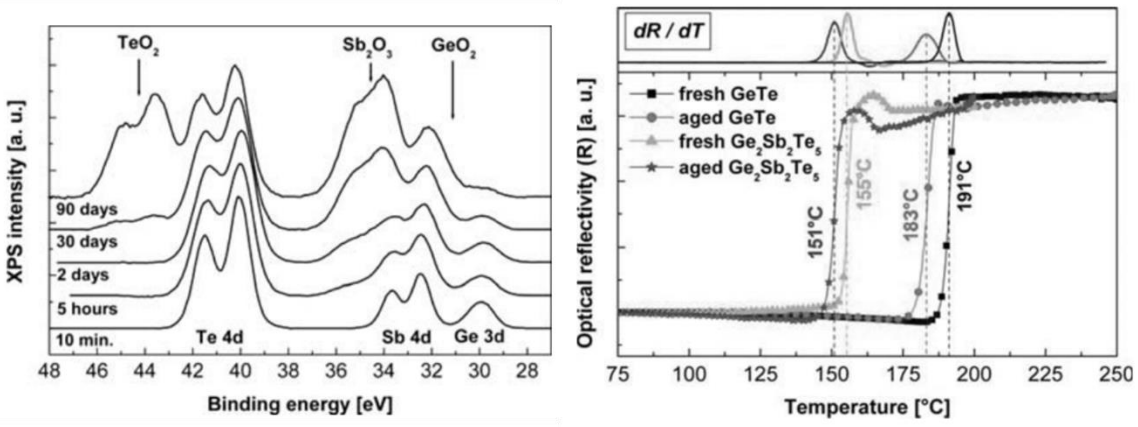

Figure 3.1. (left) XPS analysis of $Ge_2Sb_2Te_5$ film after several air exposure lapse-time, (right) evolution of $Ge_2Sb_2Te_5$ and GeTe optical reflectivity for fresh and aged samples [3].

3.2.2. Experimentation

3.2.2.1. Sample preparation

20 nm thick films were amorphously grown by PVD on 300 mm Si (001) wafers, using industrial multi-chamber PVD deposition tool Endura 300 from Applied Materials. The films were deposited in a chamber with 60 °C under 10 mTorr pressure and Argon flow of 40 sccm (standard cubic centimeter per minute). We deposited elementary (Ge, Sb and Te), and ternary ($Ge_2Sb_2Te_5$, Ge-rich GST) films from single targets (150 mm diameter). The binary films (GeTe and Sb_2Te_3) were deposited by co-sputtering from elementary targets, and we also generated binary films with significant composition variations along X and Y lateral direction by deliberately not rotating the substrate. Co-sputtering of binaries (GeTe, SbTe) without substrate rotation aimed at probing composition-dependent surface effect with significant composition variations on one-only wafer, allowing for easier control of queue time and ageing kinetics when compared with multiple samples. In order to study the surface effects due to crystallization (e.g. change of composition or different oxidation effects), crystalized Sb_2Te_3 was grown at 220 °C. Table 3.1. summarizes all the deposited films with their respective deposition parameters.

Table 3.1. Summary of deposited films, they are all 20 nm thick deposited on 300 mm Si (001) wafers.

Deposited film	***Deposition mode***	***Deposition temperature (°C)***
Ge	***Sputtering***	***60***
Sb		
Te		
GeTe	**Co-sputtering**	**60**
Sb_2Te_3		**60 and 220**
GeTe	**No rotation, deliberately for compositional gradient**	**60**
Sb_2Te_3		
$Ge_2Sb_2Te_5$	**Sputtering**	
Ge-rich GST	**Sputtering**	

3.2.2.2. Methodology to probe surface effects by XPS

In order to study the oxidation effects on the deposited films, we evaluated the surface effects with the films non-oxidized, and after 10 min and 2 months of exposure to air. The procedure to characterize the non-oxidized films by XPS consisted to employ dedicated vacuum carriers. As illustrated in Fig. 3.2, the thin layered materials are first deposited on 300 mm wafers and stored at 10^{-7} mbar ; Secondly, the wafers are picked and placed in a transfer chamber operated at 10^{-7} mbar, and then transferred to a vacuum carrier operated under dynamic vacuum (10^{-5} mbar) in which the wafers stays during 24 hours. Once the transfer is accomplished, the vacuum carrier is disconnected and keeps the wafer in a mini-oxygen free atmosphere in the 10^{-2} mbar range.

The quality of this mini-oxygen free atmosphere was evaluated by Pelissier et al. [2]. In his work, he evaluated the oxidation effects on Ge wafers maintained in the vacuum carrier (static vacuum) for several days. The absence of oxidation was confirmed, since the Ge-O component showed no variation along the storage period. Although the atmosphere inside the carrier is oxygen-free, it was observed a significant increase in the surface oxygen content attributed to carbon contamination, unavoidable even in Ultra-High-Vacuum (UHV) chambers. The carbon contamination is mainly composed of C-C bonds, but also C-O bonds from hydrocarbons.

Then, after transferring the wafer into the vacuum carrier, we bring it towards the in-line XPS tool which is connected to a dedicated pod for the wafer transfer. From there, the wafer is transferred to the XPS chamber at an ultra-high vacuum of 10^{-9} mbar.

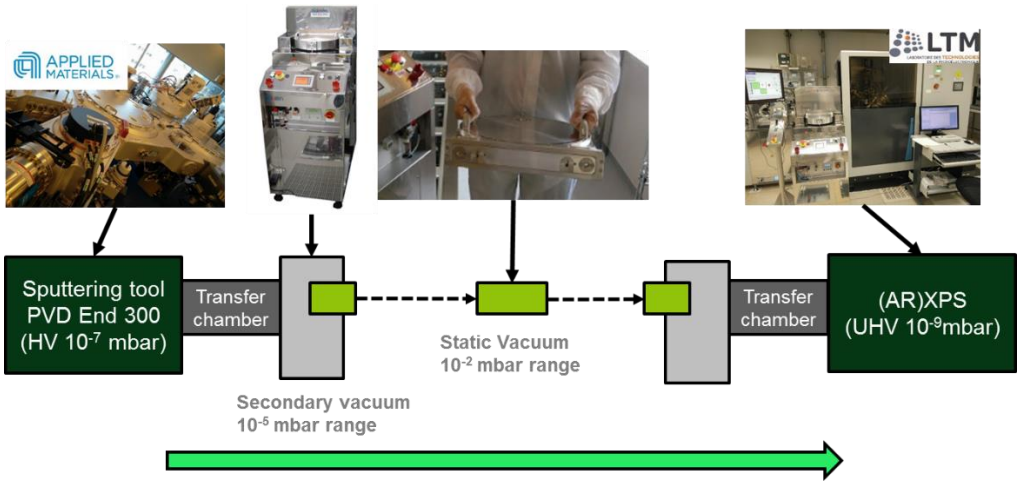

Figure 3.2. Procedure to perform *quasi-in-situ* XPS by means of vacuum carrier. The gree arrow indicates the order of steps from the deposition tool to the in-line XPS [2].

The XPS analysis of the non-oxidized and oxidized films were performed with the ThermoFischer Theta 300 spectrometer with an Al-Kα source (described in chapter II). We evaluated the surface effects by measuring high and middle energy core-levels (Ge 2p, O 1s, Sb 3d and Te 3d,) as well as low-energy core-levels (Ge 3d, Sb 4d and Te 4d) as summarized in table 3.2. The analyses were recorded at a pass energy of 40 eV, 0.05 eV step size, and 400 µm beam size. For the quantitative analysis discussed in this chapter, we determined the atomic content (at %) of elements based on standard Scofield parameters, attenuation length (λ_{AL}) from TPP-2M method [4]. The data were processed by best-model calculation using ThermoFischer Avantage software package.

Table 3.2.Binding energy of Core-levels taking C1s (284.8 eV) as reference.

Core-level	Binding energy (eV) [5]	Sampling depth ($3*\lambda_{AL}$) (nm) [4]
Ge 2p3/2	1217 – 1221	2.2
O 1s	530-533	5.0
Sb 3d5/2	528 -531	5.0
Te 3d5/2	573 – 577	5.2
Ge 3d5/2	29 – 33	7.1
Sb 4d5/2	31 – 36	
Te 4d5/2	40 – 44	

3.2.3. Results and discussions

In order to properly evaluate the effects of oxidation, we first describe the surface effects on elementary films (Ge, Sb and Te) through vacuum carrier procedure and 10 min Queue-time. We further extended the analysis to binary films, firstly evaluating the impact of oxidation on different Ge/Te and Sb/Te proportions from films deposited with no wafer rotation and 10 min air-break (e.g. air-exposure in cleanroom environment). The detailed analysis on elementary and binary films allowed to forecast the oxidation effects on $Ge_2Sb_2Te_5$, by studying the evolution of oxidation after air-break and further ageing. Lastly, we summarize the peak deconvolution (i.e. binding energies, FWHM, split, ratio, etc) from vacuum carrier analysis for further determination of sensitivity factors (SFs) and recalculation of Scofield parameters for chemical quantification and elementary depth-profiles in next chapters.

3.2.3.1. Elementary films

- Ge elementary film

Figure 3.3.a illustrates the behavior of the germanium film after transfer through vacuum carrier. We can observe that even though we employed the vacuum carrier, there is a slight oxidation on Ge$2p_{3/2}$. Although this slight surface oxidation is observable at high binding energy (Ge $2p_{3/2}$), the Ge 3d doublet component can be modeled without any introduction of oxidized states. Therefore, despite high reactivity of Ge towards oxidation, only 6.7 % of sub-oxidized germanium (GeO) is observed in the 2 nm uppermost surface (Ge $2p_{3/2}$ core-level). This very limited oxidation might be related to hydrocarbons trapped in the inner surface of the vacuum carrier.

In the case of 10 min air break, the presence of oxidation is already important, as we can see from Fig.3.3.b. Even with such a short queue-time, the high reactivity of Ge leads to formation of GeO and GeO_2 observable in the Ge $2p_{3/2}$ core-level range. On the other hand, no substantial effect of oxidation is evidenced in the Ge 3d region. From the standard Scofield parameters and the corresponding probed depth of the core-levels, the oxidation of Ge $2p_{3/2}$ corresponds to 30% (GeO + GeO_2) at 2.2 nm

depth, while Ge 3d is only 6 at% oxidized for 7 nm depth. This slight oxidation in volume might be related to the auto-passivation of germanium from its oxides (GeO_2 and GeO) [6].

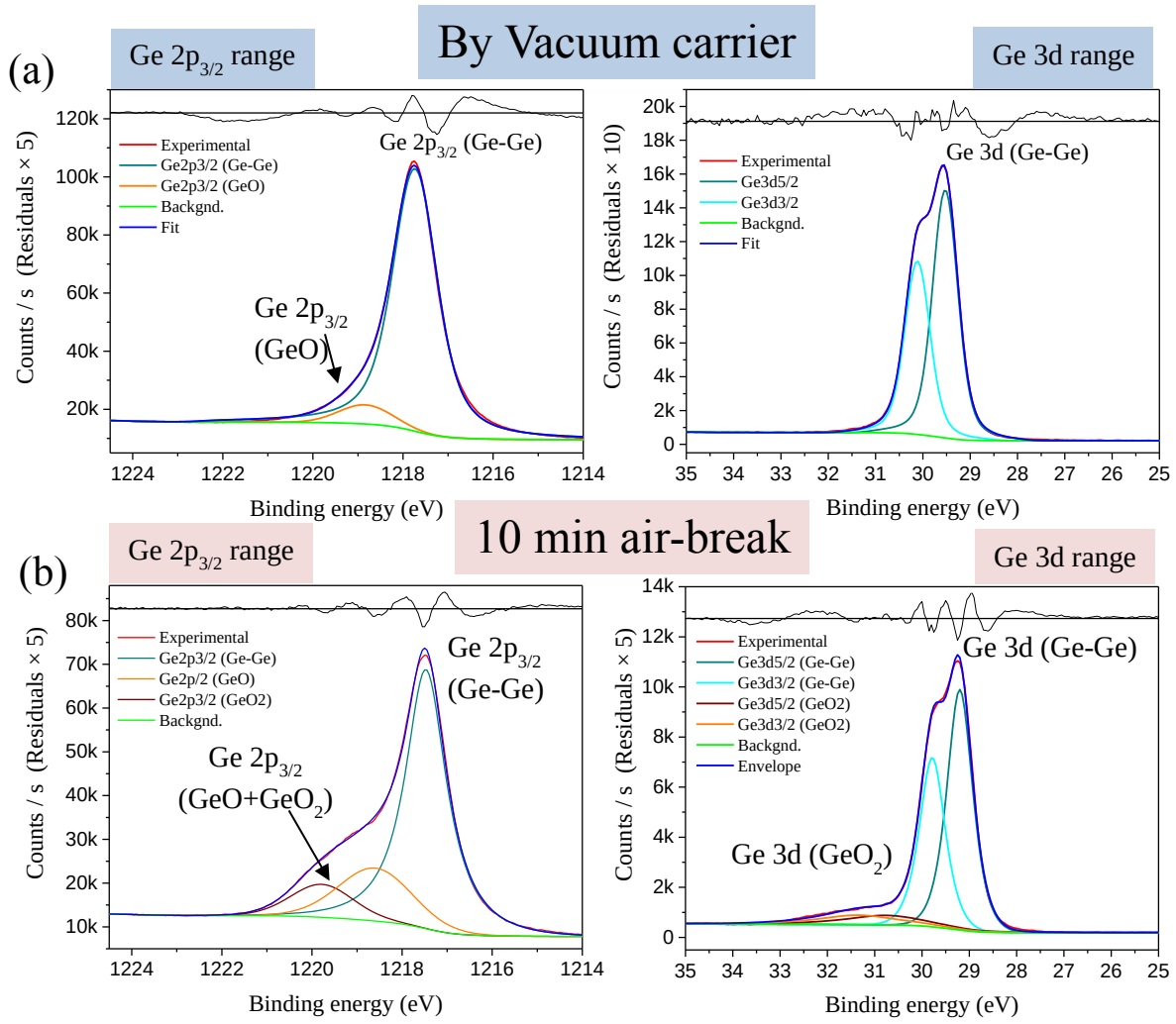

Figure 3.3. 20 nm thick Ge film, (a) by vacuum carrier (b) 10 min air-break. Energy difference and intensity ratios for Ge 3d spin orbit components were set to same values for Ge-Ge and Ge-O states.

- Sb elementary film

Antimony thin layered material features slightly different oxidation behavior from the Germanium one. As we can see in Fig.3.4.a, the Sb film analyzed from the vacuum carrier does not show any oxidation. The O1s contribution in the foot of Sb $3d_{5/2}$ component is not present on Sb $3d_{3/2}$. As O 1s includes all oxidation states (e.g. potentially C-O from carbon contamination) and since the Sb $3d_{3/2}$ shows no Sb-O contribution, we can deduce that this oxidation comes mostly from the carbon contamination (hydrocarbons).

In the case of 10 min air-break (Fig. 4b), antimony rapidly oxidized. Indeed, the high reactivity towards oxidation leads to formation of Sb_2O_3 states, observed in both Sb3d and Sb 4d region. The oxidation of antimony corresponds to 40 % in 5 nm probed depth (Sb 3d core-level range), and 30 % averaged into 7 nm depth (Sb 4d core-level). This oxidation level is much higher compared to the Ge film; the high reactivity is firstly related to the fact that the enthalpy of formation ($\Delta_f H^\circ$) to form Sb_2O_3 is much lower than the GeO_2 one, -972 kJ and -580 kJ respectively [7]. Second reason is that antimony oxides do not seem to behave as auto-passivation layers as Ge oxides do.

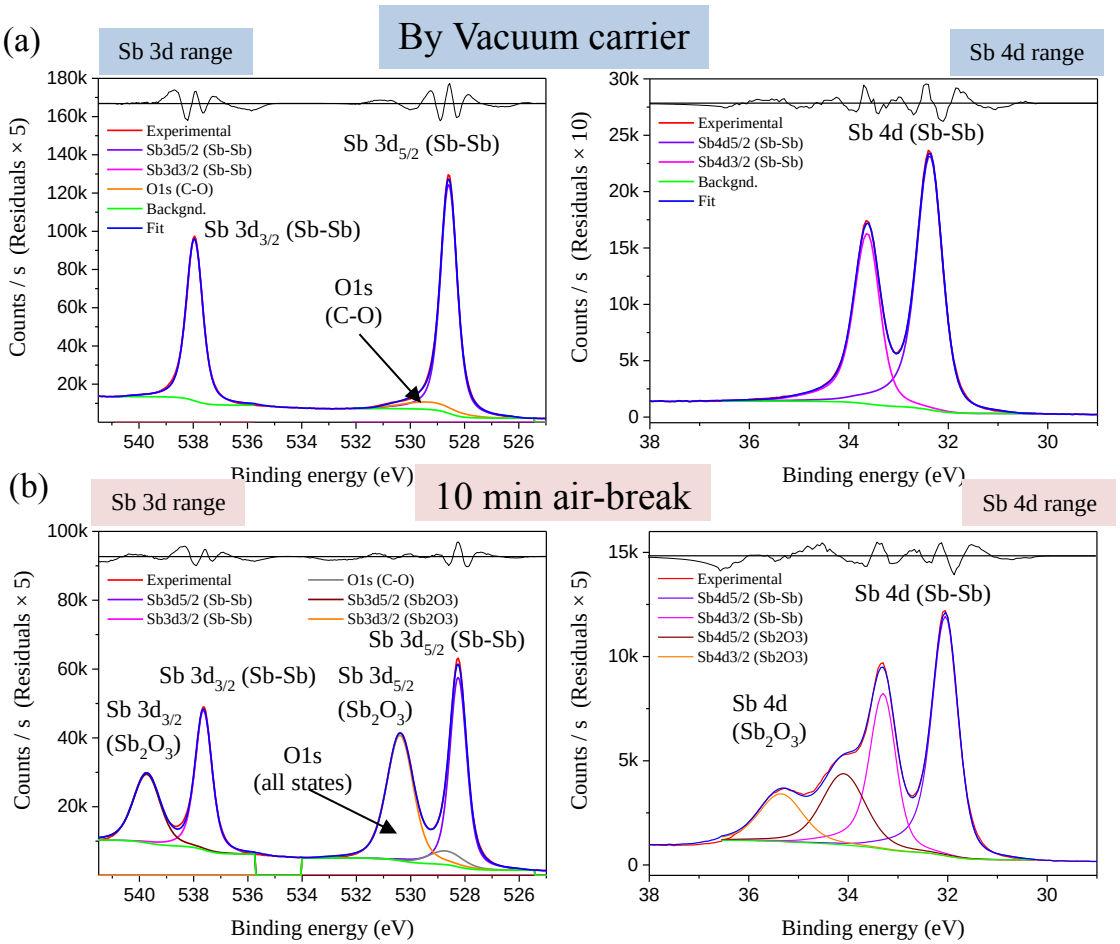

Figure 3.4. 20 nm thick Sb film (a) vacuum carrier (b) 10 min air-break Energy difference and intensity ratios for Sb 3d and Sb 4d spin orbit components were set to same values for Sb-Sb and Sb-O states.

- Te elementary film

The evolution of tellurium films is significantly different from Ge and Sb. In the evaluated experimental conditions (vacuum carrier and 10 min air break), tellurium did not oxidize at all. From Fig. 3.5.a, we can see that measurements through the vacuum carrier do not show any evidence of oxidation states neither for Te3d nor for Te 4d region. This same behavior is observed after 10 min air-break. Indeed, the enthalpy of formation $\Delta_f H^\circ$ Te→ TeO_2 is -322.6 kJ [7], hence the oxidation takes place less spontaneously than for Ge or Sb species. Therefore 10 min Queue-time is completely tolerable.

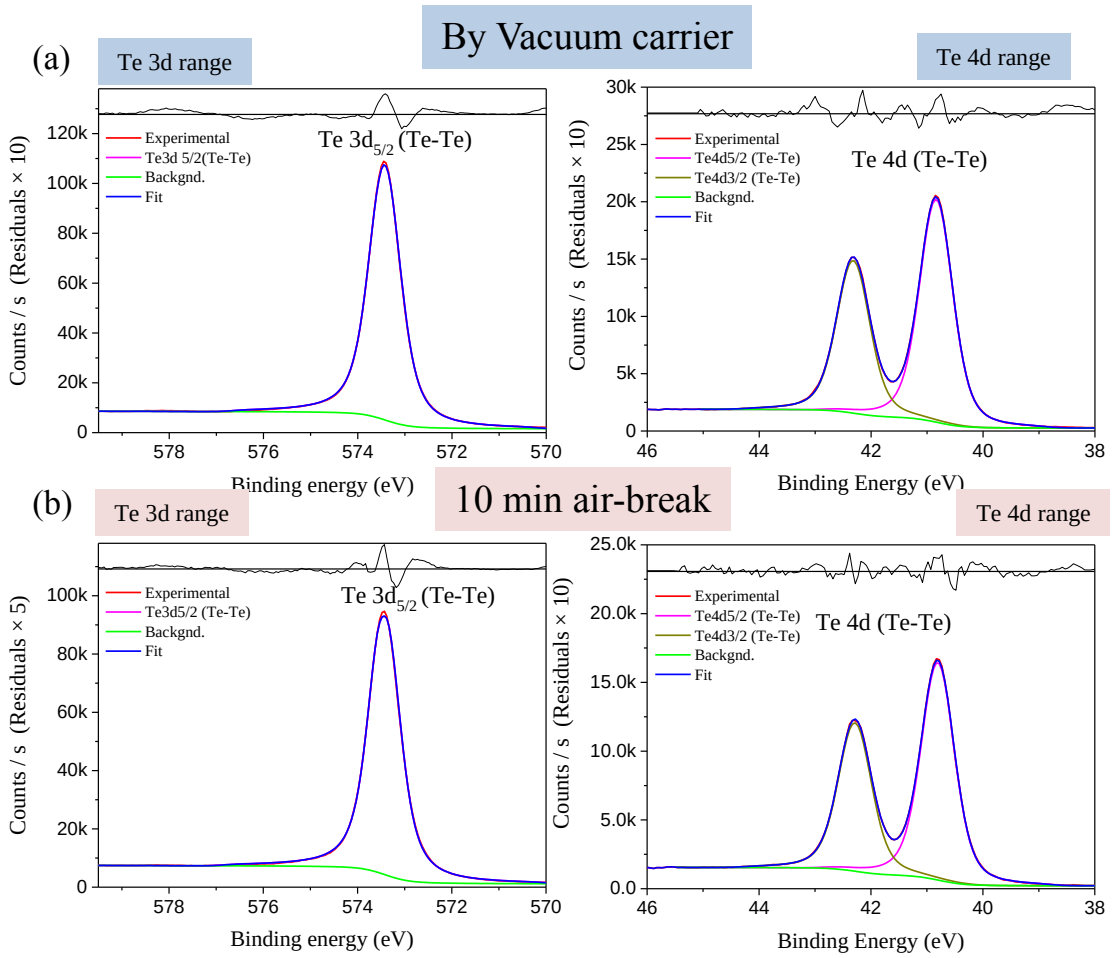

Figure 3.5. 20 nm thick Te film (a) by vacuum carrier (b) 10 min air-break.

3.2.3.2. Binary (GeTe, SbTe) films

Following the evaluation of the binding states of elementary Ge, Te and Sb thin material using *quasi in-situ* XPS analysis or controlled queue-time (10 minutes of air break), we hereafter report on the characterization of Te-based binary compounds (GeTe and SbTe) with different compositions, using similar protocol.

- GeTe films

We have shown that 10 min air-break is tolerable for tellurium films; we now evaluate the influence of tellurium content in GeTe on the oxidation of these binary materials. We used co-sputtering of individual Ge and Te PVD targets without substrate rotation so as to probe composition-dependent surface effect in GeTe films with significant composition variations on one-only wafer, allowing for easy control of queue time. As an illustration, we compared Te-rich GeTe film (point A) and Ge-rich GeTe layer (point B). The analysis took place after 10 min air-break. The different elemental proportions translate in Ge/Te ratios equal to 0.33 for point A and 2.22 for point B.

Figure 3.6.a shows the XPS analysis from the Te-rich GeTe film. Both Ge $2p_{3/2}$ and Te $3d_{5/2}$ core levels show a lack of oxidation of Te-rich GeTe material, whereas similar conclusions can be drawn

when Ge/Te=1 (Fig. 3.6.b). However, when increasing the Ge content, this un-reactivity is not observed anymore, and slight impact of oxidation is observed. As illustrated in Fig. 3.6.c, both Ge-O and Ge-Te binding states are present in the Ge $2p_{3/2}$ region, and the weak Ge-O signal results in ~ 5 at % oxidation for ~2 nm probed depth. Tellurium, on the other hand, shows no evidence of oxidation state as we can see from the Te 3d core-level. Hence, the increase of germanium on GeTe matrix only induces its own oxidation in the form of GeO (mostly at the top surface, ~ 2 nm probed depth).

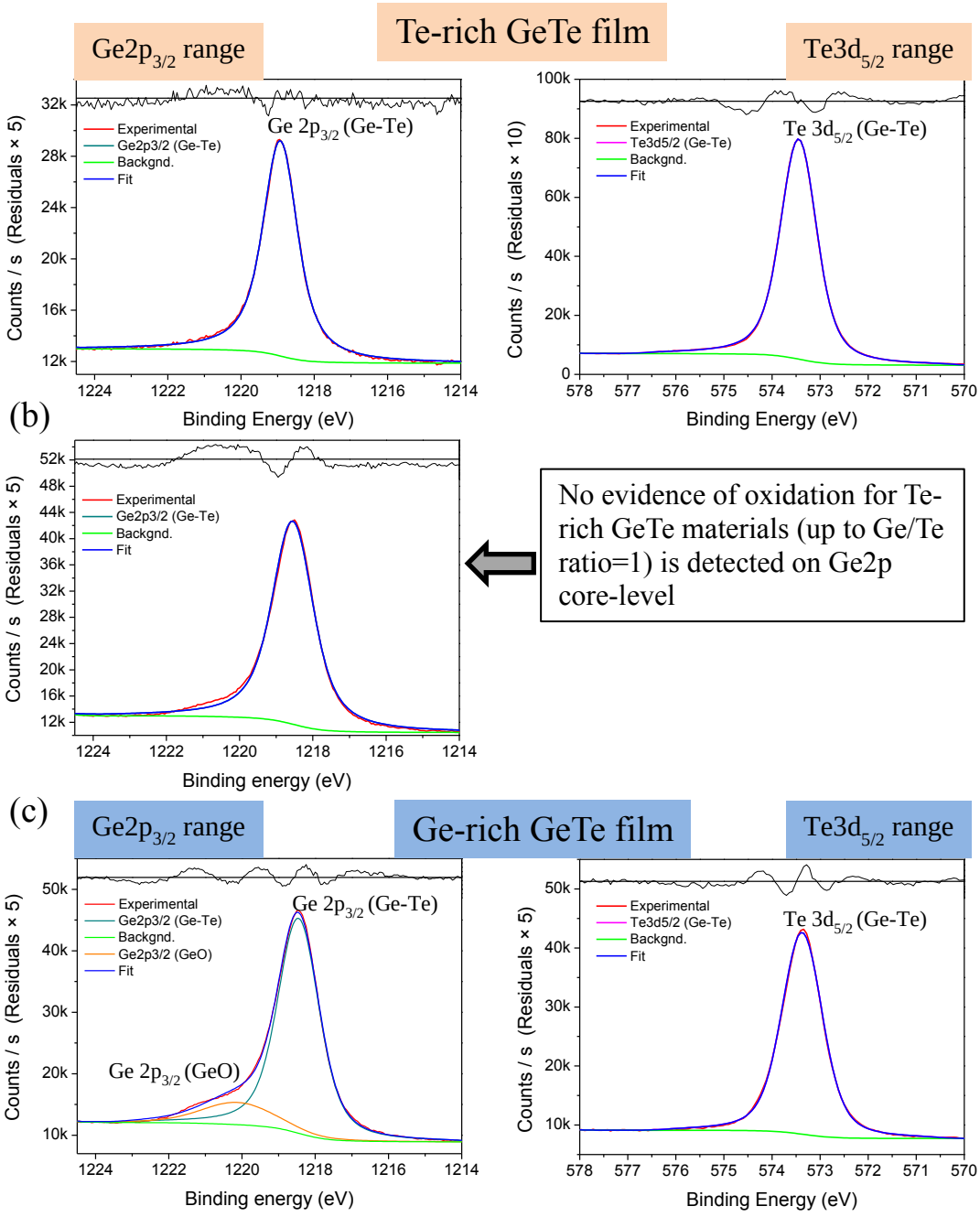

Figure 3.6. XPS spectra related to GeTe film deposited without wafer rotation after 10 min air-break, (a) Te-rich GeTe, Ge/Te =0.33, (b) Ge/Te =1, (c) Ge-rich GeTe, Ge/Te = 2.22.

A further evaluation of GeTe film was conducted, using homogeneous Ge/Te ratio equals to 1 over the wafer (thanks to wafer rotation), first employing the vacuum carrier and then compared to 2 months air exposure. As we can see in Fig. 3.7.a, the analysis through vacuum carrier confirms the lack of oxidation. After 2 months of exposure to air, germanium becomes completely oxidized in the form

of GeO_2 with partial presence of TeO_2 (18.0 at %) on the surface (~ 2nm depth). Tellurium is also present in metalloid state (Ge-Te bonds) but mostly in TeO_2 state. From the probed depth of each core-level, we could illustrate the final configuration of the GeTe film after 2 months aging, as shown in Fig. 3.8. We can observe the substantial impact of oxidation, as for 7 nm probed depth, the GeTe proportion becomes poor in germanium.

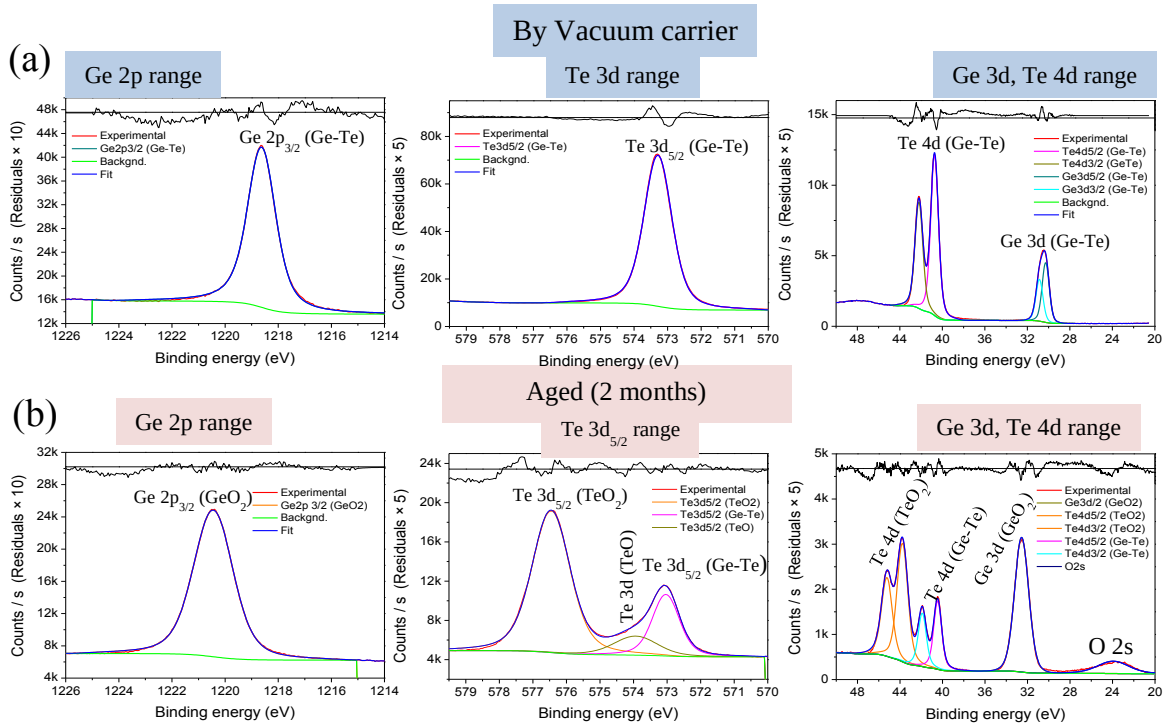

Figure 3.7. XPS spectra of 20 nm GeTe film with Ge/Te=1 (a) by vacuum carrier (b) after 2 months of ageing.

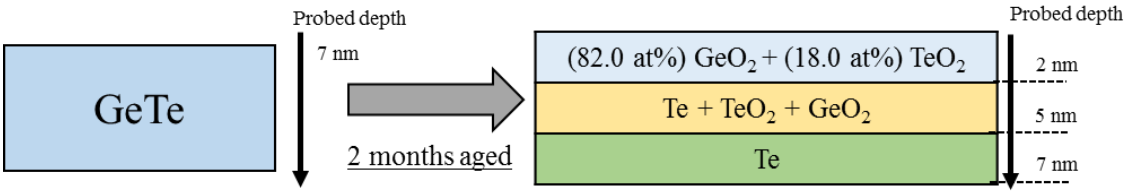

Figure 3.8. Possible evolution of GeTe layer after 2 months of ageing.

- SbTe films

Similarly to GeTe films, we used co-sputtering of individual Sb and Te PVD targets without substrate rotation so as to probe composition-dependent surface effect in SbTe films with significant composition variations on one-only wafer We here illustrate the influence of the composition on the binding states with two points of significantly different Sb/Te ratios: one Te-rich SbTe (Sb/Te=0.3), the other Sb-rich SbTe (Sb/Te=2.0). In the Te-rich SbTe material (Fig. 3.9a), Sb 3d core-level reveals partial oxidation in the form of SbO, contributing to 15 at % oxidation of antimony. Tellurium, on the other hand, shows no signal of oxidation, but the Te $3d_{5/2}$ core-level evidences the presence of two components: one corresponding to Sb-Te bonds and the other to Te-Te bonds due to the tellurium excess in the film.

The Sb-rich SbTe material comes not only with a more substantial effect of oxidation, but also with Sb-Sb bonds as evidenced in the Sb3d region, due to Sb in excess. The oxidation contributes to 30 % of

the Sb signal, and it is mostly in the form of Sb_2O_3, as we can see in Fig. 3.9.b. Similarly to the Te-rich material, tellurium shows no oxidation state. Moreover, Te $3d_{5/2}$ is modelled with one-only component corresponding to Sb-Te bonds, in agreement with the reduction of Te content.

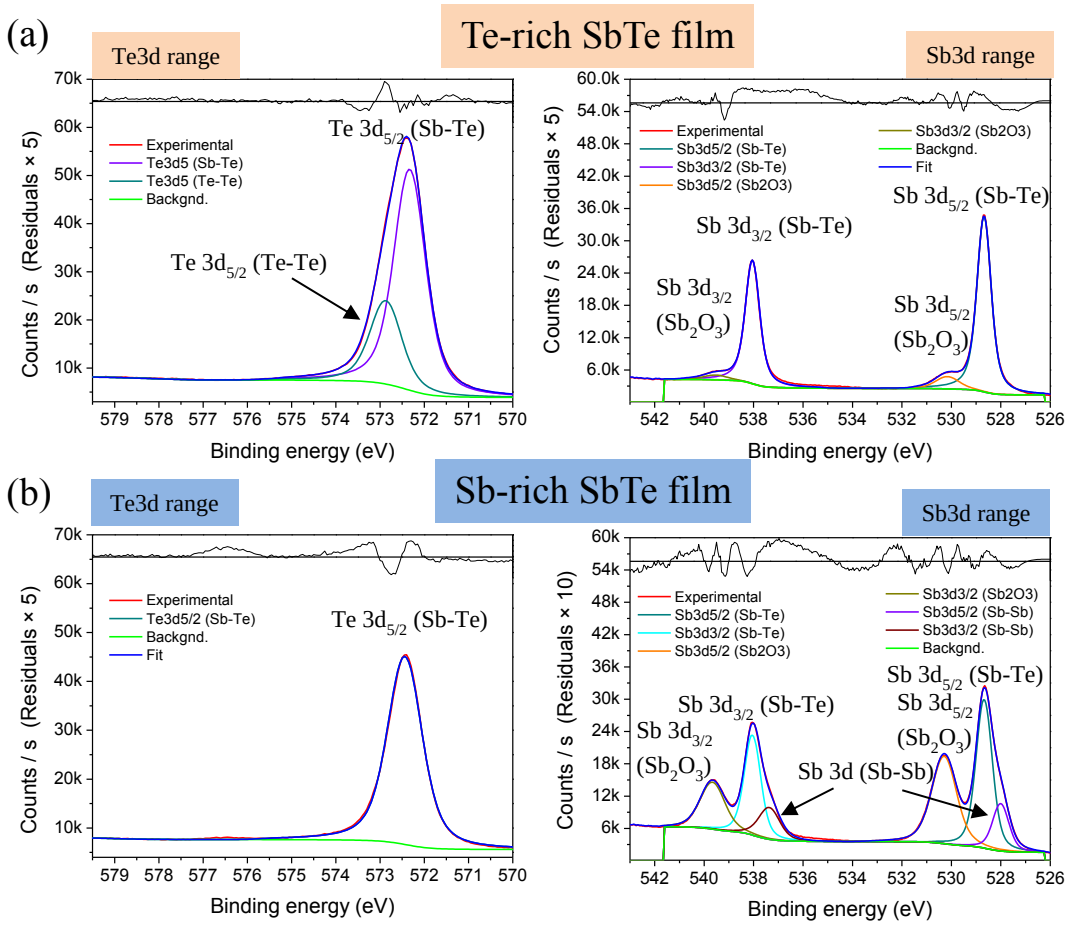

Figure 3.9. XPS spectra related to SbTe film deposited without wafer rotation after 10 min air-break, (a) Te-rich SbTe, Sb/Te = 0.3, (b) Sb-rich SbTe, Sb/Te = 2.0.

We also evaluated a Sb_2Te_3 material (deposited using wafer rotation), first by vacuum carrier and then 2-months aged, as illustrated in Fig. 3.10. From Fig. 3.10.a, vacuum carrier procedure leads to un-oxidized material. Furthermore, two components related to Sb-Te and Te-Te binding states, are needed to depict both Te 3d and Te 4d core-levels. This Te-Te additional component reveals an excess of tellurium, which was confirmed by the estimate of the Sb/Te ratio (0.56 instead of 0.67 as targeted).

After 2 months of exposition to air (Fig. 3.10b), as for the GeTe film, we observe that tellurium is partially in its initial state but mostly in its oxidized state (TeO_2). Antimony, compared to Ge from GeTe film, can still be found in its initial state although in very small quantity. From Sb 4d, we can deduce that antimony oxide is present in two states: Sb_2O_3 and Sb_2O_5 [8, 9]. The latter is the major component as shown by Sb 3d core-level. Figure 3.11 approximatively illustrates the final configuration of the SbTe film after 2-months of ageing. The model is illustrated according to two probed depths: 5 nm for (Te and Sb 3d), and 7 nm (Te and Sb 4d).

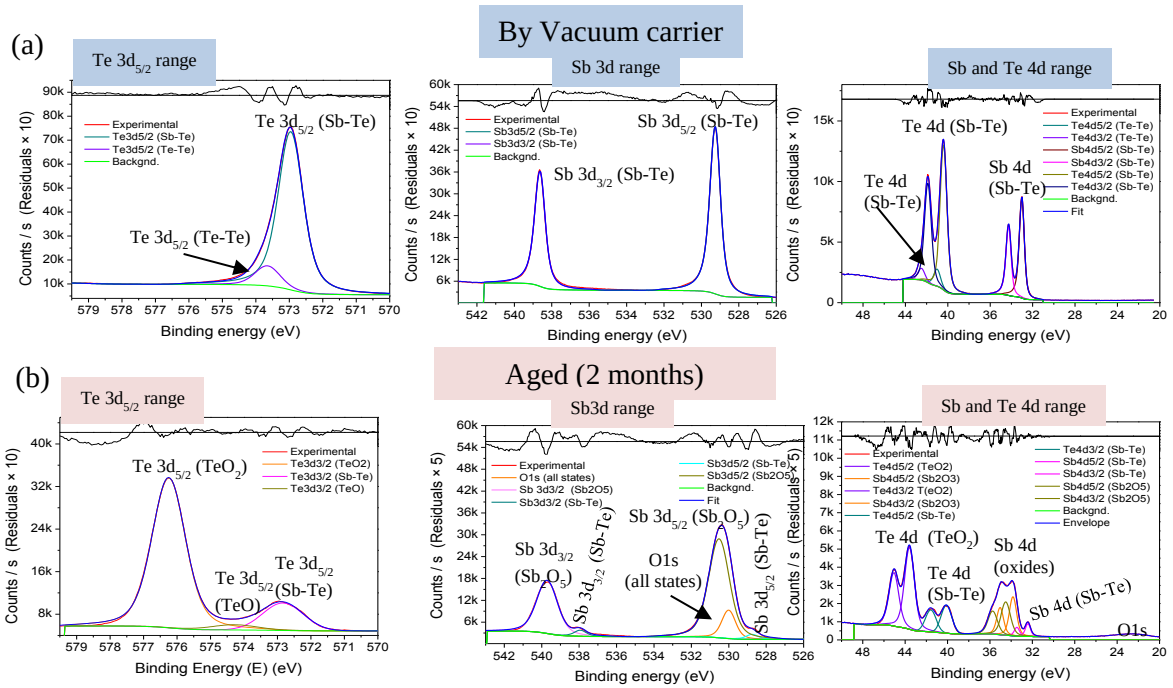

Figure 3.10. XPS spectra of 20 nm Sb_2Te_3 film with Sb/Te=0.56 (a) by vacuum carrier (b) after 2 months of ageing.

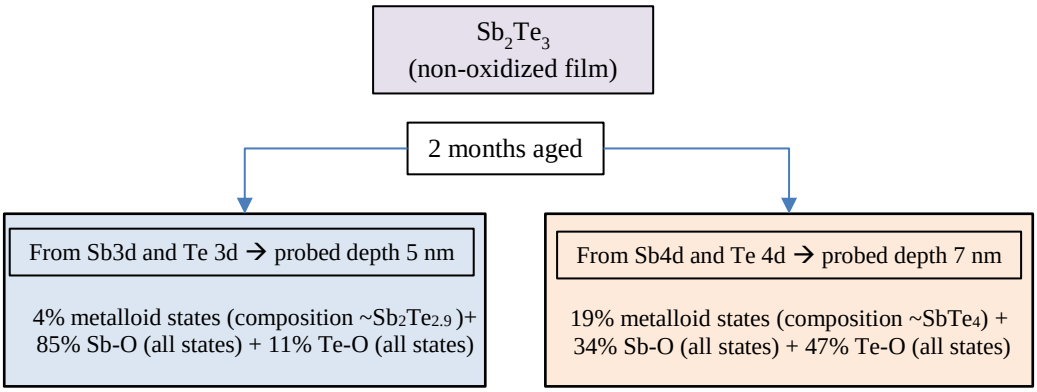

Figure 3.11. Possible configuration of Sb_2Te_3 after 2 months ageing according two probed depth.

Sb_2Te_3 may be deposited either amorphously at 60°C or in crystalline state at 220°C for Interfacial PCRAM stacks. We evaluated the impact of the process temperature using XPS analysis by vacuum carrier, hence for non-oxidized films. Fig. 3.12 compares XPS spectra of Sb_2Te_3 film deposited at 60 °C and 220 °C keeping the others deposition parameters constants.

The modeling of XPS spectra of both films (Fig. 3.10.a. and 3.13, 60°C and 220°C, respectively) shows that Te-Te additional component is only present in the amorphous film. Quantifying the stoichiometry of both samples from the 4d region leads to slightly different compositions, i.e for the amorphous film (36 at% Sb and 64 at% Te), whereas for the crystalline film (41 at% Sb and 59 at% Te) much closer to the Sb_2Te_3 stoichiometry. In addition, the peak width of both Te3d and Te 4d core-levels is slightly reduced for crystallized materials (FWHM are synthetized in Table 3.3), whereas the process temperature has no impact on the 3d and 4d components of antimony.

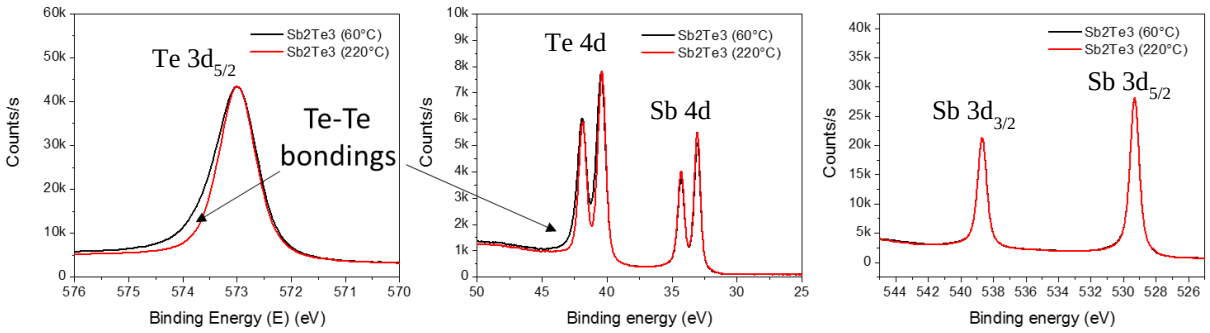

Figure 3.12. 20 nm Sb_2Te_3 films deposited at 60°C feature additional Te-Te binding states along with slight increase of FWHM of Te 3d and Te4, when compared to crystalline films deposited at 220°C.

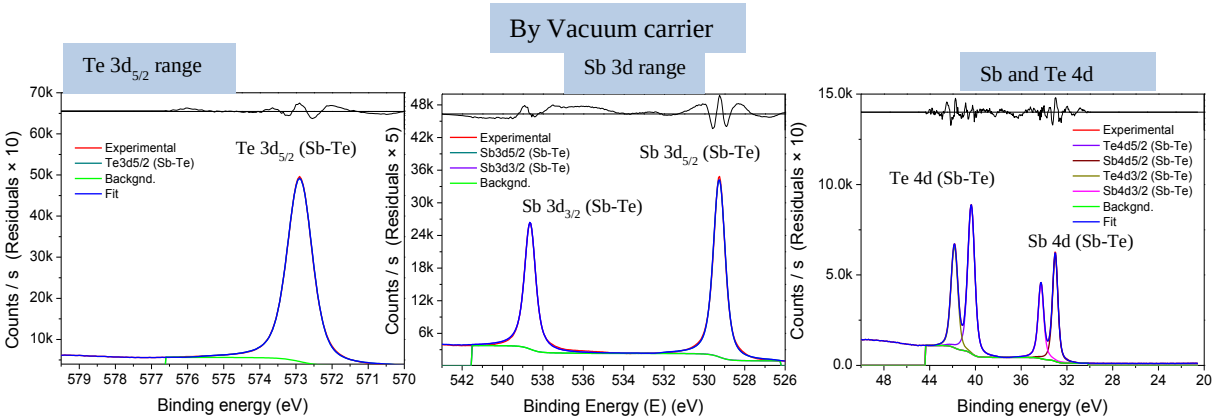

Figure 3.13. Deconvolution of XPS spectra of crystallized Sb_2Te_3 film shows no evidence of Te-Te binding states.

3.2.3.3. Ternary $Ge_2Sb_2Te_5$

Following the evaluation of elementary and binary films, we evaluated the binding states of GeSbTe ternary systems. Although different stoichiometry have been studied during the PhD work, we report only on $Ge_2Sb_2Te_5$ in this document, not only because it is most relevant composition reported in the scientific community but also due to non-confidentiality concerns related to this specific composition.

Our study was focused on the 20 to 70 eV range in binding energy, as it includes Ge 3d, Te 4d and Sb 4d core levels. The related photoelectrons feature almost identical kinetic energy, resulting in identical probing depth of ~ 7 nm, all these characteristics making this range particularly relevant for XPS-based compositional metrology of GeSbTe thin materials. In addition, as illustrated by Fig. 3.14.a, Ge 3d, Te 4d and Sb 4d doublets are perfectly separated for films measured using the vacuum carrier (no oxidation was observed), hence the quantification can be determined without any ambiguous deconvolution. On the other hand, oxidation leads to significant overlap of Ge 3d (Ge-O) and Sb 4d (Sb metalloid) which impacts the accuracy of the quantification, as we can see in Fig.14.b.

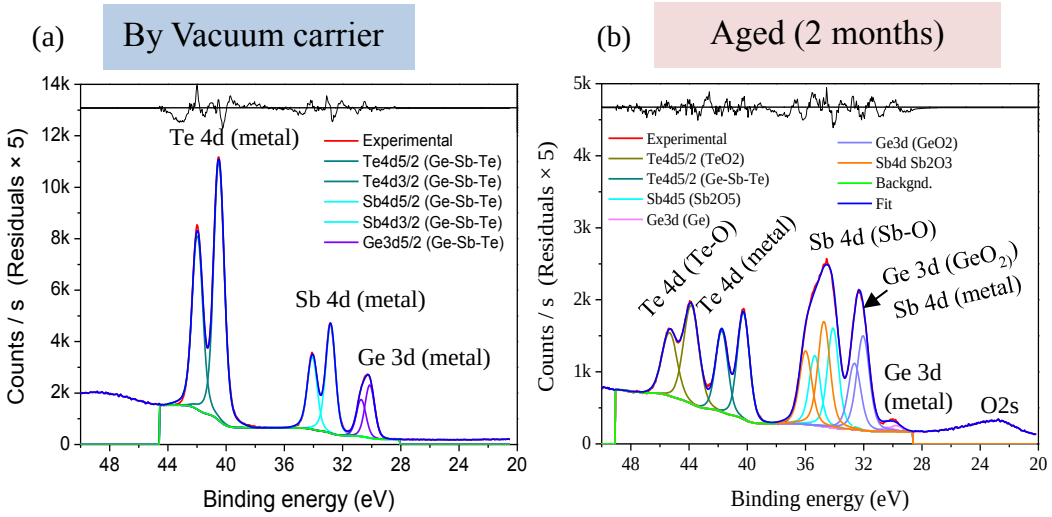

Figure 3.14. 20 nm $Ge_2Sb_2Te_5$ film XPS analysis (a) by vacuum carrier (b) 2-months aged.

Although Fig.3.14 shows the oxidation behavior after 2 months, limited queue-time can be accomplished according to the stoichiometry of the Ge-Sb-Te alloy to be deposited. For instance, Te-rich and Sb-poor GST films can withstand few minutes exposed to air, since its thermodynamic behavior is not as prone as Ge or Sb elements, as highlighted in Te-rich GeTe analysis in Fig.3.6. The same can also be true for Ge-rich Sb-poor GST films, since Ge oxides auto-passivate the GST film for a limited time, also demonstrate in Fig.3.6. Therefore, limited queue is possible for the ternary alloy as long as the GST film is reduced in Sb content.

Surface effects overview

Although Ge-Sb-Te films are prone to oxidation, each element behaves differently towards oxidation effects. For instance, among the three elements, Te films are quite tolerant to limited queue-time (10 min). Furthermore, this present protocol demonstrated to be very powerful to deduce Te-Te or Sb-Sb bonds on Sb-Te films, and not mistakenly considering them as Te-O or Sb-O.

The detailed study about the oxidation effects was not only able to forecast the possibility of queue-time, but is also essential for chemical quantification based on non-oxidized surfaces. We summarize in table 3.3 the binding energies as well as the full-width half medium (FWHM) of non-oxidized peaks. In addition, Fig. 3.15 depicts the influence of the element electronegativity on the binding energy of core-levels, we can see for example, the reduction of the binding energy on Te $4d_{5/2}$ and Te $3d_{5/2}$ of approximately 0.5 eV with the addition of Sb forming Sb_2Te_3 in well agreement with Scrocco et al. [15] who observed 0.4 eV reduction between Te and Sb_2Te_3 compounds.

Table 3.3. Calculated binding energies of studied films by vacuum carrier.

Compound	Ge $2p_{3/2}$	Ge $3d_{5/2}$	Te $3d_{5/2}$	Te $4d_{5/2}$	Sb $3d_{5/2}$	Sb $4d_{5/2}$
	Binding energy and FWHM of the spectra (in parentheses)					
Ge	1217.77 (1.17)	29.56 (0.63)	-	-	-	-
Sb	-	-	-	-	528.54 (0.72)	32.33 (0.59)
Te	-	-	573.45 (0.81)	40.87 (0.7)	-	-
GeTe	1218.59 (1.27)	30.23 (0.78)	573.25 (0.98)	40.67 (0.87)	-	-
SbTe (60°)	-	-	572.90 (0.89)	40.35 (0.77)	529.23 (0.66)	32.99 (0.55)
SbTe (220°)	-	-	572.86 (0.83)	40.33 (0.72)	529.23 (0.7)	32.99 (0.57)
$Ge_2Sb_2Te_5$	1218.40 (1.23)	30.23 (0.78)	572.98 (0.95)	40.45 (0.84)	528.97 (0.91)	32.75 (0.76)

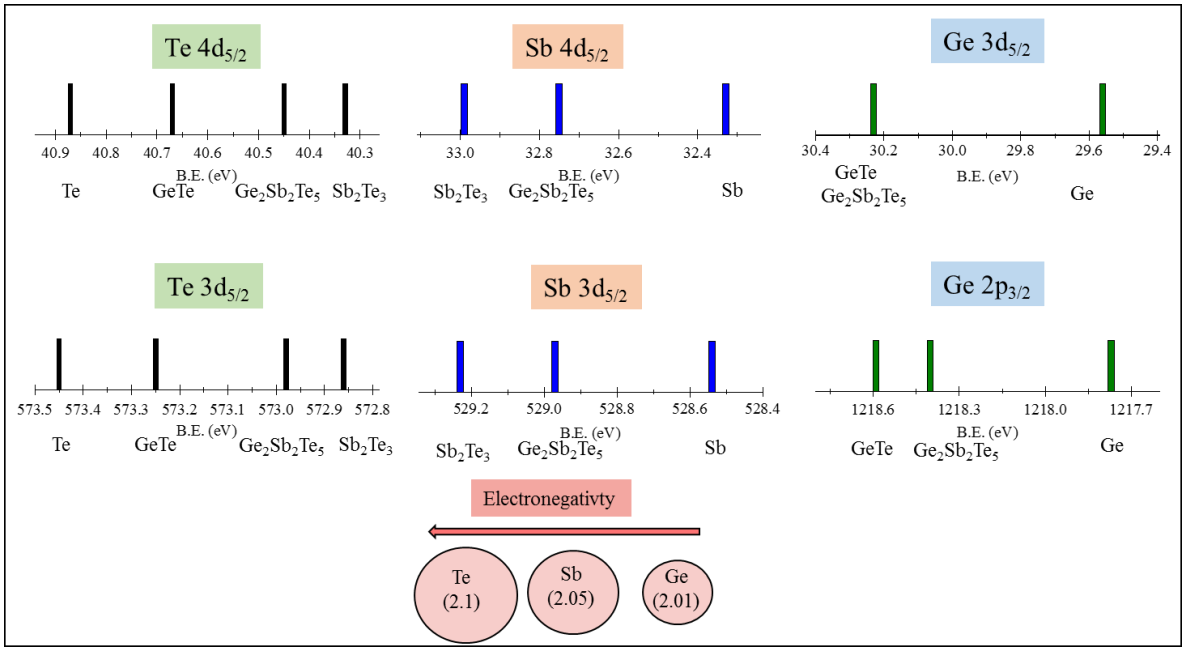

Figure 3.15. Influence on the binding energy of core-levels according to the electronegativity of the Te, Sb and Te elements. We can see that adding Sb or Ge into Te films reduce the binding energies of Te core-levels, as well as, adding Te into the Sb or Ge films increase binding energy of Sb and Ge core-levels.

3.3. Evaluation of capping efficiency as barrier layers

3.3.1. Introduction

Thin chalcogenide materials are often part of a multilayer stack. In PCRAM memory device, for instance, the chalcogenide-based phase change material is sandwiched between the bottom and the middle electrodes whereas the chalcogenide-based material of the Ovonic Threshold Switch (OTS) is sandwiched between the middle and the top electrodes, as illustrated in Fig.3.16 [10]. Chalcogenide films may be grown on top of or capped with different thin layers, such as metals (electrodes), dielectrics

or other materials with fine-tuned characteristics (passivation efficiency, thermal conductivity, …).

Nonetheless, the performances and the reliability of the device put strong requirements on the interfaces between the chalcogenide materials and either electrodes (Ta, TiN, W, etc.) or insulators (SiO_2, SiN). Interdiffusion, segregation or stress may degrade the properties of the chalcogenide materials, therefore affecting the functionality of the device. For example, Simpsons et al [11] studied the crystallization of 2 nm GeTe film deposed on Si substrate and sandwiched by two TiN layers. It was observed a substantial increase of crystallization temperature by 150 ºC due to the compressive stress exerted by TiN contact layers.

Although several studies highlighted the impact of interfacial effects on PCM ultra-thin films (< 10 nm) [1, 12], no substantial work has been performed about capping layers mainly because these effects are not considerably observed for PCM films with thicknesses above 100 nm. However, as the next technological nodes (90 nm and below) are approaching, interfacial effects studies will be, with no doubts, more and more crucial. Therefore, the objective of this section consists to develop a dedicated XPS metrology protocol to evaluate capping layers efficiency. The approach was employed for oxidation effects as well as interfacial effects of Ta, SiN and C capping layers interacting with Te-based and Se-based films. These capping layers were deposited *in-situ*, in the same PVD process tool as the chalcogenide material of interest, with no air break between the growth of chalcogenide and the deposition of the capping layer.

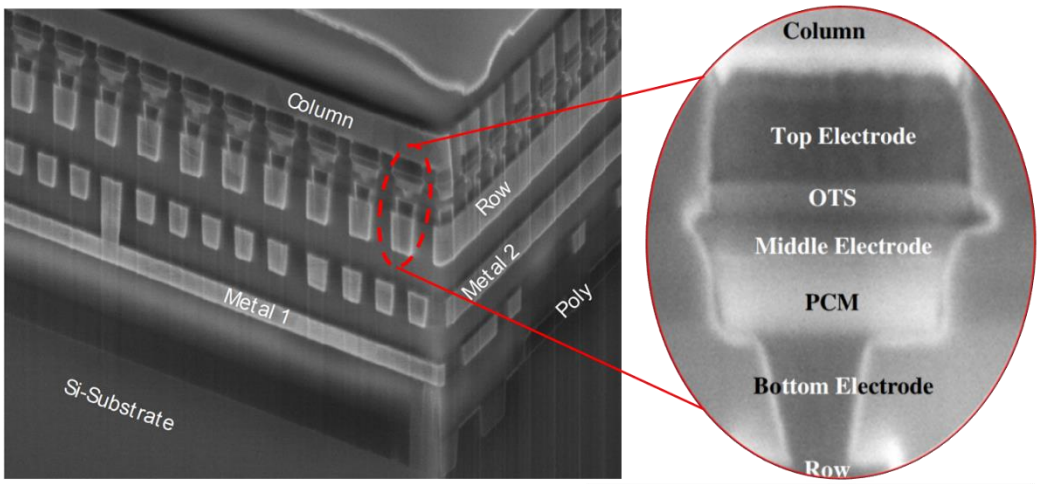

Figure 3.16. PCRAM cell fully integrated in CMOS device. The OTS selector above the PCM is necessary to provide correct information storage and data retrieval [10].

3.3.2. Experimental

The metrology protocol presented here was developed to probe Te-based and Se-based chalcogenide films. Both layered systems are widely developed at CEA-LETI for random access memories (CBRAM, PCRAM). The samples were amorphously grown by magnetron sputtering on 200 mm Si(001) wafers, using industrial multi-chamber PVD deposition tool Evatech CLN 200 at process pression ~ 6.10^{-4} torr, process temperature below 60 ºC and using 40 sccm of Ar flow. Table 3.4 shows a summary of the deposited samples with their respective capping layers.

Table 3.4. Main parameters of TiTe and N-doped GeSeSb films with the their respective depostion method.

Chalcogenide film			*In-situ* capping layer		
Elements	Deposition method	Thickness (nm)	Elements	Deposition method	Thickness (nm)
TiTe	• Alternation of chambers • Deposition sequence: Te-Ti-Te • Each deposition step result in < 1 nm layer	10	Ta	Sputtered	5
	Co-sputtered	5	SiN	Sputtered (SiN target)	5 and 10
GeSeSbN	Co-sputtered GeSe and Sb with N flow	100	C	Sputtered (C target)	3 and 5

The XPS metrology protocol was developed using Thermo Scientific Theta 300 inline tool operating at monochromatic Al-Kα X-ray source (1486.6 eV), with 400 µm beam diameter and a pass energy of 40 eV resulting in 0.6 eV resolution.

Two different approaches were employed to evaluate whether the capping layers could fit in the chalcogenide-based process. First, we investigated the efficiency of thin tantalum and thin silicon nitride layers deposited *in-situ*, as passivation layer for TiTe thin films by analyzing Ti-Te materials with various Ti/Te ratios (Te ranging from 30 to 60 at%). The thickness of tantalum or silicon nitride films were kept constant over the sample set, which allowed to characterize passivation efficiency and investigate possible inter-diffusion.

Secondly, we evaluated the efficiency of thin carbon layers as passivation layers for selenium-based materials being developed for OTS applications. The thickness and composition of the chalcogenide film was kept constant whereas the thickness of the carbon capping was varied so as to evaluate the minimal thickness of the carbon capping layer as protection layer for the Se-based films.

3.3.3. Results and discussions

3.3.3.1. Capping layers for Te-based films

The XPS measurements were firstly performed on the TiTe samples with 5 nm-thick tantalum layer. Te 3d, Ti 2p and Ta 4f core levels were recorded on every TiTe samples, along with reference spectra acquired on two elementary samples: i/ thin tantalum film and ii/ thin tellurium layer capped with tantalum, both grown on silicon, as shown on Fig. 3.17.

At first, only one contribution ($Ta4p_{1/2}$) is present in the Ti2p region, whatever the titanium content in the TiTe layer. The absence of Ti 2p peaks suggests that titanium did not diffuse into tantalum capping layer. (Ti 3p is superimposed with Ta 5p3)

The Te 3d region includes broad contribution of oxidized tantalum (Ta 4s) and Te 3d doublet (Te $3d_{5/2}$ and Te $3d_{3/2}$) that should have been fully attenuated by 5 nm of dense tantalum capping layer.

Te3d binding energies reflect metallic states of tellurium, which suggests that tellurium partially diffused towards tantalum capping layer, resulting in the formation of Te-Ta binding states. This hypothesis is well-aligned with the increase of Te 3d intensity with tellurium content in TiTe layer (Figure 3.16, Te 3d region).

Lastly, Fig.3.17 shows the Ta 4f region which contains metallic and oxide states of tantalum. The binding energy of Ta 4f metalloid states shifts towards higher energies when increasing the tellurium content in the TiTe layer, which confirms the formation of Ta-Te states, since electronegativity of tellurium (resp. tantalum, titanium) equals 2.1 (resp. 1.5 and 1.54).

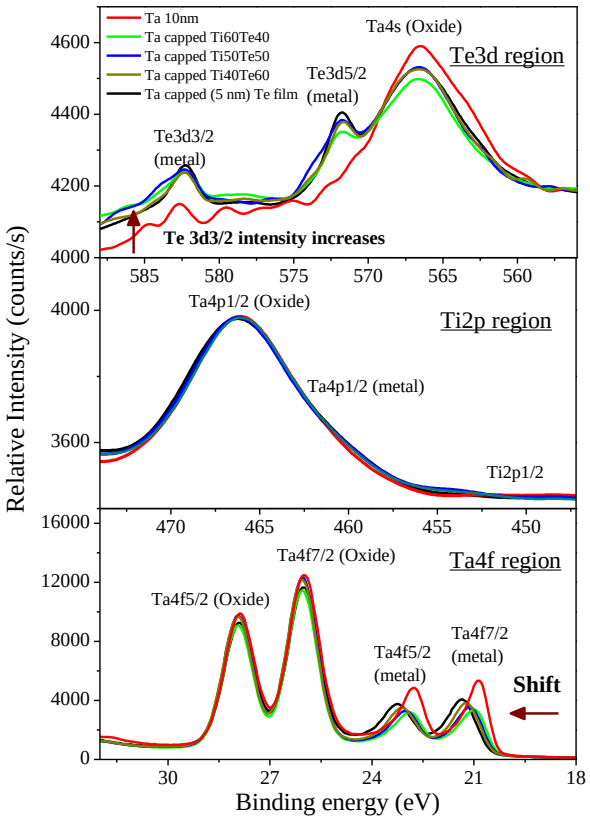

Figure 3.17. Te3d, Ti2p and Ta4f regions of TiTe (Te, 40-60 at%). Tantalum-capped Te layer and thin tantalum layer grown on silicon were also measured as references.

The reason why we do not observe any diffusion of titanium towards tantalum layer comes from the PVD deposition conditions of TiTe films. As described in the experimental procedure, the 10 nm thick TiTe film was deposited by a multilayer process in the order tellurium – titanium – tellurium, each elementary layer being thinner than 1 nm as depicted in Fig.3.18. Then, the tellurium layer (the top ultrathin layer of the TiTe multilayer process) completely interacts with Ta atoms forming Ta-Te covalent bonds. Hence, although Ti and Ta are soluble with one another, no significant Ti diffusion towards Ta layer is expected, firstly because the last layer is Te-rich, and second because Ti-Ta metallic bonds are weaker than Ta-Te and Ti-Te covalent bonds.

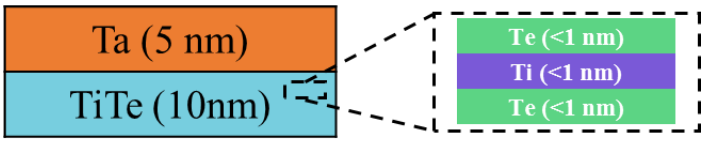

Figure 3.18. TiTe films were deposited by chamber alternation, Te < 1nm, then Ti< 1nm up to desired thickness and Ti/Te proportion. This process leads a substantial diffusion of tellurium towards tantalum and no evidence of diffusion of titanium.

In the case of SiN capping layer, we evaluated the capping efficiency for 5-nm thick TiTe co-sputtered films. This time, the methodology consisted only to evaluate 5 nm-thick SiN capping layer, keeping constant the TiTe film, as illustrated in Fig. 3.19.

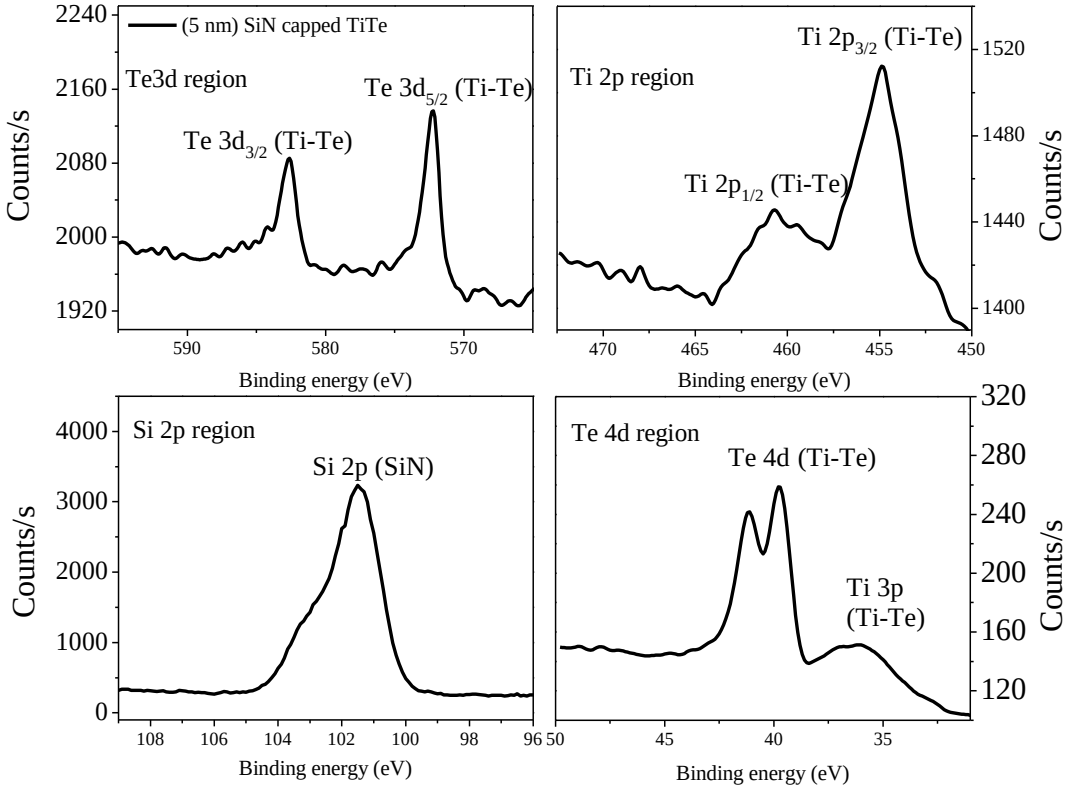

Figure 3.19. SiN as capping layer is very effective, no diffusion was observed. Although 5 nm SiN film has more Ti and Te signal because it is a lighter matrix, it effectively protects against oxidation.

Although the Ti 2p, Te 3d and Te 4d photoelectrons are significantly absorbed by the 5 nm-thick SiN capping layer when probed using a standard low-energy aluminum X-ray tube, related intensities are sufficient to show the lack of diffusion of Ti and Te atoms towards SiN layer. Te 3d and Te 4d doublets are observed at 582.6-572.2 eV and 39.75-41.15 eV, respectively. These binding energies correspond to the metallic state of tellurium (as we determined at section 3.2). Compared to the non-oxidized elementary Te films analyzed in section 3.2, they show a slight shift towards lower binding energies due to Ti-Te bonds (as Ti is less electronegative than Te, 2.1 and 1.5, respectively).

Concerning the Ti 2p region, in spite of low statistics, the Ti 2p doublet can be observed (at ~454 and 460 eV for c Ti $2p_{3/2}$ and Ti $2p_{1/2}$, respectively), which is aligned with titanium metalloid (Ti-Te) states with no evidence of noticeable oxidation. In addition we can guarantee that Si or N atoms are not prone to bond with Ti, since the standard enthalpy of formation of Si_3N_4 (-744.75 kJ) is much lower than for TiN (-337.65 kJ), [14]).

The overall of the evaluation of Ta and SiN as capping layer against oxidation is depicted in Fig. 3.20. Comparison with the XPS measurements of non-capped TiTe film shows that both capping layers efficiently act against oxidation. However, inter-diffusion between tantalum and the chalcogenide material exclude tantalum as candidate for capping layer in industrial device. On the contrary, SiN cap appears to be able for protection of the chalcogenide material against oxidation with no evidence of inter-diffusion concerns.

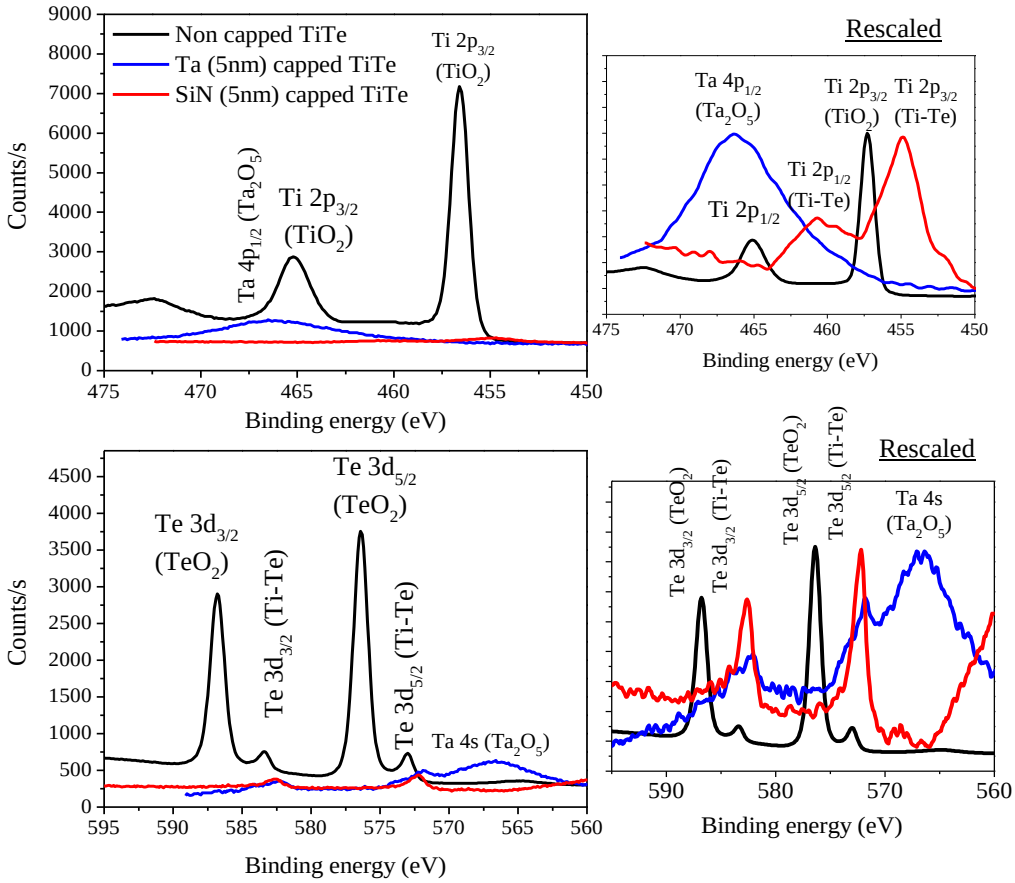

Figure 3.20. In overall both Ta and SiN are very effective as protective layers against oxidation. The graphs of the right column are rescaled for better visualization of the core-levels.

3.3.3.2. Capping layers for Se-based films

Innovative carbon layers have recently been investigated at LETI as capping layers for various thin materials, among which are N-doped GeSbSe films developed for as Ovonic Threshold Switch (OTS) in PCRAM device. We compared high-resolution XPS spectra in the binding energy region of Ge 3d and Sb 4d (28 to 38 eV range) for various 20 nm-thick N-doped GeSbSe layers amorphously deposited on silicon substrates by co-sputtering of GeSe and Sb targets, and capped *in-situ* with thin carbon layer. Uncapped layer was compared to C-capped layers with carbon thickness ranging from 2 to 5 nm. Fig. 3.21 illustrates the significant oxidation of the film for carbon thickness below 3 nm, Ge 3d being mostly in Ge-O binding states. On the contrary, for carbon films with thickness at least equal to 3 nm, Ge 3d are mostly in metalloid state, which ensure that such thin carbon film can be foreseen as effective protective barrier against oxidation.

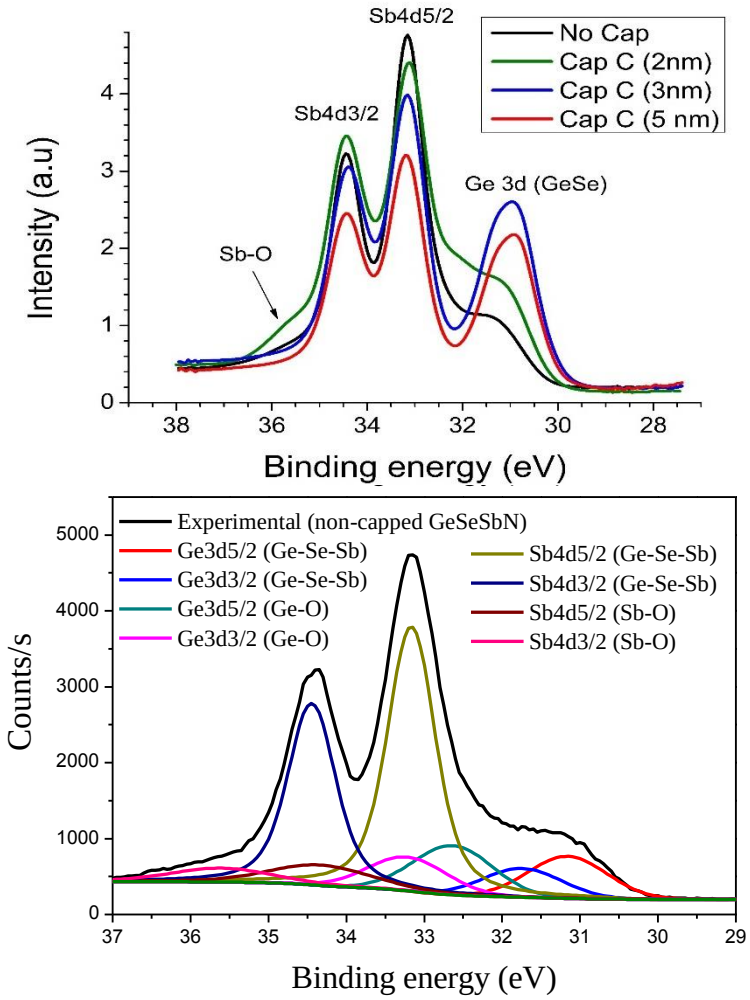

Figure 3.21. High resolution XPS spectra around Ge 3d and Sb 4d as a function of the thickness of carbon capping layer (top) and deconvolution of XPS spectra related to uncapped film (bottom), showing the various metalloid and oxidized contributions.

As complement, a deeper study was performed at LETI by Verdy et al. [14] about the electrical properties of OTS layer with and without carbon film as intermediary layer between OTS and top electrode TiN (Fig.3.22). The leakage current of the C capped and non-capped samples were evaluated before and after the initialization process, referred as firing (Fig.3.22). Before firing, it was observed a leakage current around 1 pA for both samples, regardless the presence of the carbon layer. After triggering process, a high leakage current (up to 10 μA) of the selector without Carbon layer was observed causing a substantial volatility of the data. By contrast, the stack with the carbon layer has a sharp distribution around 10 pA (i.e. drastical low OFF current for an OTS). The substantial difference between both samples is due to Ti atoms diffusion towards the OTS layer, which was suppressed by the carbon layer. Therefore, the use of carbon film as intermediary layer is viable solution to avoid electrode diffusion/interaction induced by thermal budget of back-end of line (BEOL) integration.

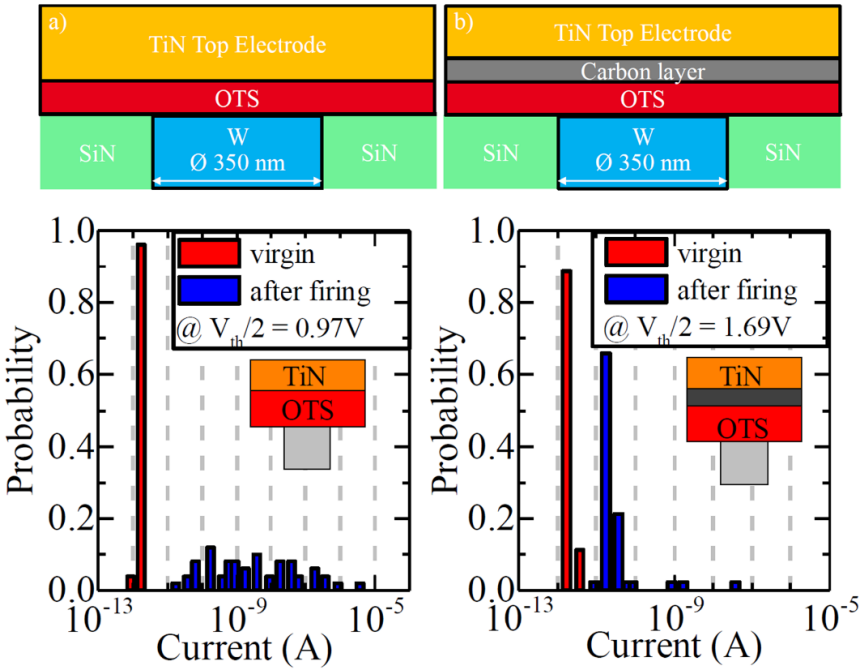

Figure 3.22. OTS selectors with and without carbon as barrier layer. Employing the carbon layer drastically reduces leakage current, and improves data reliability [14].

3.4. Conclusions

In this chapter we evaluated the influence of surface and interface effects towards the chemical composition of telluride based films. First, *quasi in-situ* XPS strategies were developed to investigate the chemical states of non-oxidized and oxidized (with controlled queue-time) Ge-Sb-Te elementary films and compounds. Elementary Ge and Sb films rapidly oxidized in the first minutes, which makes even short queue-time unsuitable. Tellurium, on the other hand, takes longer time to react with oxygen and showed no evidence of oxidation after 10 minutes queue-time. The kinetics towards oxidation is in good agreement with the enthalpy of formation (ΔH_f°) of oxides (Sb < Ge < Te is -972 < -580 < -322.6 kJ mol^{-1}, respectively). Similar to pure tellurium film, Ge-Te compounds show no evidence of oxidation after 10 minutes of air break for Te-rich materials (Te/Ge ≥ 1). On the contrary, Ge-rich GeTe and SbTe layers show fast partial oxidation when exposed to air.

By probing binaries Sb-Te films with significantly different Sb/Te ratio, we were able to determine Sb-Sb or Te-Te bonds as evidence of excess element addition. All the information reports in Chapter III about the composition-dependent deconvolution of XPS spectra of Ge-Sb-Te compounds, along with the impact of queue-time on oxidation of these compounds will be extensively used in Chapter IV to build reliable and accurate XPS-based quantification strategies.

In the second part of this chapter we evaluated the efficiency of Ta, SiN and C thin layers as barrier layers for Te and Se based materials. All these three films act as efficient protection against oxidation for thickness at least equals to 5 nm (efficiency was even demonstrated for a 3 nm carbon cap). However, inter-diffusion between tantalum and the chalcogenide material exclude tantalum as candidate for capping layer in industrial device. On the contrary, both SiN and carbon cap appear to be able for protection of the chalcogenide material against oxidation with no evidence of inter-diffusion concerns.

3.5. References

[1] S. Raoux, J. L. Jordan-Sweet, and A. J. Kellock, "Crystallization properties of ultrathin phase change films," *J. Appl. Phys.*, vol. 103, no. 11, p. 114310, Jun. 2008.

[2] B. Pelissier, H. Kambara, E. Godot, E. Veran, V. Loup, and O. Joubert, "XPS analysis with an ultra clean vacuum substrate carrier for oxidation and airborne molecular contamination prevention," *Microelectron. Eng.*, vol. 85, no. 1, pp. 151–155, Jan. 2008.

[3] E. Gourvest, B. Pelissier, C. Vallée, A. Roule, S. Lhostis, and S. Maitrejean, "Impact of Oxidation on Ge2Sb2Te5 and GeTe Phase-Change Properties," *J. Electrochem. Soc.*, vol. 159, no. 4, pp. H373–H377, Jan. 2012.

[4] S. Tanuma, C. J. Powell, and D. R. Penn, "Calculations of electron inelastic mean free paths. V. Data for 14 organic compounds over the 50–2000 eV range," *Surf. Interface Anal.*, vol. 21, no. 3, pp. 165–176, 1994.

[5] *Moulder, John F., et al. "Handbook of X-ray photoelectron spectroscopy: a reference book of standard spectra for identification and interpretation of XPS data; Physical Electronics: Eden Prairie, MN, 1995." (2000): 261.* .

[6] Q. Xie *et al.*, "Germanium surface passivation and atomic layer deposition of high- k dielectrics—a tutorial review on Ge-based MOS capacitors," *Semicond. Sci. Technol.*, vol. 27, no. 7, p. 074012, 2012.

[7] J. Cox, D. D. Wagman, and V. A. Medvedev, *CODATA key values for thermodynamics*. Chem/Mats-Sci/E, 1989.

[8] W. E. Morgan, W. J. Stec, and J. R. Van Wazer, "Inner-orbital binding-energy shifts of antimony and bismuth compounds," *Inorg. Chem.*, vol. 12, no. 4, pp. 953–955, Apr. 1973.

[9] C. D. Wagner, "Chemical shifts of Auger lines, and the Auger parameter," *Faraday Discuss. Chem. Soc.*, vol. 60, p. 291, 1975.

[10] D. Kau *et al.*, "A stackable cross point Phase Change Memory," in *2009 IEEE International Electron Devices Meeting (IEDM)*, 2009, pp. 1–4.

[11] R. E. Simpson *et al.*, "Interfacial phase-change memory," *Nat. Nanotechnol.*, vol. 6, no. 8, pp. 501–505, Aug. 2011.

[12] N. Ohshima, "Crystallization of germanium–antimony–tellurium amorphous thin film sandwiched between various dielectric protective films," *J. Appl. Phys.*, vol. 79, no. 11, pp. 8357–8363, Jun. 1996.

[13] M. W. Chase Jr, "NIST-JANAF thermochemical tables," *J Phys Chem Ref Data Monogr.*, vol. 9, 1998.

[14] A. Verdy *et al.*, "Carbon electrode for Ge-Se-Sb based OTS selector for ultra low leakage current and outstanding endurance," in *2018 IEEE International Reliability Physics Symposium (IRPS)*, 2018, pp. 6D.4-1-6D.4-6.

[15] M. Scrocco, "X-ray and electron-energy-loss spectra of Bi, Sb, Te and Bi2Te3, Sb2Te3 chalcogenides," *J. Electron Spectrosc. Relat. Phenom.*, vol. 50, no. 2, pp. 171–184, 1990.

4. Chapter IV: Chemical quantification protocols

4.1. Introduction

From chapter I, we highlighted that chalcogenide materials are highly influenced by the chemical composition and that chalcogenide properties can therefore be scaled by fine tuning the stoichiometry of the thin chalcogenide material for the next technology generations. Hence, dedicated metrology protocols need to be developed not only to assist process optimization required to scale chalcogenide properties but also for the inline monitoring of chalcogenide process in the semiconductor industry.

Therefore, we developed dedicated protocols to quantify the stoichiometry of chalcogenide films by in-line metrology based on Wavelength Dispersive X-ray Fluorescence (WDXRF) and X-ray Photoemission Spectroscopy (XPS). These protocols are intended to cover large range in terms of stoichiometry (for chalcogenide compounds without light elements), film thickness (from 1 to 200 nm) and spatial resolution (from few 10 µm on product wafers to mm on blanket wafers). These protocols were created by probing Ge-Sb-Te and N-doped Ge-Sb-Te films, using by Ion Beam Analysis (IBA) such as Rutherford Backscattering (RBS) as possible reference technique.

The first part of this chapter concerns the development of a protocol for GST films by WDXRF evaluated by IBA. The WDXRF protocol was then employed for the development of an XPS protocol based *quasi in-situ* dedicated procedure from chapter III.

The second part of this chapter is dedicated to the development of a protocol to probe N-doped GST films by WDXRF, where the addition of light elements strongly affects the chemical quantification. The protocol was compared to IBA using by Elastic Backscattering and Nuclear Reaction Analysis (NRA) for nitrogen quantification.

The last part of this chapter describes a protocol related to the metrology of sulfur-based 2D dichalcogenides. The accuracy of this protocol was evaluated by comparison with reference-free XRF analysis conducted at the German Institute of Metrology (PTB). We demonstrated that the combination of WDXRF and XPS was particularly adequate to assist the development of ultrathin layers of MoS_2 or WS_2. More specifically, we applied this metrology toolbox to provide process people developing a novel pulsed-MOCVD deposition route for WS_2 with relevant information on the impact of the main deposition parameters on both film stoichiometry and deposited mass.

4.2. Chemical quantification of Ge-Sb-Te film

The term quantitative analysis by definition concerns the measurement of a physical quantity associated with its uncertainty to indicate its degree of reliability [1]. In X-ray metrology, the final uncertainty related to the quantitative information (composition, deposited mass, …) depends on three main contributions: i/ the accuracy of the values of the fundamental parameters of the material of interest in the instrumental conditions of interest (e.g the energy of the probing X-ray beam), ii/ the accuracy in the knowledge of the numerous instrumental parameters (resolution, geometrical data such as distances, solid angle of collection, …), and iii/ accuracy in the measured signal (spectra statistics, possible need for deconvolution, …).

- Fundamental parameters

Reliable data about the fundamental parameters (photo-absorption cross-sections, mass attenuation coefficients, fluorescence yield, etc) is essential to reduce the uncertainties on quantitative analysis. Most of fundamental parameters have been mostly determined in last decades by extensive studies and published in referenced handbooks and websites (e.g. CXRO X-ray booklet [2], NIST [3], X-ray lib [4]) as tabulated data. Nevertheless, the uncertainties of certain fundamental parameters are too high to meet industrial requirements of accurate composition analysis. For example, Fig.4.1 represents the photo-absorption cross-section coefficient of Ag L-lines, we observe some deviations between measured data and reference sources. As a consequence, National Metrology Institutes from numerous countries are performing a common long-term work through the "Fundamental Parameter Initiative" in order to improve the accuracy of the tabulated / published values so that the related uncertainties meets the requirements of industrial developments. These new, more accurate fundamental parameters are continuously determined and the values are published and propagated to suppliers of X-ray instruments.

The fundamental parameters utilized in this work comes from X-ray lib [4], Scofield [5] and Rigaku embedded library (compilation of NIST, other sources and their experimental values).

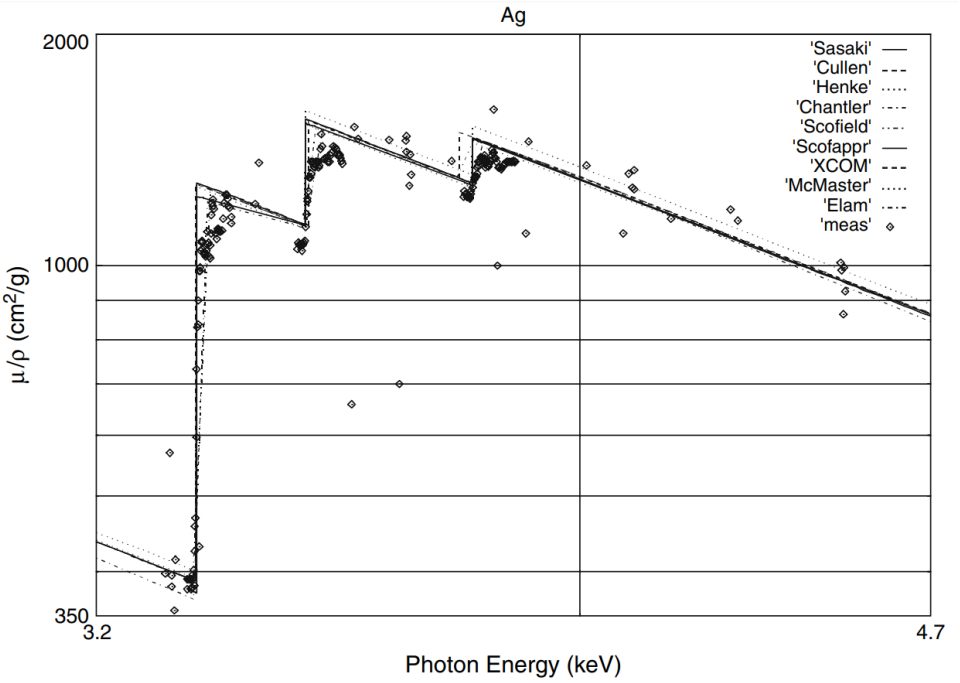

Figure 4.1. Measured data and tabulated data from several reference libraries for L-lines region of silver [6].

- Instrumental parameters

The uncertainty related to instrumental parameters such as beam divergence, angular resolution, energy resolution, solid angle of detection, etc have a crucial influence on the ability of XPS, XRR and XRF techniques to provide users with accurate quantified information on the investigated samples. For instance, precise values of the illuminated and detected areas must be included in the analysis of GIXRF data so as to correctly model the data (Fig.4.2). Two main strategies can be used to access these instrumental parameters. The most rigorous one consists in the exhaustive metrology of the instrument, in terms of distances, angles, efficiencies, etc. Such a strategy is a long term story that can only be conducted by National Metrology Institutes working on dedicated (for instance synchrotron-based) instruments, but in return permits unique capabilities such as XRF-based reference-free analysis of composition and deposited mass [19]

However, to develop such a strategy in a Lab or for inline tool is not possible, first because it would require too many resources (time, manpower) when compared to the expected short term benefit or to the time to obsolescence of the metrology tools. In addition, most Lab tools, and above all inline fully automatized tools come with lots of embedded proprietary features and non-accessible geometrical parameters that cannot even allow to foresee a full metrology of the instrumental parameters of the tools. As a consequence, one can only determine estimates of instrumental functions of Lab and inline tools, using dedicated samples (standards, pure elements or at least stable over time extensively characterized samples).

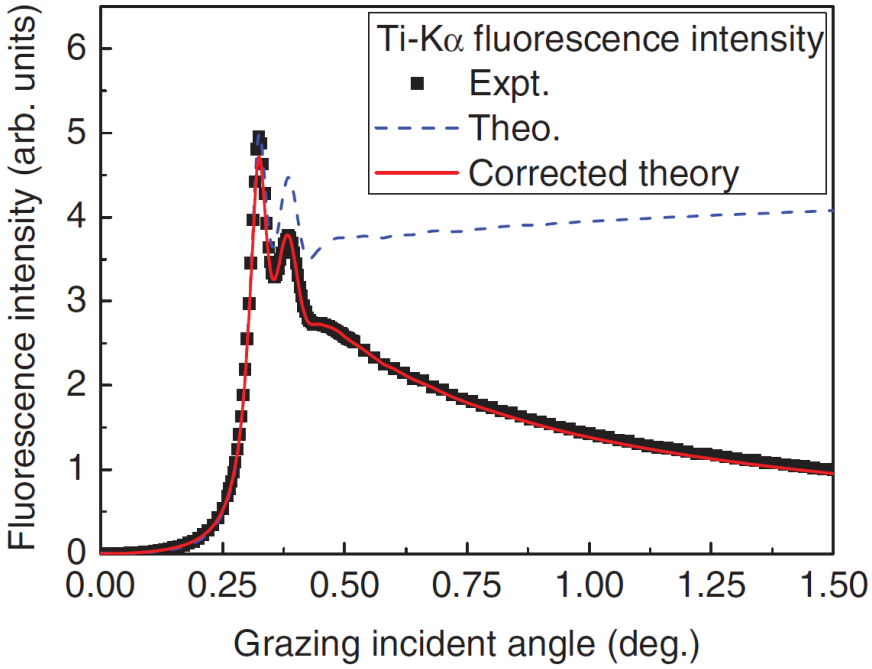

Figure 4.2. Geometric setup (detected illuminated zones) influence on GIXRF data. In this case, the theoretical data is corrected by width of the detected are which decrease as function 1/sin(θ) [7].

For instance, Rotella et al. [24] showed how a thin layer of nickel deposited by PVD on silicon substrate could be used to determine the instrumental function in GIXRF experiment, and propagate this function in the GIXRF analysis software so as to quantify chemical depth-profiles in gallium-doped ZnO films. In the case of inline WDXRF, the instrumental parameters are neither directly determined nor accessible to users, but their contribution to the quantified analysis is calculated by Rigaku software based on the measurement of samples with known properties such as pure elements or layers with well-characterized composition and deposited mass. As a consequence, the total uncertainty of WDXRF-deduced quantitative data cannot be rigorously determined. Thus we'll only calculate and report on uncertainties related to the measured signal for this technique. In addition, we conducted repeatability measurements which consists in measuring the same sample spot on the same conditions several times. This approach is only valid for samples which do not evolve with exposure to hard X-ray. Through this approach, we determined uncertainty of this equipment to be inferior to ±0.35 at% (100 times repeatability of a $Ge_2Sb_2Te_5$ film 100 nm).

- Spectra statistical uncertainty

If no background issue needs to be addressed, the spectra uncertainty is purely related to the number of photons recorded and highly depends on the signal/noise ratio. For spectrometry techniques, the uncertainty can be calculated by:

$$\sigma = \frac{1}{\sqrt{I_m t}} \quad \text{(eq.4.1)}$$

Where I_m is the measured intensity (the peak net area, (counts/s)), and t is the measuring time (s). The expanded uncertainty is then expressed as 3σ that should as low as possible (and less than 1%)

for industry-driven applications. Figure 4.3, for example, shows how to optimize the measurement time for Te-Lα spectra from GeSbTe films acquired by WDXRF. The layer thickness, and consequently the deposited mass of Tellurium drives the signal to noise ratio and the 3σ value of for the XRF line of interest. In order to obtain 3σ <1%, the acquisition time ranges from 4 seconds for 100 nm-thick layer to 100 seconds for 4-nm thick film.

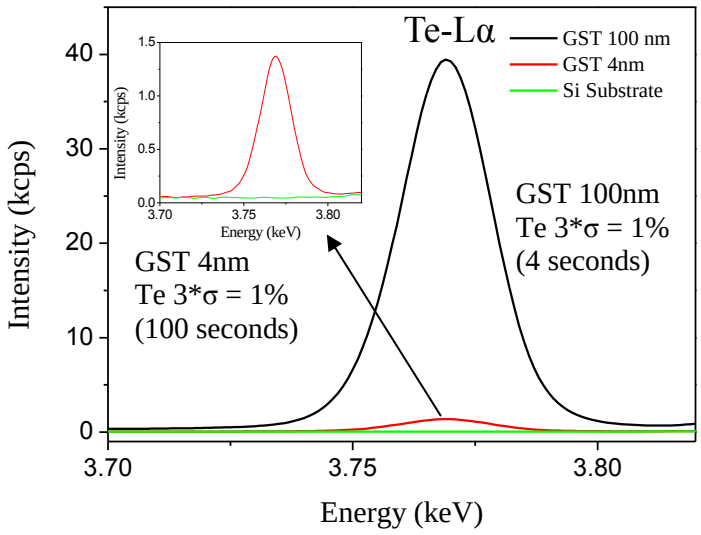

Figure 4.3. Te-Lα spectra uncertainty for 100 and 4 nm GST film. The thin film (inset) needs 94 seconds more of statistical time than the thick one.

Similarly, for the XPS analysis, only the spectra statistics uncertainty was considered, since the uncertainty of the instrumental parameters was not available during this work. These XPS uncertainty values will be discussed in the second part of this section (XPS quantification).

4.2.1. Chemical quantification by WDXRF spectrometry

As we discussed in chapter II, two main approaches exists to quantify compounds: Empiric method and Fundamental parameters (FP). We have seen that although empiric method can be simple it is limited to the calibrated empiric parameters (i.ee. only valid to certain range of composition or thickness). Hence, FP method is a more robust approach taking into account all the physical, instrumental and sample parameters, and hence it is more versatile, quantifying, for example, the whole compositional range of the probed film.

- Determining the measurement conditions

As we had to develop WDXRF-based protocols to quantify the deposited mass and the composition of Ge-Sb-Te compounds with huge variety of composition, thickness, sub-layers and capping layers, we only considered the fundamental parameter (FP) method (see Chapter II) using pure elements for calibration, as the empirical method would have required a non-reasonable amount of calibration samples. FP method is a more robust and flexible approach taking into account all the physical, instrumental and sample parameters, and is more appropriate for the characterization of processes under development with fine tuning of stoichiometry.

- Determination of the measurement conditions

Quantification by FP method starts with extensive analysis of the qualitative data to determine the main factors impacting the fluorescence spectra, such as overlapping peaks and background handling. From the in-line WDXRF tool employed in this work, the main possibilities of superimposed spectra are due to :i/ the sample itself (overlap of XRF peaks from the different chemical species, ii/ the the polychromatic rhodium source (diffraction peaks) and iii/ the wavelength-based detection setup (N^{th} order satellite peaks from the X-ray tube or the sample matrix). Sample-related overlaps can be tackled by different means: changing the analyzer crystal (increasing spectral resolution to differentiate overlapping peaks from sample), choosing another non-overlapped XRF line or developing appropriate deconvolution strategies. Energy-filtering of the primary beam and/or rotating the sample, either by selecting the most appropriate azimuth or by rotating the sample during the measurement, help reducing or even suppressing N^{th} orders satellites and diffraction peaks. In addition, background must be carefully handled, essentially in the soft X-ray range. We hereafter present the way we determined all the above-listed factors in order to improve the signal/noise ratio and reduce the spectra uncertainty ($3\sigma<1\%$).

Aware of these factors for quantitative analysis, we developed our metrology protocol for Ge-Sb-Te films based in the whole compositional and thickness range. Figure 4.4 shows the fluorescence spectra lines of 100 nm and 4 nm thick $Ge_2Sb_2Te_5$ films with 5 nm Ta capping (deposited *in-situ*) to avoid ageing effects. This range of thickness allows us to refine the measurement conditions for both classical condition (thin film, with thickness down to ~ 50 nm) and ultra-thin film for which instrumental factors can induce substantial bias.

For instance, the germanium element may be characterized using Ge-Kα or Ge-L XRF lines. In both cases the Ge spectra shows no overlap by any other element from the film. Ge-Kα is well defined and does not overlap with neighbor fluorescence lines (Ta-Lβ_2) or Rh-Kα 2^{nd} satellite. However, a diffraction peak of the crystalline silicon substrate shows up at exactly the same energy as Ge-Kα, even when using a Cu filter. This diffraction-induced contribution affects drastically the ability to conduct metrology of Ge-based ultrathin films based on the analysis of Ge-Kα.

Ge-Lα XRF lines region is affected neither by overlaps from the matrix nor by diffraction peaks; hence Ge-Lα can be used regardless the film thickness. On top of that, the intensity of Ge-Lα line is significantly higher (factor ~ 10) than for Ge-Kα for thin layers, which makes use of Ge-Lα XRF line perfectly suitable for the development of thin Ge-Sb-Te compounds. However, the non-linear background in the soft X-ray region must be handled carefully by measurement and subtraction of the substrate contribution, for proper extraction of the net intensity.

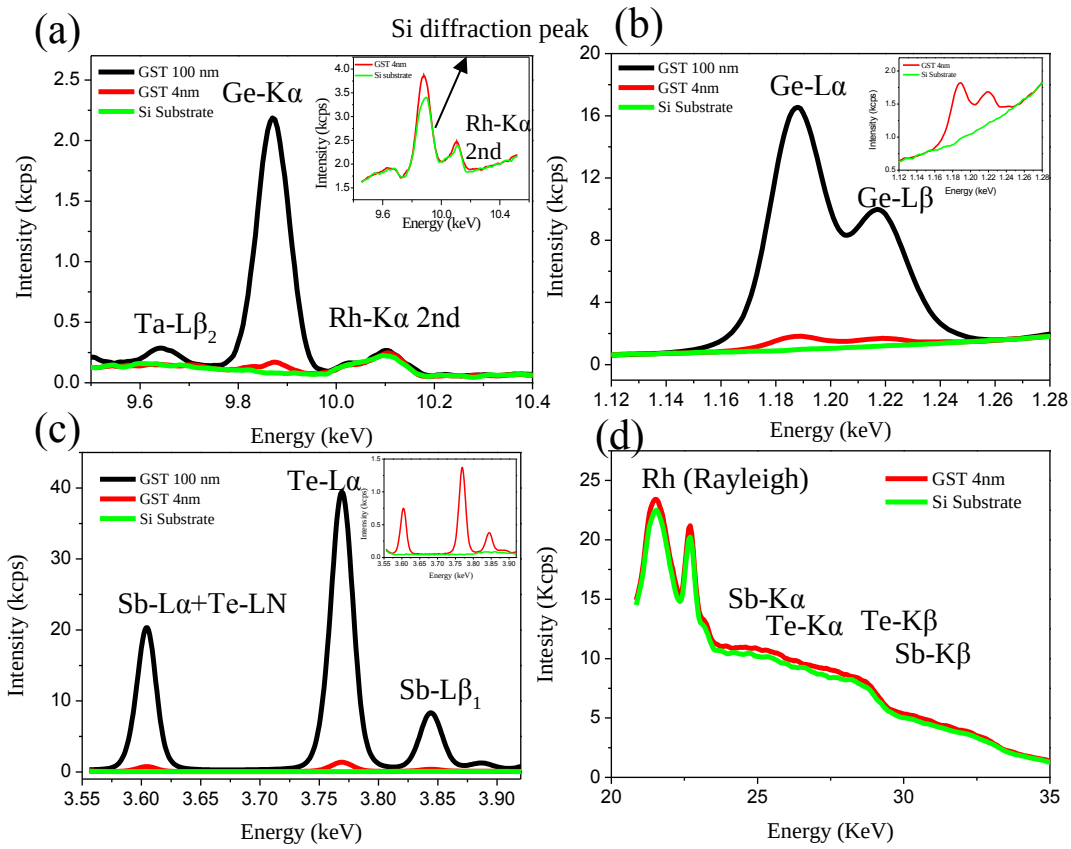

Figure 4.4. XRF spectra from L and K lines of Ge, Sb and Te that can be used to probe Ge-Sb-Te compounds with WDXRF. The choice of the most appropriate XRF line is driven by the lack of overlapping contribution such as Rh-satellites and diffraction peaks as illustrated in Ge-Kα spectra, and by sufficient signal to noise ratio (which is not the case for thin GST probed with Sb-K and Te-K lines). The insets correspond to 4 nm thick GST films.

Tellurium and antimony in thin Ge-Sb-Te films, can only be quantified by their XRF L lines, since the high energy K lines (see Fig. 4.4.d) are only slightly excited by the Bremsstrahlung of the rhodium X-ray tube (energy of Rh K lines is significantly below the K edges for Te and Sb). Moreover, the background of these L-lines range is not affected by diffraction peak.

As antimony and tellurium are neighbor elements, their XRF L-lines are also found on the same energy range (Fig 4.4.c). Whereas tellurium can be quantified using high intensity isolated Te-Lα line, Sb-Lα, on the other hand, is superimposed with Te-LN line, and Sb-$L\beta_1$ line is therefore more suitable for the quantification of antimony.

Table 4.1 shows the quantitative analysis of the two GST films from Fig.4.4 by extracting the Ge intensity either by Ge-Kα or Ge-Lα. We can see that the diffraction peak superimposed with the Ge-Kα peak has no influence in the quantification of thick layers. By contrast, for thin films, extracting the Ge at% by its Kα line leads to an under-estimate inducing deviation of 0.5 at% when compared to quantitative analysis based on Ge-L. In conclusion, both Ge-K and Ge-L lines can provide accurate values, but one must be aware to probe thin Ge-based films with its Ge-Lα line.

Table 4.1. Quantitative analysis of GST film (4 and 100 nm), Ge-Lα can be employed for any thickness, while Ge-Kα is suitable for GST films with thickness above 50 nm.

Analyze lines	Film	Ge (at%) ±0.35at%	Sb (at%) ±0.35at%	Te (at%) ±0.35at%
Ge-Kα, Sb-$L\beta_1$ and Te-Lα	GST 4 nm	23.6	21.5	55.0
Ge-Kα, Sb-$L\beta_1$ and Te-Lα	GST 100 nm	24.1	22.0	53.9
Ge-Lα, Sb-$L\beta_1$ and Te-Lα	GST 4 nm	24.1	21.5	54.4
Ge-Lα, Sb-$L\beta_1$ and Te-Lα	GST 100 nm	24.1	22.0	53.9

- Accuracy evaluation of Ge-Sb-Te films by WDXRF analysis

In order to determine the accuracy of our quantitative analysis, we evaluated our metrology protocol by measuring the same films through Rutherford Backscattering Spectrometry (RBS). RBS is a technique capable to quantify films with high absolute accuracy [8]. This technique consists to bombard a sample with an energetic ion beam (protons, He^{4+}), by measuring the backscattered particles after collisions. Hence, it is a reference-free technique, since the quantification is purely based on scattering laws and Coulomb interactions [9].

For this approach, we deposited 100 nm thick amorphous Ge-Sb-Te films on 200 mm Si (001) substrate by Physical Vapor Deposition (PVD) in industrial tool Oerlikon CLN200. Four different films were deposited, the first one being $Ge_2Sb_2Te_5$, then adding 35 at%, 48 at% and 53 at% Ge content for next deposited films. The deposited films were then capped with 5 nm amorphous Ta layer deposited *in-situ*. Probing GST films with progressive increase on Ge at% not only allow us to properly determine our XRF accuracy but also to trace down the compositional evolution with the Ge addition (*i.e*, Ge/Te and Sb/Te ratios).

The RBS measurements were performed with 2.1 MeV He^+ ion beam of few mm^2 on the sample surface, with incident current of 2.5 nA. The analysis chamber was kept at de $2x10^{-6}$ hPa with the bombarded zone from sample faced to the incoming particles. The backscattered particles from the sample atoms are collected at 160° from the initial direction. The samples are also tilted of 15° in order to avoid channeling effects reducing the low energy spectral background for improved accuracy. More details about the IBA analysis can be found in annex B.

RBS is not the optimal technique to discriminate elements with close atomic numbers (Z), which is the case of Sb and Te. Then, Sb/Te ratios were determined by Particle Induced X-Ray Emission (PIXE) which follows the same fundamentals as XRF spectroscopy. The measurements by PIXE was performed in the same instrument as RBS, irradiating the sample with a 3 MeV proton beam and mm^2 spot size. An absorber (315 µm thick) was placed in front of the detector in order to attenuate the backscattered particles and the X-ray fluorescence from the Si substrate at low energies.

The ratio Sb/Te is then determined by a dedicated software called GUPIX [25] which takes in account the fundamental parameters of XRF to model the peak surface, then making the separation of Sb from Te possible.

Figure 4.5 shows experimental data for the four different GST films probed by WDXRF (a, b) and IBA (b, c). We can see from WDXRF spectra that the intensities of Ge-Lα, Sb-Lβ$_1$ and Te-Lα follows the tendency of increasing the amount of germanium and decreasing the content of antimony and tellurium. The same goes with RBS spectra (Fig 4.5c). The Sb/Te separation by PIXE is illustrated by Fig 4.5.d, with clear separation of the contribution of Sb and Te K (2 keV energy distance and linear background). However, PIXE spectra come with too limited statistics to guarantee an accurate estimate of Sb/Te ratio (Fig. 4.5).

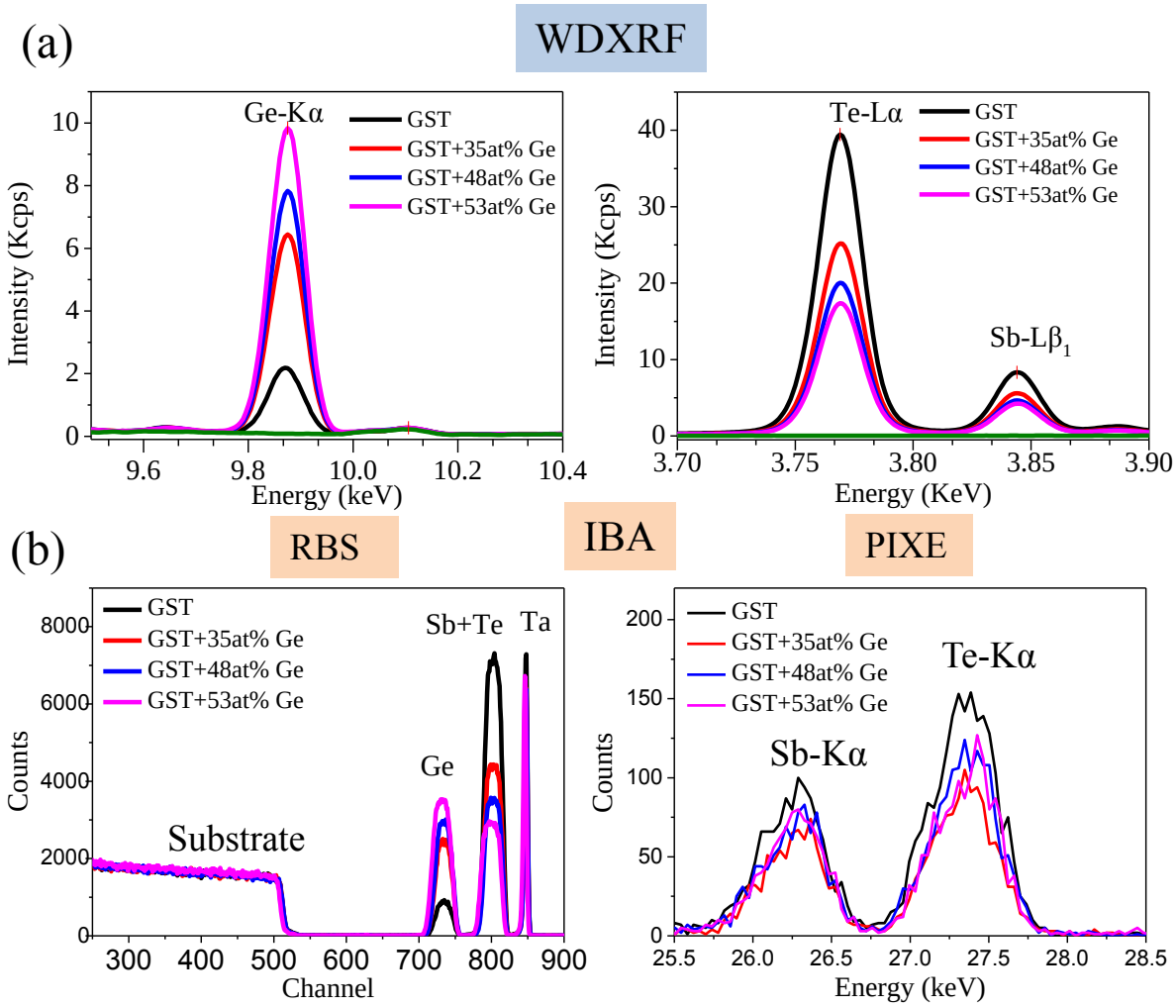

Figure 4.5. Trends in WDXRF spectra and RBS spectra are aligned with increased incorporation of Ge in the samples. PIXE spectra come with too limited statistics to guarantee an accurate estimate of Sb/Te ratio

Table 4.2 compares WDXRF-based and IBA-deduced chemical quantifications. We can see that for the whole sample set, the maximum deviation for the Ge content (where RBS-only is taken into account) is limited 0.4 at%. Sb and Te, on the other hand, show deviations significantly higher than Ge, with 1.8 and 1.6 at% deviation, respectively. This may be related to the accuracy in the Sb/Te ratios when determined by low-statistics PIXE analysis.

Table 4.2. Chemical quantification obtained by WDXRF and IBA.

Sample	Ge (at%)		Sb (at%)		Te (at%)		Sb+Te (at%)	
	WDXR ±0.35 at%	RBS ±1.0 at%	WDXR ±0.35 at%	RBS ±1.0 at%	WDXR ±0.35 at%	RBS ±1.0 at%	WDXR ±0.35 at%	RBS ±1.0 at%
GST225	23.7	23.7	22.7	23.9	53.6	52.4	76.3	76.3
GST225 + 35 at% Ge	59.1	58.9	12.5	14.3	28.5	26.8	41.0	41.1
GST225 + 48 at% Ge	69.8	69.5	9.7	10.8	20.5	19.6	30.2	30.4
GST225 + 53 at% Ge	75.6	75.2	8.0	9.2	16.4	15.6	24.4	24.8

Figure 4.6 shows the evolution of the Sb/Te ratio determined by PIXE as well as WDXRF. Whereas both techniques roughly highlight similar decrease of Sb/Te ratio with Ge content, the discrepancy between the quantified values extracted from the two techniques is not constant, ranging from 0.04 to 0.1.

In the case of WDXRF, the ratio Sb/Te as well as the chemical composition is determined by fundamental parameters by means of pure metals for calibration, and the statistical uncertainty being limited to ±0.4 at%. By contrast, the accuracy of the Sb/Te ratio by PIXE is certainly impacted by the low signal/noise ratio due to non-optimized counting time, low values of interaction cross sections and perfectible modeling of spectra with GUPIX.

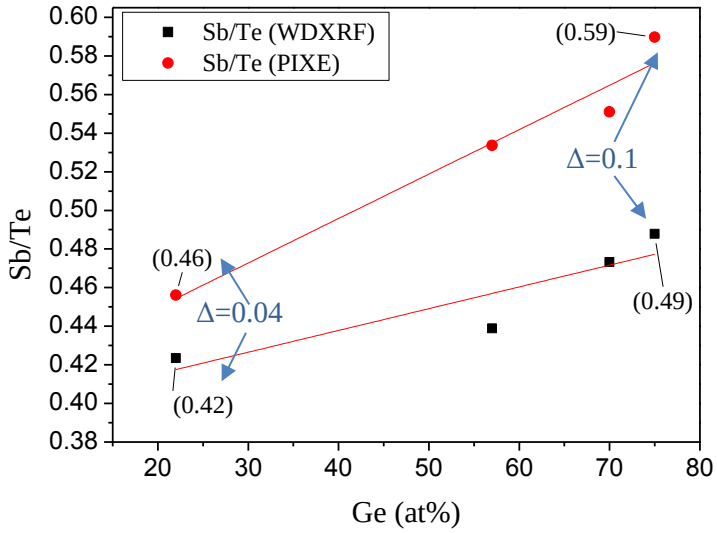

Figure 4.6. Evolution of Sb/Te ratio with increasing Ge content in Ge-Sb-Te compound, as quantified by WDXRF and PIXE.

As the of PIXE-deduced estimate of Sb/Te ratio were not aligned with expectation, we compared WDXRF and X-ray diffraction evaluations of Sb/Te ratios of crystallized Sb_xTe_y films investigated for IPCRAM. Kowalczyk et al [10] performed WDXRF chemical quantification of crystallized SbTe films sputtered from a Sb_2Te_3 target as function of Te content addition from a second target (Te) as co-sputtering deposited on 200 m Si (001) wafers. First, the film deposited without any addition of power

applied shows Te deficiency. The non-stoichiometry quantified by WDXRF (Fig.4.7.a) was confirmed by XRD diffraction (Fig.4.7.b), since its out-of-plane diffraction pattern cannot be indexed as Sb_2Te_3 crystalline phase. The addition of Te by co-sputtering yields a stoichiometric composition Sb_2Te_3 confirmed by XRD. All diffraction peaks of the out-of-plane diffraction pattern of the film deposited by co-sputtering can be indexed as (0 0 *l*) peaks (hexagonal indexation) of the Sb_2Te_3 rhombohedral phase, and it is in good agreement from literature values from bulk stoichiometric Sb_2Te_3 [11].

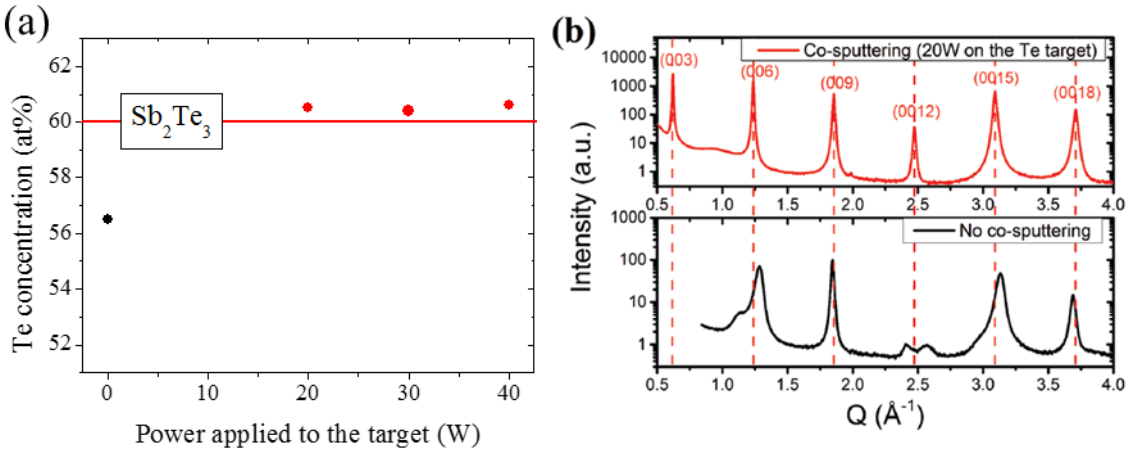

Figure 4.7 (a) Te concentration measured by WDXRF of 100 nm Sb_2Te_3 films as function of the power applied in the (Te) target, (b) Out-of-plane XRD patterns (λ = 1.4907 Å) in the $\omega/2\theta$ geometry for film without co-sputtering and with co-sputtering Te (20 W) [10].

In summary, WDXRF strategies based on FP metal using pure metals was demonstrated here, and we demonstrate it accuracy with 0.4 at% deviation related to RBS spectrometry. The separation of Sb from Te by PIXE for IBA quantification of the here elements revealed some 1.8 at% discrepancy compared to WDXRF, probably due to low signal to noise ratio of the PIXE spectra. Nonetheless, WDXRF accuracy to separate Sb from Te was demonstrated by quantifying crystallized Sb_2Te_3 film, confirmed by out-of-plane XRD analysis which was able to identify all diffraction peaks corresponding to Sb_2Te_3 rhombohedral phase.

4.2.2. Chemical quantification by XPS

We demonstrated in the previous section that WDXRF was able to meet < 1% accuracy in the compositional analysis of thin Ge-Sb-Te compounds. However, Lab and Fab WDXRF tools feature spot size from 10 to 40 mm, which excludes their use for measuring product wafers. In addition, even when using optimized measurement strategies for WDXRF, the accuracy of the compositional analysis might degrade slightly when probing GST films with thickness below 1 or 2 nm that can be deposited to investigate the first deposition steps. As a consequence, we developed XPS-based strategies for the compositional metrology of GST, since XPS is capable for measurement in areas of few $(10\ \mu m)^2$ with detection limit fully compatible with the analysis of sub-nm GST films. The remaining difficulty lies in the accuracy of the compositional metrology of GST using XPS. We'll demonstrate how WDXRF can be used to refine XPS relative sensitivity factors, resulting in more accurate XPS-based quantification of GST stoichiometry.

As discussed in chapter II, chemical quantification by XPS is usually performed by determining the sensitive factors (SFs) of the instrument for a specific component (element and defined core level). From chapter II section 2, we have seen that the calculated SF is implemented in the equation to determine the chemical concentration of elements as:

$$[A]\ at\% = \frac{\frac{I_a}{SF_a}}{\sum\frac{I}{SF}} \times 100 = \frac{\frac{I_a}{\sigma_a K_a \lambda_a}}{\sum\frac{I}{\sigma K \lambda}} \times 100 \quad \text{(eq. 4.2)}$$

Where [A] at% is the concentration of element A determined by measuring the net photoelectron intensity I_a of the core level of interest, σ_a is the photo-ionization cross-section, k_a is transmission function and λ_a is the attenuation length of photoelectrons of the core level of interest.

By default, XPS ThermoFischer theta probe 300 tool includes tabulated values from the Scofield library [5] as sensitivity factors, with sensitivity factor of C1s=1 as reference. The transmission function (k_a) is automatically determined in the ThermoFischer Avantage software, using a polynomial fit taking into account the measurement condition (e.g pass energy) and the kinetic energy of the photoelectrons. The attenuation length λ_a is calculated from the TPP-2M method [12].

Although chemical quantification by XPS can be straightforward as shown in eq. 4.2, accurate compositional metrology may still be challenging, not only because of the uncertainty of the matrix-dependent relative sensitivity factors of the various elements, but also because the information depth of the photoelectron signal can vary significantly with the kinetic energy of the photoelectron (information depth ranges from 1.5 to 7.5 nm typically in GST matrix using Al-Ka primary beam). The accuracy of XPS compositional analysis using photoelectrons of strongly different kinetic energies may be degraded by surface effects (segregation, oxidation …) and material in-depth non-uniformity at the nm scale.

A reasonable strategy lies in trying to select photoelectrons of elements coming from the same sampling depth, which results in similar values of transmission function and attenuation lengths and equal sensitivity to material in-depth non-uniformity. In addition, the selection of photoelectrons with the highest possible kinetic energy can help reducing the impact of surface effects (segregation, oxidation …).

In the case of Ge-Sb-Te films, the 30 to 50 eV region (in binding energy) includes core levels of all the elements of interest (Ge 3d, Te 4d, Sb 4d), with almost identical probing depth and transmission function, and high kinetic energy resulting in ~ 7 nm probing depth. In return, as reported in chapter III and illustrated in Fig 4.8, the compositional analysis using higher energy region may be strongly affected by oxidation: even a limited queue –time can induce overlap of Sb 4d states by Ge 3d (Ge-O) states, resulting in a difficult deconvolution of Ge and Sb contribution and degraded accuracy of the deduced stoichiometry. To avoid oxidation-related uncertainty, we used the *quasi-in-situ* XPS metrology protocol by means of vacuum carriers already explained in chapter III.

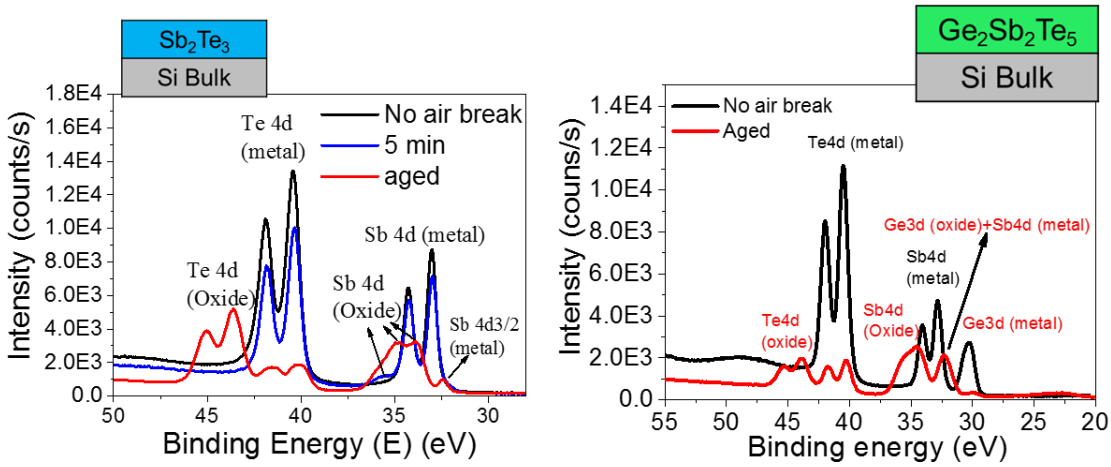

Figure 4.8. XPS spectra of Sb_2Te_3 and $Ge_2Sb_2Te_5$ without air break and after ageing. Composition-dependent oxidation kinetics must be carefully taken into account to allow for accurate compositional metrology

We used WDXRF quantification of thin binary (Sb_2Te_3, GeTe) and ternary ($Ge_2Sb_2Te_5$) films to adjust the XPS sensitivity factors for Ge 3d, Te 4d and Sb 4d core levels. The adjusted SFs were calculated by two approaches. The first one was based on the binaries GeTe and Sb_2Te_3. We first determine the sensitivity factor of Te keeping the Ge initial value, then we implemented the adjusted SF of Te into the function to determine the SF of Sb from the Sb_2Te_3. The equations of this approach are given by:

$$SF_{Te4d5/2(adjusted)} = SF_{Te4d5/2(XPS^0)} \times \left[\frac{SF_{Ge3d5/2(adjusted)}}{SF_{Ge3d5/2(XPS^0)}}\right]\left[\frac{\left(\frac{at\%_{Ge}}{at\%_{Te}}\right)WDXRF}{\left(\frac{at\%_{Ge}}{at\%_{Te}}\right)XPS^0}\right] \quad \text{(eq.4.3)}$$

$$SF_{Sb4d5/2(adjusted)} = SF_{Sb4d5/2(XPS^0)} \times \left[\frac{SF_{Te4d5/2(adjusted)}}{SF_{Te4d5/2(XPS^0)}}\right]\left[1/\frac{\left(\frac{at\%_{Sb}}{at\%_{Te}}\right)WDXRF}{\left(\frac{at\%_{Sb}}{at\%_{Te}}\right)XPS^0}\right] \quad \text{(eq.4.4)}$$

Where $SF_{Ge3d5/2(XPS^0)}$, $SF_{Te4d5/2(XPS^0)}$ and $SF_{Sb4d5/2(XPS^0)}$ are the initial values from the Scofield library, while $\left(\frac{at\%_{Ge}}{at\%_{Te}}\right)WDXRF$, $\left(\frac{at\%_{Sb}}{at\%_{Te}}\right)WDXRF$, $\left(\frac{at\%_{Ge}}{at\%_{Te}}\right)XPS^0$ and $\left(\frac{at\%_{Sb}}{at\%_{Te}}\right)XPS^0$ are the Ge/Te and Sb/Te ratios from WDXRF and XPS with initial SFs, respectively.

The second approach consists to determine the SFs from a ternary film $Ge_2Sb_2Te_5$ by adjusting the three SFs simultaneously with eqs. (4.3 and 4.4) until the quantification by XPS converges to the WDXRF one. Figure 4.9 shows Ge 3d, Sb 4d and Te 4d core-levels photoelectrons spectra for the GeTe and Sb_2Te_3 binary films as well as for the $Ge_2Sb_2Te_5$ ternary film. We used 20 nm-thick films amorphously by PVD on Si (001) wafers, with deposition parameters already described in Chapter III. *Quasi in-situ* XPS analysis were conducted (no air break) on these samples.

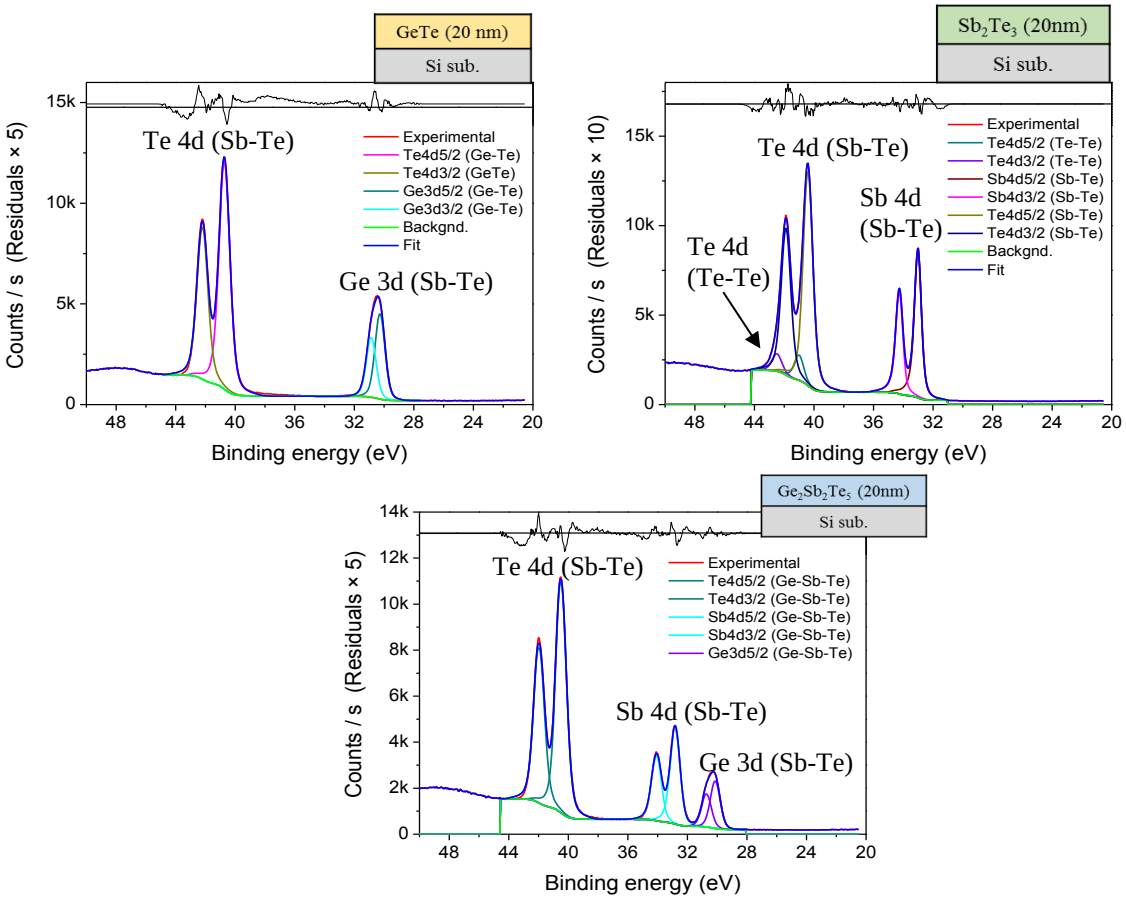

Figure 4.9. Peak deconvolution of GeTe, Sb_2Te_3 and $Ge_2Sb_2Te_5$ non-oxidized films.

Figure 4.10 shows the chemical quantification of the three films determined by initial and adjusted SFs compared to WDXRF quantitative analysis. To highlight the difference in chemical quantifications, we chose to show the quantitative analysis as deviation from WDXRF result ± at%.

Hence, from our XPS quantification, we can highlight that:

- Quantification of the composition of binary films (GeTe and Sb_2Te_3)
  - The discrepancy between WDXRF and XPS using initial values of SFs can be as high as 2.2 at% among all results
  - The composition of binaries using SFs adjusted from binaries of course results in exactly the same value as the WDXRF one, since we constrained the calculated SF_{Te4d} and SF_{Sb4d} in eqs. (4.3 and 4.4) using WDXRF quantification
  - The composition of binaries using SFs adjusted from both binaries and ternary samples results in optimized ≤ 1.0 at% deviation.

- Quantification of the composition of ternary film ($Ge_2Sb_2Te_5$)
  - The discrepancy between WDXRF and XPS using initial values of SFs can be as high as 1.4 at% among all results
  - The quantification from SFs adjusted from binaries do not allow to reduce the overall deviation with WDXRF (up to 1.3 at% deviation);
  - On the other hand, using SFs adjusted from both binaries and ternary samples results in optimized ≤ 0.3 at% deviation.
- In overall, the deviation between XPS-deduced and WDXRF-deduced quantification is reduced from 2.2 at% down to 1.0 at% when using WDXRF-based instead of tabulated values for XPS sensitivity factors.

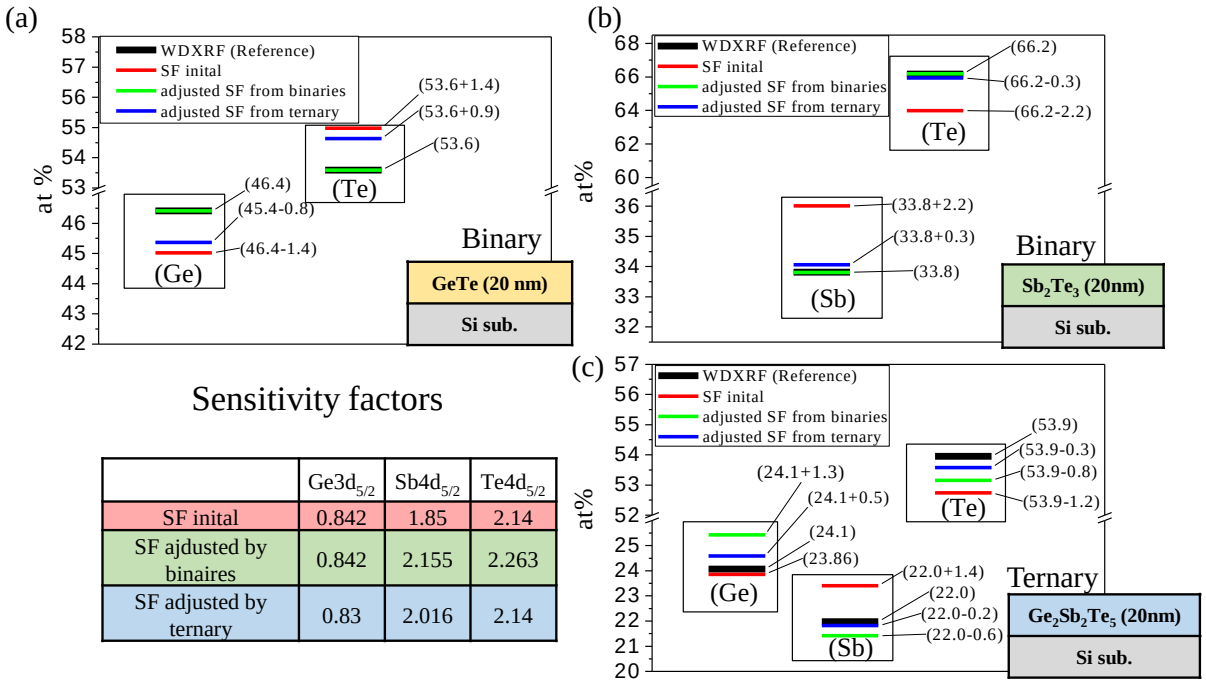

Sensitivity factors

	$Ge3d_{5/2}$	$Sb4d_{5/2}$	$Te4d_{5/2}$
SF inital	0.842	1.85	2.14
SF ajdusted by binaires	0.842	2.155	2.263
SF adjusted by ternary	0.83	2.016	2.14

Figure 4.10. Chemical quantification overview by WDXRF and sensitivity factors. WDXRF results (black line) are reference values, the other values are shown as WDXRF ± at% deviation.

We then used these optimized SF values to investigate the first deposition steps of amorphous $Ge_2Sb_2Te_5$ films deposited by PVD. Figure 4.11 shows the WDXRF spectra and the XPS spectra of samples deposited with 4, 8 and 12 seconds of process time, resulting in ~ 1, 2 and 3 nm film thickness. Note that 4 seconds is the time needed to complete a full rotation of the wafer in the process chamber, which is required to guarantee industry-compatible uniformity of the film at the wafer level.

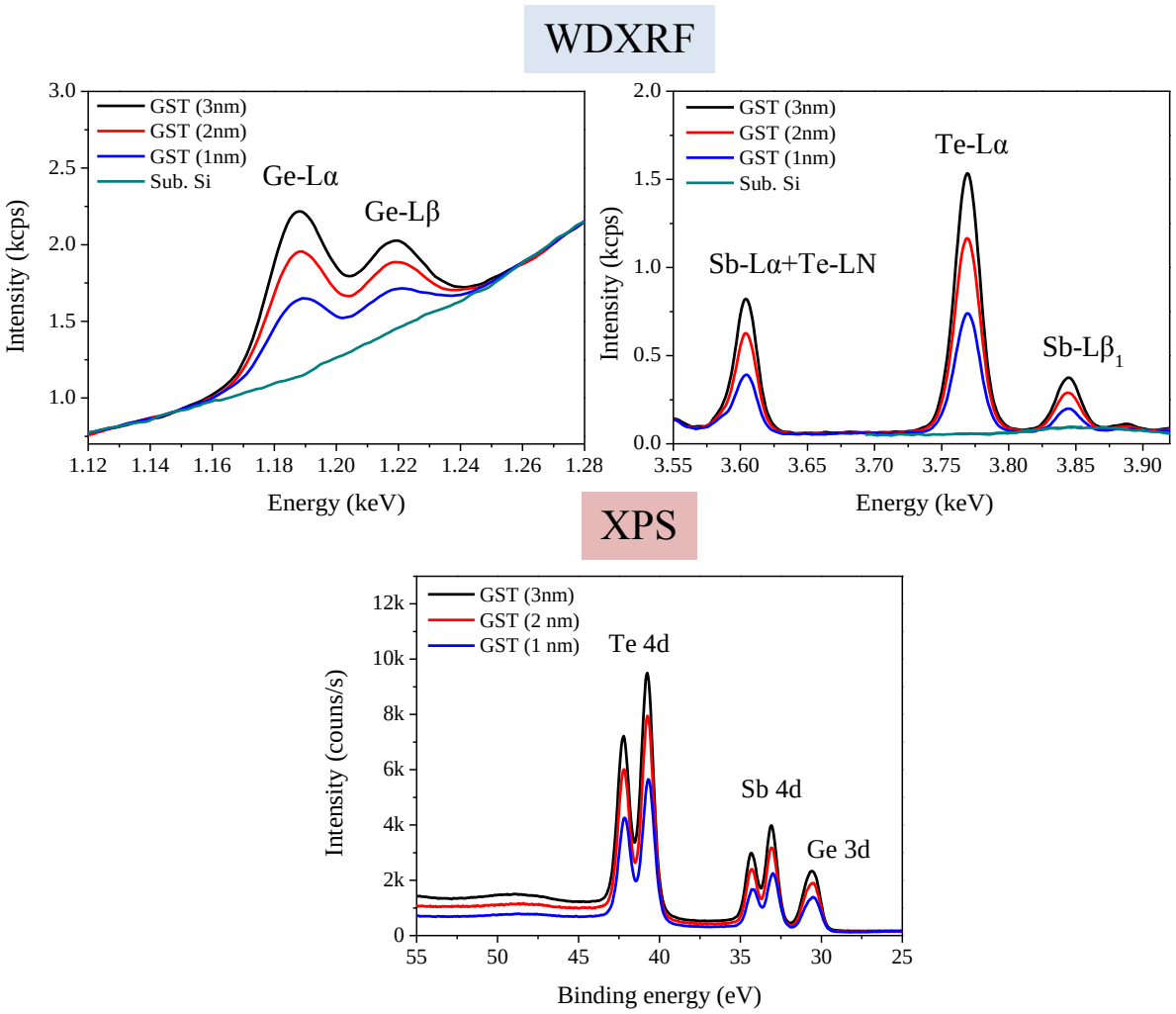

Figure 4.11. WDXRF and XPS spectra of ultra-thin GST films (1, 2 and 3 nm thick).

Figure 4.12 illustrates the chemical quantification of XPS and WDXRF techniques as a function of the film thickness. We can first observe reasonable agreement of the quantitative information deduced from the two techniques, as a maximum deviation of 1.4 at% observed for the thinnest film (1 nm), certainly due to the limited statistics in the WDXRF spectra. Both techniques indicates that the 1 nm thick film is slightly richer in Te (1.2 at% more compared to the 2 nm thick film, XPS analysis) and slightly poorer in Sb (0.7 at% less compared to the 2 nm thick film, XPS analysis), while Ge is approximately constant along the thickness.

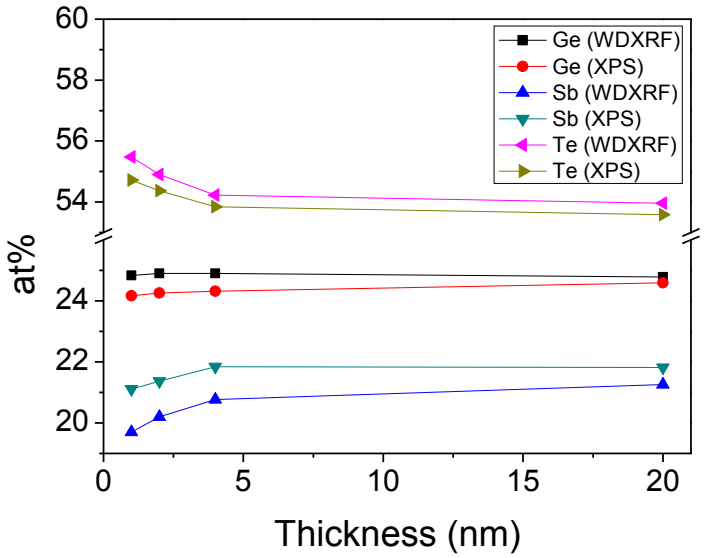

Figure 4.12. Chemical quantification of GST films from 1 to 20 nm thick.

In conclusion, we developed an XPS protocol using adjusted SFs based on WDXRF quantification. This protocol allowed us to reduce the deviation between XPS- and WDXRF-deduced quantification from 2.2 at% down to 1.0 at% for the 20 nm films (note that complementary work, not shown here, indicates that this deviation drops from 5.0 at% to 1.0 at% when dealing with Ge-rich GST materials). Finally, the combination of XPS and WDXRF allows to determine the composition of GeSbTe materials within 1.0% accuracy, for layers deposited on blanket or product wafers and with film thickness ranging from 1 nm to 200 nm at least.

Although the XPS quantification methodology proposed here was validated on non-oxidized homogenous films, it can still be employed to partially oxidized films, using appropriate deconvolution strategies that will certainly degrade the overall uncertainty.

4.3. Chemical quantification of N-doped Ge-Sb-Te films

As seen in chapter I, the addition of nitrogen in Ge-Sb-Te films increases the crystallization temperature as well as the activation energy of the crystallization, then improving the thermal stability of the amorphous phase of the film and its data retention. Therefore, N-doped GST films are valuable candidates for the embedded applications of PCM cells in the automobile industry where the information must be stored at elevated temperatures (10 years 150°C), whereas the $Ge_2Sb_2Te_5$ films have unsuitable low retention due to lower crystallization temperature.

Hence, the quantification of nitrogen on GST matrix is required to tune and then monitor the properties of the final film. Inline WDXRF operated under primary vacuum and featuring dedicated analyzing crystal with large *2d* values (synthetic crystal) is capable for detection of low-energy nitrogen fluorescence line (0.392 keV for N-Ka) simultaneously with contributions from the other constituents of the film (Ge, Sb, Te) as demonstrated in the previous section. However, WDXRF-based quantification of Nitrogen content in thin films with industry-compatible accuracy is highly challenging for the following reasons: i/ in the low energy range, X-ray fluorescence is not the predominant interaction, and therefore features low interaction cross sections, ii/ The energy resolution of crystals with large 2d is not suitable for low energy range, hence it makes more difficult to isolate the N-Kα contribution from M-lines of Sb and Te constituents on the matrix, iii/ the analysis may suffer from difficulty to take into account the different matrix effects (absorption of N-Kα in the matrix, enhancement due M-lines of Sb and Te, thickness-dependent effect of high-energy photoelectrons) as the literature does not provide extensive and accurate values for such corrections, iv/ the calibration needed for WDXRF to determine quantitative compositional information should be based either on Nitrogen pure element (of course not available) or samples from similar matrix as the final compound, with nitrogen contents accurately evaluated by other techniques.

In this section, we'll first highlight some of the major matrix effects relating to the analysis of nitrogen in Ge-Sb-Te compounds. Secondly, we'll discuss about the use of Ion Beam Analysis techniques to determine the composition of N-doped Ge-Sb-Te compounds as needed to calibrate WDXRF for the inline metrology of such complex compounds.

Figure 4.13 shows the WDXRF spectra in the 0.36 to 0.54 keV energy range corresponding to fluorescence region of N-Kα (0.392 keV), Sb-Mz (0.428 keV), Te-Mz (0.461 keV) and O-Kα (0.525 keV). We can first notice that the intensity of N-Ka, when using an analyzing crystal able to clearly separate the different contributions (RX45, 2d=11.09 nm) is very low even for 200 nm-thick N-doped GST films of different compositions (Te-rich, Ge-rich and Sb-rich GST materials, same target for N content ~ 5 at%). As a consequence, the contribution to statistical uncertainty to the final result may be significant, above all when dealing with thinner films (50 nm or below). In addition, the background of N-Ka line is strongly affected by the contribution of Sb-Mz and Te-Mz neighbor peaks, which increases the difficulty to accurately extract the integrated intensity of N-Ka in an inline fully-automated

metrology process, except in the case of WDXRF-based protocols dedicated to small variations around a target composition. Lastly, significant matrix-induced enhancement of N-Ka are expected, as the energy of Sb-Mz and Te-Mz are just above the energy of N-K edge (0.410 keV). The estimation of the matrix effect is rather complex in this energy range, especially since very little is available about Sb-Mz and Te-Mz lines: for instance, neither XRF yield nor cross section are accessible in XRay Lib.

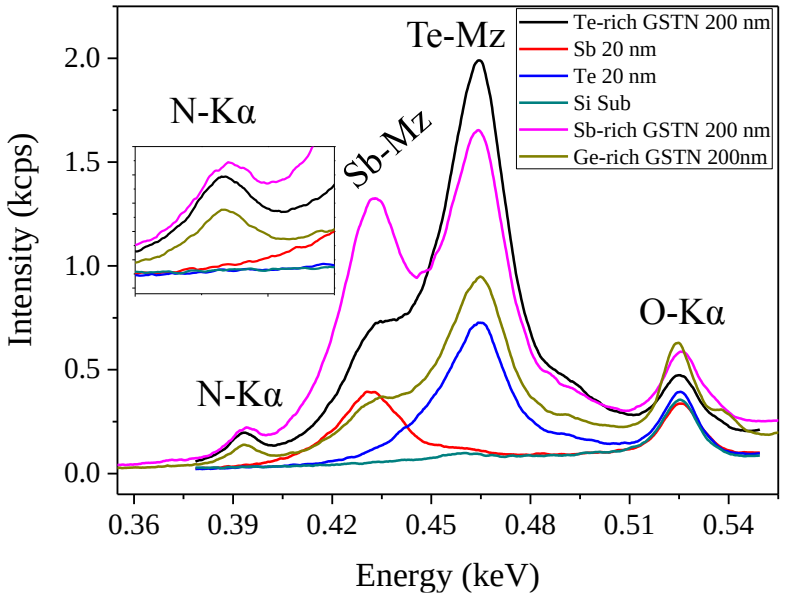

Figure 4.13. WDXRF spectra of N-Kα, highlighting the impact of neighbor contributions (Sb-Mz and Te-Mz) on the complex background for N-Kα.

Fig.4.14 illustrates the ability of WDXRF to reveal strong variation of nitrogen contents in 100 nm-thick Ge-rich GST films, which is the easiest case study since contribution of Sb-Mz and Te-Mz are minimized. The WDXRF sensitivity can be improved when choosing another analyzing crystal with smaller 2d value (5.44 nm instead of 11.09 nm), resulting in significantly higher intensity of N-Ka at the price of more complex convolution-related issues.

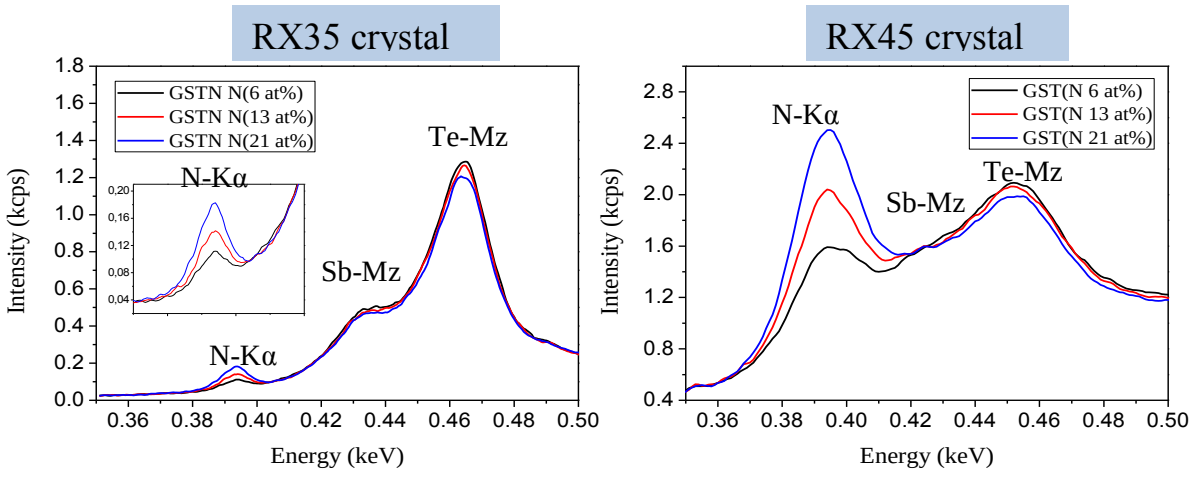

Figure 4.14. WDXRF spectra of 100 nm-thick Ge-rich GST layers with various N contents. We used two different analyzing crystals with different 2d values (5.44 nm for RX35, 11.09 nm for RX45), resulting in significant difference in terms of energy resolution and XRF intensity.

As N-doped Ge-rich GST materials were of primary interest for LETI developments during our PhD, we first focused on this material system. Fig.4.14 shows that the contribution of Te-Mz and Sb-Mz to the background of N-Kα is almost constant for constant layer thickness and Sb/Te ratio in the Ge-rich matrix, regardless the analyzing crystal.

We investigated the use of WDXRF quantification of N-doped Ge-rich GST layers using RX45 crystal so as to obtain the highest intensity for N-Kα. WDXRF analysis was based on Ge-Lα, Sb-Lβ_1, Te-La and N-Kα intensities. Pure Ge, Sb and Te samples were used for the calibration of the matrix elements. N-doped 100 nm Ge-rich GST films (Ge-rich GST, Ge-rich GST + N <10 at% and Ge-rich GST + N > 20%) were amorphously deposited by low temperature PVD on CLN 200 tool and then sent to Arcane laboratory (Bordeaux, France) for quantification of the stoichiometry of the film by Ion Beam Analysis, *i.e* RBS (for Ge and Sb+Te), PIXE (for Sb/Te ratio), and Nuclear Reaction Analysis (NRA) for nitrogen content. As discussed in the previous section, Sb/Te ratio deduced from PIXE were carefully refined using WDXRF measurement. The exact duplicates of the layers characterized by IBA were kept at LETI so as to build WDXRF calibration for N-Kα (Fig.4.15), taking IBA values as references. Note that the three GST layers dedicated to N-Kα calibration had been capped *in-situ* with 5 nm-thick tantalum layer in order to preserve them from long term ageing as part on inline WDXRF calibration set. *In-situ* capping with SiN would have not have been appropriate to probe N-doped GST films, and carbon capping was not available as this date. In addition, the potential effect of tantalum inter-diffusion on the intensity of the N-Kα should be very limited.

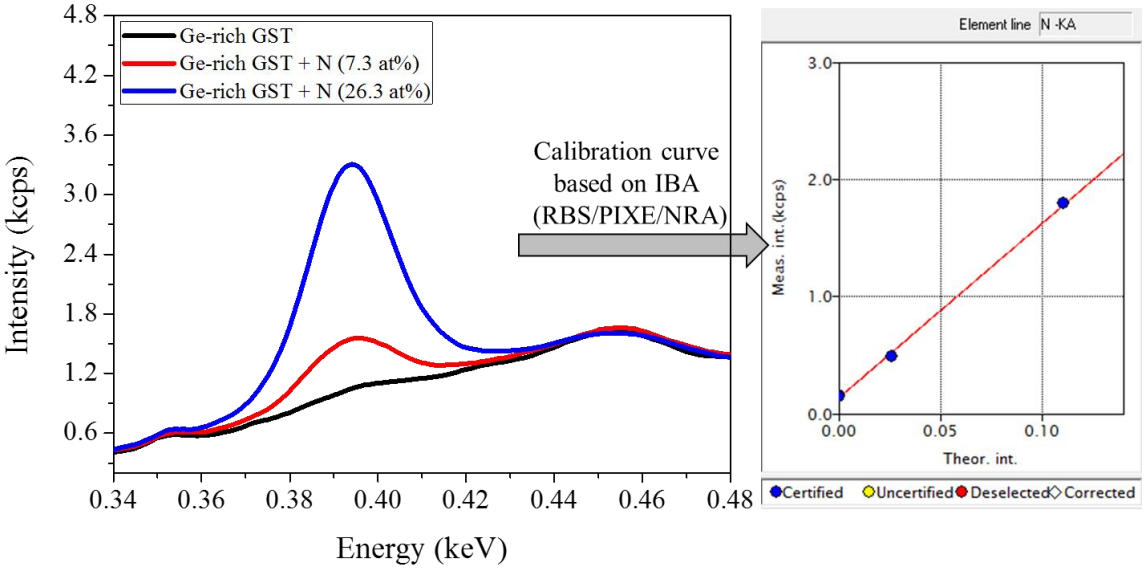

Figure 4.15. FP calibration curve for N-Kα is based on the N-Kα net intensities of un-doped and N-doped Ge-rich GST films, IBA-deduced quantification being taken as reference values.

In order to evaluate the WDXRF-based quantification strategy, 100 nm thick N-doped Ge-rich GST films were amorphously deposited on 300 mm Si (001) wafers by PVD (Applied Materials Endura 300). In total, five films were grown on Si wafers. All deposition parameters were kept constant, except to the nitrogen gas flow which was varied in order to increase the nitrogen content in the GST sample set.

The accuracy of the WDXRF analysis was evaluated by comparing WDXRF quantification with various Ion Beam Analysis. Three different laboratories were engaged to quantify these samples: two laboratories (lab.1 and lab.3) employed similar combination of IBA techniques: RBS for the Ge and (Sb+Te) contents and nuclear reaction analysis (NRA) for nitrogen concentration. The other laboratory (lab.2) used Elastic Backscattering Spectrometry (EBS) which is derivate of RBS but more sensitive to nitrogen when operated at a specific resonant energy (3.717 MeV). The details of the quantification methodology of each laboratory can be found in appendix B.

Figure 4.16 first illustrates the reasonable agreement between WDXRF and RBS for the quantification of Ge and (Sb+Te) content. The deviation is kept within ± 1% accuracy expect for GST film with highest Nitrogen content. For this specific film, discrepancy can even be noticed among IBA-deduced quantification (± 1.3 at %), WDXRF values falling in the global IBA range.

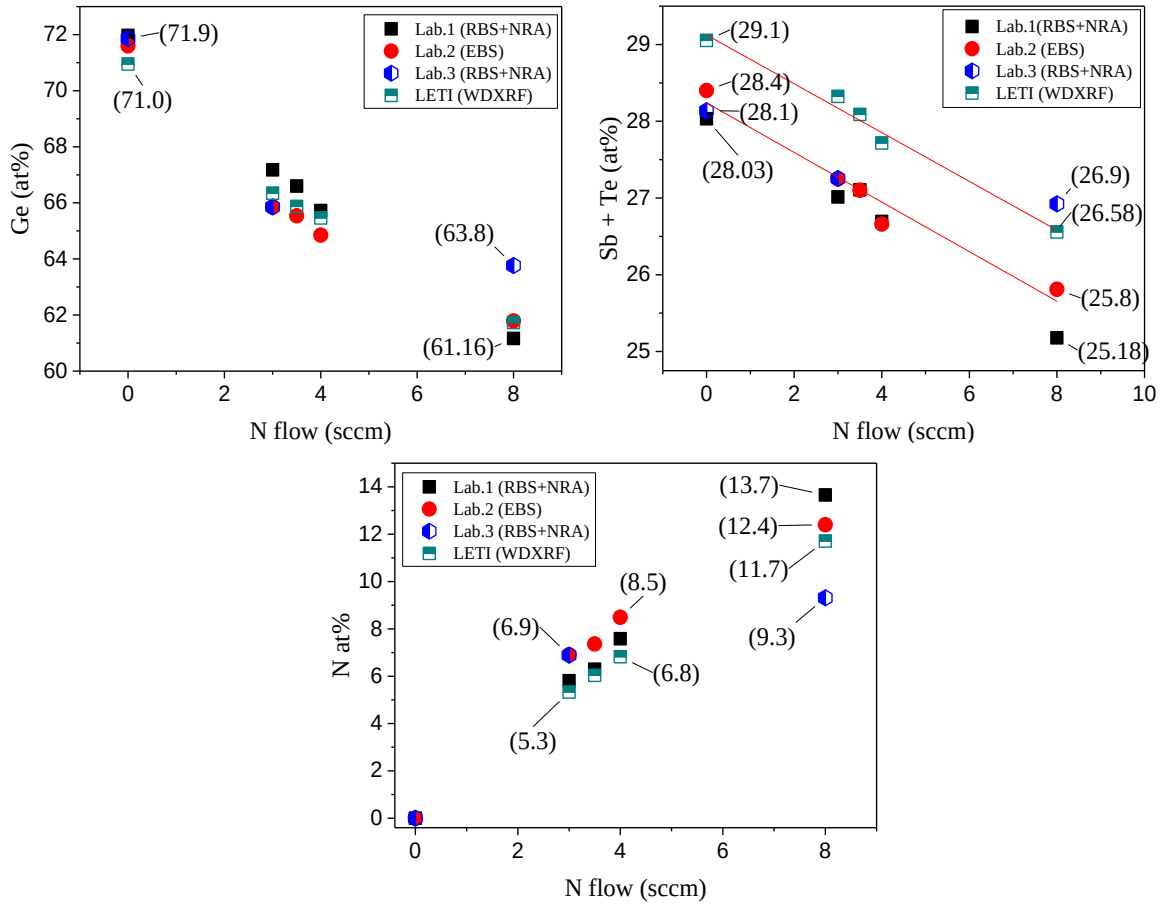

Figure 4.16. Quantitative analysis of N-doped Ge-rich GST films by WDXRF and IBA

Concerning IBA analysis, the major (unexpected) difficulty relates to the huge discrepancy of nitrogen contents determined by the different laboratory from exact duplicate samples. The highest discrepancy is found between Lab.1 and Lab.3 results for GST sample with highest N content: the absolute deviation of 4.4 at% result in ±20% relative uncertainty, which is not compatible with industry-driven requirements. As we can see from Fig.4.16, this discrepancy tends to increase with nitrogen content. This high deviation between lab.1 and lab.3 might be related to the nitrogen quantification method by NRA. Both laboratories calculate the N concentration (at/cm^2) through a linear ratio between the measured spectra and their own standard (Si_3N_4), and this sensitive curve dictates the deduced N

concentration. Figure 4.17 shows how different the NRA sensitive curves from lab.3 and lab.1 can be, resulting in significant deviations in the quantified values of nitrogen content. We cannot guarantee that this only factor is responsible for this deviation as we are lacking exact information about the way sub-contracting laboratories 1 and 3 convert the spectra intensity in N concentration (at/cm^2). Moreover the spectra intensity of each laboratory are not straightforward comparable, since they come from different instruments. Lastly, as already noticed about PIXE data for estimates of Sb/Te in GST materials, the poor statistics of NRA data (Figure 4.17) might not be fully aligned with targeted accuracy in the Nitrogen quantification.

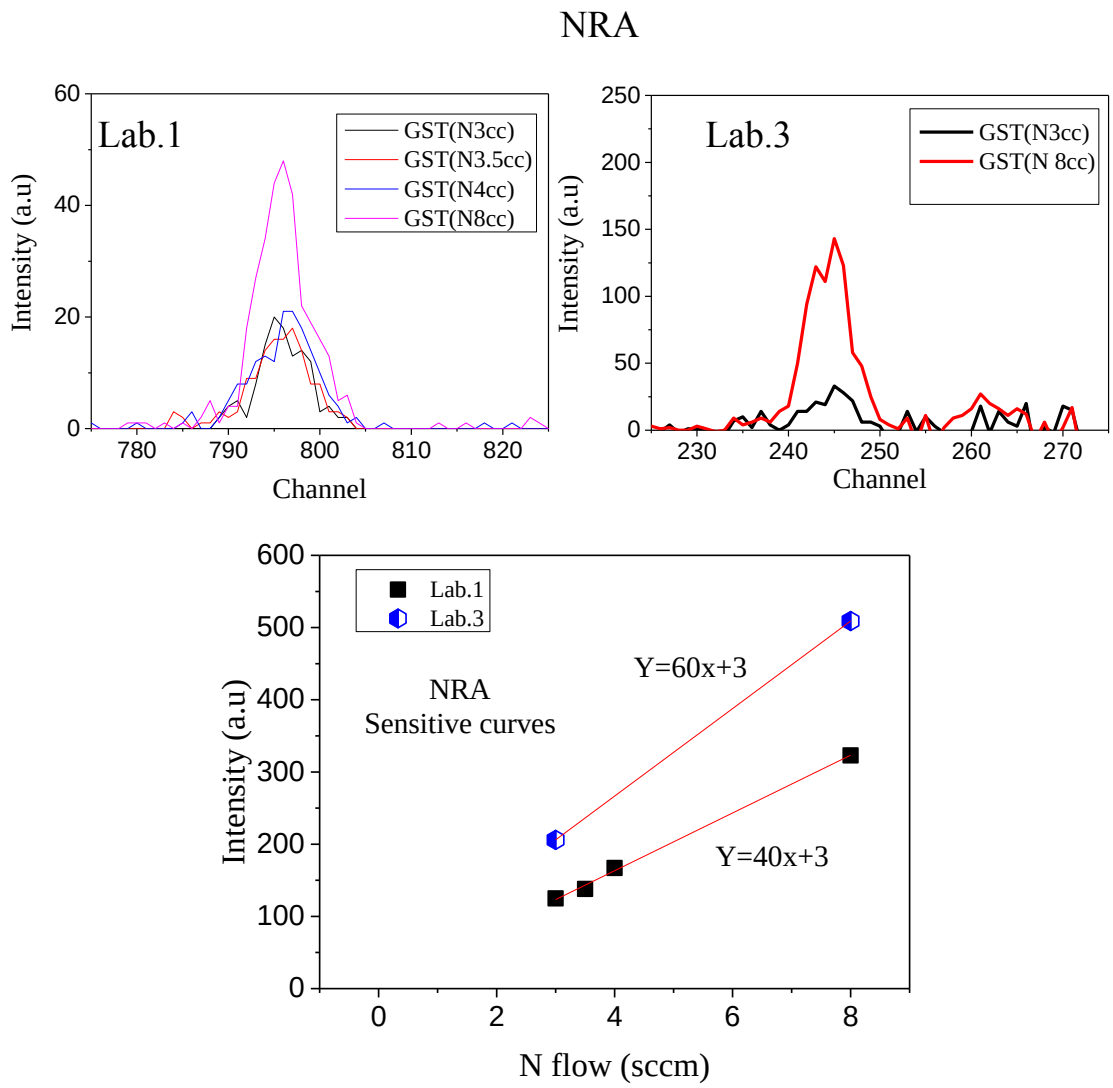

Figure 4.17. NRA analysis conducted at Lab.1 and Lab.1 feature poor statistics and noticeable differences in the NRA sensitive curve for nitrogen quantification.

Inline WDXRF tool at LETI uses non monochromatized hard X-ray beam from a rhodium tube. When high energy X-ray photons (for instance at the energy of the Rh-Ka line, *i.e* 20.216 keV) are absorbed by an atom of the Ge-Sb-Te matrix in an inner shell, photo-electrons are emitted which carry the energy-difference between the photon and the electron's binding energy. As a consequence, a large amount of high energy photoelectrons (up to 20 keV) are generated during the WDXRF analysis of N-

doped GST materials, these photoelectrons being able to excite the fluorescence of light elements such as nitrogen [26] In addition, the probing depth of these photoelectrons is rather high (> 50 nm) due to their high energy.

We have not been able to rigorously investigate this thickness-dependent matrix effect. However, we briefly studied the impact of varying the thickness of N-doped GST layer on the WDXRF quantified results deduced from preliminary calibration reported above. Figure 4.18 shows spectra acquired from samples having the same deposition conditions (fixed N2 flow for doping Te-rich GST, *i.e* GST225), with increased sputtering time so as to tune the deposited thickness of the amorphous films. As illustrated in Figure 4.18, the progressive increase of layer thickness induces a substantial increase on N-Kα intensity, and a noticeable variation of the related background, due (at least partially) to Te-Mz and Sb-Mz contribution in these Te-rich layers. High-resolution analyzing crystal was used to probe these films in order to limit deconvolution concerns.

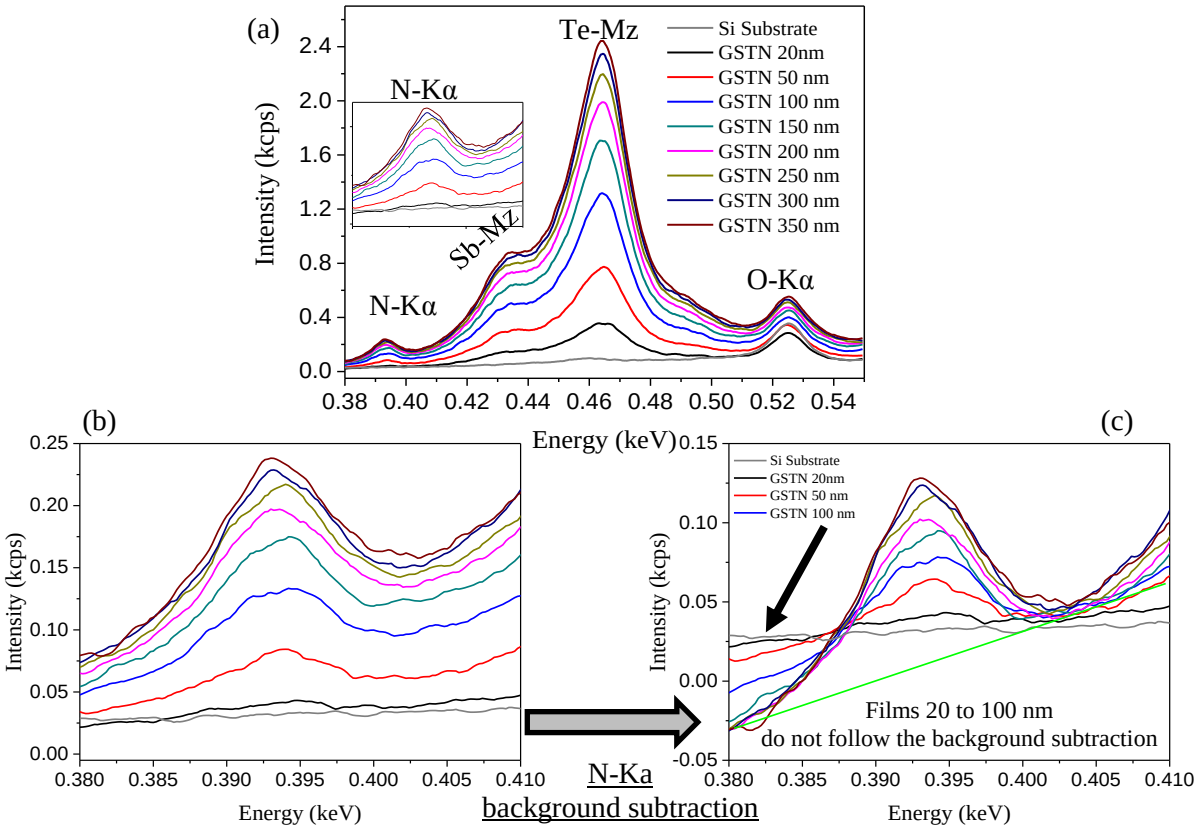

Figure 4.18. Influence of film thickness on N-Kα spectra. Background subtraction may be handled by two points straight-line in a first approximation.

We tried to remove the thickness-dependent background, using linear approximation in a very short energy range as a first approximation (Figs. 4.18b and c). This correction did not apply correctly for GSTN films ranging from 20 up to 100 nm, whereas a first estimate of N-Kα intensity was possible for thicker films. As a result, the chemical quantification presented here after features significant uncertainty, especially for thickness below 100 nm.

We took into account the background subtraction to determine N-Kα net intensities, and used previously elaborated N-Kα calibration based on N-doped Ge-rich GST films instead of Te-rich films, with no guarantee in terms of accuracy.

Figure 4.19 shows the WDXRF-deduced N content as function of thickness. Although the nitrogen flow (5.6 sccm) was kept constant for all the wafers, WDXRF results suggest that the nitrogen concentration gradually increases with thickness in the 20 to 100 nm range, then almost stabilized for thicker films at ~13 at%.

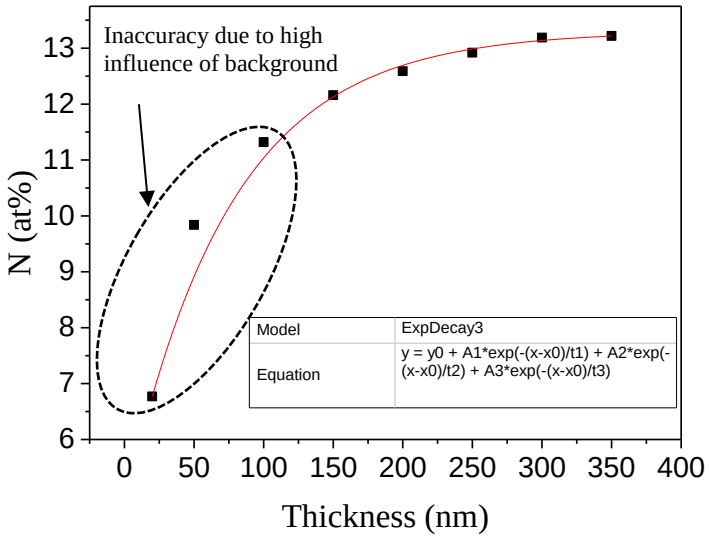

Figure 4.19. Nitrogen quantification by our quantitative method. Although it is not accurate, N seems to follow an exponential increase with thickness.

The analysis was further complemented with Fourier Transform Infrared Spectroscopy (FTIR), as shown in Fig.4.20. The analysis gives the film absorption of the Ge-N bonds vibrating at 690 cm^{-1}, normalized by the film thickness. We can see that regardless the film thickness, we have the same Ge-N intensity, which means the same Ge-N density bonds for all the films (despite the high signal to noise ratio for the 20 nm film). Therefore, the nitrogen content variation observed by WDXRF is not conclusive, since it is highly impacted by the background and matrix effects.

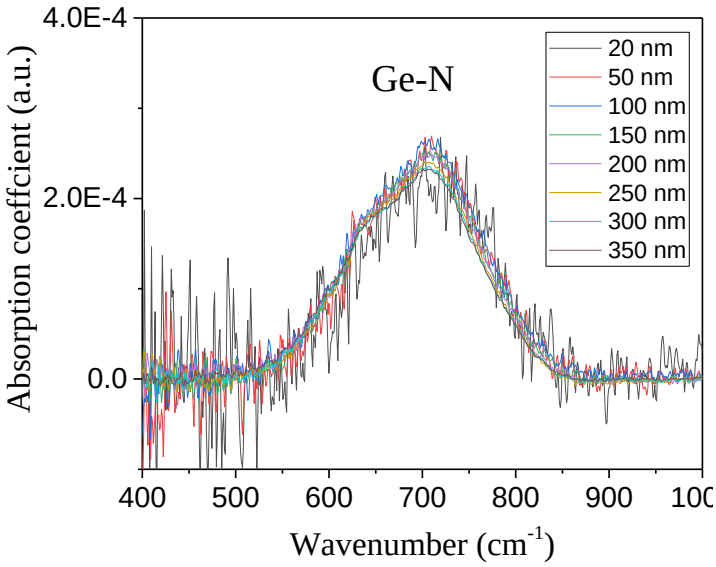

Figure 4.20. FTIR spectra of Ge-N bonds vibrating at 690 cm^{-1}.

In summary, we investigated the use of WDXRF for the quantification of nitrogen in Ge-Sb-Te matrix. We demonstrate that the quantification of N-doped Ge-rich films thicker than 100 nm was definitely accessible with WDXRF, even though the accuracy of the deduced nitrogen content may be discussed. One unexpected conclusion of this work is the unexpected variability of the nitrogen content deduced from IBA techniques that should have been considered reference techniques able to feed WDXRF calibration with accurate values and mastered uncertainties. Further interaction with IBA experts is definitely needed in order to improve the accuracy of IBA-deduced quantitative information for low-Z elements. We also pointed out the complexity of WDXRF-based analysis of Te-rich and Sb-rich N-doped GST films due the predominant influence of obvious (impact on background) and hidden (secondary fluorescence, high energy photoelectrons) matrix effects. Further work will be conducted in the next years on this specific topic, including systematic comparison with FTIR-based analysis.

4.4. Probing WS_x films (2D Transitional Dichalcogenides)

4.4.1. Introduction

As discussed in chapter 1, 2D Transition Metal Dichalcogenide materials (TMDCs) are receiving an extensive interest for applications ranging from electronics to energy storage, and they are often referred as “next-graphene generation”. Although TMDCs are easily synthetize as “bulk” materials, they exhibit unique electrical and optical properties only when thinned down to few atomic layers [13]. Up to now, the synthesis of 2D TMDCs monolayers has been reported either through micromechanical exfoliation [16] or by high-temperature CVD [14, 15]. These methods are not well suited for industrial production due to the lack of homogeneity and reproducibility at the wafer scale [16].

A novel route to synthetize 2D TMDCs is under development at the nano-chemistry laboratory in École Supérieure de Chimie Physique Électronique (CPE) Lyon in partnership with CEA-LETI by the 2D factory project [23]. The method called pulsed-MOCVD works similarly to MOCVD, nonetheless the chalcogenide (*i.e*. sulfur) precursor is introduced into the reaction chamber periodically as a pulse. Hence, dedicated metrology needs to be developed to evaluate the chemical composition, deposited mass and surface/interfaces effects of ultra-thin films grown by this method. We introduce a non-destructive metrology strategy based on the combination of WDXRF and XPS to probe ultrathin sulfur-based materials. We first investigate the accuracy of this protocol by comparison with Ion Beam Analysis and reference-free XRF conducted at PTB, the German National Metrology Institute. Then we demonstrate the use of such metrology strategy to assist the optimization of the deposition parameters of the pulsed-MOCVD method by evaluating the impact of substrate-WS_2 interaction, temperature deposition, from the very first deposition steps.

4.4.2. Chemical quantification for Sulfur-based films

- WDXRF chemical quantification

The calibration of WDXRF for the quantitative analysis of sulfur-based films cannot include sulfur pure element sample since such sample cannot be produced as a standard. Therefore, we used the default sensitivity factors included in the embedded library of Rigaku software, which allows uncertainty ranging from 5 to 20% depending on the probed element and measurement conditions.

In order to better estimate the uncertainty induced by the use of default sensitivity factor for sulfur, we first compared the composition of 550 nm thick germanium sulfide (GeS) film amorphously deposited by PVD as deduced from WDXRF and RBS.

Ge-Kα and S-Kα lines were selected to characterize this half-micron thick layer. As illustrated in Fig.4.21, both spectra feature linear background, high net intensity for the XRF lines of interest, without noticeable contribution of any satellite or diffraction peak. The statistical uncertainty is less than 1% (3σ) for 30 seconds counting time, and instrumental setup uncertainty ±0.35 at% calculated from equipment repeatability (100 times measurements on the same spot). The FP analysis used default sensitivity factor for S-Kα, whereas the sensitivity factor for Ge-Kα was determined using a pure germanium sample. The GeS composition evaluated by WDXRF was: 43.0 at% Ge and 57.0 at% S, with S/Ge ratio of 1.34.

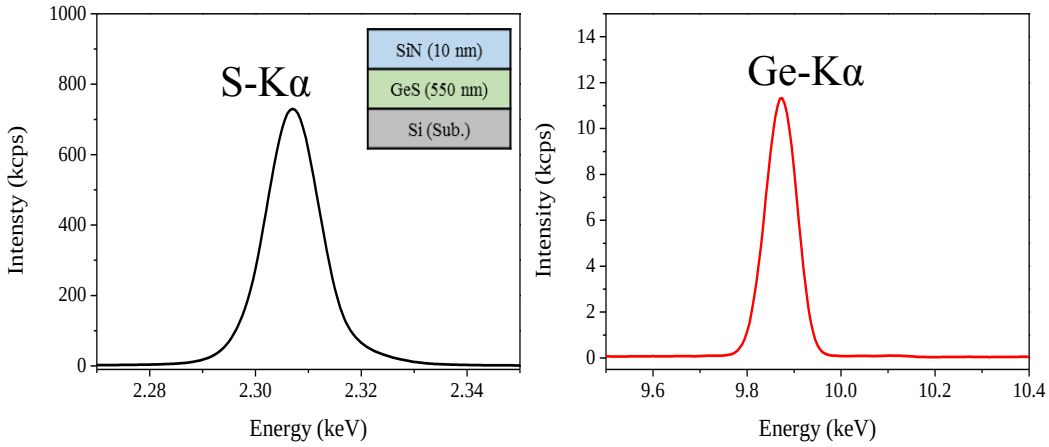

Figure 4.21. S-Kα and Ge-Kα of 550-nm thick GeS film capped with 10-nm thick SiN layer to avoid oxidation.

The RBS measurement was performed in the same conditions as for the GeSbTe films, that is: 2.0 MeV He^+ beam with detector positioned at 160° (from initial direction) and sample tilted 5° to avoid channeling (more details is found in annex B). Figure 4.22.a shows the well-separated Ge and S contributions with very good signal to noise ratio, while graph on Fig. 4.22.b compares the RBS quantification with the WDXRF one. From Fig. 4.22.b, we can see that Ge and S quantified by WDXRF using default sensitivity factors for sulfur is 3.0 at% off when compared to RBS reference values.

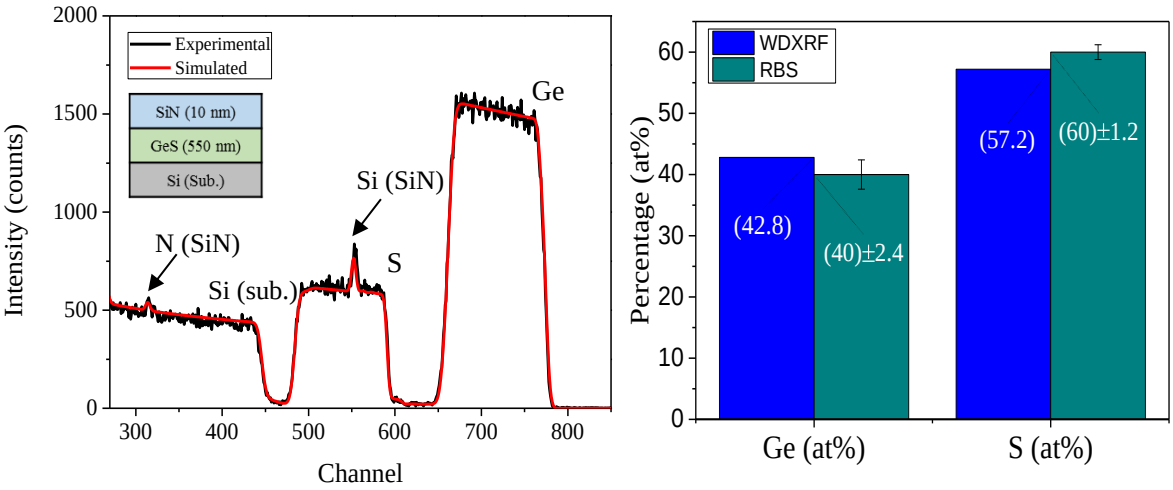

Figure 4.22. (a) RBS spectra of SiN capped GeS film, (b) chemical quantification of WDXRF is reasonable agreement with RBS results, 3% accuracy. The uncertainty associated to RBS data were calculated by the RBS subcontractor (Arcane Laboratory, Bordeaux, France)

Secondly, we estimated the ability of WDXRF to accurately probe ultrathin 2D sulfur-based materials using molybdenum sulfide (MoS_x) layers grown by Atomic Layer Deposition [23] by increasing the sulfur content on the MoS_x deposits (condition a, b, c). As illustrated in Fig. 4.23.a, the analysis of MoS_x films requires a high-resolution (few eV) WDXRF setup so as to allow the appropriate deconvolution of Mo-Lα and S-Kα contributions. The significant impact of the increase of S content in these ~ 1 nm-thick samples is shown in Fig.4.23.b. The FP analysis used default sensitivity factor for S-Kα, whereas the sensitivity factor for Mo-Lα was determined using a thin and smooth molybdenum layer deposited by PVD on a silicon substrate. This thin layer was characterized by XRR so as to access the deposited mass (calculated as product of XRR-deduced thickness and mass density) that was included in the WDXRF calibration scheme.

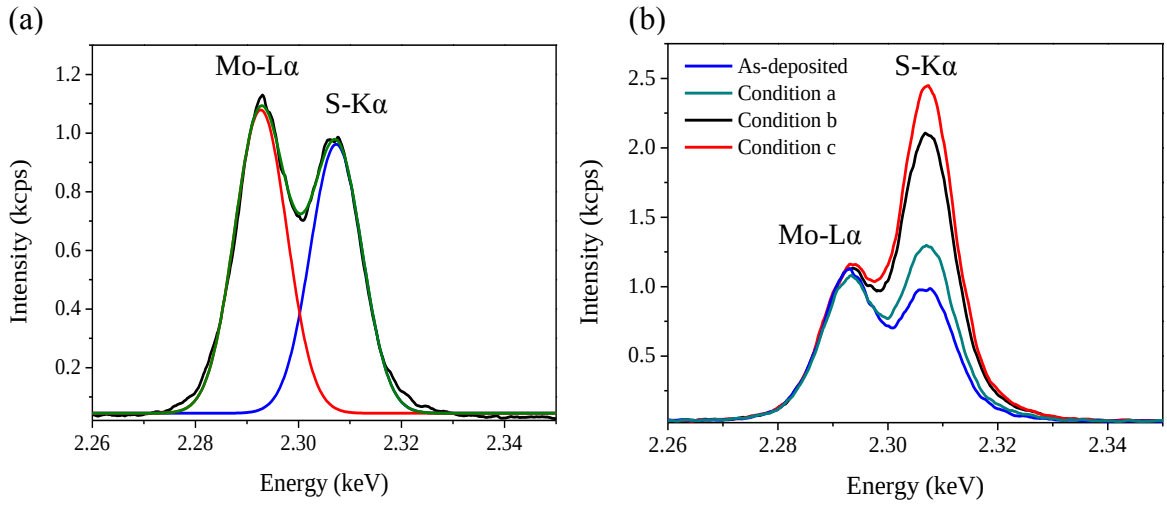

Figure 4.23. WDXRF spectra of MoS_2 with deconvolution of S-Kα and Mo-Lα contributions. The significant impact of the increase of S content in these ~ 1 nm-thick samples is shown in (b)

Once analyzed at LETI using WDXRF, the films were sent to the German National Metrology Institute (PTB) in order to get reference values with mastered uncertainties for the composition of MoS_x films. The chemical quantification was performed by reference-free XRF at the Metrology Light Source (BESSY II synchrotron, Berlin). This setup uses energy-dispersive XRF, which resolution (~ 90 eV) limits its ability to accurately discriminate Mo-Lα from S-Kα contributions. In order to overcome this difficulty, PTB took advantage of the tunable monochromatic excitation at the Metrology Light Source to run two successive XRF experiment on each sample, first using 2510 eV as primary energy to selectively excite the sulfur below Mo-L3 edge, then moving to 2575 eV, slightly above Mo-L3 edge, so as to excite both S-K and Mo-L XRF lines (Fig. 4.24). The measurements were performed in an irradiative chamber with 7-axis of rotation (similar as Castor analytical chamber at LNHB). The fluorescence signals were acquired in grazing incidence geometry, using irradiation angle of 2° with respect to the sample surface.

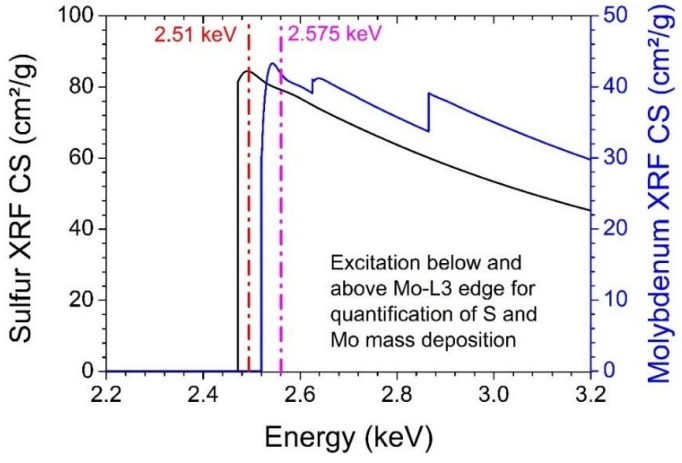

Figure 4.24. Photo-absorption cross sections of S and Mo elements from X-ray lib [4].

The reference-free XRF analysis [18] was accessible at PTB by virtue of the use of mastered instrumental uncertainties (radiometrically calibrated detectors and well-known excitation conditions) which allows the quantification of the deposited mass and the composition of layered materials without the need of any standard or calibration sample [19].

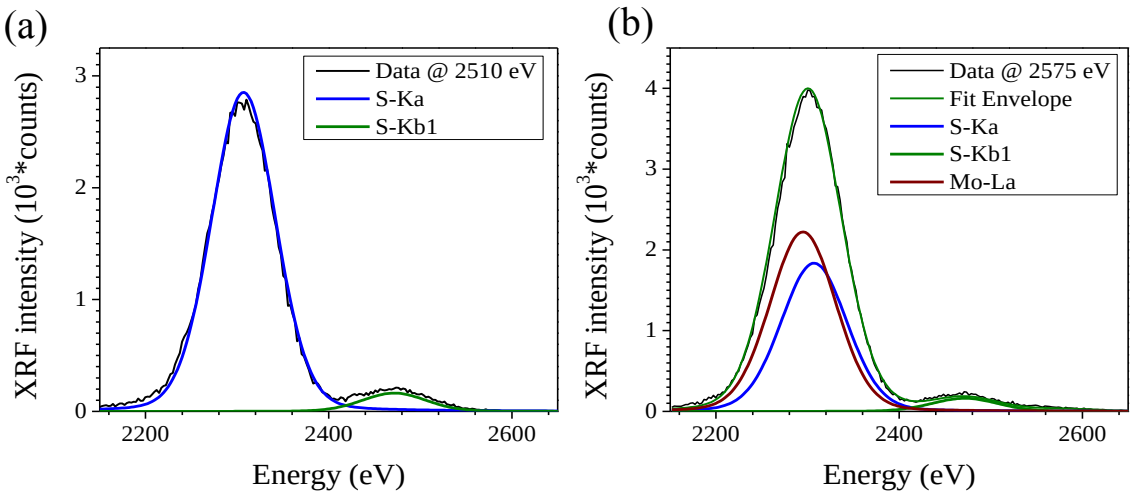

Figure 4.25. (a) S-Kα and S-Kβ_1 fluorescence spectra recorded at primary energy below Mo-L3 edge, (b) S-Kα, S-Kβ_1 and Mo-Lα contribution of the XRF spectra acquired at 2575 eV. Appropriate deconvolution was realized at PTB using extensive knowledge of the characteristics of the energy dispersive detector

Fig. 4.25 shows XRF recorded below and above the Mo-L3 edge, with highlight of appropriate deconvolution (PTB analysis) of the S-Kα, S-Kβ_1 and Mo-Lα contribution of the XRF spectra acquired at 2575 eV. Figure 4.26 synthetizes the quantitative results obtained from WDXRF and GIXRF at PTB. We can see that WDXRF results fall in the uncertainty of PTB results, which is mostly driven by the uncertainty of the fundamental parameters of S-K and Mo-L.

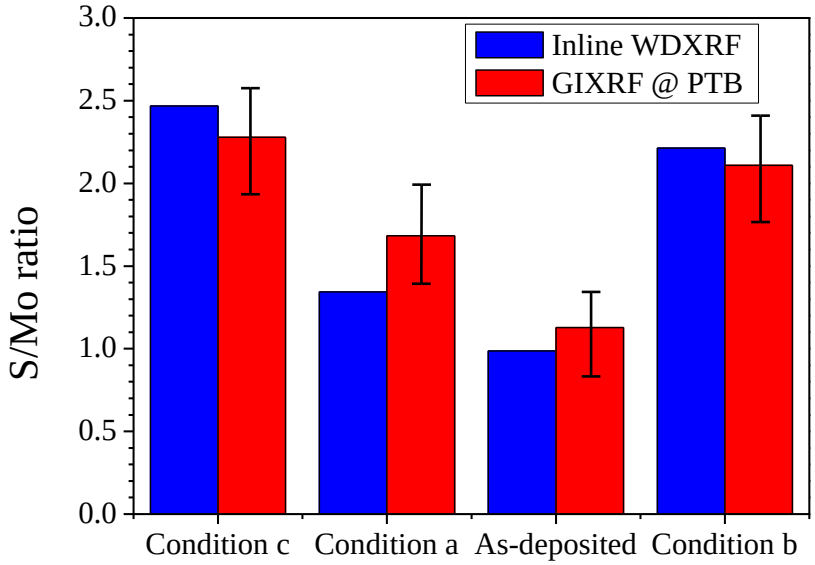

Figure 4.26. Quantitative analysis (S/Mo ratio) obtained at LETI and PTB showing that WDXRF results fall in the uncertainty of PTB results.

- XPS chemical quantification

Since we are probing just few nanosheets of dichalcogenide-based films, XPS is highly suitable not only to study the surface/interfaces effects of 2D TMDCs but also for the chemical quantification. As already discussed in the Ge-Sb-Te section, XPS quantification can be achieved using sensitivity factors from Scofield library [5] or refined values of such sensitivity factors.

In the case of MoS_2 films, the XPS quantification can be performed by probing the Mo 3d and S 2p core-levels. Sulfur S 2p environment only contains contribution from S-Mo binding states, whereas Mo 3d mostly contains Mo-S states, with slight contribution of MoO_3 oxidized states (Fig.4.27).

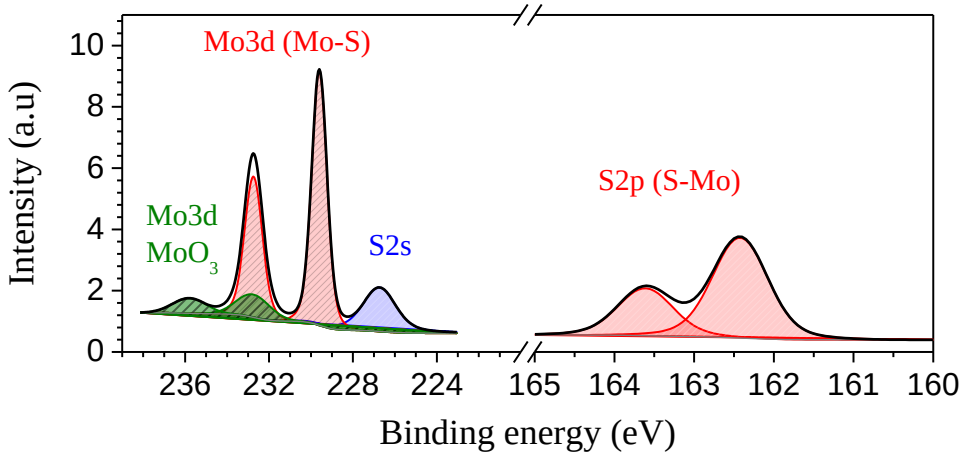

Figure 4.27. XPS spectra of MoS_2 film annealed at 800°C illustrate the predominant contribution of Mo-S binding states

The composition of MoS_x films can be determined by XPS using different strategies that may lead to slightly different results:

- First, we may consider the sum of Mo-S and Mo-O states as the contribution of molybdenum. In this case, we determine S/Mo ratio irrespective of the binding states, which results in XPS quantification being very close to WDXRF results (Table 4.3) as WDXRF quantifies the concentration of all atoms present in the film.
- However, process developers are mostly interested in the S/Mo defined from the metalloid states (S-Mo and Mo-S), therefore excluding the MoO_3 contribution, which of course leads to differences (depending of the amount of MoO_3 that should be as limited as possible) between XPS and WDXRF quantified compositions. Note that WDXRF would perfectly fit with the need of fast, operator-compatible mapping of S/Mo ratios at the wafer level, either just after MoS_2 process (limited queue-time) or using a thin dedicated capping layer to protect the 2D material from ageing.
- Lastly, S/Mo ratios from metalloid states can also be calculated using the correlation between the difference of binding energy of Mo $3d_{5/2}$ and S $2p_{3/2}$ and the S/Mo ratio. This correlation (Fig. 4.28) has been drawn by Baker et al. [20] by careful use of XPS and RBS investigation of preferential sputtering of powder-like MoS_2, sulfur being the atom preferentially sputtered.

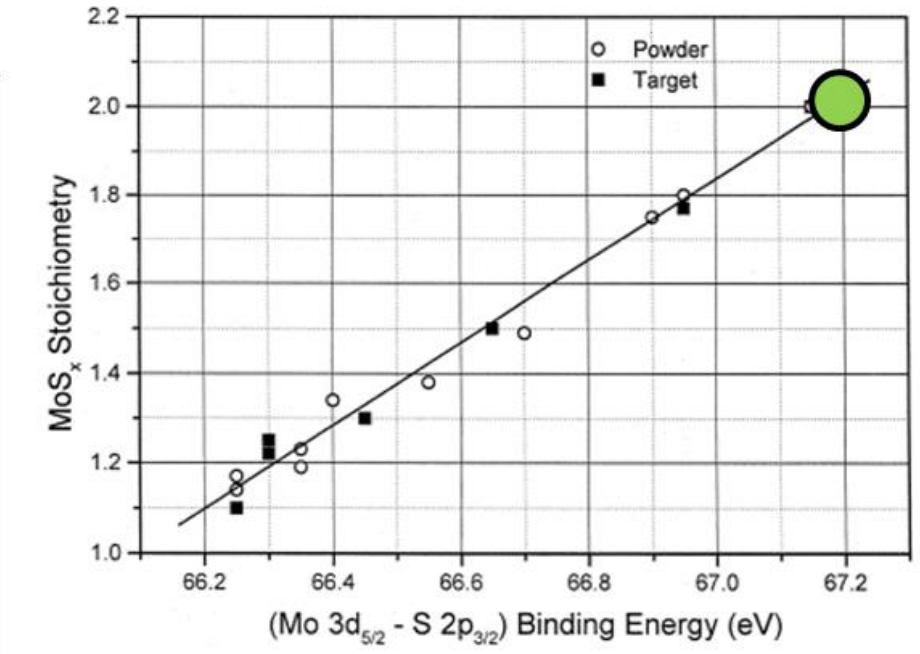

Figure 4.28. Linear dependence between MoSx stoichiometry and binding energy difference (Mo $3d_{5/2}$-S $2p_{3/2}$). Values related to optimized MoS_2 sample annealed at 800°C are illustrated by a green disc [20].

Table 4.3. S/Mo ratios obtained by WDXRF and XPS for optimized MoS_2 sample annealed at 800°C

Method	**S/Mo (%at)**
WDXRF	1.8
XPS (S/(sum Mo), sum is Mo-S with Mo-O	1.8
XPS (S/(Mo)), Mo is only Mo-S	2.0
XPS ($Mo3d_{5/2}$ – $S2p_{3/2}$) from Baker et al [20]	2.0

In overall, the stoichiometry of MoS_x samples obtained by inline XPS analysis (irrespective of the binding states), inline WDXRF using default sensitivity factor for S-Kα and reference-free GIXRF conducted at PTB are well-aligned, as illustrated in Fig. 4.29. Thanks to this extensive study for accuracy validation, these two protocols can provide unambiguous results for chemical quantification of 2D TMDCs. Therefore, in the next section we demonstrate the use of such metrology strategy to assist the optimization of the deposition parameters of the pulsed-MOCVD WS_2 process.

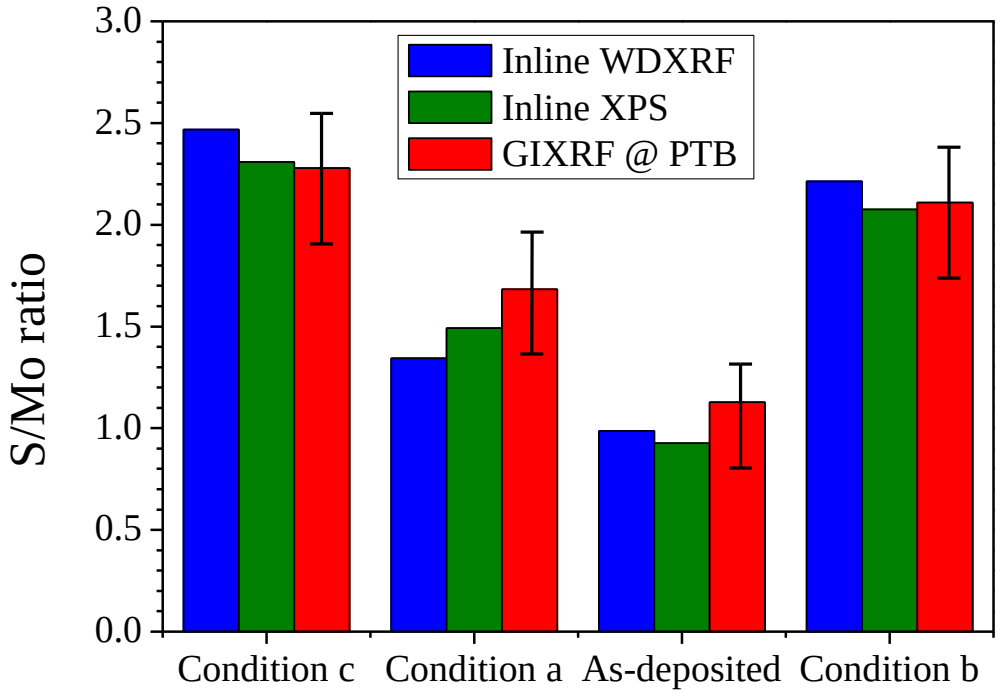

Figure 4.29. Overview of quantitative estimates of S/Mo ratio. PTB only provides mastered uncertainty that are mainly driven by the uncertainty of the fundamental parameters of S-K and Mo-L.

4.4.3. Case study: evaluating WS_2 grown by pulsed MOCVD

Pulsed MOCVD is a variant of MOCVD, where one of the precursors is injected into the reaction chamber in a pulsed regime. The typical deposition procedure consists to saturate the precursors at room temperature (RT) by gas flow (Argon or H_2) and conduct them into the reaction chamber at 10 Torr. The substrate is submitted to 220 °C temperature (below decomposition of the W precursor: $W(CO)_6$); $W(CO)_6$ is then introduced during three minutes followed by 1,2-ethanedithiol 1 min pulse every 2 min (Fig. 4.30). In this case study, tungsten sulfide films were grown on sapphire (Al_2O_3) and SiO_2 (275nm SiO_2/Si) substrates. The film deposition was performed in a homemade hybrid CVD/ atomic layer deposition reactor developed in the frame of CPE-LETI collaboration (Fig.4.30). The precursors employed for the film deposition was $W(CO)_6$ (99%, from Strem Chemicals) and 1,2-ethanedithiol (EDT ≥98% from Sigma Aldrich). As-deposited samples were stored in an argon-filled glovebox and only handled in air for quick transfer steps. Annealing was performed in a quartz tube at 800°C under 100 sccm of ultrapure argon flow.

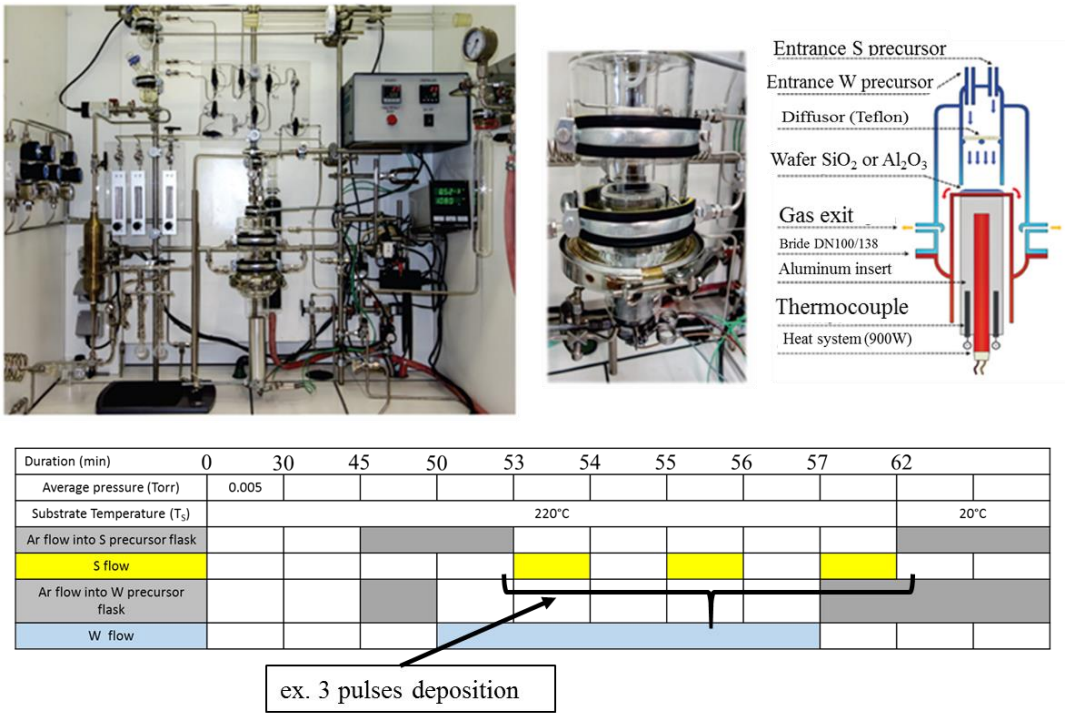

Figure 4.30. Pulsed-MOCVD apparatus (above) and typical deposition procedure (below).

Table 4.4 summarizes the set of samples conducted in this study. The process conditions were investigated by varying one parameter at time. In total, 3 set of samples were elaborated, so as to study the substrate reactivity, the first deposition cycles and the influence of the process temperature. The films were characterized by WDXRF for chemical quantification, (S/W ratios) and deposited mass (µg/cm^2). X-Ray Photoelectron Spectroscopy (XPS) was performed to study surface/interface effects and for complementary estimate of S/W ratios.

Table 4.4. Description of the process conditions for the three set of WS_x samples.

Set of samples	Nb. Cycles (pulses)	Growth temp. (°C)	Annealing temp. (°C)	Goals
#1 (2 samples)	1	200	800	<u>Study of Substrate reactivity</u> Growth on Al_2O_3 or SiO_2 • Sample 1.a. WS_2/ Al_2O_3 • Sample 1.b. WS_2/SiO_2
#3 (8 samples)	1	100-250	No	<u>Influence of Growth temperature</u> • Sample 2.a. WS_2/Al_2O_3 (150 °C) ... • Sample 2.e. WS_2/Al_2O_3 (220 °C)
#2 (5 samples)	1-21	200	800	<u>Study of first growth cycles</u> • Sample 3.a. WS_2/Al_2O_3 (1 cycle) … • Sample 3.e. WS_2/Al_2O_3 (21 cycle)

4.4.3.1. Influence of substrate composition

In order to study the reactivity between the precursors and the substrates, we probed two WS_2 samples grown on same conditions, sample 1.a (growth onto Al_2O_3) and sample 1.b (growth onto SiO_2). The WDXRF quantitative analysis were realized through measurement of W-Lα, W-Mα and S-Kα fluorescence lines intensities. In the case of W, the W-Lα overlaps with diffraction peak from silicon substrate (Fig. 4.31.a), which puts the need to use a thin titanium foil on the primary beam, therefore reducing the probability of diffraction at this specific energy. However, the titanium filter also decreases drastically the W-Lα intensity (Fig. 4.31.b), resulting in significant values of counting time in order to maintain statistical uncertainty $3\sigma = 1\%$ for net XRF intensity.

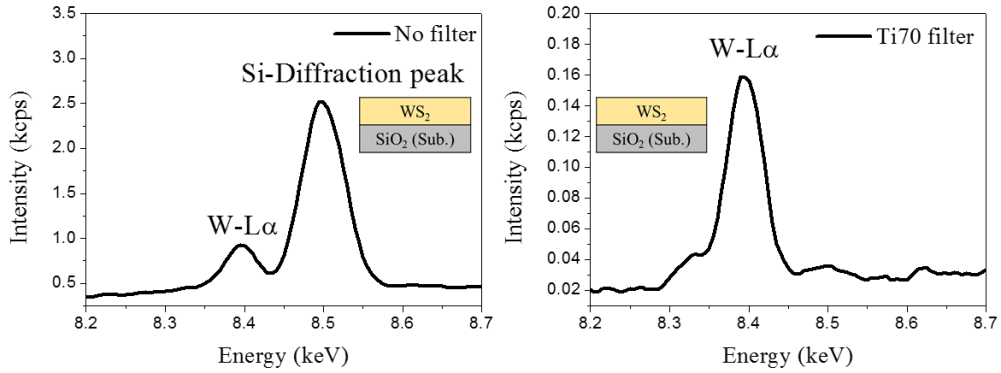

Figure 4.31. W-Lα spectra of thin WS_2 layer grown on SiO_2/Si substrate. The use of primary filter consisting in thin titanium foil is required to avoid the undesirable contribution of substrate-induced diffraction.

Another solution is to probe W through W-Mα fluorescence line. As shown on Fig. 4.32 for WS_2 deposited on sapphire substrate, the W-Mα spectra does not overlaps with any other peak, features a linear background. In addition, the intensity of W-Mα largely exceeds W-Lα one for ultrathin layers (gain is ~ *20), which allows significantly better sensitivity and detection limit. Nonetheless, this approach is only possible for WS_2 films grown on Al_2O_3 substrate, as W-Ma is totally hidden by Si-Kα XRF lines in the case of SiO_2/Si substrate.

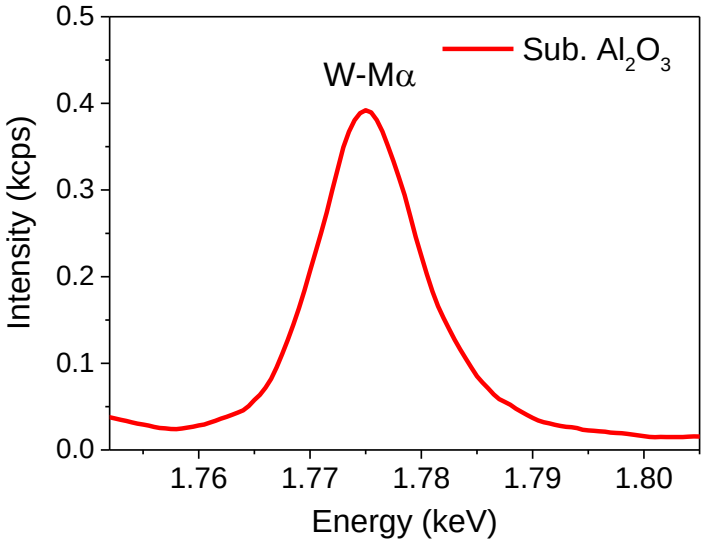

Figure 4.32. W-Mα spectra of sub-nm WS_x film deposited on sapphire.

Table 4.5 shows the quantitative data deduced from WDXRF, FP analysis using default sensitivity factor for S-Kα, whereas the sensitivity factor for W-Lα (or W-Mα) was determined using a pure tungsten sample. This table shows that the numbers of W atoms deposited on SiO_2 substrate is less than when deposited on Al_2O_3 substrate (4 tungsten atoms compared to 9.6 atoms, respectively). In the case of SiO_2 substrate, tungsten atoms deposition occurs on silanol groups [21] whereas, for sapphire, the carbonyl groups from W precursor interacts with the Al^{3+} sites which exhibit Lewis acid behavior, hence favoring more W atoms to be deposited as depicted in Fig. 4.33 and eq. 4.5. The deposition of W is more promoted on sapphire due the higher surface density of Al^{3+} sites when compared to the density of silanol groups on SiO_2 substrate. Furthermore, the lattice parameter between c-plane sapphire and WS_2 is in well agreement [22], allowing crystalline domains to be better controlled than onto SiO_2 amorphous substrate.

Table 4.5. WDXRF quantitative analysis.

Sample	Mass per unit area (µg/cm2)	Number of W atoms per nm^2
WS/SiO_2	0.135	4 atoms
WS/Al_2O_3	0.335	9.6 atoms

$$M(CO)_6 + Al^{3+}{}_{surf} \rightarrow (CO)_5M\text{-}CO\ldots Al^{3+} \quad \text{(eq.4.5)}$$

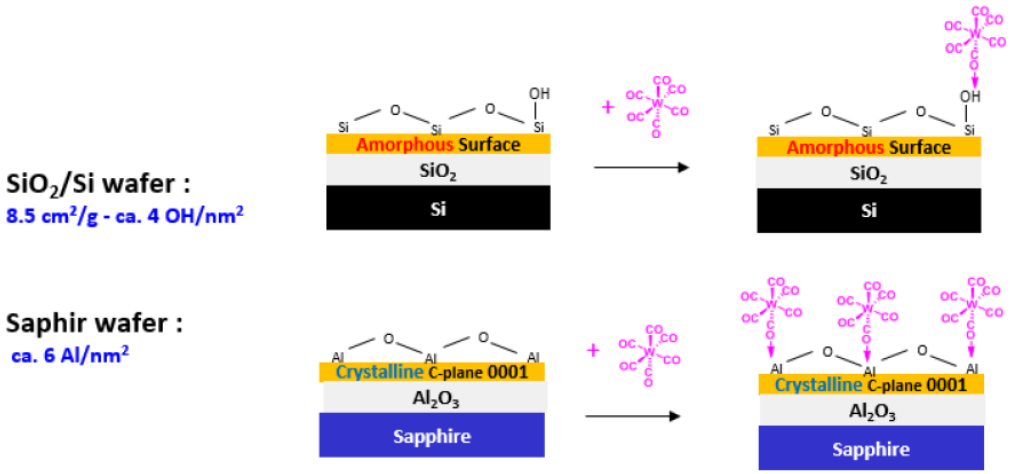

Figure 4.33. Different sorption effect of the $W(CO)_6$. In the case of SiO_2, the reaction occurs mostly with silanol groups, whereas onto Al_2O_3 substrate, the precursor interacts with all the sites Al^{+3}.

4.4.3.2. Influence of temperature deposition

The temperature of the process chamber plays an important role in the film growth, as it drives the decomposition of precursors: in the case of too low temperature, the reaction is less efficient and no deposition occurs, whereas if the temperature is too high the reaction is definitely achieved but the deposited thin layer might be non-stoichiometric. The temperature-dependent mechanism of WS_2 deposition is depicted in Fig. 4.34: i/ in the low temperature regime, the quantity of W atoms adsorbed is equivalent to the quantity of Al_2O_3 substrate sites, hence covering the total surface of the substrate; ii/ at higher temperature, stack of W atoms is promoted by carbonyl precursor decomposition due to activated decarboxylation with temperature.

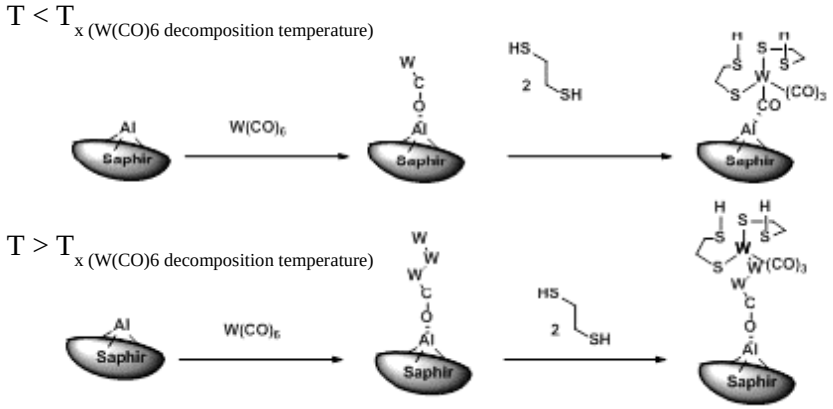

Figure 4.34. Illustrative scheme of the $W(CO)_6$ decomposition and final compound after reacting with sulfur precursor (ETD).

The influence of process temperature was investigated by WDXRF and XPS. WDXRF was used to access the deposited mass of W and S along with the composition of the ultrathin layers, whereas XPS allowed to investigate surface/interface effects.

Figure 4.35 shows the WDXRF results obtained from Tungsten Disulfide deposits (second set of samples from table 4.4) with temperature deposition ranging from 175-250 °C. We can see in Fig. 4.35 that from 150 to 175° barely no elements are deposited, then deposited mass progressively increases with the temperature, from 0.183 at 190°C up to 0.911 µg/cm^2 at 220°C. In the 190-200°C temperature range, the W atoms are completely adsorbed onto the Al_2O_3 sites, which results in constant deposited mass as measured by WDXRF. Above this range, the deposited mass increases linearly, which corresponds to the second mechanism described in Fig. 4.34. We can also note that the S/W ratio decreases with the temperature, which confirms the hypothesis that $W(CO)_6$ decomposition leads to stacks of W atoms.

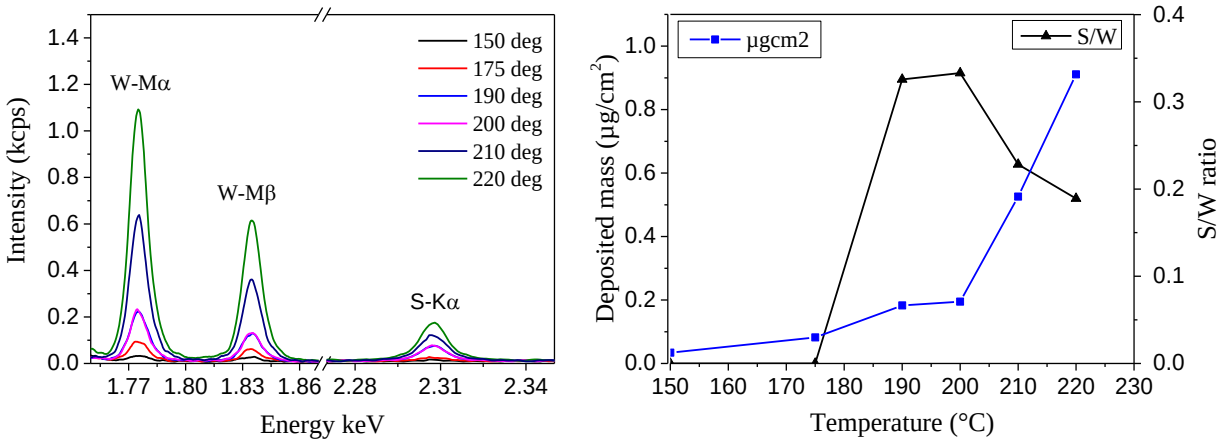

Figure 4.35. Evolution of WDXRF spectra with deposition temperature. WDXRF-deduced quantitative results (right) first show highlight the 190-200°C range where W atoms are completely adsorbed onto the Al_2O_3 sites, and decrease of S/W above this temperature range due to the $W(CO)_6$ decomposition leading to stacks of W atoms.

XPS analysis is illustrated in Fig. 4.36. In the entire temperature range, tungsten is mostly found in oxidized state (WO_3), which might be related to the interaction between $W(CO_6)$ and Al_2O_3 sites that leads, at low temperature, to the formation of oxides. We can also see that above 200 °C the intensity of W metalloid states ($W4f_{7/2}$ 32 eV) increases due to the $W(CO)_6$ decomposition leading to stacks of W atoms, as described above.

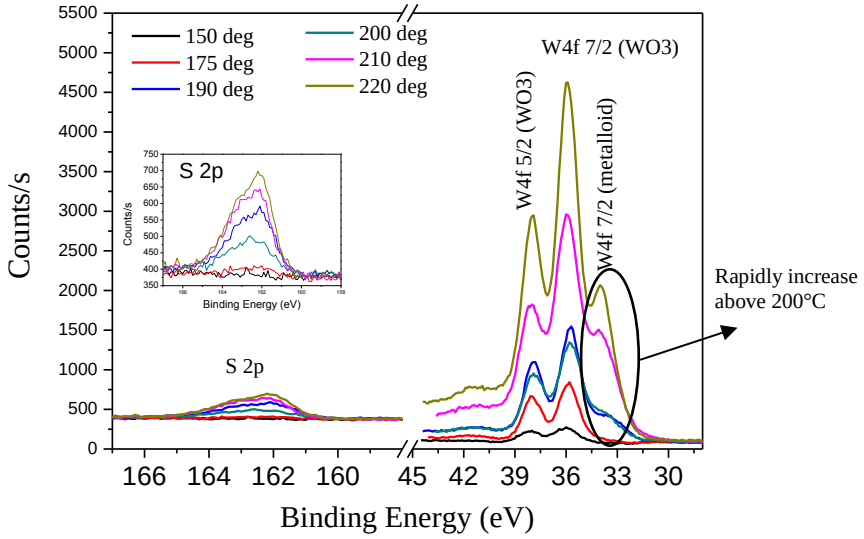

Figure 4.36. Evolution of XPS spectra (S 2p and W 4f core-levels) with deposition temperature.

4.4.3.3. Probing the first growth cycles (pulses) of deposited layers

The first deposition cycles of tungsten sulfide process were investigated by probing WSx films from 1 to 21 deposition cycles. XPS analysis based on high-resolution spectra of W 4f core-level shows that the doublet ($4f_{7/2}$-$4f_{5/2}$, 32.7 and 34.8 eV, respectively) corresponding to oxidized states (WO_3) is stronger for the first deposition cycles, as illustrated in Fig. 4.37. Indeed, the estimate of S/W with XPS (Fig. 4.37) using tabulated Scofield sensitivity factors shows that sulfur-poor films are grown during the first deposition cycles probably due to the fact that the first W atoms are covalently bounded to the Al_2O_3 substrate so as to form tungsten oxide. Similar behavior was observed in previous works on deposition of ultrathin MoS_2 [18, 23]. This results were confirmed by WDXRF analysis (Fig. 4.38).

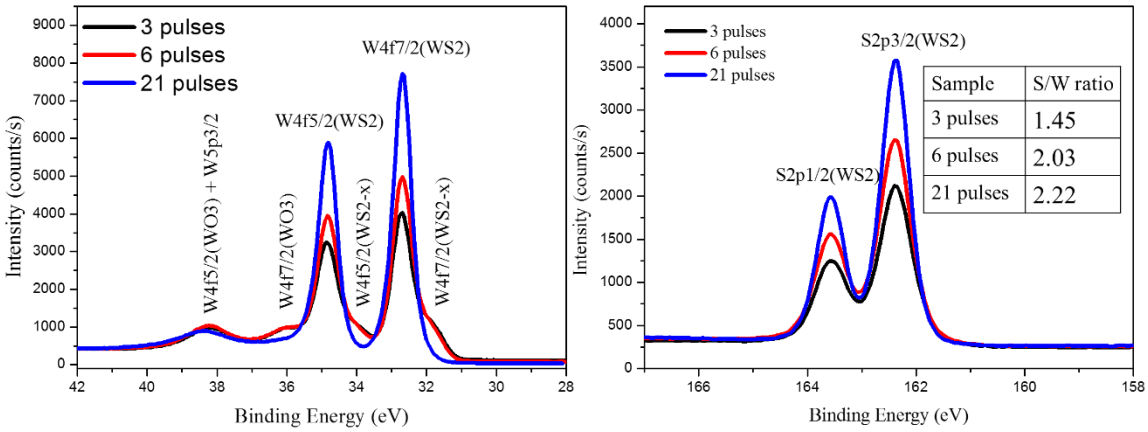

Figure 4.37. Evolution of XPS intensities of W 4f and S 2p core levels as a function of the deposition cycles. Sulfur-poor films are grown during the first deposition cycles whereas sub-stoichiometric tungsten metalloid states (WS_{2-x} or more probably W-W) are present for samples up to 6 pulses.

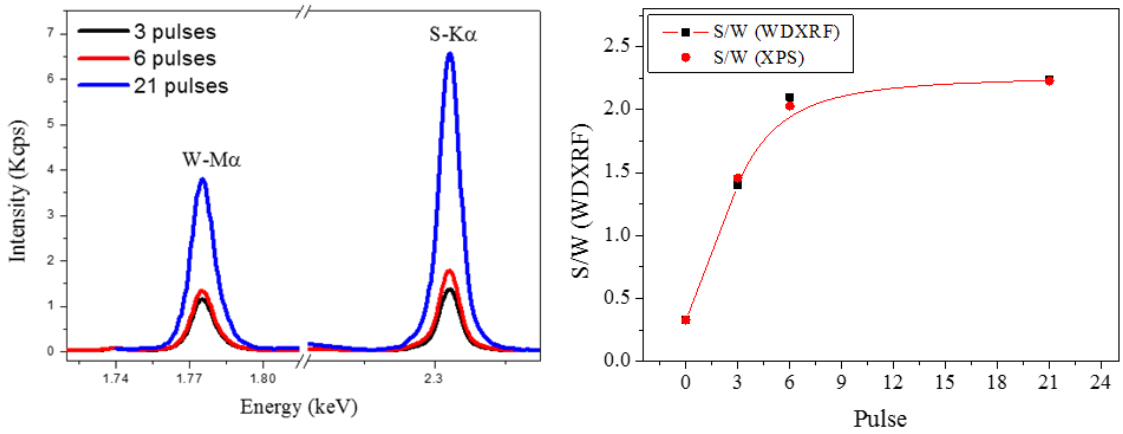

Figure 4.38. (a) WDXRF spectra of W-Mα and S-Kα, (b) S/W ratio obtained by XPS and WDXRF.

In summary, we used inline non-destructive accurate quantitative strategies based on XPS and WDXRF to investigate the impact of some important deposition parameters of ultrathin WS_x films. The fast, reliable and non-destructive access to deposited mass, stoichiometry and binding states, even for sub-nm thick layers, allowed process developers to draw the following conclusions:

- Evaluation of deposited mass and S/W ratio unambiguously shows that the deposition of WS_2 is more promoted on sapphire due the higher surface density of Al^{3+} sites when compared to the density of silanol groups on SiO_2 substrate,
- By evaluating the influence deposition temperature, we were able to determine the main temperature ranges of WS_2 deposition on sapphire, highlighting the 190-200°C range where W atoms are completely adsorbed onto the Al_2O_3 sites, whereas S/W ratio decreases above this temperature range due to the $W(CO)_6$ decomposition leading to stacks of W atoms,
- The investigation of the first growth cycles shows that sulfur-poor films are first grown and that stoichiometric film (WS_2) can be obtained from 6 deposition cycles.

4.5. References

[1] I. ISO and B. OIML, "Guide to the Expression of Uncertainty in Measurement," *Geneva Switz.*, 1995.

[2] J. H. Scofield, "X-ray data booklet," *X-Ray Data Bookl.*, 2001.

[3] "https://physics.nist.gov/PhysRefData/Xcom/html/xcom1.html." .

[4] "http://lvserver.ugent.be/xraylib-web/." .

[5] J. H. Scofield, "Hartree-Slater subshell photoionization cross-sections at 1254 and 1487 eV," *J. Electron Spectrosc. Relat. Phenom.*, vol. 8, no. 2, pp. 129–137, 1976.

[6] H. Ebel, R. Svagera, M. F. Ebel, A. Shaltout, and J. H. Hubbell, "Numerical description of photoelectric absorption coefficients for fundamental parameter programs," *X-Ray Spectrom.*, vol. 32, no. 6, pp. 442–451.

[7] W. Li *et al.*, "Geometrical factor correction in grazing incident x-ray fluorescence experiment," *Rev. Sci. Instrum.*, vol. 83, no. 5, p. 053114, May 2012.

[8] C. Jeynes, "RBS as a new primary direct reference method for measuring quantity of material," *Nucl. Instrum. Methods Phys. Res. Sect. B Beam Interact. Mater. At.*, vol. 406, pp. 30–31, Sep. 2017.

[9] C. Jeynes, N. P. Barradas, and E. Szilágyi, "Accurate Determination of Quantity of Material in Thin Films by Rutherford Backscattering Spectrometry," *Anal. Chem.*, vol. 84, no. 14, pp. 6061–6069, Jul. 2012.

[10] P. Kowalczyk *et al.*, "Impact of Stoichiometry on the Structure of van der Waals Layered GeTe/Sb $_2$ Te $_3$ Superlattices Used in Interfacial Phase-Change Memory (iPCM) Devices," *Small*, vol. 14, no. 24, p. 1704514, Jun. 2018.

[11] T. L. Anderson and H. B. Krause, "Refinement of the Sb2Te3 and Sb2Te2Se structures and their relationship to nonstoichiometric Sb2Te3−ySey compounds," *Acta Crystallogr. B*, vol. 30, no. 5, pp. 1307–1310, May 1974.

[12] S. Tanuma, C. J. Powell, and D. R. Penn, "Calculations of electron inelastic mean free paths. V. Data for 14 organic compounds over the 50–2000 eV range," *Surf. Interface Anal.*, vol. 21, no. 3, pp. 165–176, 1994.

[13] S. Manzeli, D. Ovchinnikov, D. Pasquier, O. V. Yazyev, and A. Kis, "2D transition metal dichalcogenides," *Nat. Rev. Mater.*, vol. 2, no. 8, p. 17033, Jun. 2017.

[14] T. Georgiou *et al.*, "Vertical field-effect transistor based on graphene–WS_2 heterostructures for flexible and transparent electronics," *Nat. Nanotechnol.*, vol. 8, no. 2, pp. 100–103, Feb. 2013.

[15] Y. Zhang *et al.*, "Controlled Growth of High-Quality Monolayer WS2 Layers on Sapphire and Imaging Its Grain Boundary," *ACS Nano*, vol. 7, no. 10, pp. 8963–8971, Oct. 2013.

[16] A. S. Pawbake, M. S. Pawar, S. R. Jadkar, and D. J. Late, "Large area chemical vapor deposition of monolayer transition metal dichalcogenides and their temperature dependent Raman spectroscopy studies," *Nanoscale*, vol. 8, no. 5, pp. 3008–3018, Jan. 2016.

[17] J.-G. Song *et al.*, "Layer-Controlled, Wafer-Scale, and Conformal Synthesis of Tungsten Disulfide Nanosheets Using Atomic Layer Deposition," *ACS Nano*, vol. 7, no. 12, pp. 11333–11340, Dec. 2013.

[18] J. Lubeck *et al.*, "A novel instrument for quantitative nanoanalytics involving complementary X-ray methodologies," *Rev. Sci. Instrum.*, vol. 84, no. 4, p. 045106, 2013.

[19] B. Beckhoff, "Reference-free X-ray spectrometry based on metrology using synchrotron radiation," *J. Anal. At. Spectrom.*, vol. 23, no. 6, pp. 845–853, 2008.

[20] M. Baker, R. Gilmore, C. Lenardi, and W. Gissler, "XPS investigation of preferential sputtering of S from MoS2 and determination of MoSx stoichiometry from Mo and S peak positions," *Appl. Surf. Sci.*, vol. 150, no. 1–4, pp. 255–262, Aug. 1999.

[21] A. L. Elías *et al.*, "Controlled synthesis and transfer of large-area WS2 sheets: from single layer to few layers," *ACS Nano*, vol. 7, no. 6, pp. 5235–5242, 2013.

[22] Y. Zhang *et al.*, "Controlled growth of high-quality monolayer WS2 layers on sapphire and imaging its grain boundary," *ACS Nano*, vol. 7, no. 10, pp. 8963–8971, 2013.

[23] S. Cadot *et al.*, "A novel 2-step ALD route to ultra-thin MoS_2 films on SiO_2 through a surface organometallic intermediate," *Nanoscale*, vol. 9, no. 2, pp. 538–546, 2017.

[24] H. Rotella *et al.*, "Elemental depth profiling in transparent conducting oxide thin film by X-ray reflectivity and grazing incidence X-ray fluorescence combined analysis," *Spectrochim. Acta Part B At. Spectrosc.*, vol. 135, pp. 22–28, Sep. 2017.

[25] J. Maxwell, W. Teesdale, and J. Campbell, "The Guelph PIXE software package II," *Nucl. Instrum. Methods Phys. Res. Sect. B Beam Interact. Mater. At.*, vol. 95, no. 3, pp. 407–421, 1995.

[26] M. Mantler and N. Kawahara, *How accurate are modern fundamental parameter methods?*, 2004.

5. Chapter V: Elementary depth profile protocols

5.1. Introduction

In chapters III and IV we have presented metrology protocols based on WDXRF and XPS and dedicated to the study of surface/interfaces effects in chalcogenide stacks and to the accurate analysis of the composition of thin chalcogenide materials. However, neither WDXRF nor classical XPS can reveal in-depth chemical distribution in thin chalcogenide layers, which is a required as explained in Chapter I: WDXRF has no depth-resolution (at the nm scale) whereas the use of different core levels with significantly different kinetic energy (and therefore probing depth) in classical XPS is a rather limited strategy when accurate depth-profile information is required. Furthermore, techniques such as TEM-EDX, Time of Flight Secondary Ion Mass Spectrometry (TOF-SIMS), or XPS with ion (cluster) sputtering, although very powerful to evaluate elementary depth profiles, are not likely to be used in the fabrications lines to assist process development and monitor established process, not only because they are destructive techniques, but also because they are costly, time-consuming and require highly-skilled users.

As we discussed in the end of chapter II, combined GIXRF/XRR analysis and angle-resolved XPS are both very attractive methods for the semiconductor industry. Both techniques can probe thin layered materials with depth resolution in the sub-nm range. Moreover, these two techniques can complement each other, as the large depth range of GIXRF/XRR (from few nm up to few hundred nm) can be seen as an extension of the depth range of surface-dedicated ARXPS technique (~10 nm). On the other hand, AXRPS may be used preferentially when measurement on product wafers, in ~ (10 μm^2) is required, since such capability is not accessible with the elongated primary X-ray beam used in GIXRF/XRR experiments.

Therefore, in this chapter, we report on GIXRF-XRR and ARXPS protocols dedicated to the analysis of thin layered materials based on chalcogenide. GXIRF/XRR protocols were developed on state-of-the-art tools in the lab and at synchrotron beamlines. We evaluated the effects of experimental conditions and instrumental parameters on the performances of GIXRF/XRR analysis to accurately probe chemical depth-profiles in Te-based stacks. We also investigate the effects of tuning the X-ray Standing Wave field (XSW) by means of multilayered substrates to improve the sensitivity of GIXRF/XRR analysis towards small process-driven modifications on thin films. At last, we developed an in-line ARXPS protocol to assist the development of ultra-thin chalcogenides (< 10 nm thick). The protocol was demonstrated by evaluating the first sputtering steps of GeTe and $Ge_2Sb_2Te_5$, providing insights of in-depth chemical distribution for the development PCRAM and interfacial-PCRAM materials for next technology nodes.

5.2. Probing TiTe films by GIXRF/XRR combined analysis

As described in chapter I, telluride materials (such as GeSbTe, SbTe, TiTe, etc.) have received an increasing interest for Resistive Random Access Memories (RRAM), such as Phase Change Random Access Memory (PCRAM) and Current Bridging Random Access Memory (CBRAM). They are considered the most promising candidates for the next generation of non-volatile memories.

The properties of telluride films are deeply influenced by their chemical composition and compositional depth profile. For example, the crystallization temperature of GeSbTe alloys (Fig.5.1) can be tuned by increasing the Ge proportion, resulting in better thermal stability, and therefore, better data retention [1]. Surface/interface aspects must also be considered, not only for PCRAM but also for innovative Interfacial-PCRAM based on complex stacks of ultra-thin layers such $(GeTe/Sb_2Te_3)*40$ [2].

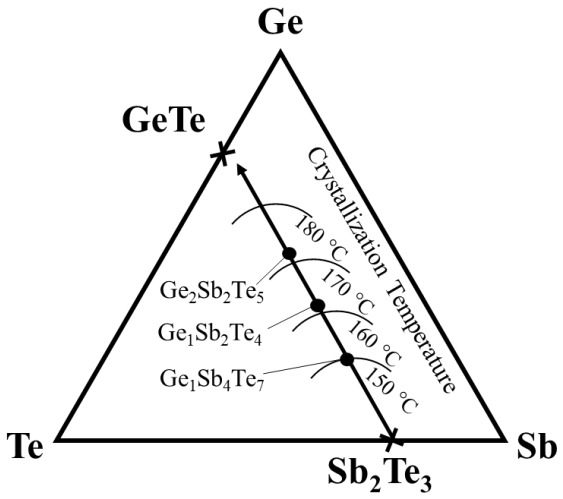

Figure 5.1. Ge-Sb-Te ternary diagram showing the increase of crystallization temperature by Ge addition.

Therefore, metrology protocols must be established in order to support the development and the monitoring of advanced thin telluride films for PCRAM. The combination of GIXRF with XRR is particularly adequate to probe telluride thin films at industrial level (i.e. the semiconductor industry) [3, 4].

As reported in chapter II, GIXRF is a highly sensitive elementary technique capable to probe chemical depth profiles in films with thickness ranging from few nm to ~ 200 nm [5, 6]. When combined with XRR, ambiguities related to thickness and mass density are drastically reduced. Indeed, GIXRF/XRR analysis determines the profiles of electronic density (XRR) and atomic density (GIXRF), resulting in improved ability to determine quantitative chemical depth-dependent information in thin layered materials. Nonetheless, as said in chapter II, the performances of GIXRF analysis may be strongly influenced by the instrumental set-up [7].

In this section, we evaluated the ability of GIXRF/XRR technique to probe small process-driven modifications in the chemical depth-profiles of thin amorphous titanium-telluride films grown by Physical Vapor Deposition and caped *in-situ* with tantalum passivation layer. The influence of the instrumental function is investigated by comparing GIXRF/XRR data collected on the same samples using different tools: two dedicated GIXRF/XRR platforms available at Elettra (XRF beamline) and

SOLEIL (Metrology beamline), and one lab platform based on Rigaku Smartlab instrument. Chemical depth-profiles deduced from GIXRF/XRR are compared with Time-of-Flight Secondary Ion Mass Spectrometry (TOF-SIMS) and Plasma Profiling Time-of-Flight Mass Spectrometry (PP-TOFMS), whereas XPS and WDXRF were performed as complementary characterizations.

5.2.1. Experimental

Titanium-tellurium thin materials were selected for both application- and metrology-driven reasons. First, Min Zhu et al [8] recently revealed that titanium is a key element on Te-based alloys for PCRAM applications. His work demonstrated that adding Ti on SbTe material provides at least one order of magnitude faster set speed than GeSbTe alloys. Second, titanium and tellurium fluorescence lines (Ti-Kα, 4.51 keV and Te-Lα, 3.77 keV) do not overlap and can easily be excited both in laboratory with a Cu-Kα source and at any synchrotron facility. Moreover, such TiTe alloys are perfectly suitable for complementary mass spectrometry analysis using TOF-SIMS and PP-TOFMS.

5.2.1.1. Sample preparation

Amorphous thin titanium-telluride films were grown by PVD on 200 mm Si(001) wafers, using an industrial multi-chamber PVD deposition tool Evatech CLN 200. Titanium and tellurium were deposited alternatively, in different chambers: titanium was first sputtered as ultrathin (< 1 nm) layer, and the wafer was then transferred to the second chamber (without air-break, i.e. *in-situ*) for the deposition of ultrathin tellurium layer. This process was repeated until the desired TiTe thickness and proportion were reached (Fig. 5.2.a). A 5 nm-thick passivation layer consisting in amorphous tantalum material was finally sputtered *in-situ* on TiTe layer in order to minimize sample ageing (i.e. oxidation). For this study, two different types of Ta-capped films were grown: *Sample a* is 5-nm thick TiTe (1:1) mono-layer, while *sample b* is made of two TiTe layers with different Ti/Te ratios and total thickness of ~ 10 nm (Fig. 5.2b).

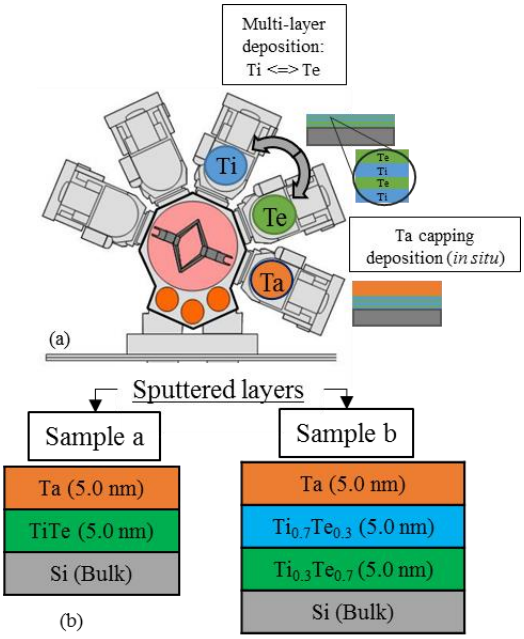

Figure 5.2. Schematic procedure of sputtering of Ti, Te and Ta elements. Figure 3.b. Definition of sample a and sample b.

5.2.1.2. Instrumentation

The GIXRF/XRR combined analysis were performed on state-of-art tools in the lab and at synchrotron beamlines. At CEA-LETI, we used Rigaku SmartLab®, the five-axis high resolution diffractometer described in chapter 2.3. GIXRF/XRR acquisitions were performed with monochromated primary beam (Cu-Kα, 8.048 keV). Beam width was set to 30 µm using dedicated slits. The X-Ray Reflectivity was measured by a Scintillation counter (SC) detector which can measure count-rates from 0.1 to several 100 000 s^{-1} after counting-loss correction. The XRR measurements were recorded in θ/ θ configuration. The XRF signal was acquired by a Hitachi Vortex 90EX silicon drift detector (SDD) mounted on a customized set-up provided by Rigaku. The SDD detector was placed at 90° from the sample surface, 10 mm above the sample.

GIXRF/XRR experiments were also conducted on the Metrology beamline at SOLEIL Synchrotron (Saclay, France), using the irradiation chamber also described in chapter 2.3. The irradiation chamber was mounted on the hard X-ray branch of Metrology beamline that can deliver monochromatic photons in the 3-35 keV range, using a Si double-crystal. Before entering into the chamber, the incoming beam is re-shaped to 300 µm (horizontal and vertical) through two set of slits which also limits its divergence to 0.012 mrad. The XRR measurements were acquired by a photo-diode in a θ/2θ configuration, while the XRF signal was measured by a high-purity germanium (HPGe) spectrometer from Oxford instruments. The XRF detector was placed at 90° from the sample surface, 10 cm away from the surface of the sample. The measurements were performed under vacuum below 10^{-6} Pa.

Lastly, titanium-tellurium samples were also measured on the Fluorescence beamline at Elettra synchrotron (Trieste, Italy) operating in the tender and hard X-ray ranges (2 to 14 keV). This beamline

is equipped with the same analysis chamber as LNHB, and GIXRF/XRR measurement procedure was therefore similar to the one used at SOLEIL. The main differences lie in the incident beam size and the detection components. The primary beam is re-shaped to 250 µm horizontal and 100 µm vertical through exit slits, resulting in 0.15 mrad divergence. The analysis chamber allows measurements in ultra-high vacuum (10^{-6} Pa). The fluorescence signal is acquired by a SDD from Bruker placed at 90° from the sample surface, 10 mm away from the surface of the sample. Experiments at SOLEIL and Elettra were both realized at 6 keV so as to improve the detection of Te-L and Ti-K lines, but with no access to Ta-L lines from the capping layer. Table 5.1 summarizes the main parameters of each set-up used for GIXRF/XRR combined analysis.

Table 5.1. Measurement conditions and instrumental parameters employed for the XRR-GIXRF analysis.

Parameter	SmartLab®	Soleil Synchrotron	Elettra Synchrotron
Source energy (keV)	8.05 (Cu-K_α)	6.00	6.00
Beam width (µm)	30.0	300.0	100.0
Beam Divergence (mrad)	0.2	0.012	0.15
Distance sample to XRF detector (mm)	10	100	10
Detected zone, Ld (mm)	7.0	40	0.8
XRF detector	SDD	HPGe	SDD
Pressure (Pa)	Atmospheric	10^{-6}	10^{-6}

Complementary characterizations were performed at CEA-LETI. TOF-SIMS depth profiles were acquired with Ion Tof GmbH TOF-SIMS 5 tool equipped with Bi liquid metal ion gun and Cs sputter source. Depth profiles were performed in the non-interlaced mode which separates cycles for sputtering, analysis and charge compensation. Additional mass spectrometry characterization was performed on Horiba PP-TOFMS instrument, based on plasma sputtering [9]. Depth profiles deduced from PP-TOFMS are presented as Ion Beam Ratio (IBR) defined as the ratio of the current of the ion of interest over the sum of the currents of all the matrix ions, all being weighted by their isotopic abundances. The details about TOF-SIMS and PP-TOFMS characterizations are found in annex B.

XPS measurements were performed on Thermo Scientific Theta 300 inline tool operating at Al-Kα monochromatic X-ray (1486.6 eV), with 400 µm beam diameter and a pass energy of 60 eV resulting in 0.7 eV resolution.

WDXRF measurements were acquired via Rigaku AZX400 inline tool using polychromatic radiation from 4 kW Rhodium tube. LiF200 crystal installed on high-resolution goniometer was used to record XRF intensities of Ti-Kα, Te-Lα and Ta-Lα. The quantitative analysis was based on the fundamental parameters method [10], using titanium and tellurium pure targets to evaluate the tool sensitivity factors.

5.2.2. Results and discussion

Prior to any quantitative analysis, we compared XRF spectra of *Sample a* acquired on the three instruments (Fig. 5.3). The overlap shows only few discrepancies: one extra peak (Zr-Lα) is present in SOLEIL spectrum due to the zirconium filter of the collimator of HPGe detector. In addition, XRF spectrum recorded in lab on Smartlab tool is affected by Ar-K peaks as measurements are not performed under vacuum.

The shape of the spectra are different for each setup, and the detector parameters (such as Fano factor and response function) were adjusted accordingly in PyMCA software used for deconvolution [11]. For the angle-dependent fluorescence analysis, only Ti-Kα and Te-Lα are discussed here, since overlapping of Si-Kα and Ta-M lines drastically increases the uncertainties in the determination of their intensities for each spectra.

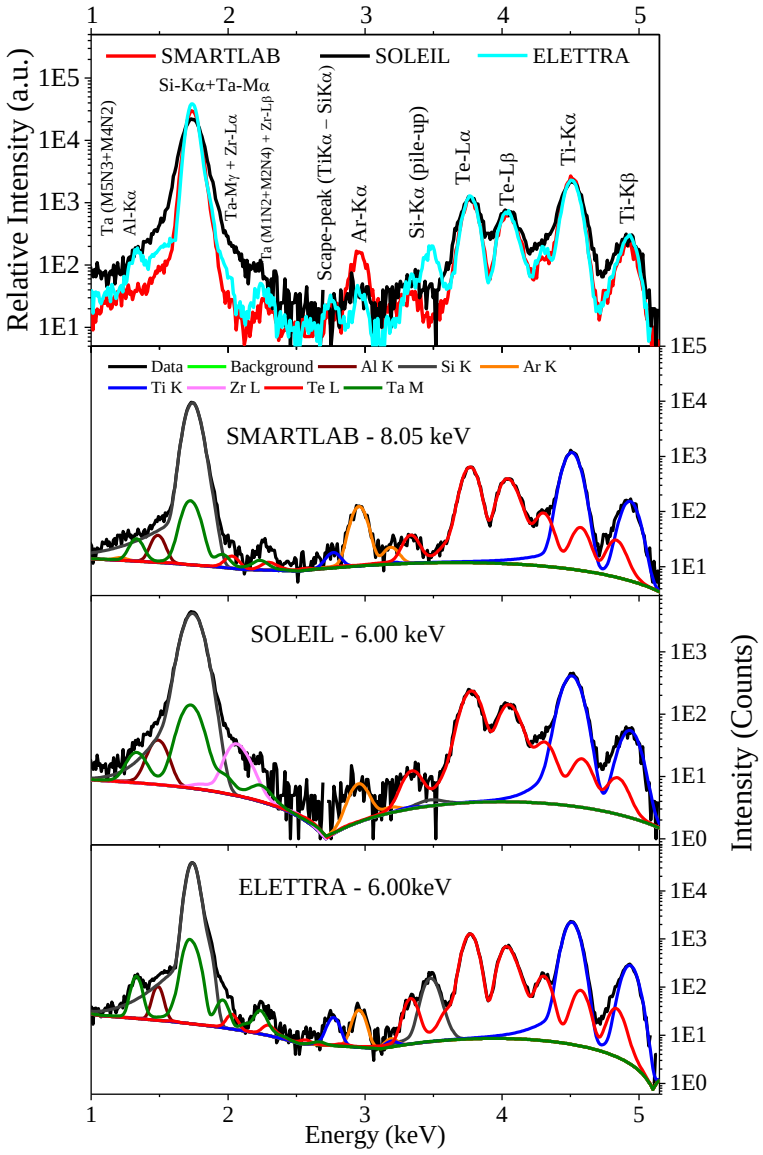

Figure 5.3. XRF spectra of sample acquired on the three different instruments and modelled using PyMCA software.

5.2.2.1. Analysis of sample a: Ta-capped TiTe monolayer

After extraction of XRF intensities at each angle using PyMCA, angle-dependent GIXRF data (for Ti-Kα and Te-Lα) and XRR data were processed using Jgixa software [12, 13]. The instrumental parameters (i.e. detected zone L_d, Gaussian beam width and divergence) were fixed from the values of table 5.1. Then, best multilayer model was estimated by simultaneously fitting of XRR/GIXRF with differential algorithm. Fig. 5.4 shows the experimental and simulated XRR and GIXRF curves for the three instruments. The curves are plotted as a function of the scattering vector q ($Å^{-1}$) so as to draw comparisons of data acquired at different energies.

From the superimposed XRR curves (Fig. 5.4), small differences among instruments are observed, mostly due to the fact that different parts of the wafer were analyzed on each instrument. Hence, thickness and roughness were slightly adjusted on each dataset, while keeping the same density and stoichiometry for the layered model. Nonetheless, XRR data collected on the three instruments are in good agreement, featuring similar critical q and period of Kiessig fringes.

Concerning the GIXRF curves, the geometrical function deeply impacts the angle dependence of the fluorescence intensity. For instance, the decrease of GIXRF intensities after critical q is more pronounced on Smartlab data than on Elettra ones, due to the combined influence of reduced beam width (30 µm) and increased detected zone (7.0 mm) on Smartlab geometrical function and hence GIXRF curve shapes. No significant difference between SOLEIL and Smartlab geometrical functions is observed. Indeed, as the geometrical function is a combination of the instrumental parameters, the larger L_d at SOLEIL (33 mm larger compared to Smartlab) is compensated by the expanding of its beam width (from 30 to 300 µm).

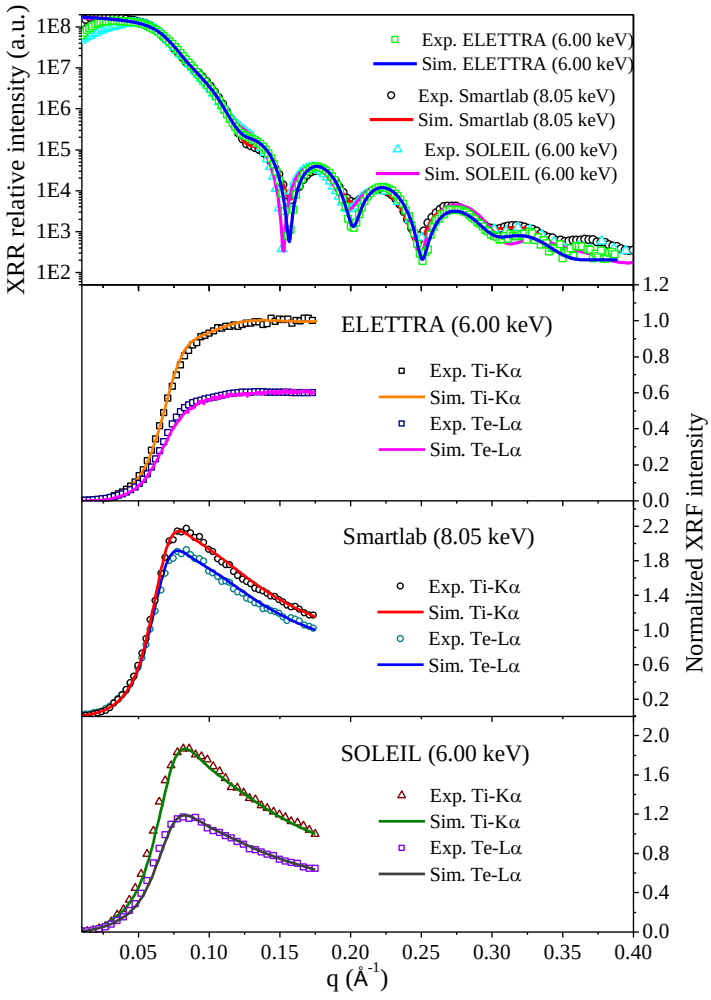

Figure 5.4. XRR and GIXRF experimental (dots) and simulated (lines) data related to sample a.

5.2.2.2. Analysis of sample b: Ta-capped TiTe bilayer

Fig. 5.5 shows the XRR/GIXRF data and best model calculation related to the TiTe bilayer. Similarly to *sample a*, XRR curves are very-well aligned, in spite of minor discrepancies due to the slight non-uniformity of the deposition process.

For the three instruments, the GIXRF features two local maxima after the critical q, thereby confirming the ability of the three GIXRF setups to reveal the bilayer structure with different Ti:Te ratios in such challenging sample. Nonetheless, the contrast between these two features differs from one instrument to another, due to noticeable differences among the geometrical functions. For instance, the two features of interest are more pronounced on Smartlab data than on Elettra data, due to different values of beam width and detected zone listed in 3.1. In addition, the contrast between these two features can be strongly influence by the beam divergence [13]. In that respect, SOLEIL setup measurements indicates the two maxima less pronounced due to higher divergence of 0.4 instead of 0.012 mrad. We still are not sure why the beam divergence substantially increase after entering the state-of-art irradiation chamber, but data process from SOLEIL results undoubtedly indicates 0.4 mrad beam divergence.

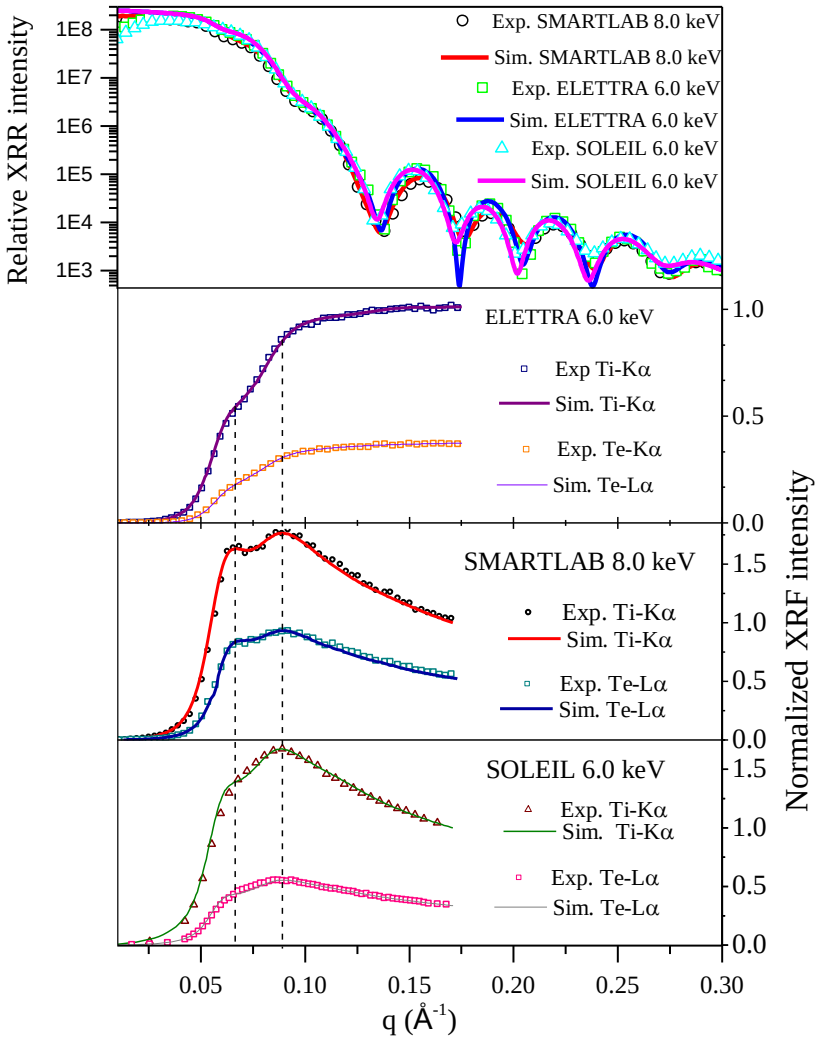

Figure 5.5. XRR curves of TiTe bilayer (sample b) recorded on the three tools show only minor discrepancies. The GIXRF curves features two maxima around 0.066 and 0.089 $Å^{-1}$, respectively, confirming the bilayer configuration.

In order to illustrate the impact of the detected zone (L_d), beam width and divergence, Fig. 5.6 shows simulations of GIXRF curve of TiTe bilayer with different sets of parameters for the geometrical correction. The incident beam energy was the same for the five simulations. The theoretical GIXRF curve (the one without correction) is taken as reference. All the curves are normalized by the theoretical curve at 3.0° for better comprehension. The three parameters impact differently the GIXRF curve. For instance, *Case I* comes with small L_d and large beam width (Elettra setup) when compared to the theoretical curve, resulting in similar shape of the GIXRF data. Nevertheless, once one decreases the beam width to 30 µm (*Case II*), the geometrical function progressively impacts the curve shape. For *Case III* (Smartlab setup), increasing the detected zone (L_d) deeply impacts the GIXRF curve, with fluorescence signal rapidly decreasing above the critical angle. This setup provides additional information around the critical angle and sounds more suitable to reconstruct the elementary depth distribution of TiTe bilayer sample. The *Case IV* illustrates the impact of the beam divergence on the GIXRF data. Indeed, comparing *Case IV* with *Case III* demonstrate how low beam divergence is key to reveal process relevant features for ultrathin films.

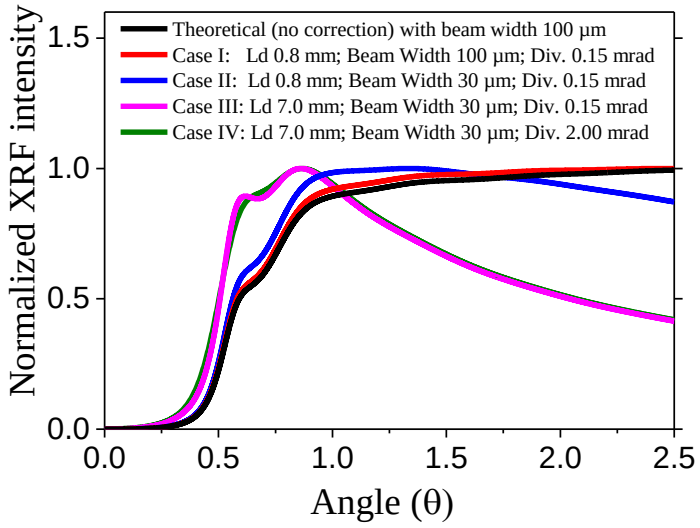

Figure 5.6. Sample b GIXRF simulations at 6 keV with sets of instrument parameters. The four cases were normalized by the theoretical curve (black) at 3.0°.

5.2.3. Elementary depth profile analysis

As stated before, the best multilayer models deduced from data collected on the three instruments are very similar, taking into account minor thickness and surface roughness variations due to slight non uniformity of the deposition process. Fig. 5.7 shows the chemical depth-profile in the TiTe bilayer sample deduced from Jgixa analysis of combined GIXRF/XRR (thickness and roughness averaged on the three datasets are reported on Fig. 5.7), then compared to mass spectrometry (TOF-SIMS and PP-TOFMS).

First, TOF-SIMS data, although collected with reasonably optimized conditions for such thin film arrangement, illustrate the difficulty of probing depth-dependent profiles in thin and complex materials. In addition, difference between relative sensitivity factors of tellurium and titanium led to tellurium signal significantly lower than titanium one. Thus, the bilayer configuration is unclearly

revealed by the TOF-SIMS analysis. Complementary measurements using PP-TOFMS resulted in better-defined elementary depth-profiles that unambiguously show the bilayer configuration where the top layer (below tantalum cap) is rich in titanium and the bottom layer is tellurium-rich.

Elementary depth-profile was reconstructed from XRR/GIXRF data by slicing the multilayer model into ultra-thin slices, the points on each curve (Fig. 5.7) corresponding to the surface/interface of the stabs. In spite of rather poor slicing resolution due to software requirements and computing power, TiTe bi-layer arrangement similar to the one deduced from PP-TOFMS is unambiguously revealed. Averaging titanium and tellurium contents over the stack leads to 58.0 at% for Ti and 42.0 at% for Te, which is reasonably well-aligned with WDXRF quantification (61.2 at% Ti, 38.8 at% Te).

PP-TOFMS and combined XRR/GIXRF were able to access depth-dependent variation in Ti:Te ratio in *sample b*, as targeted by PVD process. In addition, they both revealed unexpected inter-diffusion between tellurium and tantalum cap. Indeed, the electron affinity between Te and Ta is as strong as between Te and Ti, resulting in formation of Te-Ta alloy at Ta/TiTe interface, which is consistent with previous studies relating to tantalum-capped tellurium-based thin materials [14, 15].

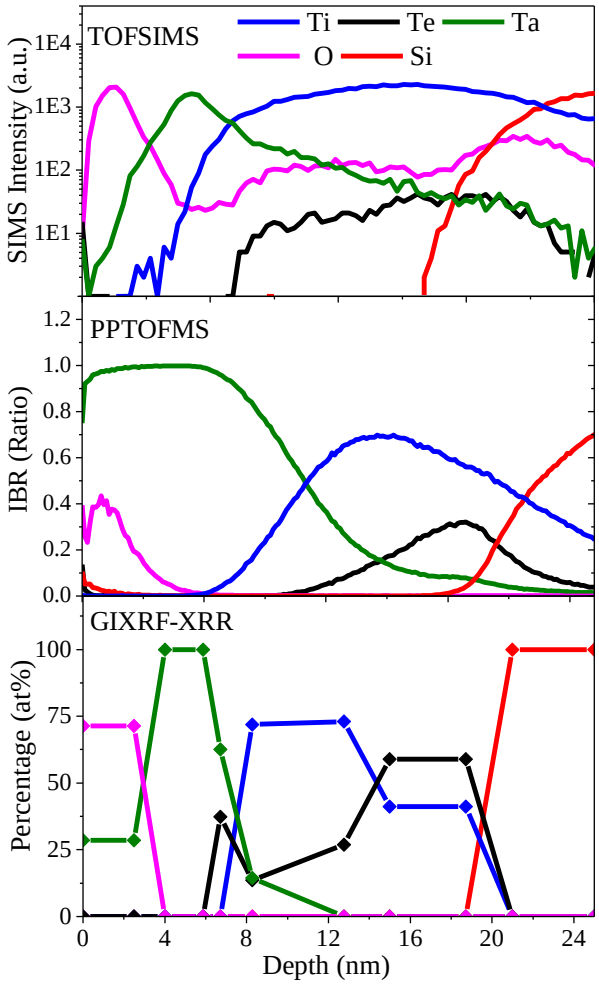

Figure 5.7. Sample b GIXRF simulations at 6 keV with sets of instrument parameters. The four cases were normalized by the theoretical curve (black) at 3.0°.

In summary, accurate chemical depth-profiles in challenging tellurium-based thin films stacks have been characterized by the GIXRF/XRR combined analysis conducted in the Lab and at synchrotron beamlines. The protocol studied the effects of instrumental parameters, and highlighted the beam

conditioning (beam width and divergence) and detected length as key parameters impacting the depth dependence analysis. GIXRF/XRR measurements as well as PP-TOFMS analysis were able to access depth-dependent variation in Ti:Te ratio in ~ 10 nm layer, as targeted by PVD process. On top of that, GIXRF/XRR revealed unexpected inter-diffusion between tellurium and tantalum cap that was confirmed by mass spectrometry techniques and XPS. These results demonstrate how appropriate GIXRF/XRR can be as non-destructive depth-profiling technique for complex thin materials with composition-driven properties. GIXRF-XRR tool with mastered instrumental function (divergence, detected length and beam width) appears particularly suitable to support process development in lab and even in fabs.

5.3. Enhancing XRF signal through Multilayer (Mo/Si) substrates

In section 5.2, we have demonstrated that GIXRF/XRR with optimized setup in the lab or at synchrotron is able to unambiguously reveal small process-driven modifications in ultra-thin TiTe layered material. However, the high surface sensitivity of GIXRF due to the XSW-induced enhancement of the XRF signal, rapidly degrades with depth. In this section, we investigate the use of (Mo/Si)*N multilayered structures (Bragg mirrors) as potential substrates for thin layer deposition. The aim is to keep high values of X-ray reflected intensity even at angles significantly higher than the critical angle, so as to generate XSW-induced enhancement of the XRF signal not only at the surface but also in the depth of the layer of interest. Moreover, the careful design of (Mo/Si)*N multilayers by optimizing the ratios of Mo and Si thickness and the number of periods, allows to tune the positions of the maxima of the XSW field, and therefore the sensitivity of GIXRF to precise depth regions for a given primary energy.

In the semiconductor industry, the use of multilayered substrates is also a possible approach to probe new ultra-thin devices such as 2-D materials and Interfacial-Phase Change memories (IPCRAM). For example, the sensitivity of GIXRF/XRR to process variations in ultra-thin PCM layered stack such as ($GeTe/Sb_2Te_3$) can be improved when the layers are deposited on multilayered substrate instead of silicon. The enhancement on generated XSW field substantially increases the sensitivity to the elementary distribution, as illustrated in Fig.5.8.

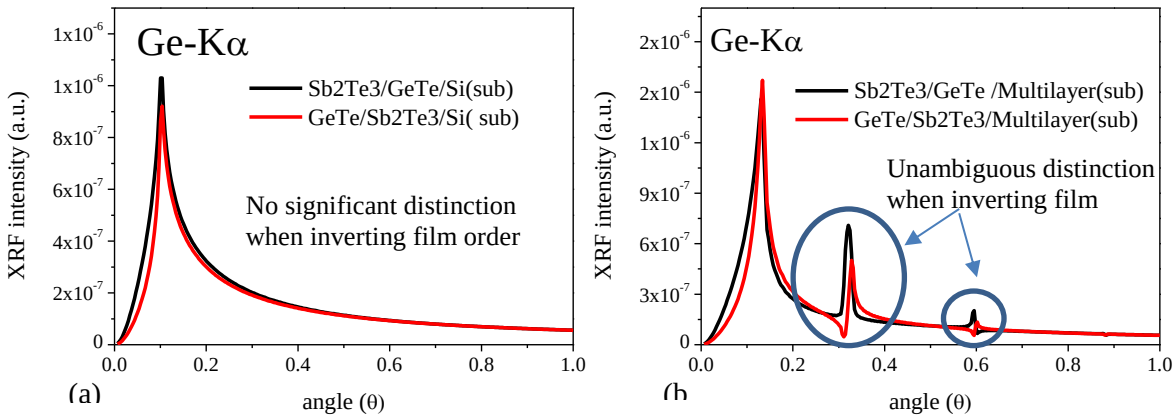

Figure 5.8. Angular dependence of Ge-Kα XRF signal in the grazing-incidence region (model only, no data) illustrates that the use of (Mo/Si)*40 Bragg mirror as alternative substrate to silicon can improve the sensitivity to small variations in ~ 3 nm thick stack

In this section we investigate the GIXRF sensitivity to process-induced variations of antimony doping in the GeSe layers developed as OTS materials. These thin layered materials were deposited on silicon and duplicates were grown on (Mo/Si)*40 Bragg mirror provided by AXO company. After a short overview of GeSe:Sb process conditions, we report on the XRR, GIXRF and XSW simulations that allowed us to tune the characteristics of the Bragg mirror that was further realized by AXO. Lastly, we demonstrate the sensitivity improvement obtained when using such a strategy.

5.3.1. Experimental

5.3.1.1. Sample preparation

Germanium-selenide films are widely studied as OTS (Ovonic Threshold Switch) materials for PCRAM applications. In addition, this material can be amorphously deposited by PVD at low temperature (60 °C). This deposition condition will guarantee that the properties of the Bragg mirror used as substrate will not be degraded during the growth of GeSe:Sb layer by temperature induced Mo-Si intermixing for instance. Furthermore, this compound was chosen as it features perfectly distinct, easily accessible XRF lines: Sb-Lα, Ge-Kα and Se-Kα lines (respectively at 3.604, 9.886 and 11.222 keV). In addition, significant difference in the mass of the constituents should facilitate further characterization by mass spectrometry (TOF-SIMS and PP-TOFMS).

Germanium-selenide films were grown by PVD using industrial multi-chamber PVD deposition tool Evatech CLN 200. The films were deposited on 200 mm Si(001) wafers and duplicates were grown on {Si(5nm)/Mo(2nm)}*40 thin multilayered substrates. Ge and Se atoms were sputtered from the same $GeSe_2$ target to form the $GeSe_2$ layer. Still in the same chamber, Sb-doped GeSe layer was deposited by co-sputtering from a Sb target and the above-mentioned $GeSe_2$ target. The multilayered substrates were primarily elaborated at LETI (for first investigation) by PVD and then provided by Applied X-ray optics AXO Dresden GmbH Company (for Bragg mirror of high quality). In overall, the two stack configurations are depicted in Fig. 5.9. Once the films were deposited, a 5-nm thick carbon capping layer was sputtered *in-situ* as protective layer.

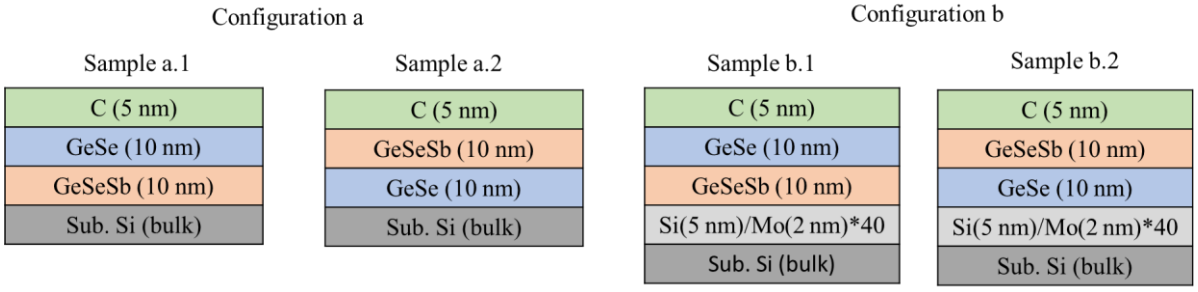

Figure 5.9. Sb-doped GeSe films studied in this protocol.

5.3.1.2. Instrumentation

This protocol was also developed with the laboratory Rigaku SmartLab® tool and the irradiative chamber at SOLEIL synchrotron. The measurements at SOLEIL synchrotron were performed with a SDD detector at 10 mm from the sample with 1 mm diameter as pinhole of the collimator. This modification substantially reduces the detection zone (Ld) from 40 to 1 mm, table 5.2 summarizes the main parameters. The measurement at the laboratory was only intended to evaluate the Sb distribution by probing the Sb-Lα.

Table 5.2. Measurement conditions and instrumental parameters employed for the XRR-GIXRF analysis.

Parameter	SmartLab®	SOLEIL synchrotron
Source energy (keV)	8.05 (Cu-K_α)	13.5
Beam width (µm)	30.0	300.0
Beam Divergence (mrad)	0.2	0.012 (0.4 mrad was used as global divergence for data processing)
Distance sample to XRF detector (mm)	10	23
Detected zone, Ld (mm)	7.0	1
XRF detector	SDD	SDD
Pressure (Pa)	Atmospheric	10^{-6}

Similar to previous section, elementary depth profiles were also analyzed at LETI by TOF-SIMS and PP-TOFMS and compared to GIXRF/XRR elemental distribution.

5.3.2. Results and discussion

5.3.2.1. Simulations

X-ray standing wave field and X-ray reflectometry of samples deposited on silicon and Bragg mirror were first simulated using Medepy software developed at LETI [21]. Figure 5.10.a shows the XRR curves as well as the XSW angle-dependence at three different depths (0, 10 and 20 nm) of the film stack (with nominal thickness) deposited either on Si or multilayered substrates. The simulation was run at 13.5 keV primary energy, *i.e* slightly above Se-K and Ge-K edges. Medepy software was also used to tune the parameters of the Bragg mirror so as to adapt the thickness of Mo and Si layers and number of repetitions to the sample set of interest, resulting in following optimized values: 2 nm-thick molybdenum film, 5 nm-thick silicon layer, 40 repetitions.

Samples deposited on Bragg mirrors feature clear maxima of X-ray standing wave field in both undoped and Sb-doped GeSe individual layers whereas XSW intensity decreases rapidly with depth for samples deposited on silicon (Fig.5.10.b). Such simulation confirms that deposition on optimized Bragg mirror should improve the sensitivity to chemical depth-profiles.

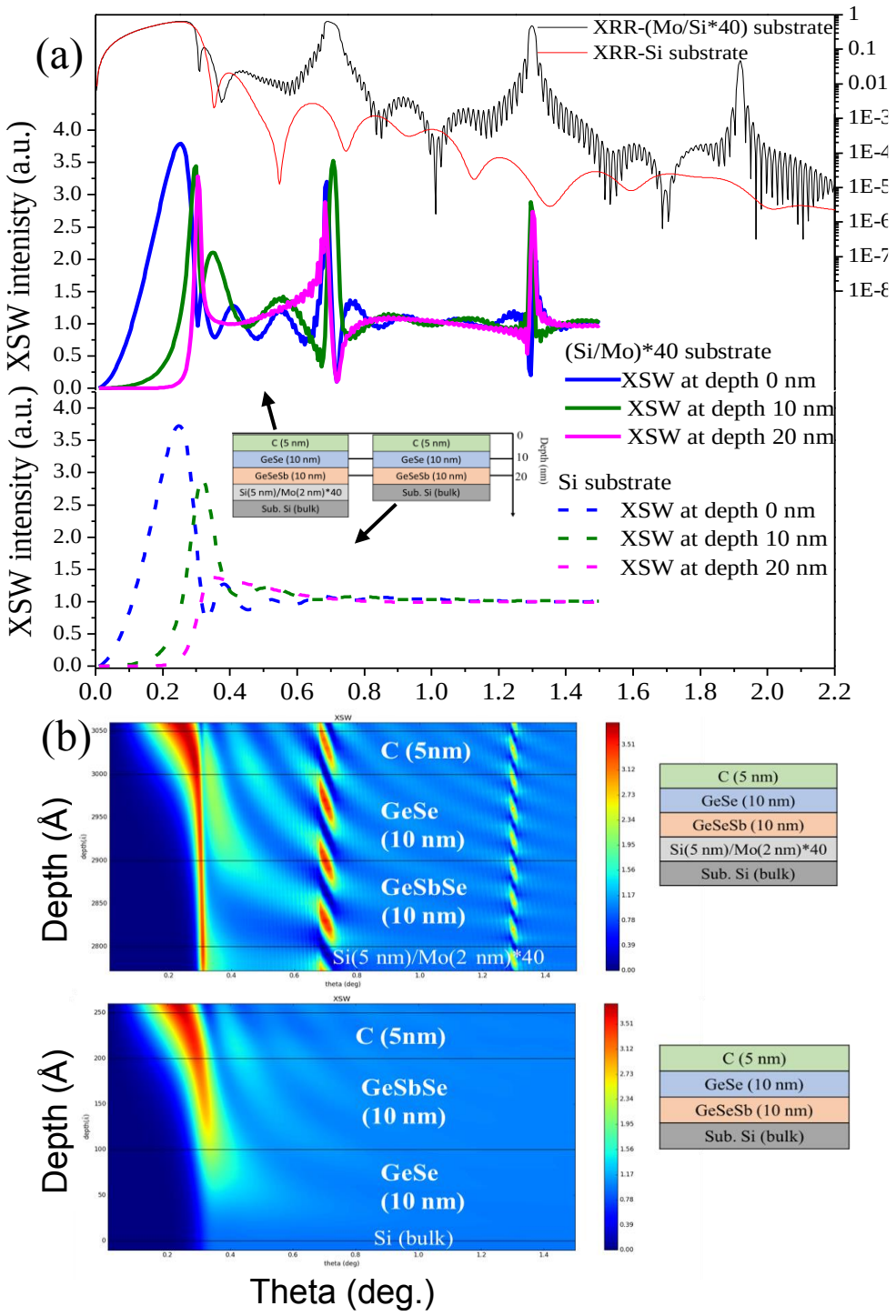

Figure 5.10. (a) XRR and XSW simulated curves at 13.5 keV for films deposited on Si substrate and (Mo/Si)*40 Bragg mirror. (b) Overall aspect of the XSW field as function of depth (Y-axis) and angle (X-axis).

Secondly, we simulate the angle-dependence of Ge-Kα and Se-Kα XRF intensity for samples grown on silicon and Bragg mirror, and using 13.5 keV as primary energy. As illustrated in Fig 5.11, the process-induced difference between stacks (Sb-doped layer on top or buried) is more clearly evidenced when using Bragg mirror as substrate.

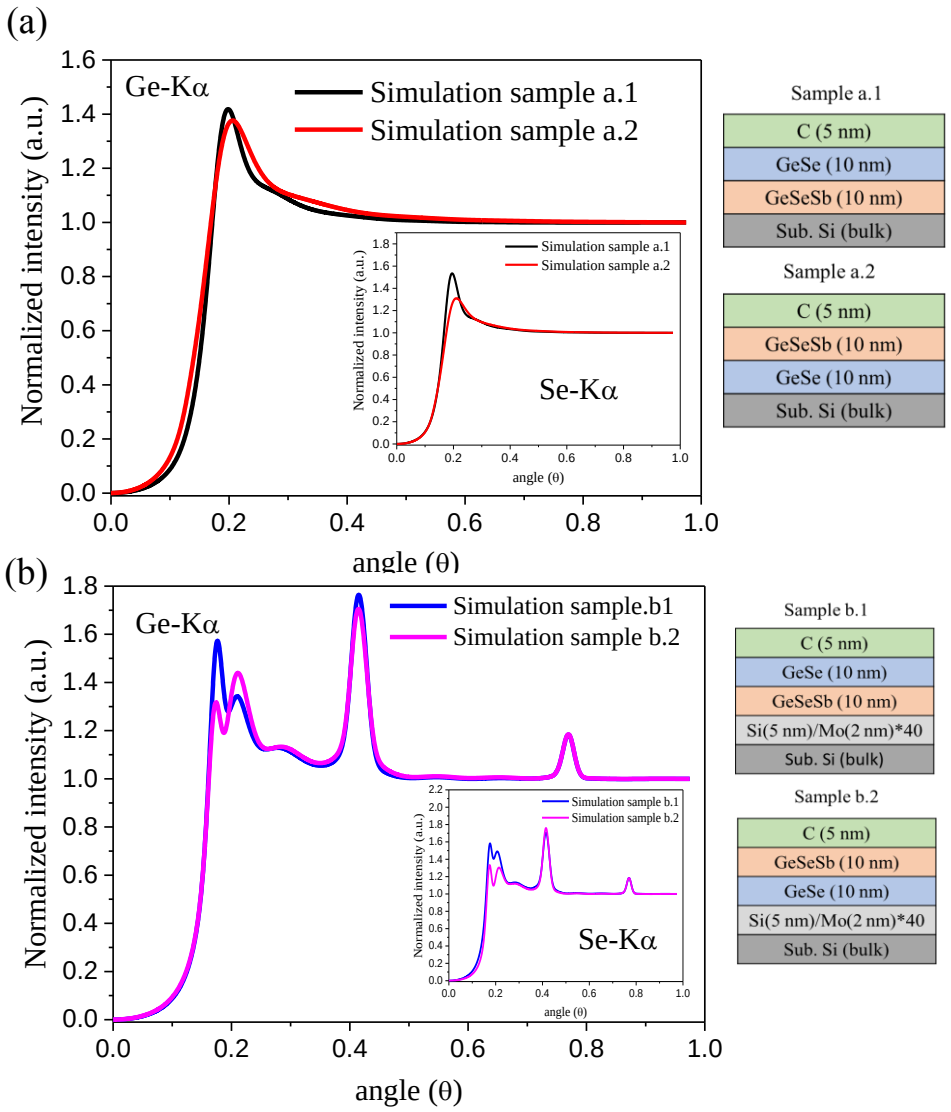

Figure 5.11. Simulated GIXRF curves at 13.5 keV for films deposited on (a) Si substrate, and (b) multilayered substrates.

5.3.2.2. Experimental results

We first run XRR measurements on the multilayer (Mo/Si)*40 substrates produced at LETI and provided by AXO. Figure 5.12 clearly demonstrates that only AXO sample shows clear Bragg peaks with reflectivity perfectly aligned with simulation of the expected stack. Sample produced at LETI using standard PVD and co-sputtering of Mo and Si targets did not allow to obtain the same quality of the Bragg mirror, due to undesired in-depth variability of individual thickness of molybdenum and siliconlayers and interfacial roughness [16, 17]. Therefore, only AXO multilayered substrates were considered for further GIXRF analysis.

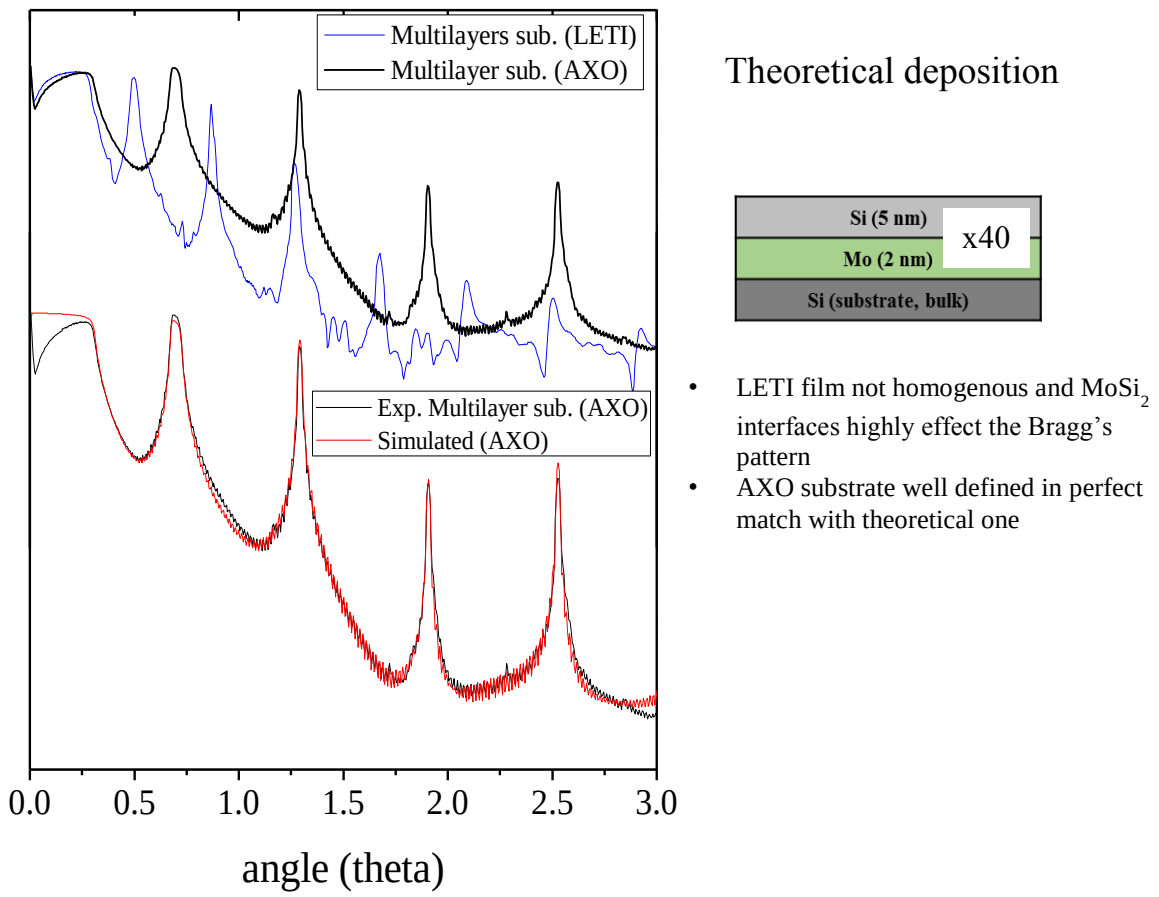

Figure 5.12. XRR measurements (8.048 keV) of multilayered substrates produced at LETI and provided by AXO.

Prior to GIXRF analysis, we evaluated the fluorescence data acquired on the two instruments (Fig. 5.13) . The sum spectra (0-3°) measured with both instruments feature clearly defined and well separated contributions of the XRF lines from the GeSe:Sb sample and from the (Mo/Si)*40 Bragg mirror. Additional contributions are due to the analysis chamber at Soleil (Cr, Fe, and Ni), to the SDD detector colimator (made of tungsten, at Soleil), or to measurement in the air (Ar-Ka contribution in Smartlab spectra) .

The XRF data were processed with PyMCA software [11] so as to extract the integrated intensities, in a similar way as described for TiTe samples in previous section. As monochromatized Cu-Ka radiation of Smartlab is closer to Sb-L3 edge than the primary energy used in Soleil experiment (13.5 keV), we decided to combine Ge-Kα and Se-Kα intensities from Soleil experiment and from lab experiment to derive quantitative depth-profiles. Complementary XRR measurements were acquired on the Lab-tool.

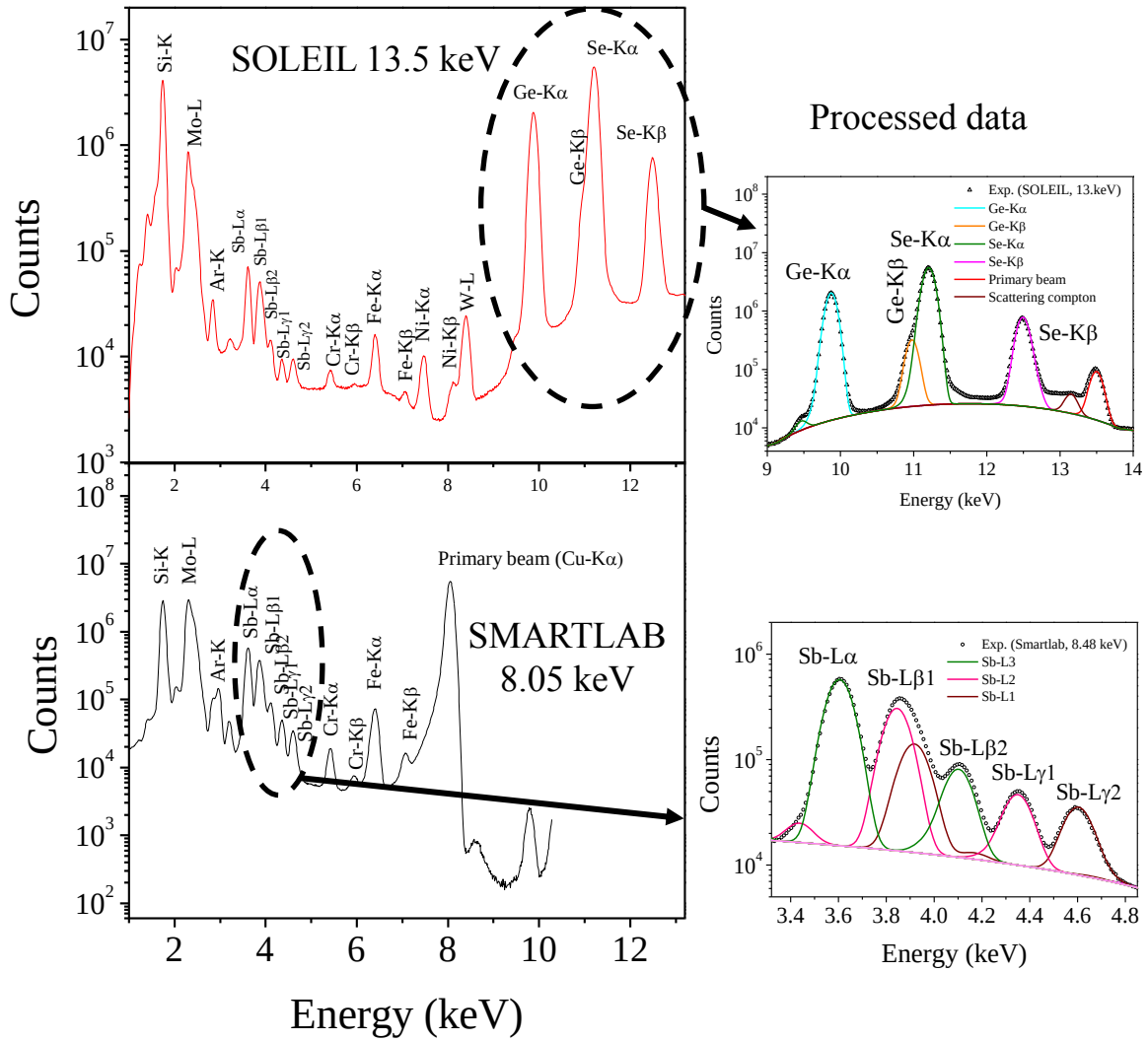

Figure 5.13. X-ray fluorescence spectra of GeSbSe/(Mo/Si)*40 sample acquired at Soleil (13.5 keV) and in the laboratory (8.05 keV).

i. GIXRF/XRR analysis

XRR along with Ge-Kα and Se-Kα GIXRF data for samples a.1 and a.2 (resp. b.1 and b.2) are displayed in Figure 5.14 (resp. Fig.5.15), whereas the influence of the Bragg mirror substrate on the GIXRF sensitivity to Sb in-depth position is evidenced by Sb-La GIXRF data in Fig.5.16. First, we observe from Fig. 5.14 related to silicon substrate that the in-depth position of Sb-doped layer in the stack has limited influence on the XRR data and strictly no influence on the angle-dependent profiles of Ge-Kα and Se-Kα. This lack of sensitivity is even clearer than on above simulations. On the contrary, Fig.5.15 evidences that XRR and above all the angle-dependent profiles of Ge-Ka and Se-Kα show significant sensitivity the in-depth position of Sb-doped layer in the stack when using Bragg mirror as substrate.

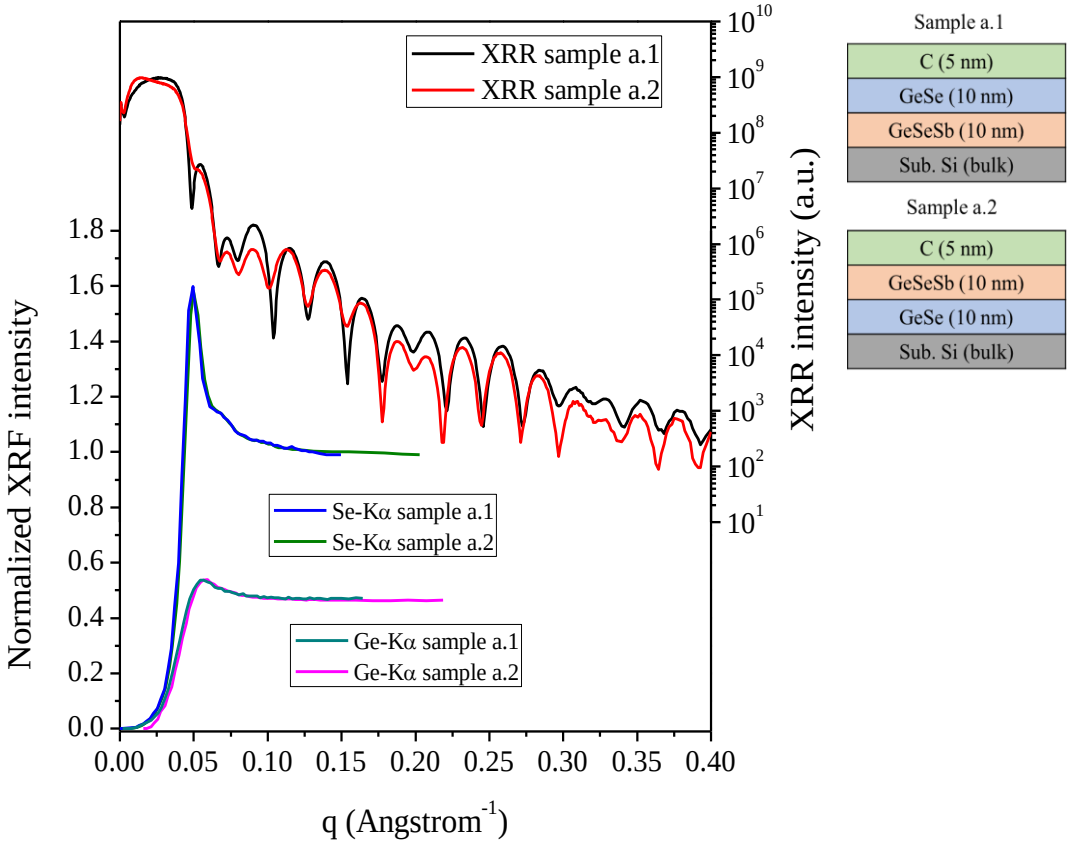

Figure 5.14. XRR and GIXRF results from sample a.1 and a.2 (deposited on Si substrate). Ge-Kα and Se-α show insignificant difference with variation of in-depth position of the Sb-doped layer. Normalized by the beam energy (13.5 keV).

As we can see from the Ge-Kα and Se-Kα GIXRF curves, when the film deposited is GeSe/GeSbSe, the first peak is higher than the second one, since more Ge and Se atoms are present in the surface and are progressively replaced along the depth. Whereas, the configuration GeSbSe/GeSe follows the opposite trend, the increase of Ge and Se atoms along the depth induces the second peak to be higher than the first one. The relative intensities of Ge-Kα and Se-Kα around the critical angles follows the in-depth distribution of Ge and Se elements in the stack. For instance, in the case of sample b.1, the first peak ("Peak 1") is more intense than the second one ("Peak 2"), since more Ge and Se atoms are present close the surface, while their atomic content decreased in the buried Sb-doped GeSe layer.

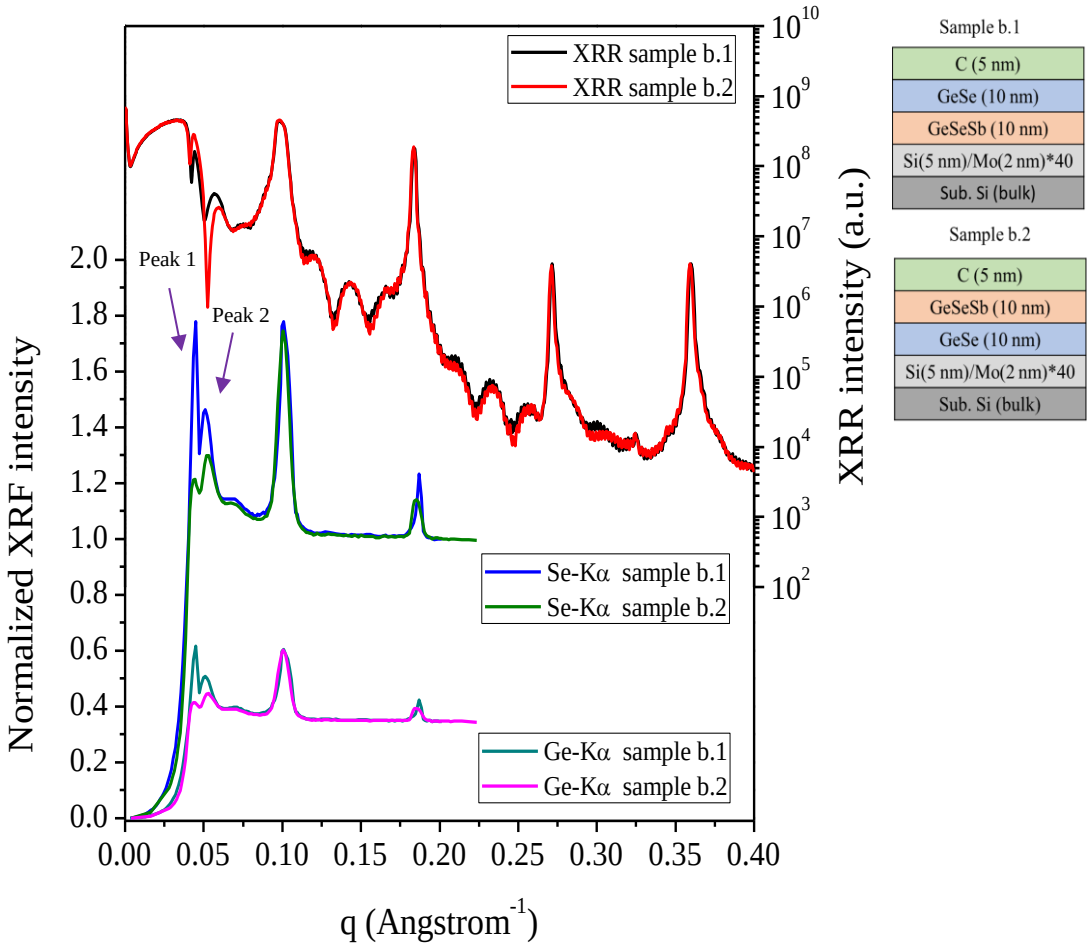

Figure 5.15. XRR and GIXRF results from samples b.1 and b.2 (deposited on multilayered substrate). Wit multilayered substrates, the position of the Sb-doped layer is easily spotted by the Ge-Kα and Se-Kα GIXRF data. Normalized by the beam energy (13.5 keV).

The improved sensitivity of GIXRF to in-depth profile when using Bragg mirror as substrate is clearly evidenced by Sb-Lα GIXRF data. (Fig.5.16).

In the case of the films deposited on the multilayered substrate (Fig. 5.16.b), Sb-La GIXRF data of samples b.1 and b.2 show significantly different features, and a higher level of information when compared to a.1 and a.2 samples. Although the difference in the layer sequence between samples (Sb-doped on top or buried) is qualitatively evidenced for both a and b type samples, with noticeable intensity of Sb-La below the critical angle when Sb-doped GeSe is on top, the full (quantitative) description of the chalcogenide stacking require the modelling of combined XRR and GIXRF data for Ge-Kα, Se-Kα and Sb-La layer. Due to qualitatively observed improvement of GIXRF sensitivity to layer sequence using multilayered substrates, we'll only deal in the following section with b type samples to extract chemical depth-profiles through combined GIXRF/XRR analysis.

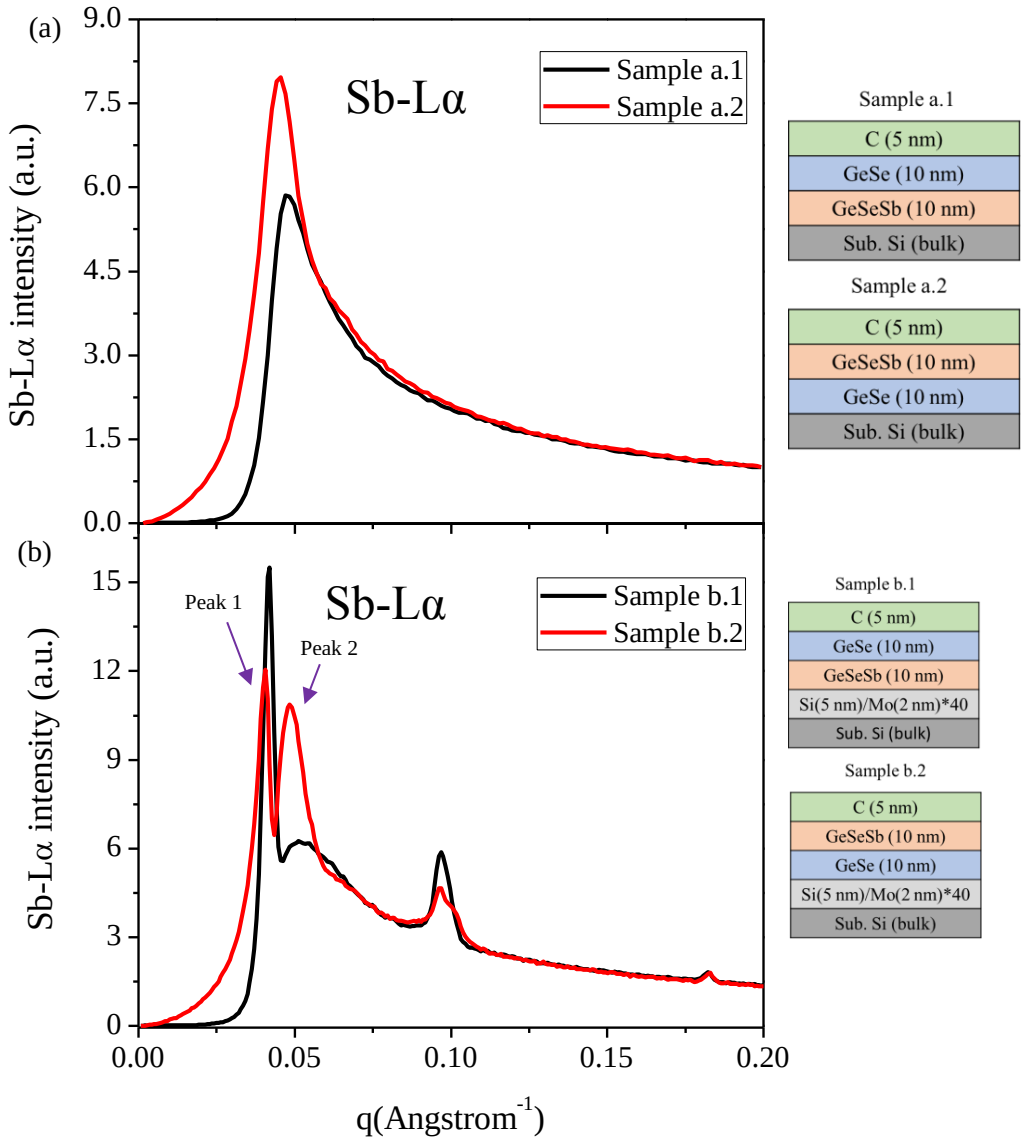

Figure 5.16. Sb-Lα GIXRF curves for samples deposited on (a) Si substrate, and (b) multilayered substrate. Normalized by the beam energy (8.05 keV).

ii. Elementary depth profiles

Chemical depth profiles were deduced from the analysis of GIXRF/XRR data with Jgixa software using differential algorithm and with fixed pre-determined instrumental parameters (*i.e.* detected zone L_d, Gaussian beam width and divergence) already listed in table 5.2. Figure 5.17 shows the comparison between experimental data and best-model calculation for samples b.1 and b.2.

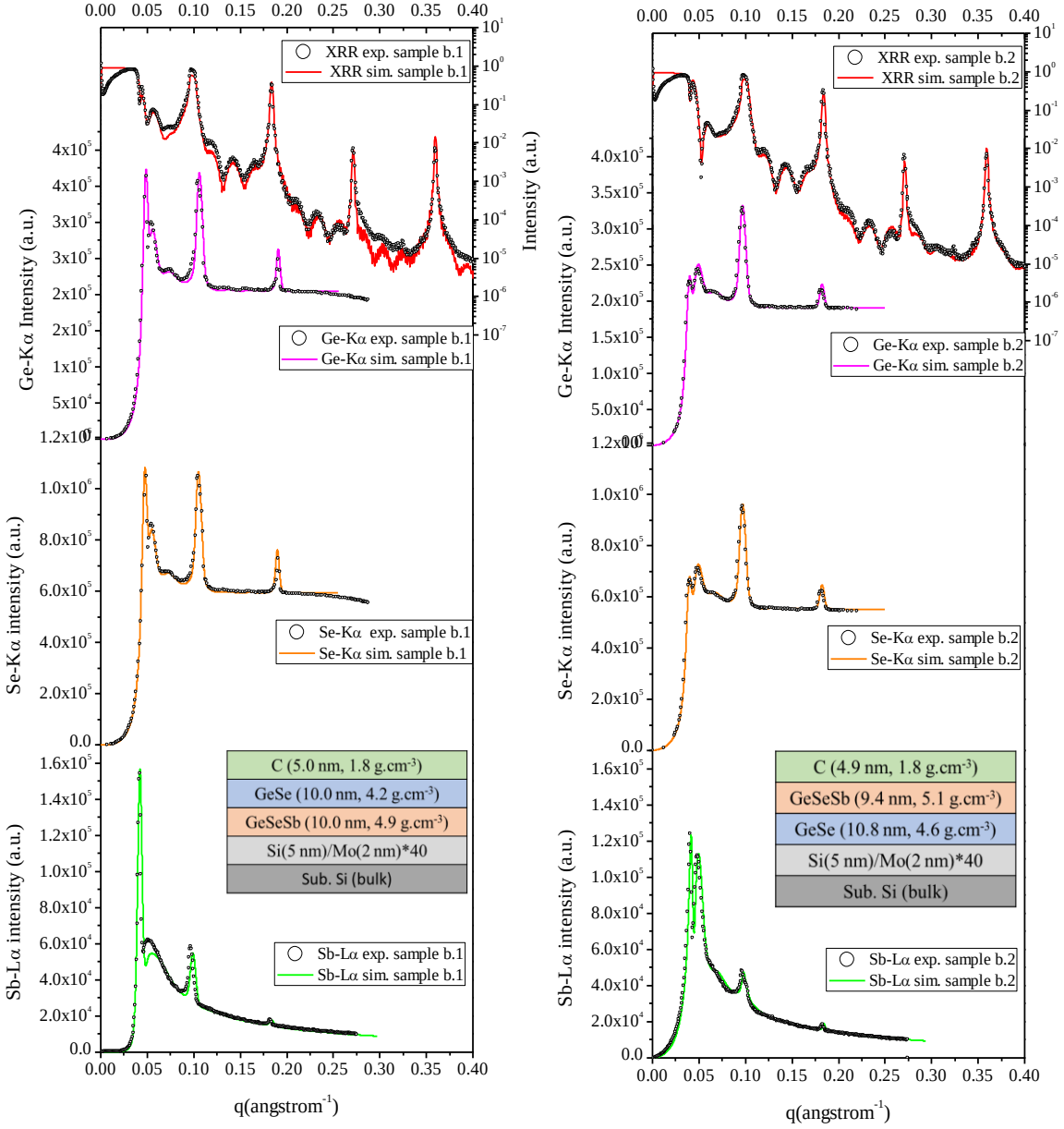

Figure 5.17. XRR and GIXRF data of samples b.1 and b.2 along with layer-based model deduced from combined GIXRF/XRR analysis with JGixa software.

The remarkable agreement between experimental and processed data is calculated from a very simple layer-based model where every individual film (carbon capping, Sb-doped GeSe and undoped GeSe) is described with one-only layer. Such a model certainly benefits from the efficiency of the carbon capping layer that protect the buried structure against oxidation while inducing no inter-diffusion with the chalcogenide layers. Sb-doped and undoped GeSe layers are clearly separated with slight variations of density of each layer depending of its position in the stack, and deduced thicknesses aligned with targets for all layers. The chemical depth-profiles deduced from GIXRF/XRR were compared to TOF-SIMS and PP-TOFMS measurements are depicted in Fig. 5.18. Both TOF-SIMS and PP-TOFMS results agree with the layer sequence unambiguously revealed by GIXRF/XRR and confirm the lack of inter-diffusion between Sb-doped and undoped GeSe layers.

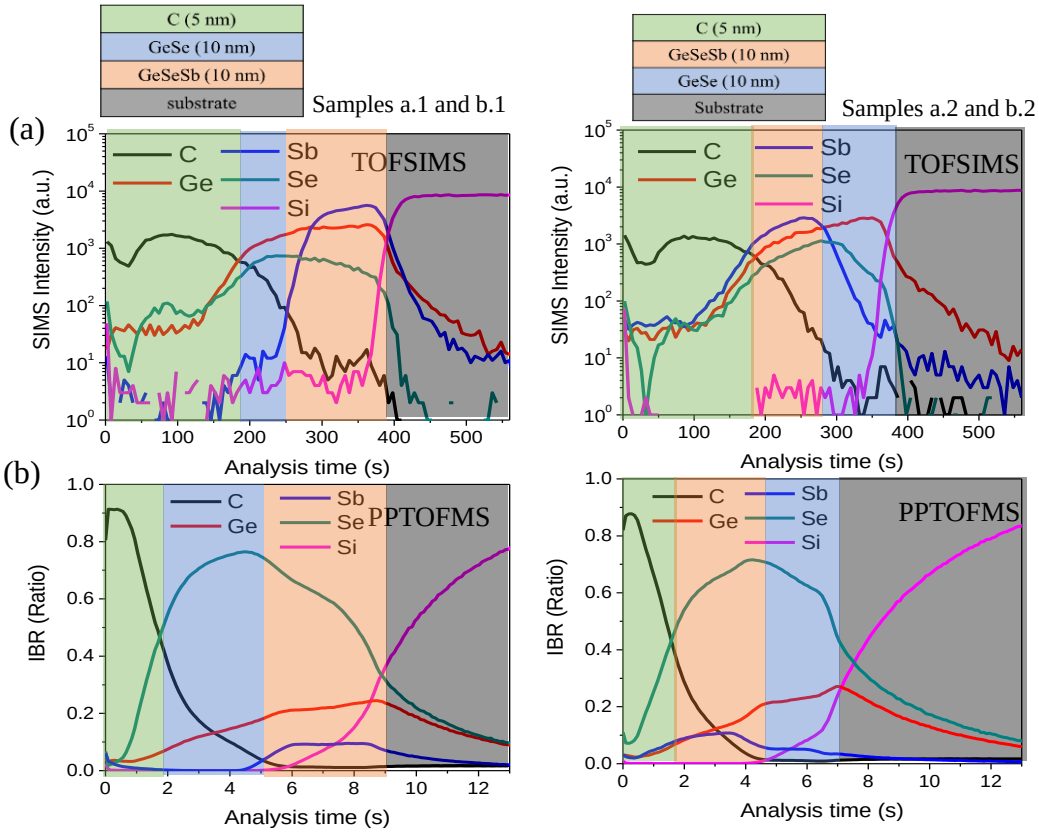

Figure 5.18. TOF-SIMS and PP-TOFMS chemical depth profiles are aligned with the layer sequence unambiguously revealed by GIXRF/XRR.

In conclusion, we have demonstrated that the sensitivity of GIXRF/XRR analysis to small variation of the in-depth chemical distribution could be significantly improved by fine tuning the profile of the X-ray standing wave field by the use of Bragg mirror as alternative substrate. This first encouraging demonstration on complex Se-based compounds for OTS applications showed that GIXRF/XRR was capable for elemental depth-profiling in thin layered stacks with SIMS-like sensitivity and depth resolution.

5.4. Probing Te-based films by angle-resolved XPS

With the substantial thickness reduction of chalcogenide films for the development of new 2-D materials as well as interfacial-Phase Change materials, dedicated protocols are needed to determine the elemental depth distribution in the nm range. At this ultra-thin scale, the elements are highly prone to inter-diffusion as well as surface/interfaces effects.

Such a depth resolution can hardly be obtained with sputtering-based XPS because of roughness and potential intermixing induced by ions or ion-clusters. On the contrary parallel angle-resolved XPS (p-ARXPS) appears suitable to probe complex ultra-thin stacks as it allows depth-profile reconstruction without degrading the sample (no sputtering) and without modifying the geometrical setup during the experiment, therefore reducing the alignment-related uncertainty that may affect conventional AR-XPS experiments.

In this section, we report on the ability of p-ARXPS technique to analyze the first deposition steps of amorphous GeTe and $Ge_2Sb_2Te_5$ films with thickness ranging from 1 to 4 nm. The profiles deduced by p-ARXPS were compared to XPS-WDXRF combined analysis of sub-layers with thickness ranging from 1 to 4 nm with 1 nm step so as to mimic the depth-profile in the final 4 nm-thick layer.

This approach aims first to study the in-depth elemental distribution when only few monolayers are deposited, hence providing insights to the development of Te-based films for IPCRAM applications, and, secondly, to assess p-ARXPS as process monitoring technique for ultra-thin films.

5.4.1. Experimental

- Sample preparation

Similarly to the deposition scheme used to grow Ge-Sb-Te thin materials and reported in chapter III, the films were amorphously sputtered on 300 mm Si (001) wafers, using industrial multi-chamber PVD deposition tool Endura 300 from Applied Materials. Since we are evaluating the first PVD deposition steps, it is important to highlight the very short "strike" step (usually less than one second) which consists to adjust the cathode power and/or chamber pressure in order to ensure that the plasma is appropriately activated for the sputtering regime. Hence, if the cathode has low (resp. high) power density ($W.cm^{-2}$), both parameters are increased (resp. reduced).

Once the strike step is performed, the sputtering regime is subsequently triggered to deposit the film with desired thickness and stoichiometry. The GeTe films were grown by co-sputtering, each element being sputtering from one 150 mm diameter cathode, Ge and Te cathodes being placed one opposite to the other above the substrate. The $Ge_2Sb_2Te_5$ films, on the other hand, were deposited from only one 150 mm diameter cathode with fixed stoichiometry. The main parameters of each deposited film are listed in table 5.3.

Table 5.3. Summary of deposition parameters, two different conditions have been evaluated for the deposition of GeTe layers (a and b).

	Deposition parameters	a-GeTe	b-GeTe	$Ge_2Sb_2Te_5$
Strike step	Ge power (W)	230 (DC)	230 (DC)	--
	Te power (W)	**200 (RF)**	**150 (RF)**	--
	GST 225 power (W)	--	--	300 (DC)
	Chamber pressure (mTorr)	0.68	0.68	0.47
	Argon flow (sccm)	10	10	5
Sputtering regime	Ge power (W)	230 (DC)	230 (DC)	--
	Te power (W)	150 (RF)	150 (RF)	--
	GST 225 power (W)	--	--	300 (DC)
	Chamber pressure (mTorr)	0.44	0.44	0.47
	Argon flow (sccm)	5	5	5
	Deposited films	• a-GeTe (1nm) • a-GeTe (4nm)	• b-GeTe (1nm) • b-GeTe (4nm)	• $Ge_2Sb_2Te_5$ (1nm) • $Ge_2Sb_2Te_5$ (2nm) • $Ge_2Sb_2Te_5$ (3nm)

- Sample characterization

Once the films were deposited, the wafers were transferred to the XPS tool by means of a vacuum carrier with oxygen-free mini environment, as described in chapter III. The XPS measurements were performed with monochromatic beam Al-Kα (1486.68 eV) and spot diameter 400 µm onto the film surface. As discussed in chapter III and IV, we selected the Ge 3d, Sb 4d and Te 4d core-levels that features same probing depth of ~ 7 nm. The films were probed with pass energy 40 eV and 0.05 eV as energy step, resulting in 0.6 eV resolution. Furthermore, the ARXPS measurements were performed within the inelastic angle range (from 20° to 63°). XPS and ARXPS quantification were based on attenuation lengths λ_{AL} calculated from TPP-2M formalism [18] along with the adjusted sensitive factors (corrected Scofield parameters) determined in chapter IV.

After ARXPS analysis, the wafers (exposed to air) were measured by WDXRF for chemical quantification, using Ge-Lα, Sb-$L\beta_1$ and Te-Lα fluorescence lines. The quantification was performed by fundamental parameters method with calibration based on pure metal samples, as described in chapter IV.

5.4.2. Results and discussions

- GeTe films

  - Chemical quantification

Figure 5.19 shows the XPS and WDXRF spectra of the two set of samples, a-GeTe and b-GeTe. From Fig.5.19.a, we can see that the intensities Te 4d and Ge 3d (both in metalloid-only states, Ge-Te

bonds) evolves only with the film thickness, irrespective of the a and b process conditions.

By contrast, the WDXRF measurements (after films exposed to air) surprisingly highlight some differences among the probed films. Whereas 4 nm GeTe films feature similar Ge-Lα and Te-Lα intensities for a and b conditions, hence in good agreement with XPS analysis, noticeable difference can be observed between Te-Lα spectra of 1 nm thick a-GeTe and b-GeTe films (lower intensity for a-GeTe).

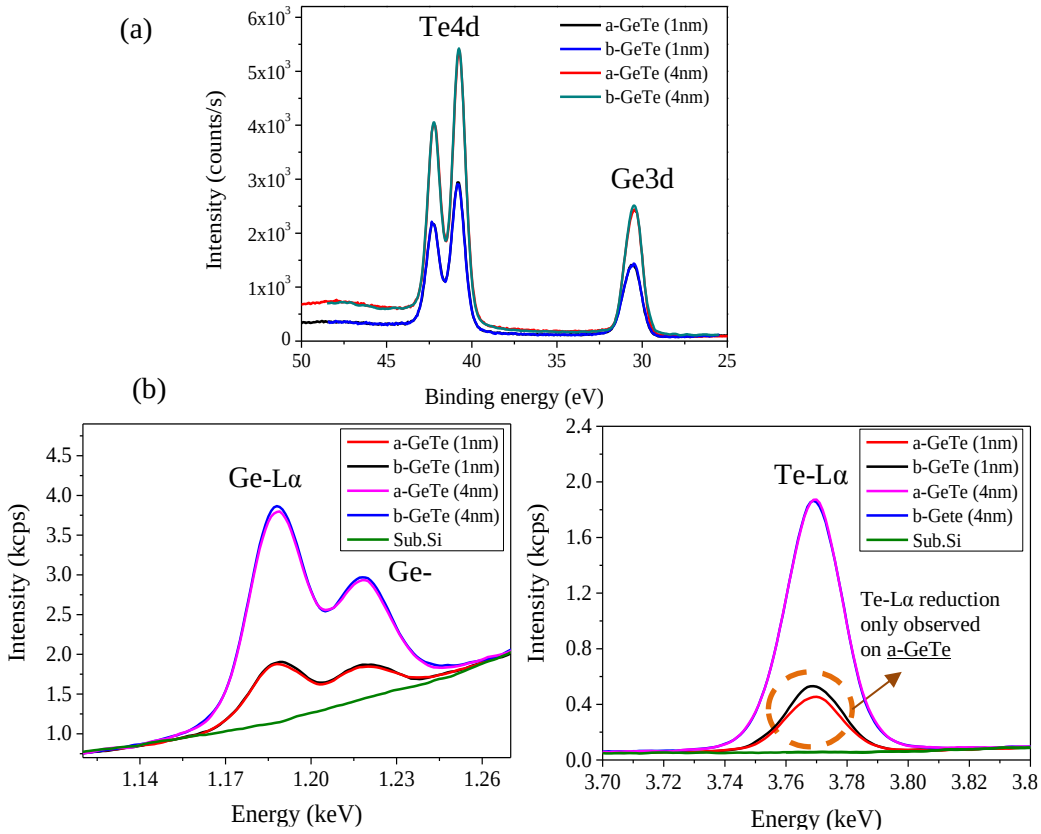

Figure 5.19. Qualitative spectra of the ultra-thin GeTe films (a) high resolution XPS spectra of Te 4d and Ge 3d core levels (b) WDXRF spectra of Ge-Lα and Te-Lα. Te-Lα intensity for 1 nm a-GeTe film is unexpectedly less than for b-GeTe (1nm) whereas XPS data are almost perfectly identical.

The reduction of Te-Lα intensity in the a-GeTe (1nm) film ranslates in a variation of the deposited mass (table 5.4) and an increased Ge/Te ratio. This unexpected result, only evidenced on 1 nm-thick layer, might be related to Te atom loss after the film exposed to air.

Table 5.4. deposited mass extracted from WDXRF quantitative analysis.

Sample	Deposited mass (µg.cm^{-2}) = thickness*density
a-GeTe (1nm)	**0.57**
b-GeTe (1nm)	0.65
a-GeTe (4nm)	2.43
b-GeTe (4nm)	2.43

Works about this kind of behavior is very limited, but a remarkable study has been conducted

by Lee et al [19]. In his work, he evaluated 20 nm tellurium poly-crystalline films deposited on polymethil methacrylate (PMMA) substrates by thermal evaporation. By sensitive quartz crystal microbalance, he observed that Te films lost weight when exposed to an ambient (85% relative humidity and 25 °C) with 500 l/min air flow. The frequency change of the microbalance is linearly proportional to the weight change for small frequency change. As shown in Fig. 5.20, the initial frequency drops (oxidation and adsorption of water vapor), and subsequently increases, indicating weight loss in Te films. For films with lower deposition rate, the effect seems to occur more rapidly. In addition, films deposited at 200 A/min or more, no weight loss was detected over the identical testing period. In spite of this remarkable work, the detailed mechanisms of Te volatilization is not yet perfectly understood from our knowledge. Lee's work cannot strictly compare to our study, as films deposited at LETI were sputtered on Si substrates in a controlled industrial cleanroom environment. However, process- (a versus b) and thickness-dependent loss of Te atoms in GeTe thin film has been observed after air break and exposition to intense polychromatic hard X-ray radiation in a WDXRF measurement chamber maintained at 36°C and in primary vacuum conditions, WDXRF measurement time being significant (400 seconds) so as to meet the required statistical uncertainty even for 1 nm film.. Therefore, further rigorous investigation about this effect should be planned so as to explain the evolution of Te-based ultra-thin films when exposed to air and above-described WDXRF environment.

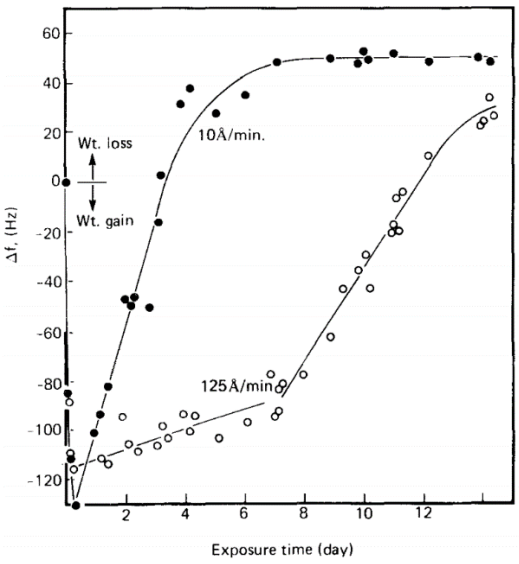

Figure 5.20. Frequency changes of microbalance as a function of exposure time in a dedicated chamber with 85% relative humidity and at 25°C. Difference between ageing of 20 nm thick tellurium films with low (1 nm/min) and high (12.5 nm/mn) deposition rate are illustrated [19].

The quantitative analysis by WDXRF and XPS is depicted in Fig. 5.21. We can see that both XPS and WDXRF reveals very little increase of Ge/Te for b films (with notable exception of WDXRF analysis of 1 nm films as reported above) which may relate to the lower RF power of the Te target during the strike step for b samples (150 W instead of 200 W for a samples).

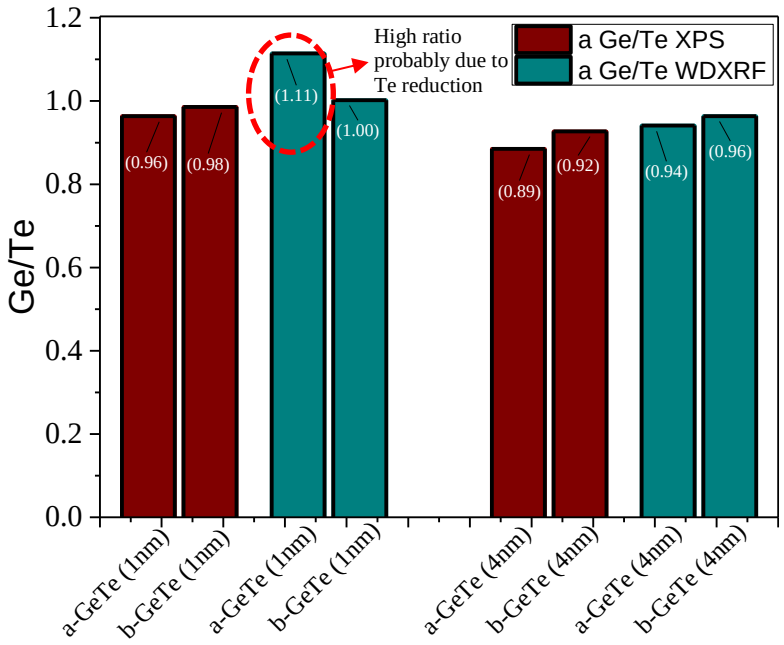

Figure 5.21. Ge/Te ratios obtained from XPS and WDXRF quantification.

- Elementary depth profiles

The p-ARXPS data of 4 nm GeTe films were processed by the maximum-entropy method [20] using the dedicated configuration in Thermofischer Avantage software. Figure 5.22 depicts the in-depth chemical profiles deduced from p-ARXPS analysis. Both films feature a thin (< 0.5 nm) carbon surface layer due to carbon contamination in both the transfer chamber of the process tool and the vacuum carrier. However, the in-depth distribution of Ge and Te elements differs significantly in sample a and sample.

In the case of 4 nm-thick a-GeTe (Fig.22.a), we can see that Ge and Te are almost homogenously distributed in depth down to the silicon substrate. By contrast, the 4 nm-thick b-GeTe film features more heterogeneous Ge and Te distribution with Ge-rich region close to the silicon substrate(depth ranging from 4 to 2.5 nm), followed by a Te-rich range (~ 2.5 to1.0 nm depth). This variability of Ge and Te depth distribution was unexpected as the chemical quantification of both films indicates almost the same Ge/Te ratio (from Fig.5.21). This non-uniformity of Ge and Te distribution in the 4 nm-thick b-GeTe (4nm) film might be related to the strike step during the deposition. As shown in table 5.4, *b* samples are deposited with constant power delivered to Ge (resp. Te) cathode during the strike and the sputtering steps, power values being set to 230 W (resp. 150 W) for both steps.). On the contrary, the deposition of *a* samples include a strike step at higher power delivered to the Te cathode (200 W instead of 150 W). The lower power delivered to Te cathode during the strike step may explain the Te-poor interfacial layer formed in 4 nm-thick b-GeTe samples.

Although the strike-step induced effect appears as a reasonable hypothesis, it is difficult to prove, since only little is known about the strike process. In fact, the term “strike” is mostly used in discussion with industrial partners, but not really reported in the literature, as this step is included in the whole sputtering process. In our case 0.5 second of strike corresponds only to 1/9 of the first wafer rotation.

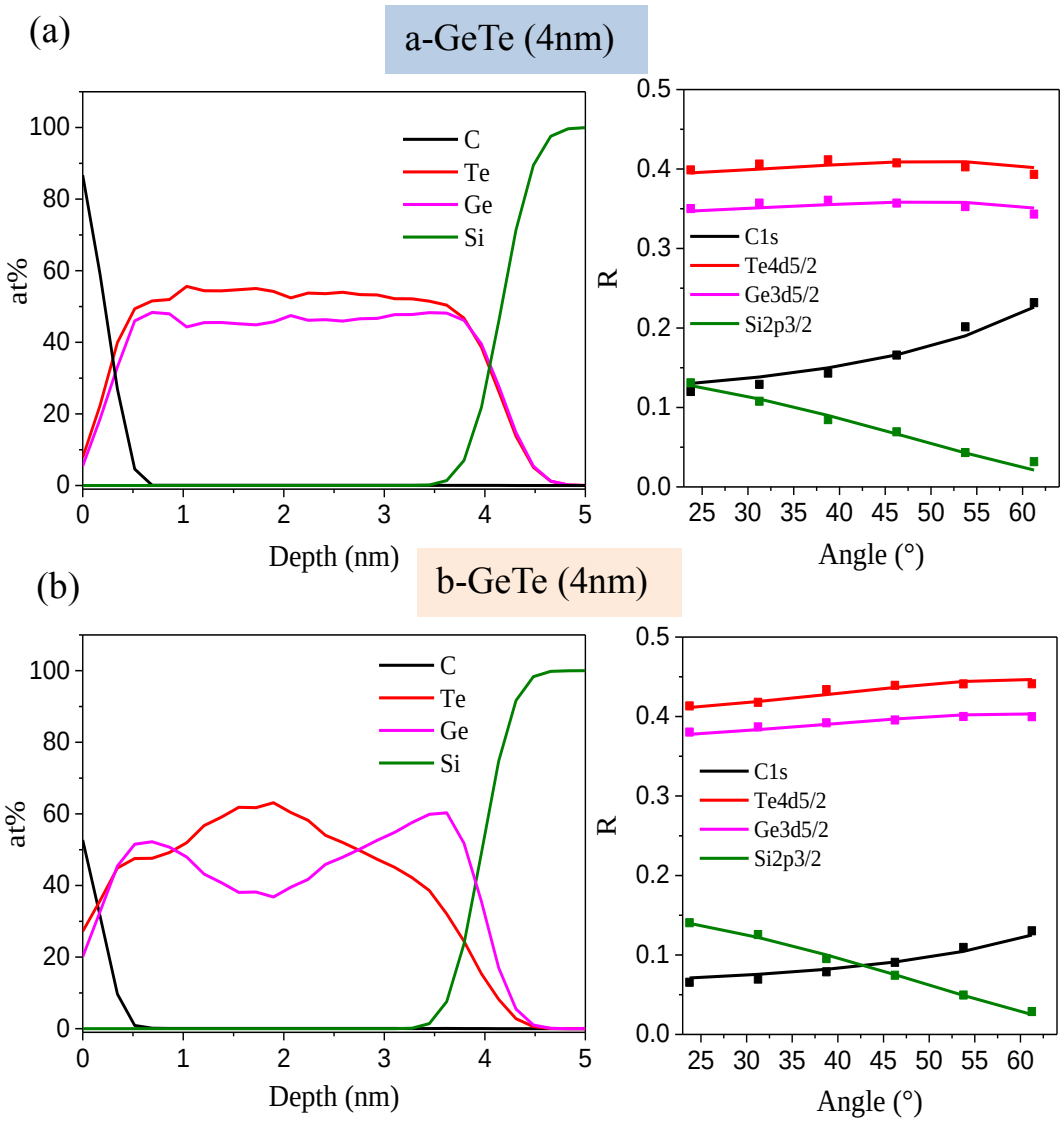

Figure 5.22. ARXPS elementary depth-profiles of 4 nm-thick GeTe films deposited using a and b condition reveals non-uniform distribution of Te and Ge in b-GeTe film.

- $Ge_2Sb_2Te_5$ films

The first deposition steps of $Ge_2Sb_2Te_5$ films were partially evaluated in chapter IV to support the evaluation of the accuracy of XPS quantification against WDXRF. Figure 5.23 synthetizes the quantitative results discussed in chapter IV, which first illustrate the good agreement between the two techniques, but more interestingly evidence a Te-rich (1.3 at% more than the bulk) and Sb-poor region close to the substrate.

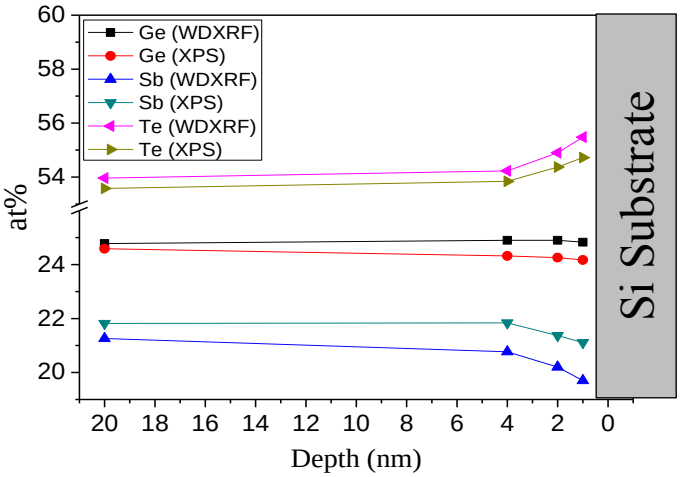

Figure 5.23. Chemical quantification of GST films from 1 to 20 nm thick as deduced from XPS and WDXRF.

Similar in-depth distribution of Ge, Sb and Te was observed in the p-ARXPS analysis of 4 nm thick $Ge_2Sb_2Te_5$ film, as shown in Fig. 5.24. The Te-rich interface is highlighted when restricting the displayed quantified values to Ge, Sb and Te only (with exclusion of carbon, native SiO_2 layer and silicon substrate) as illustrated in the inset of Fig. 5.24. Although the p-ARXPS highlights slight Te-enrichment of the GST-substrate interface, it is difficult to provide a process-related reason for this elemental distribution that would be difficult to probe with complementary techniques such as mass spectroscopy or sputtering-based XPS.

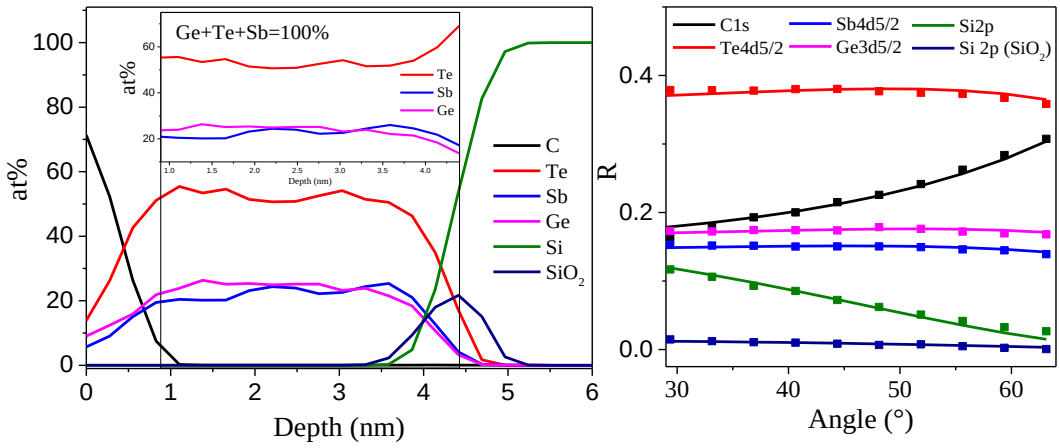

Figure 5.24. In-depth chemical distribution by ARXPS reveals slight Te-rich Ge-Sb-Te region close on the interface with SiO_2.

5.5. Conclusions

Elementary depth profiles protocols were developed using GIXRF/XRR combined analysis as well as parallel-ARXPS. We evaluated the performance of GIXRF/XRR combined analysis to probe ultra-thin Te-based films with small process-driven modifications. In-lab and synchrotron-based strategies were able to unambiguously reveal inter-diffusion between the tantalum capping layer and the chalcogenide film. Furthermore, the GIXRF/XRR combined analysis was able to access depth-dependent variation in Ti:Te ratio in 10 nm thick TiTe layers, as targeted PVD deposition. The elementary depth profiles were further confirmed by mass spectrometry (PPTOFMS). These results demonstrate how appropriate GIXRF/XRR can be as non-destructive depth-profiling technique for complex thin materials with composition-driven properties. GIXRF-XRR tool with mastered instrumental function (divergence, detected length and beam width) appears particularly suitable to support process development in lab and even in fabs.

Furthermore, we demonstrated that the use of multilayered substrate instead of Si substrate allowed fine-tuning of the depth-dependent X-ray standing wave field, resulting in improved sensitivity of XRR/GIXRF strategies. This approach was validated by probing Sb-doped GeSe thin-films with two distinct Sb depth distribution. The films deposited on Si substrate showed insignificant difference in GIXRF/XRR data regardless the Sb distribution, whereas when deposited on multilayered substrate, unambiguous in-depth distribution of Ge, Sb and Se was observed for similar films deposited on (Mo/Si)*40 Bragg mirror. In addition, layer-based modeling of the GIXRF/XRR deduced in-depth elemental distribution was further confirmed by mass spectrometry (TOF-SIMS and PP-TOFMS).

At last, we developed protocol to evaluate the first sputtering deposition steps of GeTe and $Ge_2Sb_2Te_5$ films (1 to 4 nm thick). The approach not only revealed good agreement between XPS and WDXRF quantification but also unexpected loss of Te species for 1 nm thick GeTe film after ageing. An extensive study about this Te loss is previewed as future work. By probing these films by parallel-ARXPS, we revealed process induced variabilty of the in-depth distribution of Ge and Te in 4 nm thick GeTe film, and we highlighted the possible impact of the strike step conditions on this elemental distribution. In the case of $Ge_2Sb_2Te_5$ film, both WDXRF and ARXPS strategies revealed a slightly Te-rich interface with the silicon substrate. The combination of WDXRF, XPS and p-ARXPS is highly sensitive to small in-depth variations of the elemental distribution at the nm level, and should be more systematically included in the development and monitoring of innovative ultra-thin Te-based films for PCRAM applications.

5.6. References

[1] A. Kiouseloglou *et al.*, "A Novel Programming Technique to Boost Low-Resistance State Performance in Ge-Rich GST Phase Change Memory," *IEEE Trans. Electron Devices*, vol. 61, no. 5, pp. 1246–1254, May 2014.

[2] R. E. Simpson *et al.*, "Interfacial phase-change memory," *Nat. Nanotechnol.*, vol. 6, no. 8, pp. 501–505, Aug. 2011.

[3] H. Rotella *et al.*, "Elemental depth profiling in transparent conducting oxide thin film by X-ray reflectivity and grazing incidence X-ray fluorescence combined analysis," *Spectrochim. Acta Part B At. Spectrosc.*, vol. 135, pp. 22–28, Sep. 2017.

[4] B. Caby *et al.*, "Study of annealing-induced interdiffusion in In2O3/Ag/In2O3 structures by a combined X-ray reflectivity and grazing incidence X-ray fluorescence analysis," *Spectrochim. Acta Part B At. Spectrosc.*, vol. 113, pp. 132–137, 2015.

[5] D. De Boer, A. Leenaers, and W. Van den Hoogenhof, "Glancing-incidence x-ray analysis of thin-layered materials: A review," *X-Ray Spectrom.*, vol. 24, no. 3, pp. 91–102, 1995.

[6] A. J. G. Leenaers, J. J. A. M. Vrakking, and D. K. G. de Boer, "Glancing incidence X-ray analysis: more than just reflectivity!1This paper was presented at the 6th Conference on 'Total Reflection X-Ray Fluorescence Analysis and Related Methods' (TXRF '96) held in two parts in Eindhoven (The Netherlands) and Dortmund (Germany) in June 1996, and is published in the Special Issue of Spectrochimica Acta, Part B, dedicated to that Conference.1," *Spectrochim. Acta Part B At. Spectrosc.*, vol. 52, no. 7, pp. 805–812, Jul. 1997.

[7] W. Li *et al.*, "Geometrical factor correction in grazing incident x-ray fluorescence experiment," *Rev. Sci. Instrum.*, vol. 83, no. 5, p. 053114, 2012.

[8] M. Zhu *et al.*, "One order of magnitude faster phase change at reduced power in Ti-Sb-Te," *Nat. Commun.*, vol. 5, p. 4086, 2014.

[9] W. Grimm, "New glow discharge lamp for optical emission spectral analysis," *Spectrochim. ACTA PART B-At. Spectrosc.*, no. 7, p. 443, 1968.

[10] Y. Kataoka, "Standardless X-ray fluorescence spectrometry (Fundamental parameter method using sensitivity library)," *Rigaku J.*, vol. 6, no. 1, pp. 33–39, 1989.

[11] V. Solé, E. Papillon, M. Cotte, P. Walter, and J. Susini, "A multiplatform code for the analysis of energy-dispersive X-ray fluorescence spectra," *Spectrochim. Acta Part B At. Spectrosc.*, vol. 62, no. 1, pp. 63–68, 2007.

[12] D. Ingerle *et al.*, "Combined evaluation of grazing incidence X-ray fluorescence and X-ray reflectivity data for improved profiling of ultra-shallow depth distributions," *Spectrochim. Acta Part B At. Spectrosc.*, vol. 99, pp. 121–128, 2014.

[13] D. Ingerle, G. Pepponi, F. Meirer, P. Wobrauschek, and C. Streli, "JGIXA — A software package for the calculation and fitting of grazing incidence X-ray fluorescence and X-ray reflectivity data for the characterization of nanometer-layers and ultra-shallow-implants," *Spectrochim. Acta Part B At. Spectrosc.*, vol. 118, pp. 20–28, Apr. 2016.

[14] G. E. Ghezzi *et al.*, "The effect of Ta interface on the crystallization of amorphous phase change material thin films," *Appl. Phys. Lett.*, vol. 104, no. 22, p. 221605, Jun. 2014.

[15] P. Noé, C. Sabbione, N. Bernier, N. Castellani, F. Fillot, and F. Hippert, "Impact of interfaces on scenario of crystallization of phase change materials," *Acta Mater.*, vol. 110, pp. 142–148, 2016.

[16] M. Nayak, G. S. Lodha, R. V. Nandedkar, S. M. Chaudhari, and P. Bhatt, “Interlayer composition in Mo–Si multilayers using X-ray photoelectron spectroscopy,” *J. Electron Spectrosc. Relat. Phenom.*, vol. 152, no. 3, pp. 115–120, Jul. 2006.

[17] H. Maury *et al.*, “Interface characteristics of Mo/Si and B4C/Mo/Si multilayers using non-destructive X-ray techniques,” *Surf. Sci.*, vol. 601, no. 11, pp. 2315–2322, Jun. 2007.

[18] S. Tanuma, C. J. Powell, and D. R. Penn, “Calculations of electron inelastic mean free paths. V. Data for 14 organic compounds over the 50–2000 eV range,” *Surf. Interface Anal.*, vol. 21, no. 3, pp. 165–176, 1994.

[19] W. Lee and R. H. Geiss, “Degradation of thin tellurium films,” *J. Appl. Phys.*, vol. 54, no. 3, pp. 1351–1357, Mar. 1983.

[20] G. Smith and A. Livesey, “Maximum entropy: A new approach to non-destructive deconvolution of depth profiles from angle-dependent XPS,” *Surf. Interface Anal.*, vol. 19, no. 1–12, pp. 175–180, 1992.

[21] Caby B. et al, “Comparison of four data analysis software for combined X-ray reflectivity and grazing incidence X-ray fluorescence measurements,” 16th International Conference on Total Reflection X-ray Fluorescence Analysis and Related Methods (TXRF) 2015.

Conclusions

In this PhD work, we have tried to assess characterization strategies based on non-destructive X-ray techniques for the three main metrological issues that should be addressed to assist the scaling of chalcogenide materials: investigation of surface/interface effects, accurate quantification of chemical composition and elementary depth profiles. We have demonstrated the benefits of systematic use of XPS, WDXRF and combined GIXRF/XRR techniques to assist the development of new chalcogenide films such as Ge-Te-Se phase change materials and Se-based OTS for PCRAM applications, or innovative ultrathin sulfur-based transition metal dichalcogenides.

We have shown that *quasi in-situ* XPS allowed fine investigation of composition-dependent binding states and ageing of tellurium compounds, whereas the careful combination of XPS and WXDRF could be used to refine XPS composition-dependent relative sensitivity factors for Ge-Sb-Te compounds, resulting in improved accuracy of in-line XPS-based quantification at the wafer level.

We have overcome the lack of standards for quantitative of sulfur compounds with WDXRF, and we have demonstrated the interest of systematic XPS/WDXRF metrology of the deposited mass and composition to assist the development of new deposition process for sulfur-based transition metal dichalcogenides (MoS_2, WS_2).

We have highlighted the importance of the optimization of the instrumental conditions in combined GIXRF/XRR experiments, and we have demonstrated that optimized non-destructive GIXRF/XRR strategies, even developed in the Lab, were able to unambiguously reveal elemental depth distribution and/or inter-diffusion with SIMS-like sensitivity. On top of that, we have shown that the sensitivity of GIXRF/XRR analysis to small variation of the in-depth chemical distribution could be significantly improved by fine tuning the profile of the X-ray standing wave field by the use of multilayer substrate (Mo/Si)*40. This first encouraging demonstration on complex Se-based compounds for OTS applications will be followed by other experiments using Bragg mirrors with fine-tuned characteristics as substrates for deposition of chalcogenide stacks and further non-destructive evaluation by GIRXF/XRR. In addition, XRF in grazing emission geometry should also be evaluated as this setup would overcome the spot size limitation of GIXRF where elongated spot cannot fit in measurement areas of product wafers.

We have investigated the use of different capping layers to protect chalcogenide films against ageing. Apart from their interest in the final device that will be further studied (for instance for carbon layer in OTS stacks), *in-situ* capping with low density material (SiN, C) is now extensively used to relax queue-time constraints for XPS measurements for instance.

We have started with the evaluation of inline metrological solutions for thin chalcogenides films doped with low-Z materials. However, this topic was too large to be fully addressed in the frame of this PhD. We have highlighted some difficulties, not only related to the importance of matrix effects in XRF-based analysis of N-doped complex compounds, but also in the accuracy of the quantitative information provided by Ion Beam Analysis.

6. Annex A: Ion Beam analysis (IBA)

When an energetic Ion beam 1-5 MeV (e.g. He^{+}) interacts with a sample, nuclear as well as electronic process take place as illustrated in Fig.1. These interactions are the basis of Ion Beam Analysis such as Rutherford backscattering spectrometry (RBS), nuclear reaction analysis (NRA) and particle-induced X-ray emission (PIXE).

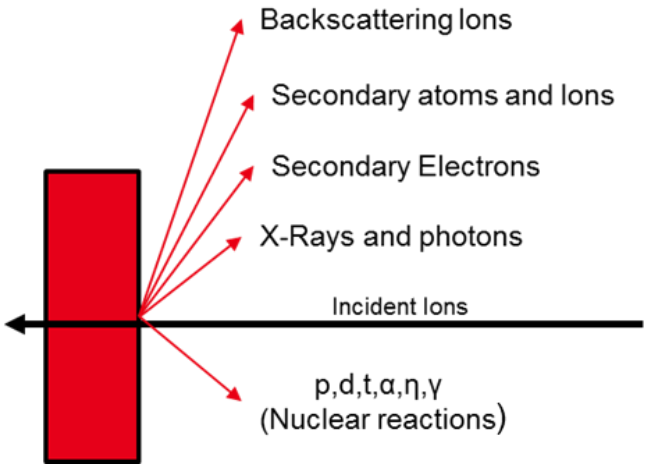

Figure 6.1. Processes induced with the energetic Ion beam interacting with the sample.

- Rutherford backscattering spectrometry (RBS): It is an analytical method for chemical composition with full metrological traceability of very high absolute accuracy based on Coulombic interaction following classic scattering laws. When a sample is bombarded with a beam of high energy particles, the energy measured of the backscattered particles at a given angle depends upon two processes. i/ particles lose energy when passing through the sample, and the amount of energy lost depend on the material's stopping power. ii/ Particles also lose energy by means of collision only. This loss is dependent on the projectile mass as well as sample mass. The ratio of the energy of the projectile before and after collision is called the kinematic factor. Hence, the number of backscattering events that occur from a given element in a sample depend upon two factors: the concentration of the element and the effective size of its nucleus. The probability that a material will cause a collision is called scattering cross section [1] [2].
- Elastic backscattering spectrometry (EBS): also known as non-Rutherford backscattering spectrometry. It is similar to RBS, but with enhanced sensitivity towards light elements (e.g. C, N, O). It works when the Coulomb barrier is exceeded and the cross-section fluctuates in non-Rutherford regime. In this case Nuclear Reactions may also arise, the analysis can be tuned by choosing a resonance energy corresponding to the nuclear reaction of the light element to be quantified. In the case of nitrogen on heavy matrix (Ge-Sb-Te), the chosen energy was 3697 keV resonance of the $^{14}N(\alpha,\alpha)^{14}N$ reaction (see Figure 2) [2] [3].

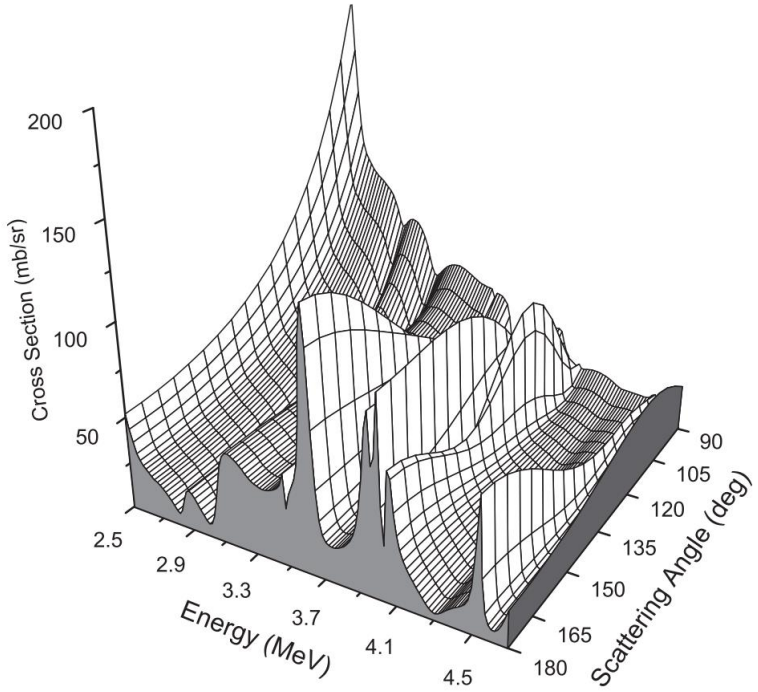

Figure 6.2. Evaluated EBS cross-sections for alphas on nitrogen [3].

- Nuclear reaction analysis (NRA): It is a technique for quantification of light elements (e.g., C, N, O, etc). It works when the incident energetic Ion beam exceeds the coulombic barrier triggering nuclear reactions on the analyzed material. The ejected particles have characteristic kinetic energies of the induced nuclear reactions. In this doctoral work, the quantitative analysis of the N concentration on GeSbTe matrix was based on well-known SiN standards [2].

- IBA analysis chamber

The main sample chamber components are a stage, one or more detectors, a beam entrance, and the vacuum system. The chamber can be as simple as a flange with a sample and a single energy dispersive spectrometer attached (see Fig. 6.3). More typically, the samples mount on a five-axis goniometer, which is convenient for loading many samples into the vacuum system and analyzing them sequentially. The goniometer can also tilt and rotate the samples. Comparing spectra obtained at different incident and exit beam angles provides better characterization of sample composition as a function of depth. Tilting the sample is also possible to reduce channeling effects undesired for quantification of amorphous thin layered materials on crystalline substrate. Two surface barrier detectors (one normal angle, one grazing exit), are included in a typical RBS sample chamber [2].

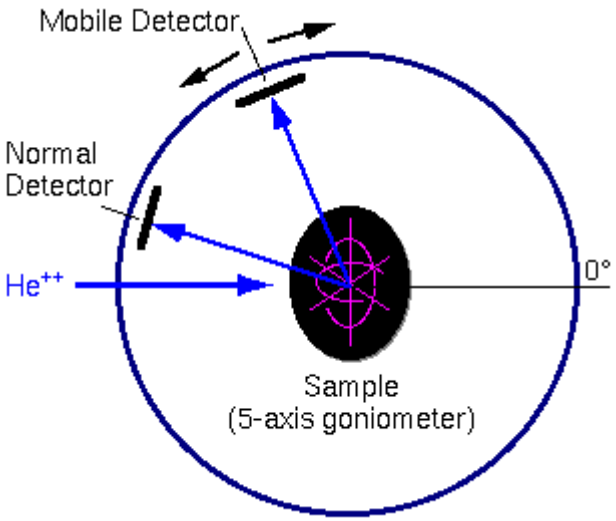

Figure 6.3. Schematic view of an Ion Beam Analysis chamber.

- RBS and EBS measurement conditions of laboratories

Table 6.1. Measurement conditions RBS and EBS.

Parameter	Laboratory 1 (RBS)	Laboratory 2 (EBS)	Laboratory 3 (RBS)
Ion Beam Energy (MeV)	2.1 (He^{+})	3.717 (He^{+}) at $^{14}N(\alpha,\alpha)^{14}N$	2.275 (He^{++})
Normal Detector Angle (°)	160	173.4	160
Second Detector Angle (°)	No	139.7	118 (grazing)
Tilted sample	15°		
Beam size	1x1 mm2		

- NRA measurement conditions

Table 6.2. Measurement conditions NRA.

	Laboratory 1	Laboratory 2
Deuterium D+ beam (MeV)	1.2	1.0
Analyzed reaction	$^{14}N(d,\alpha)^{12}C$	N(d,p)
Normal detector angle (°)	150	
Attenuators	10µm of mylar	
Quantification	SiN standard	

- Sb and Te separation

RBS and EBS cannot separate Sb and Te spectra, since they have close atomic number. Laboratory 1 and 3 were able to separate both elements with additional techniques PIXE (laboratory 1) and WDXRF (laboratory 2).

- PIXE measurement of laboratory 1

Particle induced X-ray emission (PIXE) is a technique based on the emission characteristic X-ray fluorescence photons of the material after the energetic Ion beam bombardement. The technique rely in the principles of X-ray fluorescence discussed in this work. It is complementary analysis of RBS, not only because it is performed in the same analysis chamber, but also because elements with close atomic number can be easily distinguished. The technique is suitable for high X-ray range, since at low-energy range, the XRF photons are attenuated by a dedicated absorber to reduce the influence of backscattered particles and the high intensity of photons emitted from the Si substrate [2].

Sb and Te separation was performed by 3 MeV protons beam easily exciting the K-lines of Sb and Te. A carbon absorber (315 μm) was placed in front of the EDX detector to stop the backscattered particles and reduce the influence of XRF photons from the Si substrate. The Sb/Te ratio was determine by dedicated software GUPIX taking in account all XRF factors (Photo-absorption cross sections, fluorescence yielding, secondary fluorescence, etc). Then the ratio is implemented in the Ge,Sb+Te quantification from RBS to determine the concentration of each element.

- WDXRF measurements of laboratory 2

The equipment used was a Rigaku Primus II WDXRF system. The samples were analyzed under vacuum using X-rays from a rhodium X-ray tube. Quantification was performed using the fundamental parameters standardless quantification software associated with the system. Fundamental parameters uses x-ray physics coupled with established sensitivity factors for pure elements. Accuracy by this method usually ranges from 5-20% for major elements. Similar to laboratory 1, the Sb/Te ratio was implemented in the Ge and Sb+Te quantification from RBS to the determine concentration of elements.

A.1. References

[1] C. Jeynes and J. L. Colaux, “Thin film depth profiling by ion beam analysis,” *Analyst*, vol. 141, no. 21, pp. 5944–5985, 2016.

[2] M. Nastasi, J. W. Mayer, and Y. Wang, *Ion beam analysis: fundamentals and applications*. CRC Press, 2014.

[3] A. F. Gurbich, I. B. Radović, Z. Siketić, and M. Jakšić, “Measurements and evaluation of the cross-section for helium elastic scattering from nitrogen,” *Nucl. Instrum. Methods Phys. Res. Sect. B Beam Interact. Mater. At.*, vol. 269, no. 1, pp. 40–44, 2011.

7. Annex B: Mass spectrometry techniques

- TOF-SIMS

Time Of Flight Secondary Ion Mass Spectrometry is an elemental and molecular surface characterization technique. It is based on the analysis of the secondary ions ejected from a sample while being bombarded by a primary focused ion beam. Mass over charge ratio of the ejected ions are determined via their flight time between the sample surface and the detector. To allow the depth profiling of the samples, a second ion beam can be used in order to sputter the sample surface. The achievable depth resolution is inferior to the nanometer. The technique is able to detect every element and all their isotopes. The mass resolution ($\Delta m/m$) of the spectrometers used is at least 10000. Generally, the technique is not directly quantitative but quantification is possible by using reference samples controlled by a different characterization technique. The technique also allows imagery as the primary beam scans the sample surface, lateral resolution is inferior to 100 nm [1].

- Measurement conditions of TiTe and GeSbSe films

TOF-SIMS experiments were performed on an IonTof TOF-SIMS instrument. Sputtering was ensured by a 500 eV Cs^+ beam and analysis by a 25 keV Bi_3^+ primary beam. Both guns were pointing at the samples surface with a 45° incident angle. The sputtered craters were 250x250 μm^2 while the analysis zones were 90x90 μm^2 positioned at the center of the sputtering crater to avoid crater wall effects. MCs^+ ions were used to depth profile all the samples. MCs+ mode reduces matrix effects leading to easier depth profile interpretation. Low sputtering energy (500 eV) was used to achieve a good depth resolution.

- PPTOFMS

PP-TOFMS (Horiba Scientific) is a sputtering-based elemental depth profiling technique. It uses a pulsed radio frequency glow discharge plasma for sample sputtering and ionization in a Grimm-type [2] source. Ionized species are extracted from the glow discharge and detected by an orthogonal time-of-flight mass spectrometer. Spatial resolution of the technique is defined by the diameter of the anode used and is typically of a few mm, prohibiting imagery. As sputtering and ionization rates in Glow Discharge Mass Spectrometry only vary slightly over the periodic table, semi-quantification can be achieved by simply taking the ration of ionic currents [3, 4] via the Ion Beam Ratio (IBR) method. Plasma parameters (namely applied power and pressure) have to be optimized depending on the material so that the resulting sputtered crater bottom is as flat as possible to achieve optimal depth resolution.

- Measurement conditions of TiTe films

A 4 mm anode diameter was used leading to 4 mm in diameter analysis craters. The measurements were performed by applying 35 W RF power and regulating the pressure in the source at 150 Pa of 6N argon gas. Pulsing period was 3 ms with a pulse width of 200 μs.

- Measurement conditions of GeSbSe films

A 4 mm anode diameter was also used. The measurements were performed by applying 40 W RF power and regulating the pressure in the source at 165 Pa of a mixture of 70 vol% Ar and 30 vol% He. Pulsing period was 1.2 ms with a pulse width of 200 μs.

B.1. References

[1] J. C. Vickerman and D. Briggs, *Tof-SIMS: materials analysis by mass spectrometry*. im publications, 2013.

[2] W. Grimm, "New glow discharge lamp for optical emission spectral analysis," *Spectrochim. ACTA PART B-At. Spectrosc.*, no. 7, p. 443, 1968.

[3] W. Vieth and J. C. Huneke, "Relative sensitivity factors in glow discharge mass spectrometry," *Spectrochim. Acta Part B At. Spectrosc.*, vol. 46, no. 2, pp. 137–153, Jan. 1991.

[4] F. L. King, J. Teng, and R. E. Steiner, "Special feature: Tutorial. Glow discharge mass spectrometry: Trace element determinations in solid samples," *J. Mass Spectrom.*, vol. 30, no. 8, pp. 1061–1075.

8. List of publications

- *International journals:*

  - **W. Pessoa**, A. Roule, E. Nolot, Y. Mazel, M. Bernard, M.-C. Lépy, Y. Ménesguen, A. Novikova, P. Gergaud, F. Brigidi, D. Eichert, "Grazing incident X-ray fluorescence combined with X-ray reflectometry metrology protocol of telluride-based films using in-lab and synchrotron instruments," *Spectrochim. Acta Part B At. Spectrosc.*, 2018. https://doi.org/10.1016/j.sab.2018.07.003.

  - P. Kowalczyk, F. Hippert, N. Bernier, C. Mocuta, C. Sabbione, **W. Batista-Pessoa**, P. Noé, "Impact of Stoichiometry on the Structure of van der Waals Layered GeTe/Sb2Te3 Superlattices Used in Interfacial Phase-Change Memory (iPCM) Devices," *Small*, p. 1704514, 2018. https://doi.org/10.1002/smll.201704514.

- *International Conferences:*

  - **W. Pessoa**, C. Sabbione, A. Roule, E. Nolot, "In-line metrology of Tellurium-based materials for advanced memory applications," European Conference on X-Ray Spectrometry (EXRS), Ljubljana, Slovenia, 2018.

  - E. Nolot, S. Cadot, W. Darwich, **W. Pessoa**, F. Martin, P. Hoenicke, C. Zech, B. Beckhoff, J. England, E. Moura-Stori, C. Jeynes, "In-line characterization of ultrathin MoS2 and WS2 materials using XRF-XPS strategies," European Conference on X-Ray Spectrometry (EXRS), Ljubljana, Slovenia, 2018.

  - Y. Ménesguen, M.-C. Lépy, **W.-W. Batista-Pessoa**, S. Torrengo, E. Nolot, "Combined XRR-GIXRF analysis at SOLEIL," 67th Deven X-ray Conference (DCX), Westminster, Colorado, USA, 2018.

  - **W. Pessoa**, C. Sabbione, A. Roule, M.C. Lépy, M. Bernard, E. Nolot, "In-line metrology of Te-based ultra-thin films for memory applications," European Conference on Applications of Surface and Interface analysis (ECASIA), Montpellier, France, 2017.

  - **W. Pessoa**, A. Roule, E. Nolot, M.-C. Lépy, Y. Ménesguen, A. Novikova, P. Gergaud, D. Eichert, F. Brigidi, "Probing Telluride-based films by in-lab and Synchrotron X-Ray metrology(XRR/GIXRF)," The 17th International Conference on Total Reflection X-Ray Fluorescence Analysis and Related Methods (TXRF), Brescia, Italy, 2017.

  - E. Nolot, A. Roule, R. Gassilloud, D. Eichert, **W. Pessoa**, M.-C. Lépy, "XRF-based analysis for advanced memories," The 17th International Conference on Total Reflection X-Ray Fluorescence Analysis and Related Methods (TXRF), Brescia, Italy, 2017.

  - C.Jeynes, E.Nolot, C. Sabbione, **W. Pessoa**, F. Pierre, A. Roule, M.Mantler, "Quantifying nitrogen in GeSbTe:N alloys," European Materials Research Society (E-MRS), Strasbourg, France, 2017.

- E. Nolot, A. Roule, **W. Pessoa**, M.C. Lépy, "Metrology challenges for thin chalcogenide layered systems: in-fab control of composition and depth-dependent properties," European Materials Research Society (E-MRS), Strasbourg, France, 2017.

- Yves Ménesguen, Anastasiia Novikova, Marie-Christine Lépy, **Walter-Wilkener Batista-Pessoa**, Hélène Rotella, Emmanuel Nolot, Jean-Michel André, Karine Le Guen, Philippe Jonnard, Diane Eichert, "CASTOR, a new tool for combined XRR-GIXRF analysis at SOLEIL," European Materials Research Society (E-MRS), Strasbourg, France, 2017.

- Walid Darwich, **Walter Batista-Pessoa**, Emmanuel Nolot, S. Cadot, François Martin, Elsje Alessandra Quadrelli, "Study of WS2 CVD growth on sapphire substrate: from W carbonyl adsorption to ultrathin sheets formation," 1st European Conference on Chemistry of Two-Dimensional Materials (Chem2DMat), Strasbourg, France, 2017

- KOWALCZYK Philippe; SABBIONE Chiara; HIPPERT Françoise; BERNIER Nicolas ; BERNARD Mathieu; MOCUTA Cristian; **BATISTA PESSOA Walter-wilkener**; DORY Jean-baptiste; CHAHINE Rebecca; NOLOT Emmanuel; Francesco D'ACAPITO; FILLOT Frederic; FELLOUH Leïla, "Impact of Te content on the structure of sputtered GeTe/Sb2Te3 superlattices," European Phase Change and Ovonics Symposium (EPCOS), Aachen, Germany, 2017.

- **W. Pessoa**, A. Roule, M.-C Lépy, E. Nolot, "Probing new thin and ultra-thin chalcogenide films with inline WDXRF and XPS metrology," European Conference on X-Ray Spectrometry (EXRS), Gothenburg, Sweden, 2016.

- A.Novikova, M.-C. Lépy, Y. Ménesguen, **W. Pessoa**, H. Rotella, J.-M. André and Philippe Jonnard; "CASTOR, a new tool for combined XRR-GIXRF analysis at SOLEIL," European Conference on X-Ray Spectrometry (EXRS), Gothenburg, Sweden, 2016.

- J.-M, André, P. Jonnard, K. Le Guen, M –Y. Wu, R. Dhawan, A. Singh, M. H. Modi, M. –C. Lépy, Y. Ménesguen, A. Novikova, **W. Pessoa**; "Yoneda effect in planar X-Ray waveguide," International conference on Vacuum Ultraviolet and X-ray Physics (VUVX), Zurich, Switzerland, 2016.

9. Résumé étendu en français

Les matériaux chalcogénures (à base de S, Se, Te) sont largement présent dans les technologies clés génériques (i.e. Key Enabling Technologies). Ils sont d'une importance fondamentale pour des mémoires non-volatiles avancées, des matériaux de récupération d'énergie et de la photonique. Ces matériaux réalisés sous forme d'alliages (binaires, ternaires, quaternaire, etc…) sont dans le centre d'intérêt à la fois comme des éléments de stockage et à la fois comme des sélecteurs pour des mémoires innovatrices à changement de phases (PCRAM) largement développées pour des appareilles portables et pour l'internet des objets (IoT). Des systèmes complexes à base de chalcogénures disposent également d'un ensemble des propriétés uniques pour des optiques non-linaires et des applications dans la gamme des infrarouge moyens : Ils font déjà partie des produits innovateurs commerciaux, des applications spatiales et militaires, et ils sont également des excellents candidats pour les prochaines générations des interconnexions chip-to-chip optiques ultra-rapides. Un numéro croissant des systèmes de récupération d'énergie sont également constitué des systèmes complexes à base de chalcogénures, non seulement pour des applications photovoltaïques mais également pour des matériaux thermoélectriques sans-plomb et pour des matériaux de récupération d'énergie mécanique et magnétique. Les composés de chalcogénures sont largement développés comme des dichalcogénures de métaux de transition pour les applications de matériaux 2-D tel que des super-condensateurs, batteries, électronique, optoélectronique et etc, comme illustré dans Fig. 9.1.

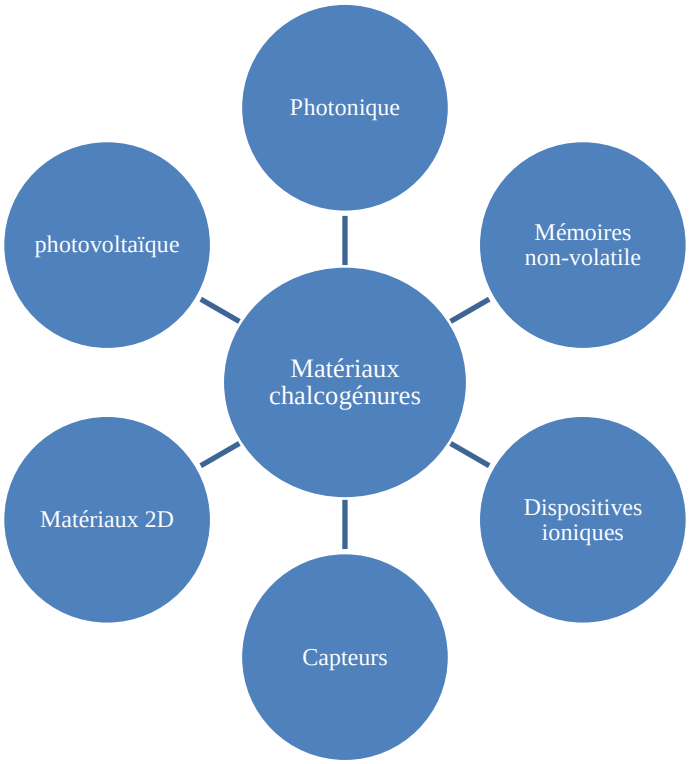

Figure 9.1. Quelques applications importantes des matériaux chalcogénures.

Les nouvelles méthodes de déposition en cours de développement doivent bientôt proportionner des méthodes adaptées pour la fabrication de couches à quelques atomes d'épaisseur à l'échelle industrielle sur des larges substrats (e.g. 300 mm de diamètre) avec une précision atomique. Les matériaux chalcogénures peuvent être synthétisés dans une large gamme stœchiométrique, et par conséquent, avec une large gamme de propriétés chimiques et physiques pouvant être utilisées pour des applications technologiques de pointe. Dans des nombreux cas, ces propriétés, telles que la bande interdite optique, la conductivité thermique et électrique ou les propriétés de changement de phase, peuvent être influencées et affinées par le ratio chalcogén/chalcogén (e.g. S/Se) ou le ratio métal/chalcogén, et également en fonction de l'épaisseur de la couche.

Donc, l'un des défis communs pour le développement et la fabrication d'applications avancées à base de chalcogénure est le contrôle quantitatif et fiable de la stœchiométrie du film ainsi que la distribution en profondeur des éléments. Ceci est une condition préalable à la corrélation précise des propriétés du film avec des conditions de synthèse du film, permettant des temps de développement plus courts et un rendement de production plus élevé.

Par exemple, les mémoires non-volatiles à base de films GeSbTe manquent encore de la stabilité thermique requise pour les applications automobiles (i.e. 10 ans à 150 ºC) ou pour le pré-encodage des données avant le processus de soudage (i.e. 2 min à 260 ºC), c'est qui est une étape très importante pour faire fondre la pâte à souder et assemblage des composants pour former le dispositif final. Ces inconvénients peuvent être résolus en ajustant la proportion de Ge ou en réduisant l'épaisseur du film, comme indiqué dans la Fig. 9.2.

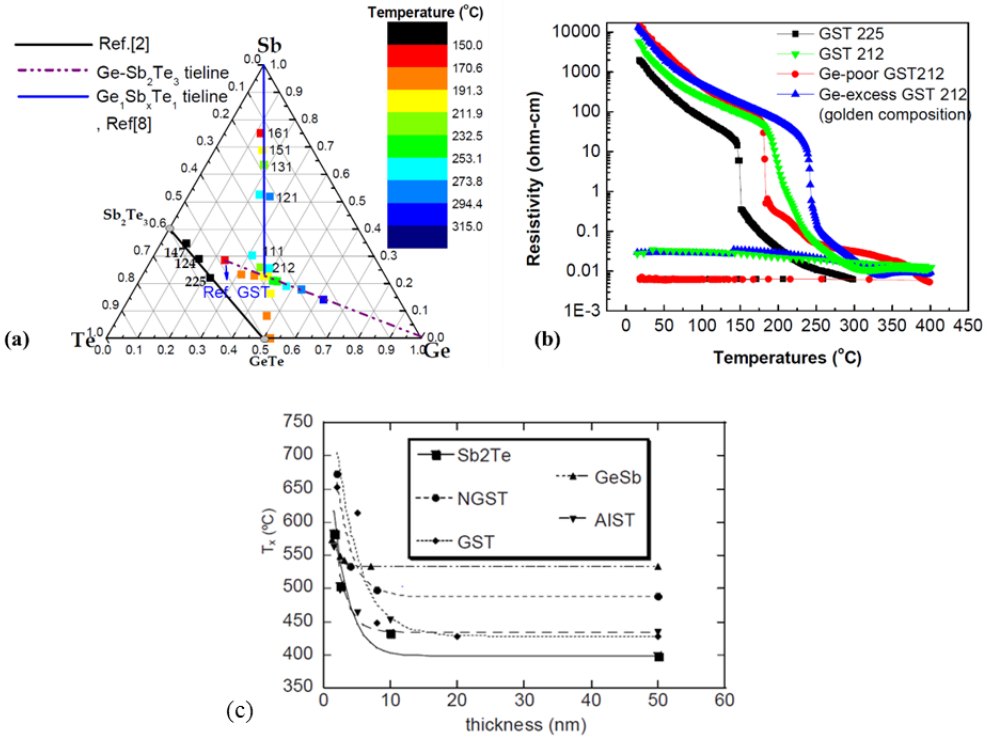

Figure 9.2. Température de cristallisation en fonction de la composition de la phase ternaire Ge-Sb-Te, (b) Résistivité en fonction de la température pour le $Ge_2Sb_2Te_5$ avec l'addition de Ge, (c) Evolution de la température de cristallisation en fonction de l'épaisseur de la couche.

Pour cette raison, la surveillance des processus et le développement de la production de nouveaux matériaux à base de chalcogénure nécessitent des techniques de métrologie couvrant une large gamme de compositions chimiques et de profondeurs sondées avec une haute résolution spatiale ainsi que une haute résolution en profondeur. Donc, dans cette thèse, nous avons développé des protocoles adaptés basés sur trois techniques avancées de rayons X: la fluorescence des rayons X en dispersion de longueur d'onde (WDXRF), la spectroscopie photoélectronique à rayons X (XPS) et la combinaison de la fluorescence des rayons X en incidence rasante (GIXRF) avec la réflectométrie des rayons-X (XRR). Les protocoles ont été principalement développés au sein du CEA-LETI ainsi qu'au synchrotron SOLEIL (Saclay, France) en partenariat avec LNHB (Laboratoire National Henri Becquerel).

Tout d'abord, nous avons développé une procédure XPS *quasi-in situ* par valise à vide dédié au transfert des plaques 300 mm de Si sans remise à l'air (Fig. 9.3). L'objectif a été donc de caractériser la surface des couches minces Ge, Sb, Te et ses composants en étudiant l'évolution de la composition dépendant de l'état surfacique juste après la remise à l'aire et également après vieillissement. L'efficacité des stratégies de capping *in-situ* pour protéger le vieillissement des matériaux en couches minces à base de Te et de Se a également été étudiée. Cette approche nous a permis non seulement d'évaluer l'impact du temps de «queue » dans le flux du processus sur la surface des couches de chalcogénure, mais également de déterminer les états de liaison dépendants de la composition dans les couches minces de chalcogénure.

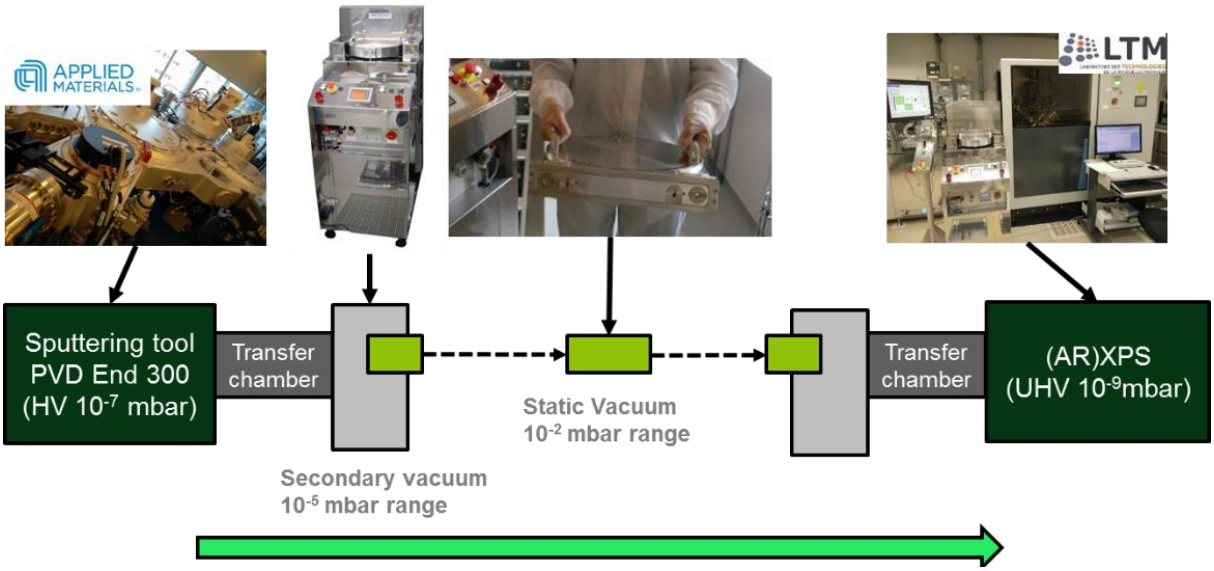

Figure 9.3. Procédure pour réaliser l'analyse XPS *quasi in-situ* par valise à vide. La flèche verte indique l'ordre des étapes à partir de l'équipement de dépôt jusqu'à XPS en ligne.

Nous avons également évalué diverses capping (Ta, SiN et C) déposées *in-situ*, non seulement pour étudier leur efficacité à protéger le matériau chalcogénure contre le vieillissement (oxydation), mais également pour évaluer leurs effets d'interface (par exemple, la diffusion) avec des films de chalcogénure. Cette analyse approfondie a révélé, par exemple, que le recouvrement *in-situ* avec un matériau à faible densité (SiN, C) était une solution efficace pour assouplir les contraintes de temps de « queue » pour les mesures XPS.

En qui concerne la quantification chimique des couches chalcogénures, nous avons développés une routine en ligne basée sur la WDXRF et le XPS. La stratégie en ligne WDXRF-XPS a été élaborée en étudiant des couches Ge-Sb-Te (1 à 200 nm d'épaisseur) et des dichalcogénures de métaux de transition ultra-minces 2D (i.e. MoS2, WS2). Cette approche a permis raffiner les valeurs des paramètres sensibilité relatives pour les électrons des cœurs Te 4d, Sb 4d et Ge3d, permettant ainsi une métrologie basée sur XPS avec une précision maîtrisée. Nous avons également évalué des matériaux PCRAM basés sur des films Ge-Sb-Te dopés au N, et nous avons souligné la nécessité d'une étude approfondie en raison d'effets matrices significatifs et la manque d'étalon pour la quantification de l'azote par WDXRF. Les analyses par faisceau d'ions ont été rigoureusement évaluées en tant que référence possible pour l'étalonnage WDXRF, et donc nous avons pu élaborer un protocole WDXRF pour une fenêtre de processus spécifique.

Concernant les analyses chimiques en profondeur, nous avons développés des protocoles par la combinaison de la fluorescence de rayons en incidence rasante GIXRF) avec la réflectométrie des rayons-X (XRR). Ce protocole a été développé avec des outils de pointe par des stratégies en laboratoire et synchrotron. Nous avons évalué les effets des conditions des mesures et des paramètres instrumentaux sur les performances de l'analyse GIXRF/XRR afin de caractériser avec précision les profils chimiques en profondeur des empilements ultra-minces à base de Te. Ces résultats ont montré à quel point la technique GIXRF/XRR peut être appropriée en tant que technique profilométrie chimique en profondeur non destructive pour des matériaux minces complexes aux propriétés induites par la composition. Donc, l'analyse combinée GIXRF/XRR avec sa fonction instrumentale maîtrisée (divergence, longueur détectée et largeur de faisceau) semble particulièrement adapté pour soutenir le développement de processus en laboratoire et même dans les lignes de production en salle blanche. En plus de cela, nous avons également étudié l'influence de l'ajustement du champ d'ondes stationnaires des rayons-X (XSW) à travers de l'utilisation de substrats multicouches (i.e. miroir de Bragg) pour l'amélioration de la sensibilité de l'analyse GIXRF/XRR en fonction des petites modifications induites par le processus de dépôt, comme illustré dans la Fig. 9.4.

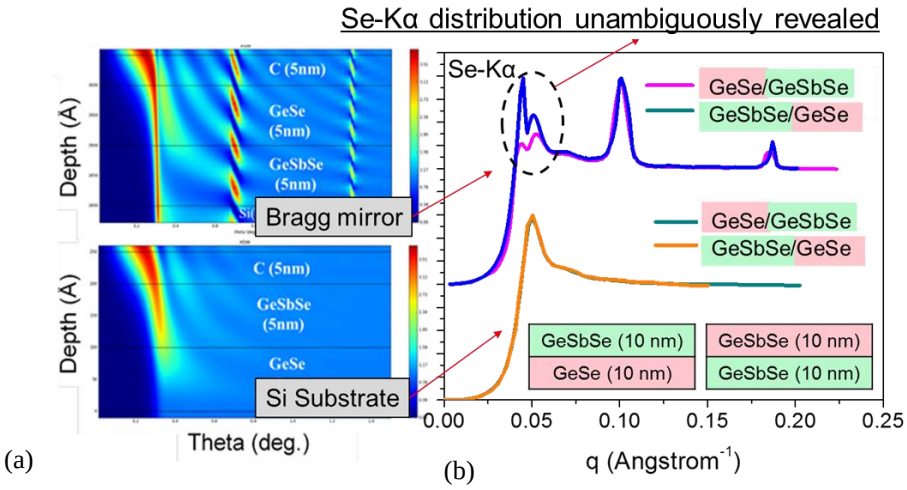

Figure 9.4. (a) Comparaison du champ d'ondes stationnaires (XSW) entre un substrat multicouches du type Bragg et un substrat simple de Si. (b) Mesures expérimentales indiquent que le substrat multicouche est plus approprié pour des empilements complexes dans ce cas : GeSe dopé Sb.

Enfin, nous avons aussi développé une stratégie pour profilométrie chimique en profondeur par ARXPS en ligne. Nous avons démontré sa performance en caractérisant les premières étapes de dépôt de GeTe et $Ge_2Sb_2Te_5$, et donc en nous fournissant des informations clés sur la distribution chimique en profondeur pour le développement des matériaux PCRAM et interfacial-PCRAM pour les prochains nœuds technologiques.

Donc, dans ce travail, nous avons non seulement élaboré des protocoles de métrologie avancés pour le développement de nouveaux films de chalcogénure, mais également des solutions métrologiques pour les nœuds technologiques suivants (28 nm et au-delà), car les outils de métrologie en ligne actuels atteignent leurs limites de détection (Fig. 9.5).

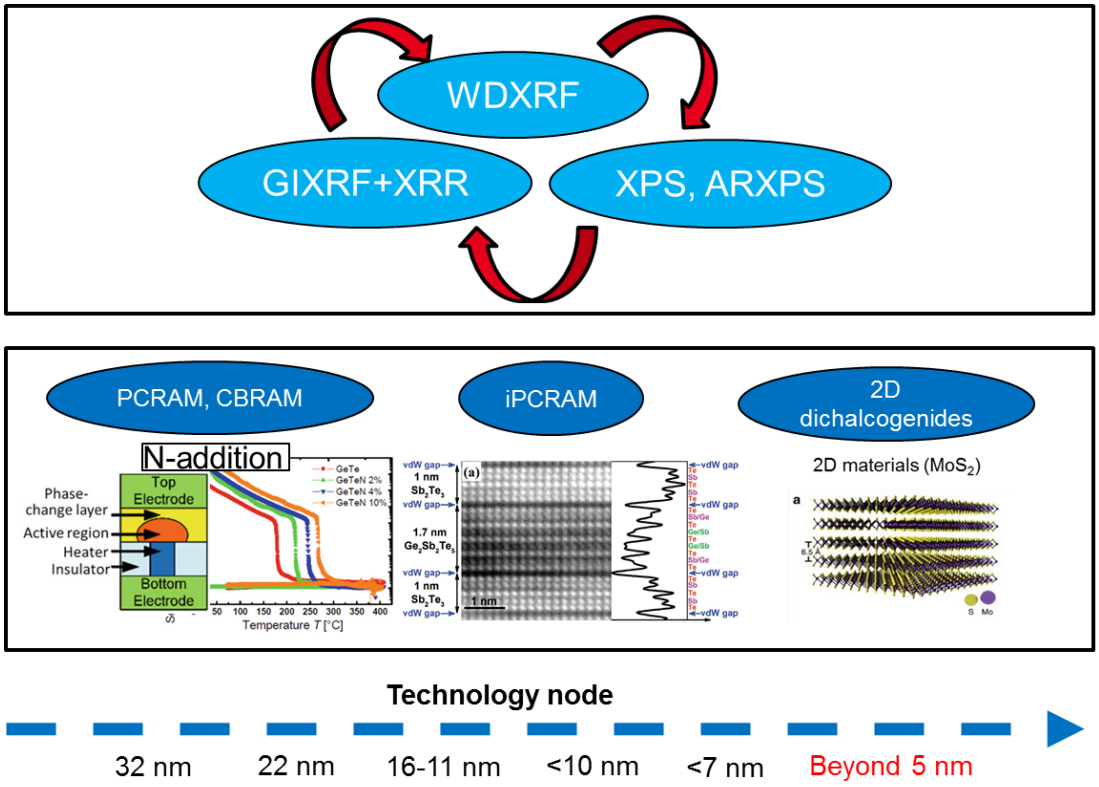

Figure 9.5. Le *fast monitoring* par métrologie des rayons-X avancée permettra de combler les défis fondamentales metrologiques (composition chimique, épaisseurs, effets surface/interfaces) pour le développments des nouveaux matériaux pour les prochains nœuds technologiques.

université PARIS-SACLAY | ÉCOLE DOCTORALE PHENIICS

Title: Probing chalcogenide films by advanced X-ray metrology for the semiconductor industry

Keywords : Chalcogenides; memories ; 2-D materials ; X-rays metrology; XRF; XPS

Abstract: Chalcogenide materials are compounds based on S, Se, and Te elements from group VI of the periodic table. They are receiving an extensive interest not only for applications in resistive memories (PCRAM and CBRAM), photonics and photovoltaics but also in the development of new 2-D materials (e.g. spintronics applications). Chalcogenide materials are already present in the semiconductor roadmaps and it is already replacing flash memories (e.g. phase change material and ovonic threshold switch in new random access memory). For the next technology nodes, chalcogenide properties can be scaled by tuning the chemical composition or by reducing the film thickness. Nonetheless, it also means that their properties become more tightly influenced by the chemical composition, the surface/interface effects and the depth-profile composition. Hence, dedicated metrology protocols must be developed, first to assist the optimization of chalcogenide materials processes in cleanroom environment, then to allow non-destructive process monitoring with industry-driven uncertainties. In this PhD thesis, we developed metrology protocols based on X-ray techniques, dedicated to thin chalcogenides materials and fully compatible with inline monitoring. First, we used *quasi in-situ* X-ray Photoelectron Spectroscopy (XPS) to characterize the surface of Ge, Sb, Te thin materials and compounds, and to study the composition-dependent evolution of the surface after air break and ageing. The efficiency of *in-situ* capping strategies to protect Te-based and Se-based thin layered materials from ageing was also investigated. Secondly, we demonstrated the ability of improved metrology strategies based on in-line Wavelength Dispersive X-ray Fluorescence (WDXRF) and XPS to accurately quantify the chemical composition of Ge-Sb-Te compounds (from 1 to 200 nm) and ultrathin 2D transition metal dichalcogenides (MoS_2, WS_2) Combined WDXRF/XPS analysis was used to determine refined values of composition-dependent relative sensitivity factors for Te4d, Sb4d and Ge3d that allow for XPS-based metrology of PCRAM materials with mastered accuracy. We pointed the need for in-depth study of the significant matrix effects that alter the ability of WDXRF to quantify Nitrogen in Ge-Sb-Te materials: ion beam analysis was carefully investigated as possible input for WDXRF calibration, and a WDXRF protocol was established for inline monitoring of N-doped Ge-Sb-Te films in a specific process window. Finally, we investigated two ways to non-destructively characterize the in-depth chemical distribution in thin chalcogenide films: we demonstrated that the combination of XRF in grazing incidence geometry (GIXRF) and X-ray reflectometry (XRR) was able to unambiguously reveal small process differences along with process-induced diffusion in 10 nm-thick stackings. We showed that the use of multilayered substrate instead of silicon allowed fine-tuning of the depth-dependent X-ray standing wave field, resulting in improved sensitivity of XRR/GIXRF strategies. We also developed an angle-resolved XPS protocol for the evaluation of the first deposition steps of GeTe and $Ge_2Sb_2Te_5$ films, revealing the process-dependent elemental distribution as a function of the film growth. Therefore, in this work we not only elaborated advanced metrology protocols for the development of new chalcogenide films but also metrological solutions for the next technology nodes (28 nm and below), since current in-line metrology tools reach their detection limits.

Université Paris-Saclay
Espace Technologique / Immeuble Discovery
Route de l'Orme aux Merisiers RD 128 / 91190 Saint-Aubin, France

université PARIS-SACLAY | ÉCOLE DOCTORALE PHENIICS

Titre: Développement des protocoles de métrologie des nouveaux matériaux chalcogénures pour l'industrie des semi-conducteurs

Mots clés : Chalcogénures; mémoires; Matériaux 2-D; Métrologie des rayons-X; XRF; XPS

Résumé : Les nouveaux matériaux de type chalcogénures (à base de S, Se, Te) font l'objet d'un intérêt croissant, non seulement pour les applications mémoires avancées, photonique et photovoltaïque, mais également autour des matériaux dichalcogénures innovants à base de métaux de transition (MoS_2, WS_2, ...). Les propriétés de ces matériaux, réalisés sous forme d'alliages binaires ou ternaires, avec ou sans dopage, dépendent fortement de leur composition, du profil de composition dans ces couches très fines, ainsi que des conditions de surface et d'interface (préparation, passivation). La maîtrise des propriétés de ces couches fines, déposées par voie chimique (CVD) ou par co-pulvérisation cathodique magnétron, doit s'appuyer sur des nouveaux protocoles de caractérisation aux uncertitudes optimisées et compatibles avec un contrôle de fabrication en ligne. Dans cette thèse, nous présentons les performances de protocoles de métrologie spécifiquement développés pour l'analyse de couches minces de chalcogénures. Ces protocoles, qui s'appuient essentiellement sur les techniques non destructives de spectroscopie de photoélectrons (XPS) et de fluorescence X (XRF), ont été optimisés pour la caractérisation surfacique des couches ultrafines, l'analyse quantitative de la composition des matériaux complexes à base de tellure ou de soufre, et la mesure du profil de composition dans des couches et empilements < 50 nm. Dans un premier temps, nous présentons l'étude par XPS *quasi in-situ* des propriétés de surface des matériaux Ge, Sb, Te ainsi que de leurs composés binaires et ternaires. Nous mettons en évidence l'évolution de la surface après remise à l'air puis vieillissement, et nous comparons l'efficacité de stratégies d'encapsulation *in-situ* de couches minces à base de Te et Se. Nous démontrons ensuite les performances de protocoles d'analyses par XRF à dispersion de longueur d'onde (WDXRF) et XPS pour la quantification précise de la composition chimique de composés Ge-Sb-Te (de 1 à 200 nm) et de couches ultrafines de dichalcogénures à base de métaux de transition (MoS_2, WS_2). L'analyse combinée WDXRF/XPS permet de mesurer l'évolution avec la composition des facteurs de sensibilité relative des composantes Ge3d, Te4d et Sb4d, et par conséquent d'améliorer la précision de mesure par XPS de la composition des matériaux à changement de phase de type $Ge_xSb_yTe_z$. Nous soulignons également l'influence des effets de matrice sur la capacité de la WDXRF à l'analyse quantitative de l'azote dans des matériaux Ge-Sb-Te. Nous évaluons la possibilité d'un étalonnage de la WDXRF fondé sur des analyses par faisceaux d'ions spécifiques, ce qui permet *in fine* un suivi en ligne de couches GeSbTeN dans une fenêtre procédé donnée. Enfin, nous présentons deux stratégies de caractérisation non destructive du profil de composition dans des couches minces de chalcogénures. D'une part, nous démontrons que la combinaison des techniques de XRF en géométrie d'incidence rasante (GIXRF) et de réflectométrie X (XRR) permet une mise en évidence non ambiguë de faibles variations dans les procédés de dépôts, voire de phénomènes de diffusion dans des empilements de 10 nm d'épaisseur. L'utilisation de substrats multicouches en lieu et place du silicium permet d'optimiser la distribution en profondeur du champ d'ondes stationnaires, ce qui conduit à une amélioration nette de la sensibilité des stratégies XRR / GIXRF. D'autre part, nous montrons l'adéquation de protocoles fondés sur l'analyse XPS résolue en angle pour la caractérisation du profil de composition dans des couches nanométriques de GeTe et $Ge_2Sb_2Te_5$, ce qui permet une étude fine des premières étapes de dépôt de ces matériaux.

Université Paris-Saclay
Espace Technologique / Immeuble Discovery
Route de l'Orme aux Merisiers RD 128 / 91190 Saint-Aubin, France